

DYNAMIC ENHANCED RECOVERY TECHNOLOGIES
CLASS I

Final Report
Part II
July 1994 - October 1995

By
Roger N. Anderson

Performed Under Contract No. DE-FC22-93BC14961

Columbia University
New York, New York



**National Petroleum Technology Office
U. S. DEPARTMENT OF ENERGY
Tulsa, Oklahoma**

DISCLAIMER

This report was prepared as an account of work sponsored by an agency of the United States Government. Neither the United States Government nor any agency thereof, nor any of their employees, makes any warranty, expressed or implied, or assumes any legal liability or responsibility for the accuracy, completeness, or usefulness of any information, apparatus, product, or process disclosed, or represents that its use would not infringe privately owned rights. Reference herein to any specific commercial product, process, or service by trade name, trademark, manufacturer, or otherwise does not necessarily constitute or imply its endorsement, recommendation, or favoring by the United States Government or any agency thereof. The views and opinions of authors expressed herein do not necessarily state or reflect those of the United States Government.

This report has been reproduced directly from the best available copy.

Available to DOE and DOE contractors from the Office of Scientific and Technical Information, P.O. Box 62, Oak Ridge, TN 37831; prices available from (615) 576-8401.

Available to the public from the National Technical Information Service, U.S. Department of Commerce, 5285 Port Royal Rd., Springfield VA 22161

Dynamic Enhanced Recovery Technologies
Class I
Part II

By
Roger N. Anderson

Work Performed Under Contract No. DE-FC22-93BC14961

Prepared for
U.S. Department of Energy
Assistant Secretary for Fossil Energy

Chandra Nautiyal, Technology Manager
National Petroleum Technology Office
P.O. Box 3628
Tulsa, OK 74101

Prepared by:
Columbia University
New York, NY 10021

Task 5 Application of Akcess.Basin to SEI Block 330 Area

A. INTRODUCTION

The AKCESS.Basin Modeling System was developed to investigate phenomena associated with hydrocarbon migration up the Red Fault of the South Eugene Island Minibasin. It is thought that hydrocarbons moved up this fault to charge Pennzoil's Block 330 oil and gas fields, which are among the largest accumulations of oil and gas in the Gulf of Mexico. Because the strata that host the oil and gas reservoirs are less than 1.5 ma old, and some only ~0.46 ma, because there are temperature anomalies along the Red Fault that are of the form that pulses of fluid flow up the fault might produce, and because some of the Pennzoil Reservoirs have produced more oil than is conventionally thought possible (up to and perhaps more than 100% of the oil originally in place), it is thought that hydrocarbon migration up the Red Fault may have occurred very recently or be taking place at the present day. As part of this project the Red Fault was drilled to investigate these possibilities. The fault was drilled at the transition zone between soft and hard overpressure; massive amounts of data were collected and analyzed.

The part of the project reported here is concerned with modeling. Our charge was to develop a modeling methodology capable of realistically addressing temperatures and fluid flow in a data cube centered on the drilled portions of the Red Fault. The modeling was to be of large enough scale to encompass phenomena associated with and recent hydrocarbon migration up the Red Fault. The models were to address: (1) the cause of pressure, temperature, fluid chemical, and porosity anomalies near the Red Fault, (2) the possible sources of oil and gas moving up the fault, and (3) the causes of organic and inorganic chemical alteration near the fault. Specific attention was to be taken of: (1) porosity and excess pressure development in the RVE, (2) hydrocarbon maturation, (3) detailed fluid flow near the fault focussing especially where high permeability sands were juxtaposed, (4) the effects of salt diapirism on subsurface temperatures, (5) the effects of fault movement on fault permeability and fluid venting out of the fault, (6) the effects of gas venting on oil migration, and (7) the effects of fluid flow (water, gas, and oil) on sediment mineralogy. The modeling was to be carried out in 3D as well as 2D.

These objectives, as reported below, have been largely met. Several new concepts of potential significance have emerged from the modeling. In particular it has been found that:

- (1) Temperature anomalies may be caused by the low thermal conductivity of the hydrocarbon reservoirs.
- (2) Hydrocarbons may migrate up faults as propagating fluid filled cracks.
- (3) Hydrocarbon gas may cause sealing and fundamentally control the pattern of fluid flow.
- (4) The porosity distribution in the study area is most compatible with a seal (pressure transition zone) that migrates upward through the section as sedimentation takes place.

Because the project reported here was very large, the DOE managers have requested that this report be kept as short as possible. As a result discussion will be focussed on the South Eugene study area itself. All material already published or in press, or that will be soon available in other form, is only summarized here. Regional modeling, important in providing a context for the SEI 330 models, will be described but not presented in detail.

B. THE GEOGRAPHIC CONTEXT OF THE MODELING

A critical question from the onset of the project was the size of the model volume required to capture the processes that drove and are driving fluid and hydrocarbon venting in up the Red Fault. Almost certainly the process scale is larger than the ~20 km dimensions South Eugene Island Block 330 Minibasin. Modeling was carried out on a range of scales to assure capture of the relevant processes: The largest scale was a 1200 km section running from the Arkansas-Louisiana boundary to the Sigsbee knolls (the Exxon #1 line). This line was used to constrain the flexural rigidity of the lithosphere and to show that salt diapirism is required to provide accommodation space for sediments deposited at the scales of the higher resolution modeling. The Exxon #1 line and location of the South Eugene Island study area is shown in Figure V.1.

The next largest scale of modeling is about a 100 x 100 km as shown in Figure V.2 (1° latitude = 110 km). As shown in Figure V.2 modeling on this scale was based on six interpreted seismic lines contributed by Arco, and two 2D seismic lines that were interpreted as part of this project by Mark Rowan and Colorado University (two bold lines).

The highest resolution modeling was carried out on a ~30 x 30 km scale. It focussed on temperature the South Eugene Island Block 330 Minibasin. The geology upon which the modeling is based was derived from the interpretation of well logs, 2D (Alexander, 1994 Cornell PhD thesis) and 3D (Coehlo, Cornell PhD thesis in progress) seismic surveys, and well logs. The detailed 3D modeling is based on nine NE-SW sections mapped across Pennzoil's 3D seismic survey that take all this information into account. These nine sections are shown in Figure V.3. The sections capture all the major sand units in the cube.

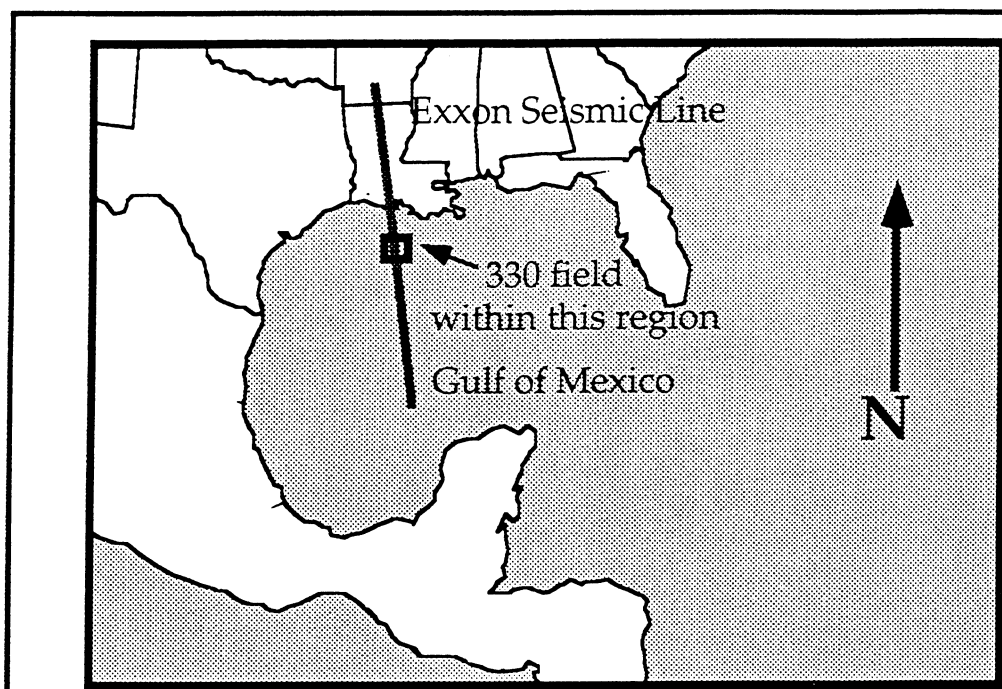


Figure V.1 Location of Block 330 study area and Exxon Louisiana #1 Line.

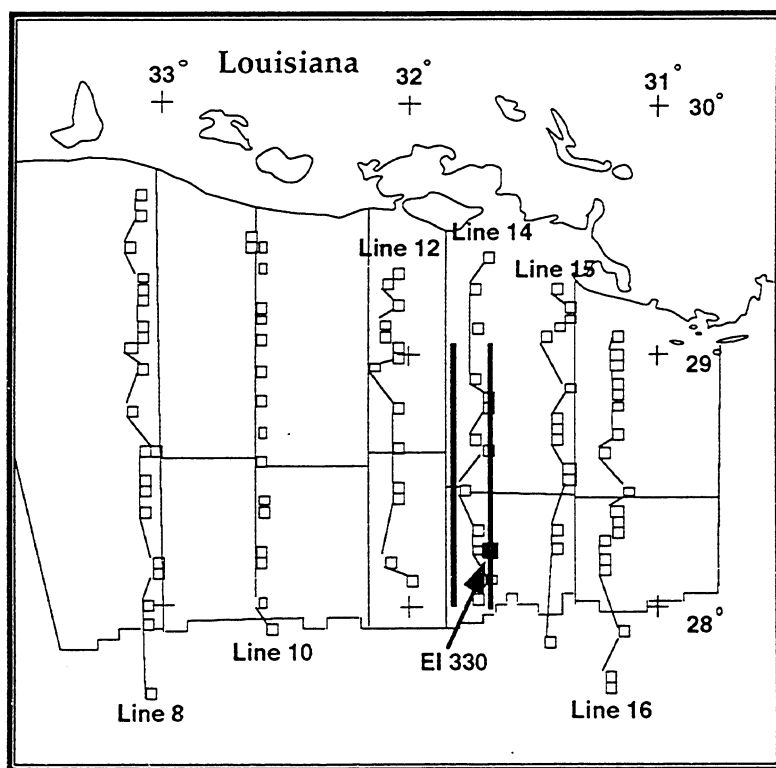


Figure V.2. Regional Arco and Rowan 2D seismic lines.

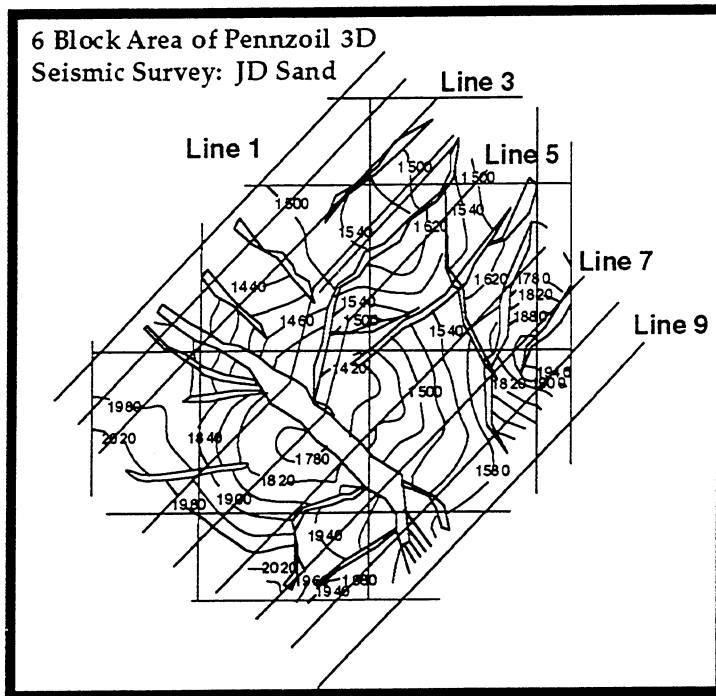


Figure V.3. The nine 2D seismic sections that comprise our 3D model of the SEI Block 330 Data Cube.

C. REGIONAL MODELING

1. 1200 km Scale (L. M. Cathles)

The largest scale modeling was carried out on the 1200 km long Exxon Louisiana Line #1 (Figure V.1). The history of sedimentation was defined by stratigraphy provided by Exxon. The loading history inferred from this stratigraphy was first used to calculate the isostatic subsidence, assuming various values for the flexural rigidity of the lithosphere in this area of the Gulf Coast. Past sea levels were inferred from the calculated isostatic adjustment, sedimentation, and calculated compaction. The sea levels were then filtered, and the high frequency changes in sea level accommodated by salt movement. Results of that modeling (Figure V.4) show that accommodation space for the 16 km thick sediment column can be provided by isostatic adjustment, provided the flexural rigidity of the lithosphere is about 10^{23} N-m. Reasonable sea levels are predicted from the present sea level and the pattern of sedimentation provided the flexural rigidity is about this value. For greater flexural rigidities, periods are predicted when sediments were substantially above sea level and significant erosion should have occurred. This is not observed. Thus the flexural rigidity of the Louisiana Gulf is about 10^{23} N-m, a figure compatible with previous estimates and estimates of the flexural rigidity in the North Sea.

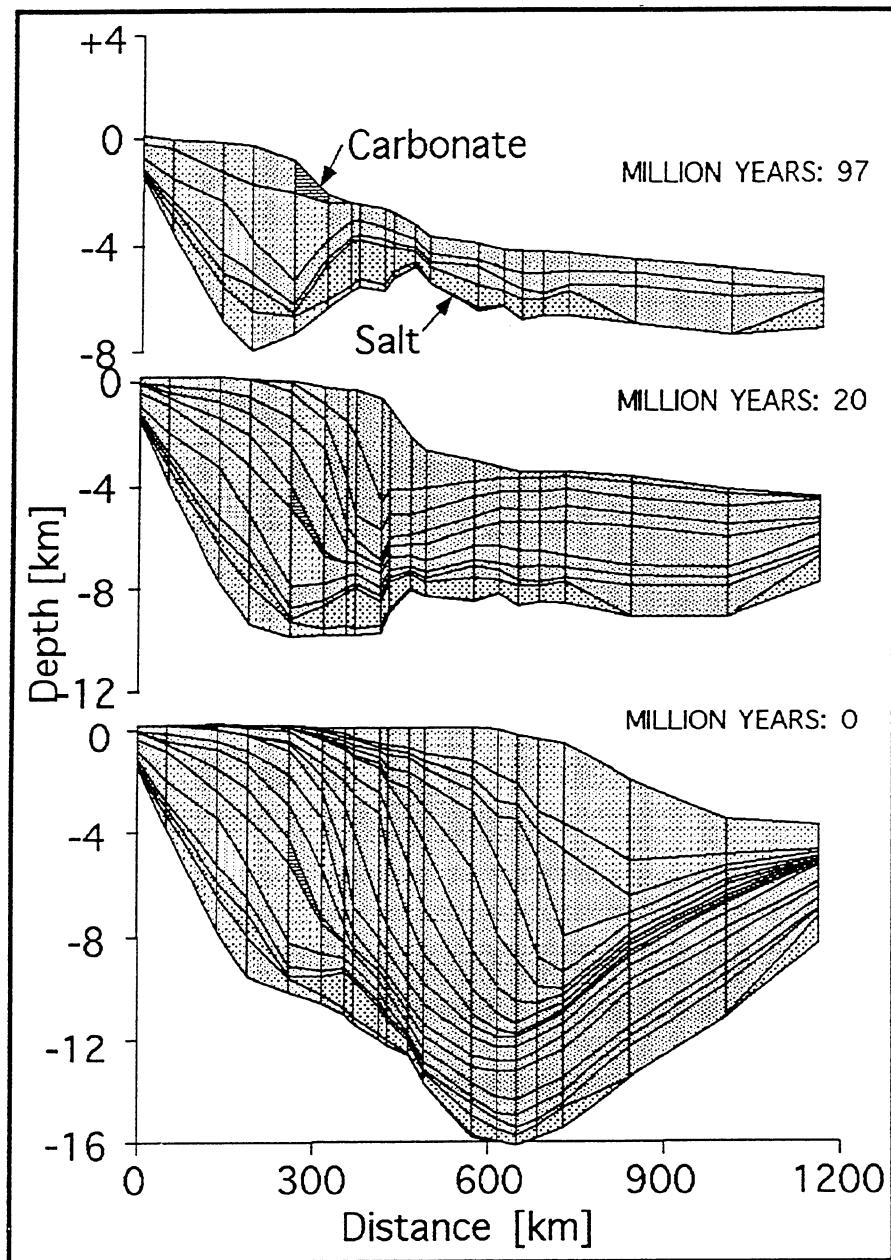


Figure V.4. Simulated evolution of Exxon Line #1, an interpreted 1200 km composite seismic line running from the Arkansas-Louisiana border to the Sigsbee Knolls. Accommodation space for the 16 km of sediment is provided by isostatic adjustment on a 10^{23} N-m lithosphere. A lithosphere with this flexural rigidity (or less) also predicts reasonable past sea levels (e.g., no significant erosional unconformities).

2. 100 km Scale Modeling (J. Huntton, MTU, and R. Cornelius, Cornell)

Modeling on this scale simulates the southward migration of the shelf edge and shows that a natural consequence of the sedimentation pattern and the requirements of conservation of sediment and salt volume is the observed redistribution of salt from sills to domes. In addition, fluid flow calculations show that there is a natural tendency for connate fluids to vent up the margins of the salt domes, even when those margins have the same permeability as sediments elsewhere.

Modeling was carried out utilizing a method by which the modeler could specify the position of the shelf margin as a function of time. The oceanward increase of water depth on the continental shelf and slope, and the maximum water depth in the oceanic parts of the Gulf Basin were assumed to be the same in the past as today. With this assumption the paleo-ocean depth profile can be specified by tabulating the position of the shelf break at all modeling timesteps. Estimates of the shelf break position were made from the thickness and character of the sediments, and the position and geometry of salt domes.

Salt was redistributed (and dissolved) according to a simple algorithm that links sedimentation above the salt to the salt movement. Where sedimentation during a particular timestep is greater than the average amount across a two-dimensional section, salt is removed from that position at that timestep. Where sedimentation is less than the average amount, salt is added to the salt body for that time step. This part of the algorithm is not new. It is utilized in several salt modeling packages. However, in addition to simple conservation of salt and sediment, we minimize the total amount of salt required to accommodate the sedimentation pattern, and require that a salt weld not re-inflate once it is formed. This methodology produces a continuously basinward migrating salt sheet that is progressively mobilized in to domes as shown in Figure V.5. The present thickness of salt is honored in the simulations. The present thickness of salt in seismic section is subject to interpretation. The results of the modeling were most geologically reasonable when the thickness of salt inferred from seismic sections was taken to be the smallest possible value (thinnest salt sills).

The results of the modeling are described here for a single case. This case is known as Arco Line 10, and it is located to the west of the Eugene Island study area. The total length of the line is 199.54 km and as shown in Figure V.2, it extends from near the shoreline due south along the boundary between East Cameron/Vermillion and East Cameron South/Vermillion South. It extends slightly basinward of the latter boundary. A previous DOE quarterly report fully described modeling of regional Arco Line 8.

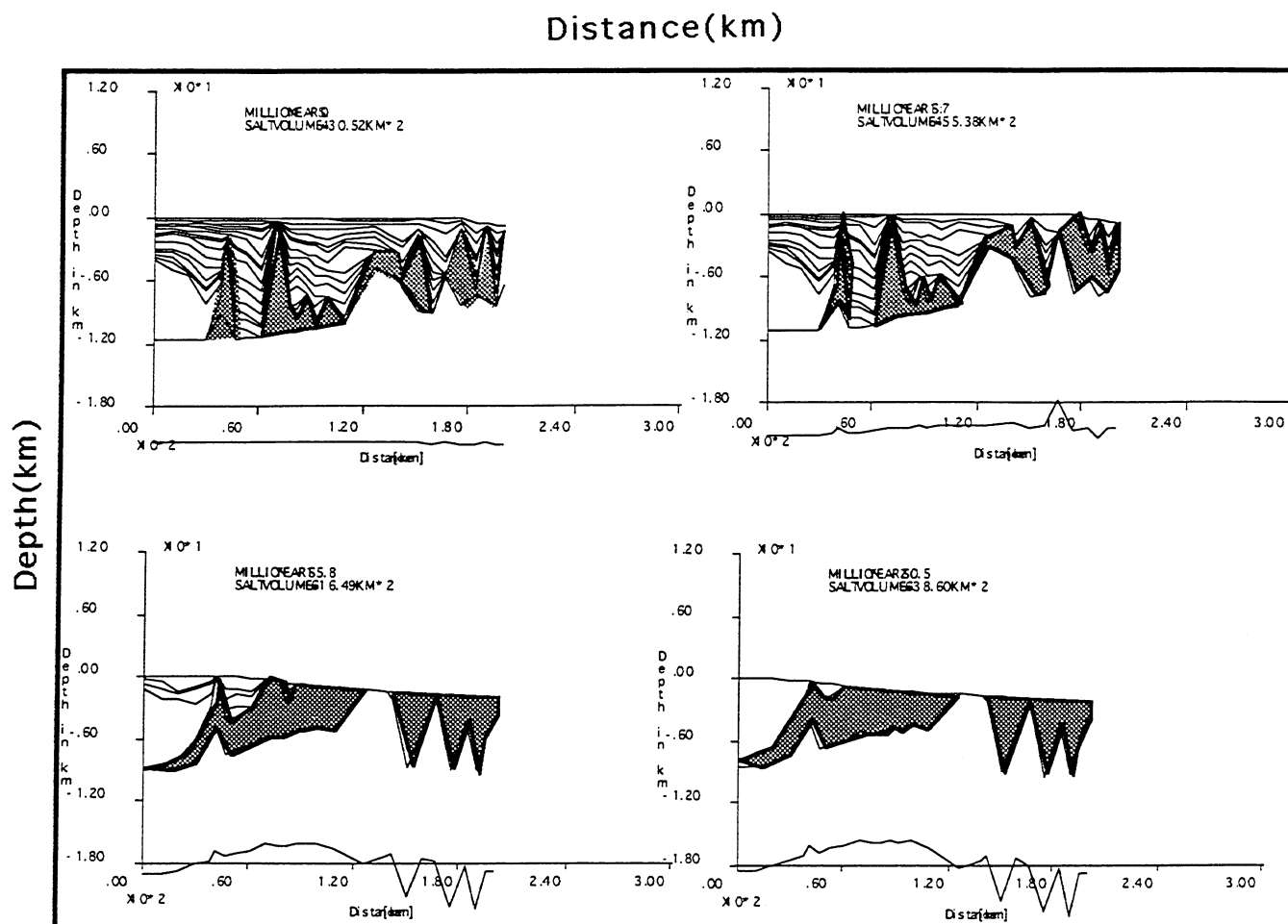


Figure V.5. Arco Line 10 AGEOHIST output at (right to left, top to bottom) 0, 1.7, 15.8, and 20.5 Ma. Sequence shows mobilization of salt from surface sill into domes. Line 10 is located in Figure V.2.

In Figure V.5, the dark subhorizontal lines represent sequence boundaries that form the upper and lower boundaries of the macro elements in the AKCESS.Basin modeling. The salt is shown in gray and, at 0 ma, is confined to isolated domes on the northern (left) side of the figure and to interconnected domes further to the south (right). This model was constructed using 27 vertical pseudowells placed appropriately to capture the basic characteristics of the subsurface. Refinement of the model is possible and desirable in areas where this first pass does not accurately reflect the subsurface geology. The base of the salt section was assumed to be absent beneath minibasins and to have a thickness below domes or walls so that its base was no deeper than the depth of the surrounding minibasin and the salt thickness was minimized. It seems likely, in light of subsalt imaging that is now appearing in vendor's displays at technical conventions, that the salt beneath domes and walls may actually be even thinner in some areas. We did not, however have extensive subsalt information so the estimates were made consistently. They can be modified in the future if necessary. Note that Figure V.5 is not plotted to scale, and that the vertical exaggeration is extreme. The abrupt boundaries on salt domes and walls that are apparent in Figure V.5 become smooth gradual features when the figure is plotted at a 1:1 scale.

The Section shown in Figure V.5 was modeled for both temperature and compactive fluid flow. Temperature at the present time, after the basin is fully developed through forward modeling, shows the temperature increases with depth from a minimum of 3.9 degrees to a maximum of 412.6 degrees. The isotherms are elevated by up to 60°C beneath minibasins and depressed up to 80°C beneath salt domes. This is a result of the

contrast in thermal conductivity between salt and sediment. Again, the anomalies may be somewhat exaggerated if the salt thickness in the model is larger than it should be. However similar magnitude temperature anomalies were computed by an extensive independent modeling study that was also part of this DOE project (Mello, 1994).

An important feature noticed by the simulations of compactive fluid flow is that fluid flow is significantly concentrated at the margins of the northernmost salt structure. This pattern of fluid flow out of minibasins and up along the margins of salt structures is observed for all of the modeled minibasins at various stages in their evolution. Most hydrocarbon migration occurs in conjunction (and possibly assisted by) connate water flow. The natural concentration of compactive flow at salt dome margins may in part account for the occurrence of hydrocarbon reservoirs above and along the margins of salt domes. It should be emphasized that the concentration of flow at the salt margins was not due to the margins having a greater than typical permeability. The permeability of the sediments adjacent of the domes in the models was the same as the permeability of the sediments elsewhere.

The modeling is described in more detail in Huntoon, et. al. (in preparation). The calculations reported there will include estimates of the regional hydrocarbon maturation and the fluid flow driven by maturation reactions as well as compaction.

D. SEI BLOCK 330 AREA MODELING

The most intensive modeling addressed processes on a 30 x 30 km scale in the main SEI study area. A three dimensional data cube was assembled and analyzed through modeling. Modeling requires a computational grid, material properties, and heat, fluid flow, and chemical computation. Below we first describe the construction and geometric analysis of the computational grid, then we describe the determination of the proper material properties and the thermal state of the data cube, and finally we describe the modeling and conclusions reached from it.

1. The 3D Modeling Grid (L. M. Cathles, Cornell)

The 9 NE-SW sections shown in Figure V.3 were processed to obtain the evolution of the SEI Block 330 area over the last 3.4 Ma. The grid consists of time horizons and appropriately-selected "pseudo-wells". Salt was redistributed in 3D by processing each section twice and solving a set of equations to make the salt redistribution as uniform as possible in 3D. The geologic evolution of all nine lines shown in Figure V.3 is shown in Figure V.6. The thickness of the present (0 ma) section is 8.5 km, and each section is about 12 km long. Figure V.7 shows three "Butterfly" diagrams. These diagrams show the top, bottom, and three sides of the 3D grid at three different stages of basin evolution. It can be seen from these two figures that at 3.4 Ma the area that now holds the South Eugene Island minibasin and the Pennzoil oil and gas reservoirs was covered by a salt sheet about 2 km thick. Over the next 0.8 Ma this salt sheet was rapidly buried by thick shales. The sheet remobilized into a large dome at the right hand side (southern margin) of the data cube, in the area that is now the SEI minibasin. The salt dome was not uniform. It was large in the west, thinner in the middle, and very large on the far eastern side of the data cube. A salt ridge remains to this day on the eastern side of the data cube. Over the next 2.6 Ma this salt dome was itself loaded with sediments and remobilized. Its collapse provided the accommodation space for the SEI Block 330 minibasin. Starting about 1.5 Ma and continuing to the present, thin sands were periodically deposited over the whole area. Many of these sands are now filled with hydrocarbons.

Although it is not evident in the small images of Figure V.6 and 7, the movement of strata on each of the four NE-SW faults is accurately resolved. The juxtaposition of sands

across these faults is of interest as many oil companies believe that fluids migrate up section by crossing the fault where a lower stratigraphic sand is juxtaposed against one higher in the stratigraphy. In this fashion fluids step up through the section. Fault plane (Allan-type) maps showing the juxtaposition of sands are often prepared from 3D seismic surveys, and the maps are then used to infer what connections there might have been at past times. The AGEOHIST pre-processor provides a way to automatically generate Allan-type sections over the full span of the basin's history, explicitly taking into account decompaction and eliminating the need for inference. Decompaction can be significant and can make a significant difference when specific sand-sand connections occur across the faults. Allan-type diagrams for the 4 main E-W faults on the northern margin of the South Eugene Island Block 330 minibasin are shown in Figure V.8.

The sections in Figure V.8 are presented such that the viewer is looking from the north (left side of sections in Figure V.6) toward the south and into the Block 330 minibasin on the far south end of the sections in Figure V.6. Sands on the upthrown (northern) side of the faults are grey. They cut across the sands in the downthrown minibasin which black. Fault 3 is the Red Fault. Fault 4 is the fault just inside the minibasin from the Red Fault. There is a break in sand continuity in most of the faults about a third of the way across all the sections. This offset represents throw on the NE-SW trending fault captured between Lines 4 and 5 (see Figure V.3). The fault plane sand connections captured by the grid and shown in Figure V.8 allows Allan-type fluid flow to be calculated in our 3D basin simulations.

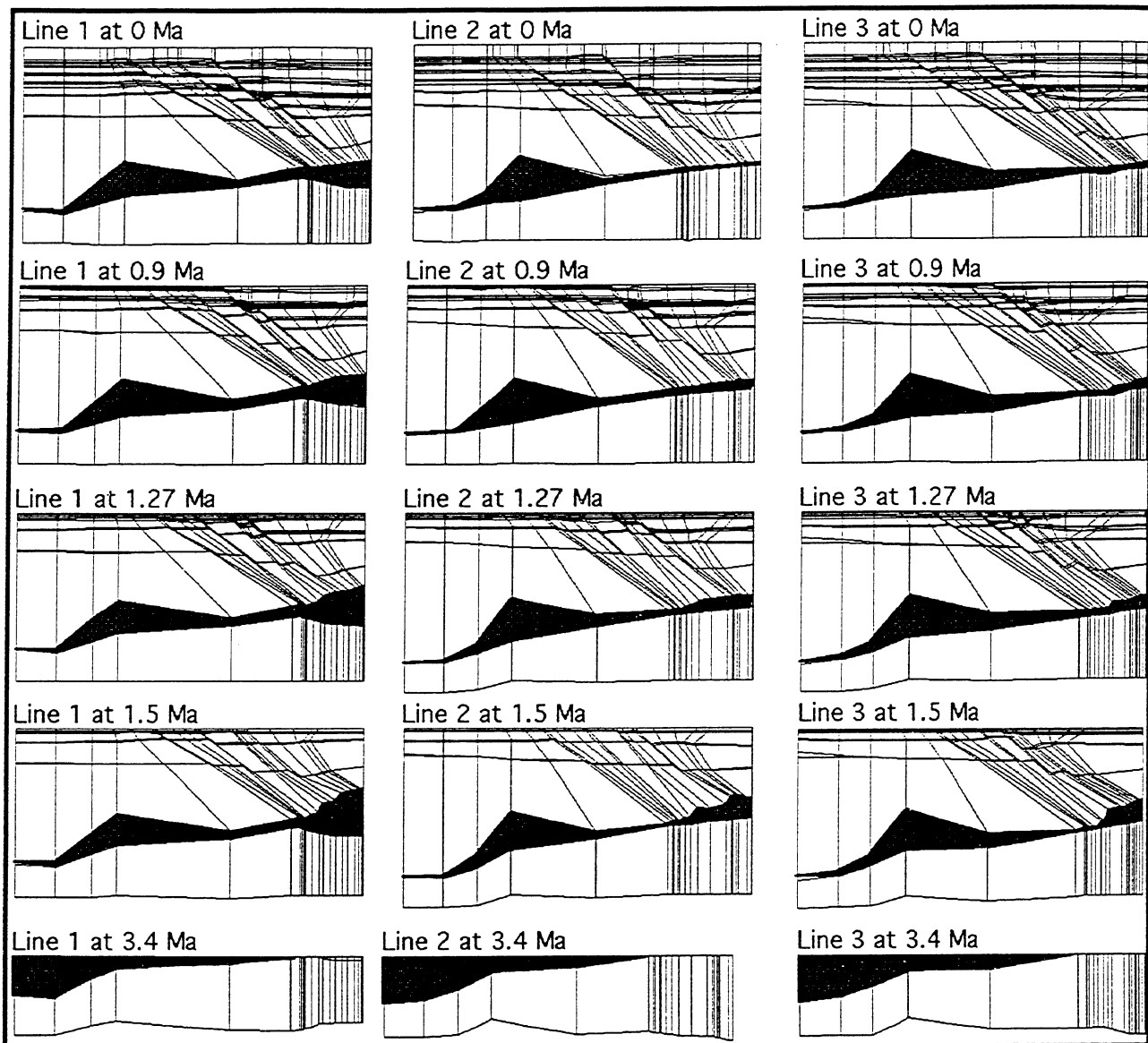


Figure V.6a. Geologic evolution of section lines 1 to 3. The present (0 ma) section is 8.5 km thick and all sections are about 12 km long. Salt is shaded in this diagram, but not in the subsequent 2 diagrams in this series. See Figure V.3 for locations.

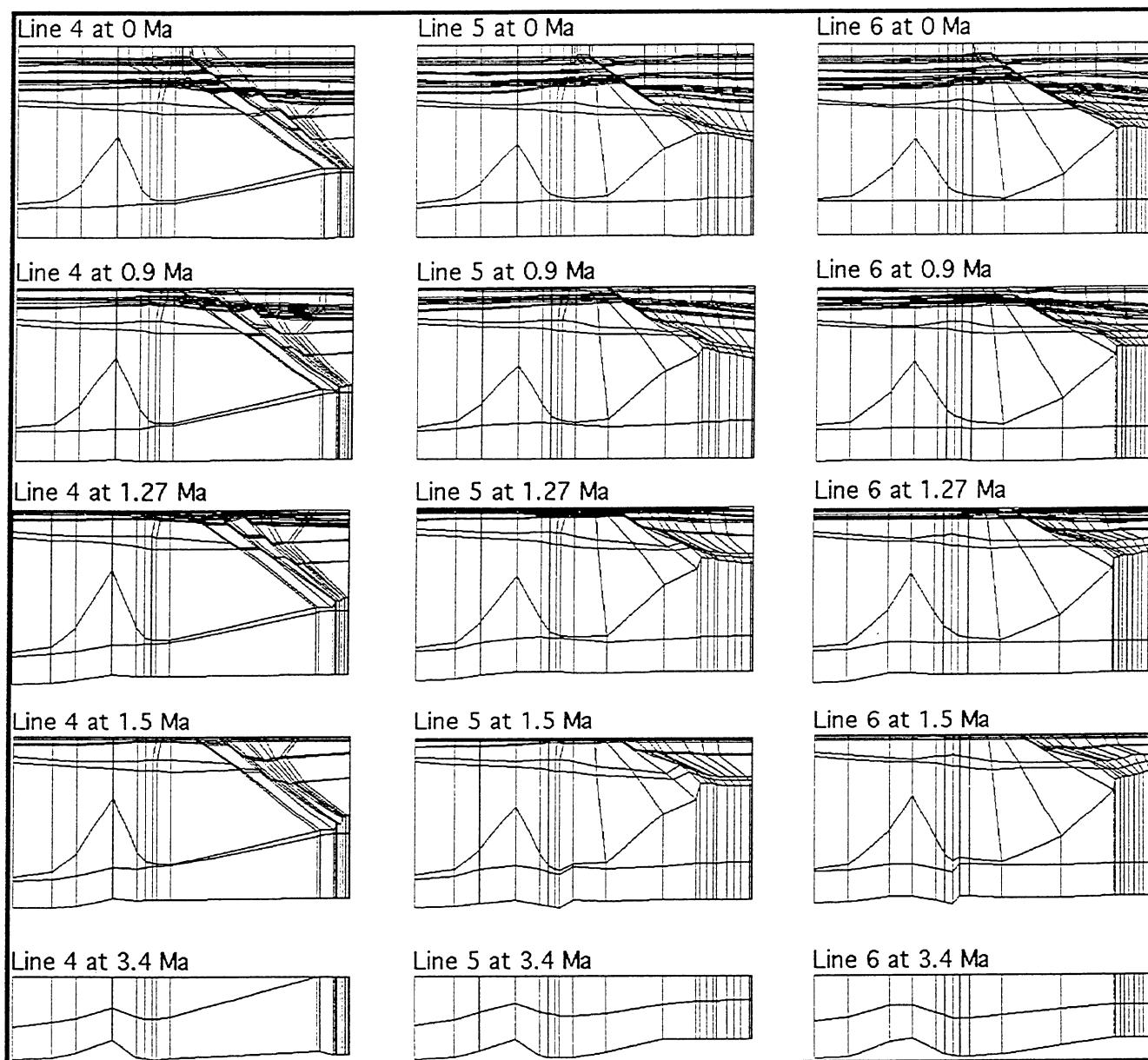


Figure V.6b. Evolution of section lines 4 to 6. The present (0 ma) section is 8.5 km thick and all sections are about 12 km long. See Figure V.3 for location.

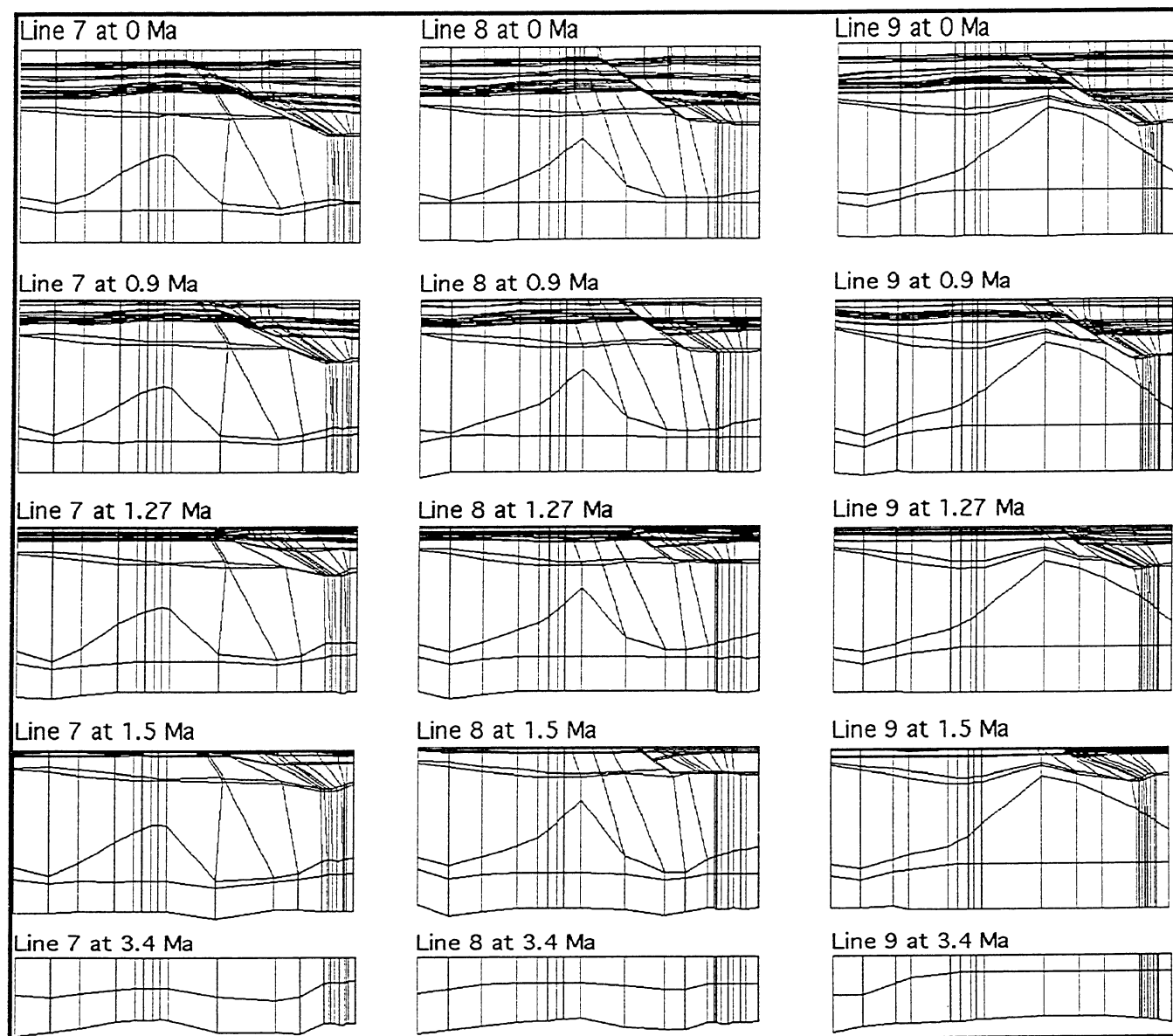


Figure V.6.c. Evolution of section lines 7-9. The present (0 ma) section is 8.5 km thick and all sections are about 12 km long. See Figure V.3 for location.

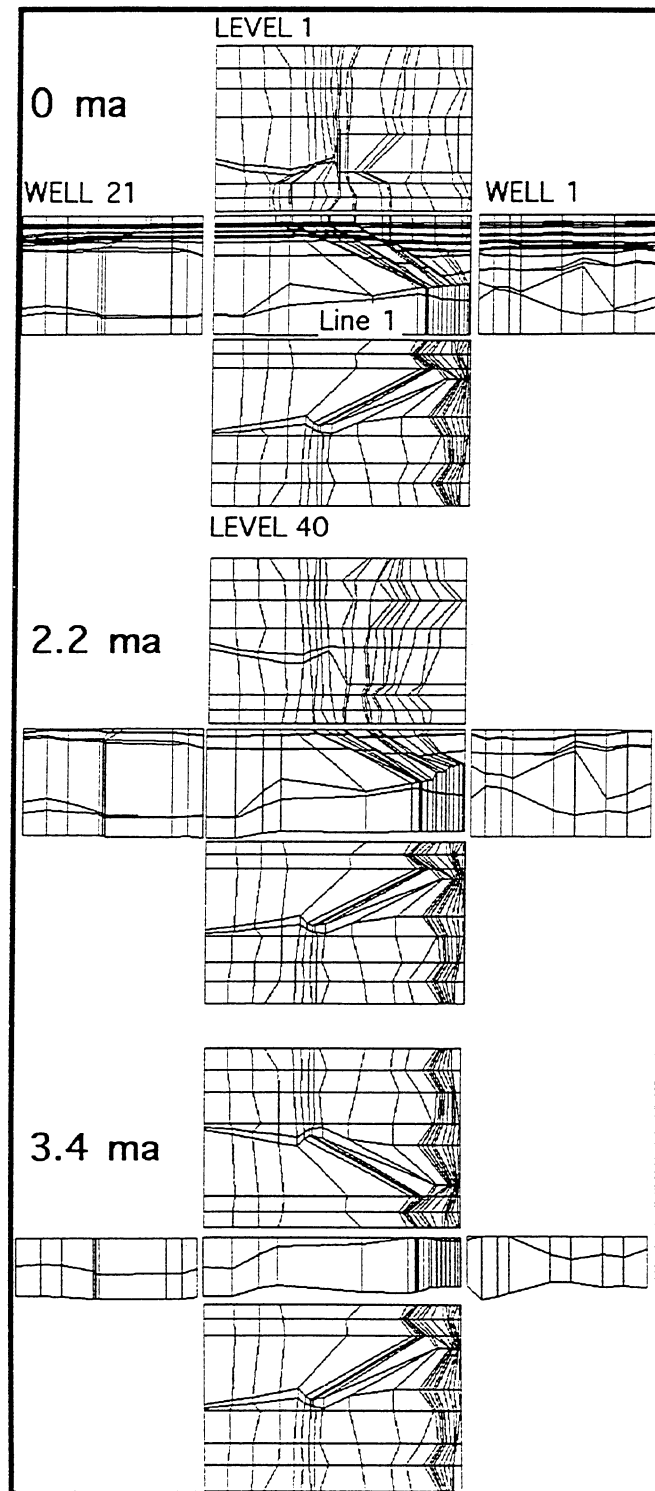
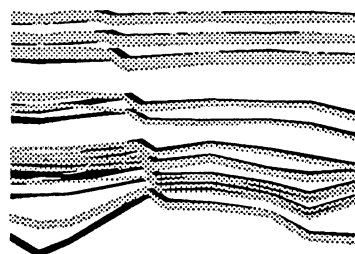
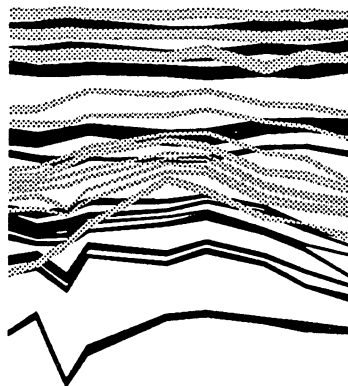


Figure V.7 Butterfly diagram showing data cube modeling grid at three stages of basin evolution. Diagram shows the top (Level 1), bottom (level 40), and sides (Well 21 and 1) of section line 1. See Figure V.3 for location of section line 1, and Figure V.6a for additional details.

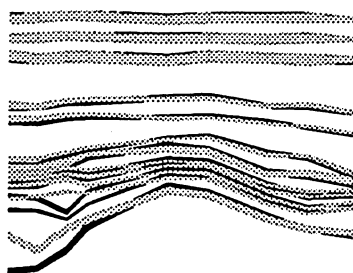
Sand juxtapositions: fault 1 at 0 Ma



Sand juxtapositions: fault 3 at 0 Ma



Sand juxtapositions: fault 2 at 0 Ma



Sand juxtapositions: fault 4 at 0 Ma

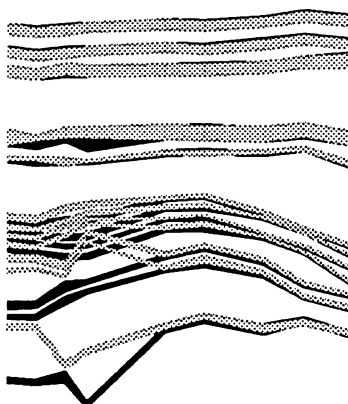
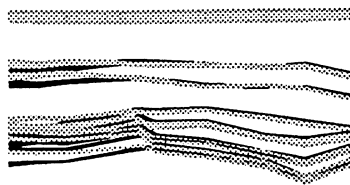
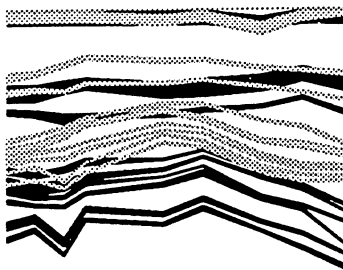


Figure V.8a. Allen-type fault plane diagrams showing the juxtaposition of sands across the four major E-W faults in the SEI Block 330 study area at the present time (0 ma)

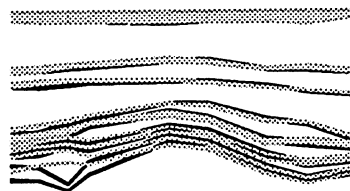
Sand juxtapositions fault 1, 0.65 Ma



Sand juxtapositions fault 3, 0.65 Ma



Sand juxtapositions fault 2, 0.65 Ma



Sand juxtapositions fault 4, 0.65 Ma

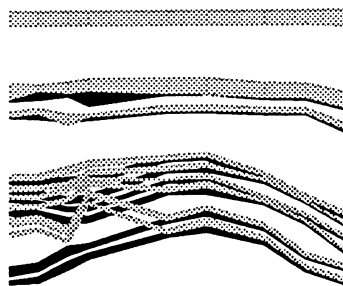
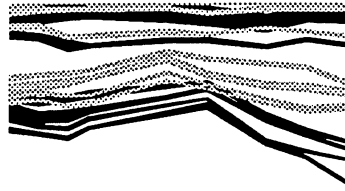


Figure V.8b. Allen-type fault plane diagrams showing the juxtaposition of sands across the four major E-W faults in the SEI Block 330 study area at 0.65 ma.

Sand juxtapositions fault 1, 0.9 Ma



Sand juxtapositions fault 3, 0.9 Ma



Sand juxtapositions fault 2, 0.9 Ma



Sand juxtapositions fault 4, 0.9 Ma

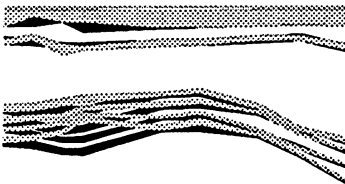


Figure V.8c. Allen-type fault plane diagrams showing the juxtaposition of sands across the four major E-W faults in the SEI Block 330 study area at 0.90 ma.

2. Temperature Anomalies in Block 330 (by D. Coehlo, Cornell University)

Present day temperature in South Eugene Island Block 330 is a particularly critical parameter for modeling. A principal hypothesis of this project, founded in geological / geochemical reasoning most recently discussed by Whelan (1995), as well as in the geometry of the anomalies with respect to the main fault system (known as the "Red Fault System"), was that the migration of hot fluids along the fault planes could be responsible for a positive temperature anomaly observed there (Holland et al., 1990). Evidence for localized fluid migration through seepages along the fault system exists at the sea bottom in the South Eugene Island area (Holland et al., 1990). However, rapid fluid migration would be necessary to produce the observed anomalies.

Guerin (1995), using bottom-hole temperature data and a steady-state finite difference heat conduction model, concluded that if the temperature field is corrected for the effect of the salt domes a positive residue is left which is probably due to fluid advection. His model assumes the thermal conductivities are constant for each layer. By comparing the pure conductive heat transfer and pure advective one, Guerin conclude that the difference is due to fluid flow along the fault system.

McKenna (1994), did a similar study in the same area and, after recognizing the impossibility of resolving the spatially restricted thermal anomaly along fault planes, concluded that the thermal anomaly in the area could be explained by sedimentation differences between the downthrown and upthrown sides of the Red Fault System. Contrary to Guerin, McKenna concluded the same temperature anomalies attributed by Guerin to fluid flow were due to differential sedimentation across the Red Fault system.

Losh et al. (1994) observed that the well 330-PZ-6ST shows geochemical evidence of significant fluid flow but the Pathfinder Well, located only 1000 ft away, does not. This suggests that the pathways for fluids along the Red Fault could be highly localized.

We followed the same steps as the previous authors, and compiled a database of bottom-hole temperatures. Our data set consists of approximately 400 measurements taken in vertical and inclined wells, as well as in exploratory and production wells. The information compiled was the depth of the temperature measurements, the temperatures and the time after stopping the mud circulation. Unfortunately, there is no data on the duration of mud circulation.

In the wells with more than one measurement at a single depth we applied the Horner plot technique as described in Dowdle and Cobb (1975) to correct for the cooling effect due to the mud circulation. The Horner method requires the mud circulation time as well as the time since the end of circulation at which multiple temperature measurements were made. Because the circulation time was not available, a sensitivity analysis was done to determine the impact of the mud circulation time on the magnitude of the Horner plot temperature correction. Figure V.9 gives an example. This plot shows that the Horner method gives similar corrected temperatures provided the circulation time is relatively short. The corrected temperatures shift significantly in the cases shown in Figures V.9 only when the circulation time exceeds about 14 hours. Dowdle and Cobb (op. cit.) pointed out that the Horner plot method is most reliable for short circulation times, basically for this reason. Common industry practice in the Gulf of Mexico makes it unlikely that circulation times exceeded 10 hours. Provided this is the case, Figure V.9 suggests it is possible to correct bottom hole temperatures to $\pm 2^{\circ}\text{F}$ by assuming a circulation time of 6 hours. The time of circulation could be a few hours or as much as 10 hours and the correction would still be accurate to $\pm 2^{\circ}\text{F}$ (1.1°C).

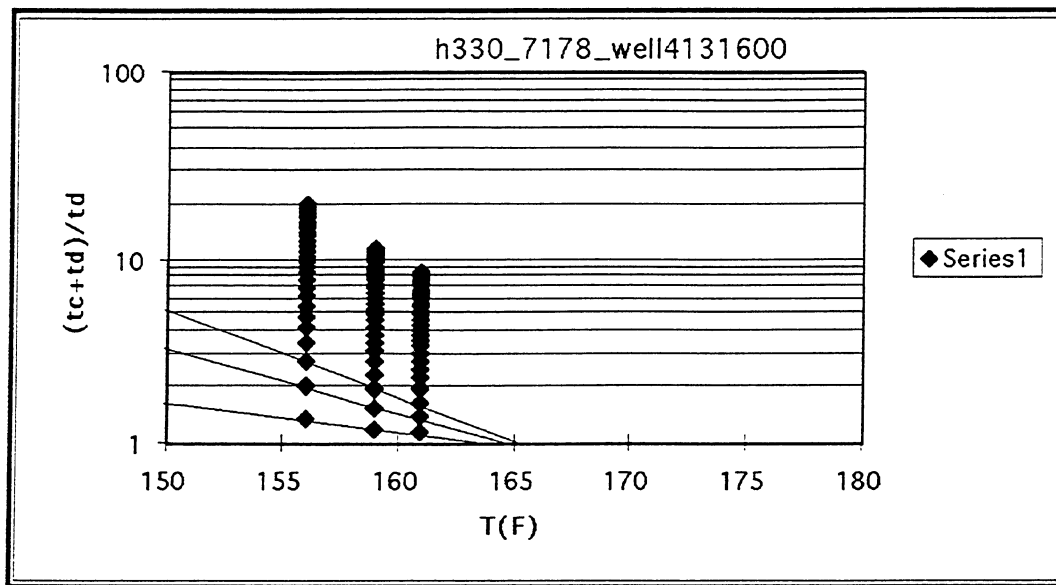


Figure V.9. Horner plot for well API # 4131600 at the depth of 7178 ft. The diamonds represent the observed temperature for different circulation times(t_c). The time after the end of circulation(t_d) was known for each of the three temperature measurements at this depth. Each diamond in a column represents an assumed circulation time, starting at the base at 2 hours circulation and increasing upward in 4 hour intervals. The lines through the diamonds project to the steady state temperature where they intersect the abscissa.

There is, however, another potentially larger source of error that must be assessed. Because of the difference in mud temperature compared to local ambient, differences in diffusivity etc., it is possible that the slope for 6 hours circulation line used in the Horner plot correction may not be the same for all depths in all wells. Figure V.10 addresses this issue using all data from different Blocks in South Eugene Island. It shows the gradients for a 6 hours circulation time obtained from the Horner plots versus depth. Neglecting the highest 4 data points as outliers, the average gradient is $9.0\text{ }^{\circ}\text{F}^{-1}$ with a standard deviation of $\pm 4.8\text{ }^{\circ}\text{F}^{-1}$.

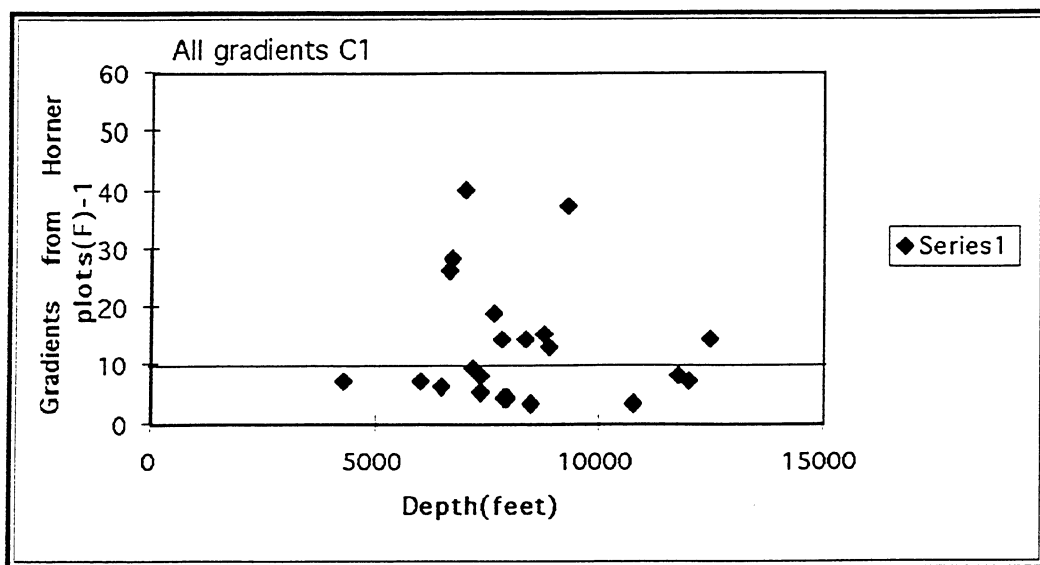


Figure V.10 : Gradients obtained from several Horner plots for 6 hours circulation time for wells spread across Blocks 314, 329 and 330. The gradients lie mostly in the range 5 to 15 (F)-1. There is no clear dependence on depth or lithology.

Considering this, we used the following formula to correct temperature measurements in the SEI 330 data cube:

$$T_i = T_w + C \text{Log} \frac{t_c + t}{t}$$

In the above formula T_i is the corrected temperature, T_w is the observed temperature, C is the slope from the Horner plot ($= 9.0 \pm 4.8 \text{ } ^\circ\text{F}^{-1}$), t_c is the circulation time, and t is the time since the end of circulation at which the temperature measurement was made. The

error in any single temperature measurement is approximately $\pm 4.8 \text{Log} \frac{t_c + t}{t}$ because the error associated with the assumption that the circulation time was 6 hours is comparatively small for a reasonable range of circulation times. By this measure, the average error associated with the Horner gradient of all the temperatures we corrected is 1.5°F or 0.83°C . The total uncertainty from both the uncertainties in circulation time and the uncertainties in Horner gradient is thus about $\pm 2^\circ\text{C}$.

Because most of the wells in the SEI 330 area are inclined, all the temperature measurements were located at their proper spatial position. Then, using a 3D Krigging algorithm from Spyglass™ with 500 meters cells, we built a 3D data cube with the interpolated observed temperatures. Slices through this data cube show the same basic features observed by the authors cited above; temperature anomalies follow the strike of the Red Fault System and change with depth.

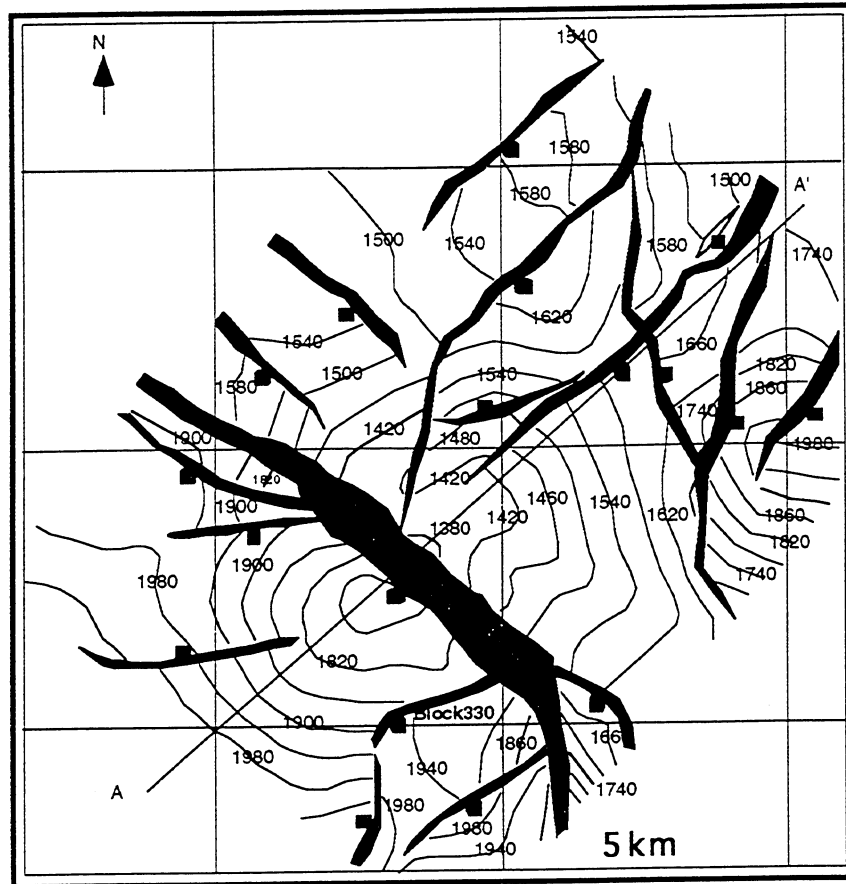


Figure V-11. The structure close to the JD sand, an important gas reservoir in Block 330. Section A-A' is shown across the area. Contours are 40 m intervals.

A representative cross-section across the area was constructed from a 3D Pennzoil's seismic survey interpretation to model the temperature field (Figure V.11). Temperatures in this section, in comparison to the ones used by the authors above, shows a much greater degree of complexity in the temperature field. Figure V.12 overlays the observed temperature field and the geological section. The main salt structures and the Red Fault are shown. This figure shows a positive temperature anomaly below and in the area of the oil reservoirs, and a negative anomaly developed above the oil zone. Temperature can also be seen to increase across the fault. The density of the temperature measurements do not allow the resolution of any large anomaly in the immediate vicinity of the fault zone, a fact already noted by McKenna (op.cit.). Because of the exploration and development activities there is reasonable resolution of temperature inside and around the oil fields. However, even in this area, the density of the temperature measurements and the temperature resolution decreases away from the oil fields and

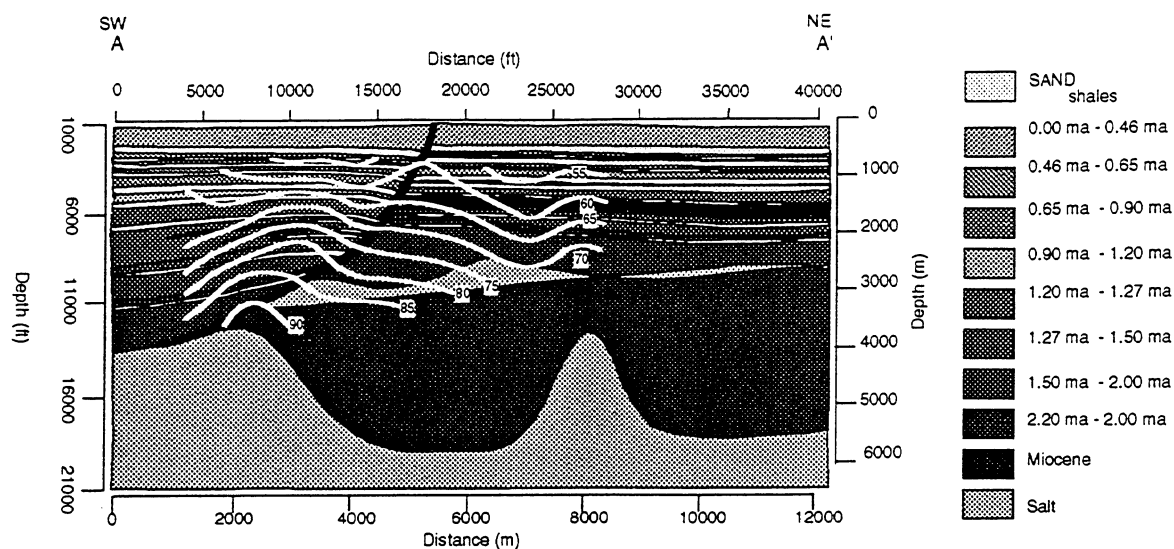


Figure V.12. Krigged temperature field projected into section A-A' (Figure V.11). Note positive temperature anomaly (isotherm anticline) of about 15 °C under hydrocarbon reservoirs along Red Fault, and negative temperature anomaly (isotherm syncline) above reservoirs.

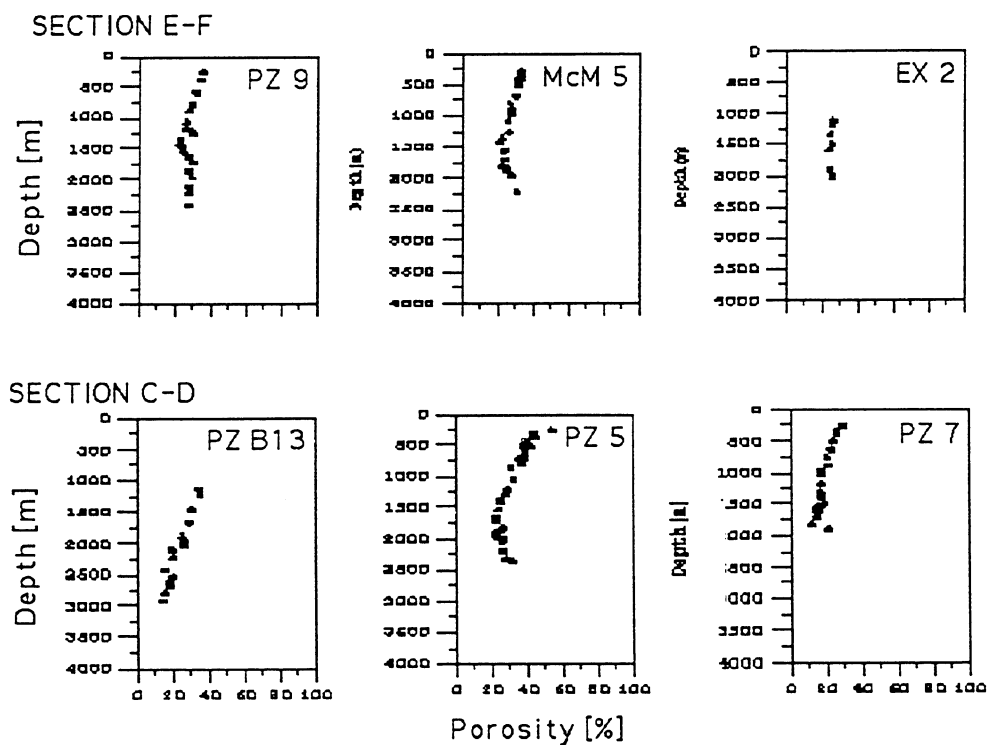


Figure V.14. Example porosity depth profiles determined from density logs. See Figure V. 13 on p. 23 for locations.

targeted reservoirs. Despite uncertainties there appears to be a negative temperature anomaly over Pennzoil's oil and gas fields of about 5°C, and a positive anomaly below the fields of about 15°C. The magnitude of both anomalies significantly exceed the ±2°C uncertainty in the temperature measurements.

3. Bottom Water Temperature (by L. M. Cathles)

The top surface of a basin depends strongly on water depth and the position of the ocean thermocline. Changes in sea level can significantly affect temperatures within a basin. For example ocean water today at depths more than a few 100 meters has a temperature of 4.5°C. Ocean temperatures above thermocline in tropical areas such as the Gulf Coast are ~25°C. Changes in sea level at a particular site by a few hundred meters could change the surface temperature by 20°C, and this surface temperature change would rapidly propagate to great depths within the basin.

The temperature of the top surface in *AKCESS.BASIN* calculations is controlled by water depth, d_i , the water temperature above the thermocline T_{water} , and the depth to the top and bottom of the thermocline, d_{tmclt} and d_{tmclb} :

$$T[\text{basin top at } x_i] = T_{\text{water}}$$

$$\text{if } d_i \leq d_{\text{tmclt}}$$

$$T[\text{basin top at } x_i] = 4.5^\circ\text{C} + (T_{\text{water}} - 4.5^\circ\text{C}) \frac{d_i - d_{\text{tmclb}}}{d_{\text{tmclt}} - d_{\text{tmclb}}}$$

$$\text{if } d_{\text{tmclb}} < d_i < d_{\text{tmclt}}$$

$$T[\text{basin top at } x_i] = 4.5^\circ\text{C}$$

$$\text{if } d_i \leq d_{\text{tmclt}}$$

For the South Eugene Island data cube, excellent data is available on the position of the thermocline (see Cathles, et. al., 1991 and references given therein). Parameter values that describe the present thermocline in the SEI 330 area well are $T_{\text{water}} = 24.5^\circ\text{C}$, $d_{\text{tmclb}} = 0.27 \text{ km}$, and $d_{\text{tmclt}} = 0.10 \text{ km}$. We assume the thermocline was in this same position over the last 3.4 ma of basin history.

4. Material Properties of SEI Block 330 Sediments (by D. Coehlo, Cornell)

Material properties such as thermal conductivity and permeability, and chemical parameters characterizing the rates of organic and inorganic reactions are needed for modeling. This section briefly summarizes the parameters used in the SEI Block 330 modeling.

a. Long Term Sediment Compressibility

Under a matching grant from the Gas Research Institute and this DOE grant, all available porosity logs in the SEI study area were obtained and interpreted. Density logs were found to give the most reliable estimates. Six wells on the hanging wall of the Red Fault, and six on the footwall were selected for analysis. The location of the wells is given in Figure V.13.

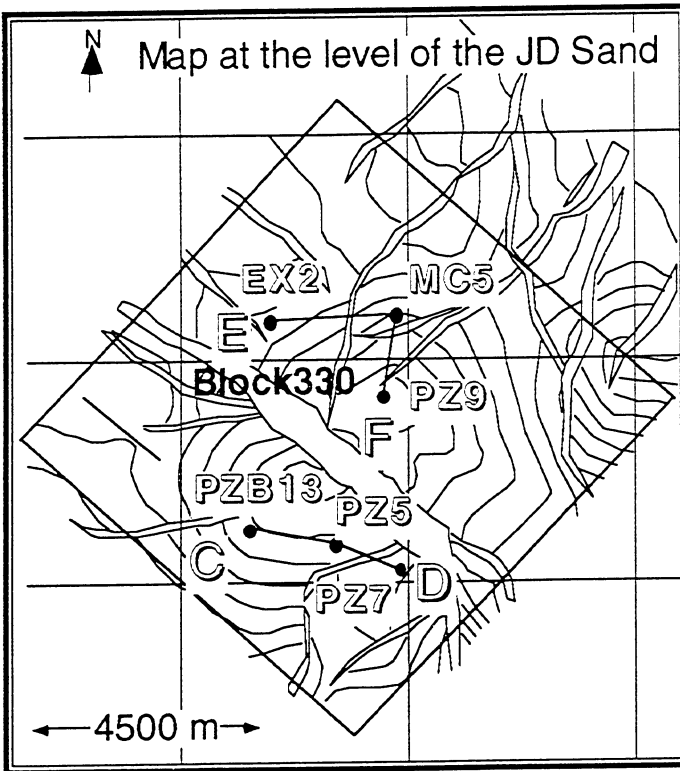


Figure V.13. Location of wells shown in Figure V.14.

Porosity versus depth profiles for section C-D and E-F are shown in Figure V.14a and b (p. 21). The wells nearest the Red Fault typically show an increase in porosity below the top of overpressure, whereas the wells more distant from the Red Fault show a flat porosity profile below the seal. From ~200 m depth to 1500 to 2000 m depth porosity decreases linearly with depth. Porosities above 200 m decrease more rapidly with depth and were not addressed in the modeling.

Depth was converted to effective stress in the hydrostatic interval above the top of overpressure, and porosity regressed linearly against effective stress:

$$\phi = \phi_0 - \frac{\sigma'}{\sigma_c}$$

where σ' is effective stress, ϕ_0 is the uncompacted (surface) porosity, and σ_c is a yield stress. Sands and shales were regressed separately as the lithologies compact slightly differently. Yield stresses and uncompacted were: sand: $\sigma' = 1750 \text{ bars}^{-1}$, $\phi_0 = 0.39$, and shale: $\sigma' = 3190 \text{ bars}^{-1}$, $\phi_0 = 0.35$. The upthrown compressibilities were about twice the downthrown for both lithologies. End member uncompacted porosity and yield strength were combined linearly to obtained parameters for mixed lithologies. Figure 15 shows the quality of the end member regressions.

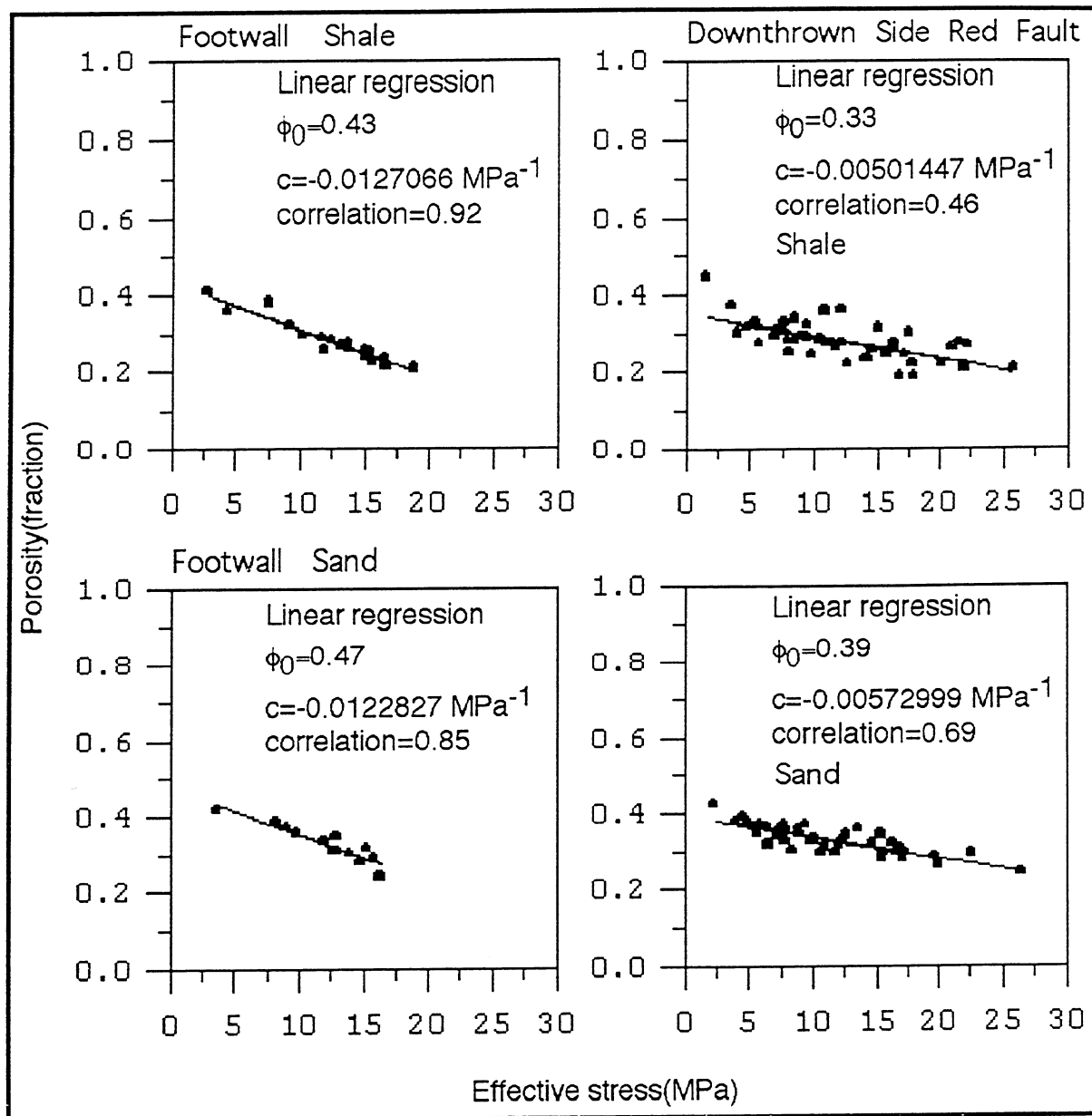


Figure 15. Regression of porosity versus effective stress on the upthrown (footwall) and downthrown sides of the Red Fault for both sands and shales. Data only from hydrostatically pressured zones.

b. Thermal Conductivity (M. Luo and J. Wood, MTU; L. Cathles, Cornell)

Thermal conductivity is a particularly critical parameter for this study. Thermal conductivity is a strong function of temperature, sediment porosity, and pore fluid composition. The temperature dependent media conductivity was obtained by: (1) obtaining the temperature-dependence of the grain, water, oil, and gas thermal conductivities, and (2) then combining them in an appropriate fabric mixture:

$$K_G = \left[\frac{1}{K_0} \left(2.412 - 0.0818 T_K^{0.5} \right) + 0.0172 T_K^{0.5} - 0.2978 \right]^{-1}$$

$$K_w = 2.231 \left(\frac{T_K}{273.15} \right)^{1.5} - 0.8812 \left(\frac{T_K}{273.15} \right)^{2.5}$$

$$K_{oil} = 0.552 - 1.123 \times 10^{-3} T_K + 1.239 \times 10^{-6} T_K^2, \text{ and}$$

$$K_{gas} = 0.061 - 8.495 \times 10^{-5} T_K + 3.027 \times 10^{-7} T_K^2.$$

In the above formulae T_K is the temperature in degrees kelvin, and K_0 is the mineral grain thermal conductivity at 25°C. The above formula apply to pure mineral grains, or pure pore fluids (oil, gas, and water). Real sediments are composed of a mixture of mineral grains, i , and their pores are filled with a mixture of pore fluids with volume fraction S_i . The thermal conductivities of these components may be combined in series or parallel as shown below. In addition a solid-fluid mixture parameter, β , may be defined that is a function of hydrocarbon saturation.

$$\beta = 0.442 - 0.37 (S_{oil} + S_{gas})$$

The final fabric theory combination of these combined elements is:

$$K_{11} = K_{22} = \beta \left\{ (1-\phi) \sum_{i=\text{sand, shale...}}^{\text{salt}} x_{Gi} K_{Gi}(T) + \phi \sum_{i=\text{water, oil...}}^{\text{gas}} S_i K_i(T) \right\} + (1-\beta) \left\{ (1-\phi) \sum_{i=\text{sand, shale...}}^{\text{salt}} \frac{x_{Gi}}{K_{Gi}(T)} + \phi \sum_{i=\text{water, oil...}}^{\text{gas}} \frac{S_i}{K_i(T)} \right\}^{-1}$$

where K_{11} and K_{22} are the temperature-dependent thermal conductivities of the porous media in the horizontal and vertical directions. Note that we assume the thermal conductivity of the sediments are isotropic.

A paper showing that a scheme very similar to the above replicates thermal conductivities of water-saturated sediments to within $\pm 10\%$ has been published by Luo et. al. (1995) as part of this DOE project. The difference between the Luo et. al. scheme and the one given above is that the parallel and series grain thermal conductivities are constructed from sums of the mineral grain thermal conductivities, rather than from sums of the grain thermal conductivities lumped into sand, shale, carbonate sand, etc., end members, where the end members are calculated from their average mineral grain compositions. We have shown that the difference between these two schemes is at most about 1.5%. The lumped approach is geological, simple, flexible (the lumped end members are easily modified), and easy to use. The errors associated with the lumping in to lithologic types are much less than the 10% uncertainty in the mineral composition estimates and thus insignificant.

The parameters used in our thermal conductivity model, plus some other parameters discussed above and below, are:

Table V.1. Material property parameters for end-member lithologies.

j	lithology	log k_{11}	log k_{22}	$K_{Gr}[25^{\circ}C]$	ρ_G	$\phi(x_2=0)$	$1/\sigma_c[\text{bars}^{-1}]$
1	sand	2	2	9.5	2.76	0.39	1 / 1750
2	shale	-3	-3	7.4	2.76	0.35	1 / 3190
3	carb-sd	2	2	8.5	2.72	0.47	1 / 820
4	carb-mud	-3	-3	8.5	2.72	0.43	1 / 787
5	salt	-9	-9	13.3	2.16	0.00	1 / 10^5

c. Permeability in Block 330 Data Cube (By D. Coehlo, Cornell)

An extensive data base on sand permeabilities in the SEI Block 330 study area was obtained from Pennzoil. It consisted of porosity and permeability measurements from core wall samples in many reservoirs in Block 330. This data base was used to develop an empirical model that describes permeability in terms of porosity and sand-shale ratio. The model fits the observed data very well and will allow, since our model calculations predict porosity changes, appropriate sand permeabilities to be ascribed at past geologic times. Our empirical relation is:

$$\log k = b + c\phi$$

where b depends on lithology as characterized by the sand-shale ratio, and c is a constant. Our log model was found to fit the observed relations between porosity and permeability much better than the Karmen-Kozeny relation. The quality of the log model fit can be appreciated if $\log k$ is plotted versus porosity (Figure V.16). The base permeability of sediments is a function mainly of the size of the mineral grains that comprise the sediment and the lithology of those sediments. The \log_{10} of the horizontal and vertical

permeabilities of end-member lithologies at 20% porosity, $\log k_{\phi=.20}$, are given in the material property table in the previous section. The effects of porosity are added to this reference value with the amplitude of the porosity dependence modified by the fraction of coarse sediment component. The sand permeabilities fit those observed in South Eugene Island Block 330 very well, as can be seen from Figure V.16. The shale permeabilities are reasonable. The precise value of the shale permeability is not too critical as long as it is substantially smaller than the sand permeability, as is the case in our lithology-porosity model for permeability. The permeability model is a smooth function of porosity and coarse

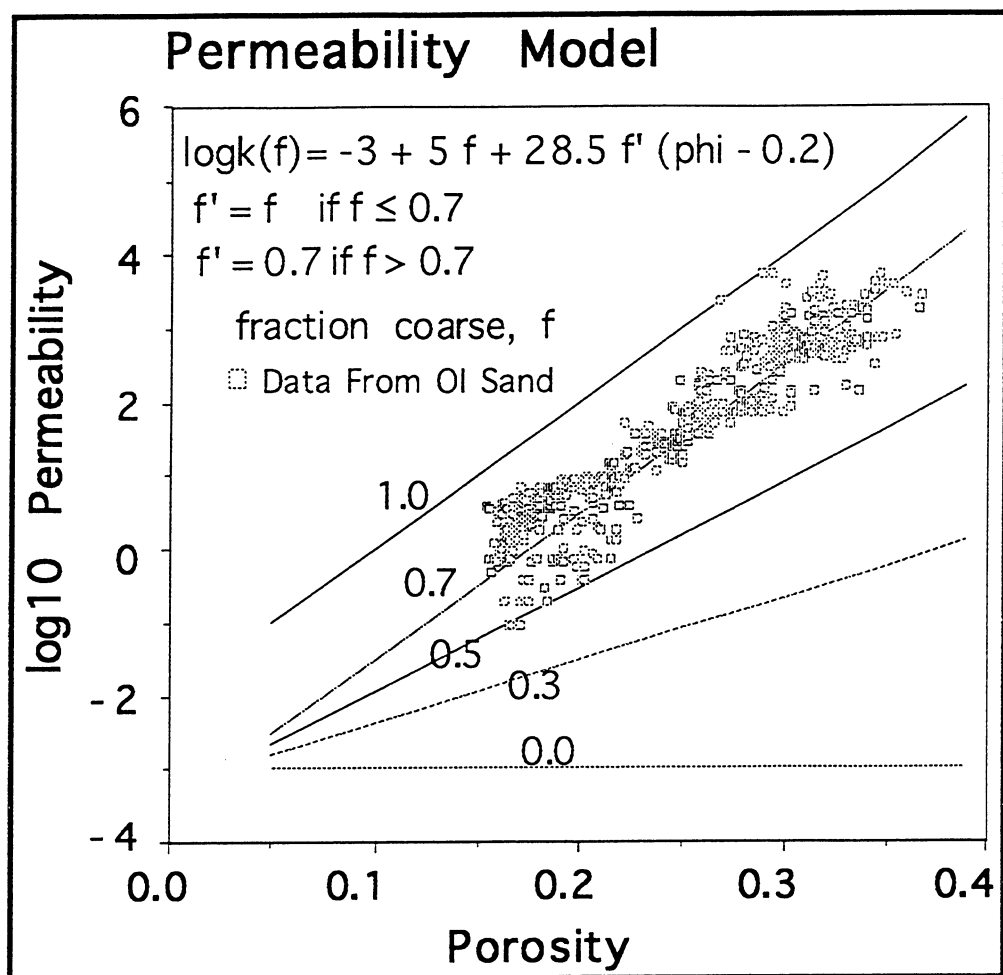


Figure 16: Permeability model used in calculations.

d. TTI and R_o Indices (M. Luo and J Wood, MTU; P. Meulbroek, Cornell)

TTI, a Lopatin-type time temperature index and vitrinite reflectance, R_o , are two measures of sediment maturity that are used in our modeling. TTI is calculated as described in Waples (1985,1990) by summing the products of the time in millions of years a sediment has spent in each 10°C temperature interval and a temperature factor. The temperature factor is determined:

$$\text{temperature factor} = 2^{\text{INT}\left(\frac{T[^\circ\text{C}] - 105}{10}\right)}$$

where INT indicates that the division result is truncated to the nearest integer. Thus, for example a temperature just above 110°C would have a temperature factor of 2, and a temperature just below 100°C would have a temperature factor of 0.5.

A Sweeny and Burnham (1990) model for the R_o measure of vitrinite reflectance is incorporated in Akcess.Basin. In this model:

$$R_d[\%] = e^{(-1.6 + 3.7 F)}, \text{ where } F = f(T, t, E, A, R, a_1, a_2, b_1, b_2).$$

In this equation T = temperature, t = time, E = activation energy, A = pre-exponential, R = gas constant, ai and bi are coefficients.

These models have both been implemented in Akcess.Basin

e. Smectite-Illite Transformation(M. Luo and J. Wood, MTU)

The conversion of smectite to illite is a useful maturation parameter that is simulated by the following equation developed by Luo and Wood as part of this project:

$$\frac{\partial S}{\partial t} = -A(S) b(T) \exp\left(\frac{E(S)}{RT}\right)$$

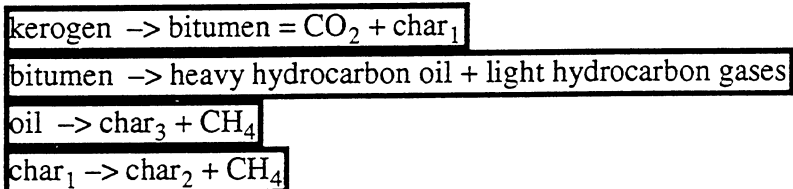
In this equation S is the mole fraction of smectite in the illite-smectite mixture, t is time in seconds, A and E are the pre-exponential factor and activation energies which have dependencies on S shown below, R is the gas constant, and b is the molar potassium ion concentration which is defined by Luo and Wood in terms of temperature under the assumption that it is buffered by rock minerals.

$$A(S) = 10^{\{0.5051 - 0.5943(1 - S)\}}$$

$$E(S) = 3.56(1 - S) + 29.0$$

f. Hydrocarbon Maturation(P. Meulbroek, Cornell; Matching funded by GRI)

The maturation algorithm used in our calculations is modified from Burnham and Braun (1988). The reactions are:



The chemistry of the light hydrocarbon gas and heavy oil can be specified in the program. The reactions have first order kinetics with the kinetic parameters as in Burnham and Braun.

The volume change associated with the hydrocarbon maturation reactions is calculated:

- (1) The specific volumes of type I kerogen is 0.83 cc/g.
- (2) The specific volumes of type II kerogen is 0.74 cc/g
- (3) The specific volume of bitumen and all chars is 0.83 cc/g
- (4) The volume of hydrocarbon fluids is determined from an equation of state:

$$= \frac{RT}{V-b} - \frac{a}{V(V+b)}$$

where a and b are mixture-specific parameters, P is fluid pressure, T is absolute temperature, V is molar volume, and R is the gas constant.

Hydrocarbon maturation is of interest in its own right because we need to know how much oil and gas could have been generated in the SEI minibasin. Hydrocarbon maturation is also important because the positive volume maturation reactions produce overpressures and drive oil, gas and water out of the basin. This maturation expulsion, as well as compaction and aquathermal pressuring, is accounted for in Akcess.Basin.

5. Modeling Results

With the bottom water temperature defined as a function of water depth, the material properties of thermal conductivity, porosity, and sediment permeability defined in terms of calculable parameters, and a realistic evolution of the SEI minibasin defined from seismic data and well logs, we are in a position to model the SEI minibasin and interpret observations made there. In what follows we first discuss porosity modeling, then temperature modeling including the effects of episodic venting, and finally chemical modeling including hydrocarbon generation and maturity indicators.

1. Porosity Modeling (L. Cathles, Cornell; Matching funded by GRI)

Porosity depends on effective stress, but the porosity profile in a basin also depends on whether there is relative movement of the pressure transition zone (seal) and the basin sediments. The Pathfinder well was logged from 6950 to 8300 ft depth in an interval where the pressure transitioned from soft (13.6 pound mud weight) to hard (16.3 pound mud) overpressure in two roughly equal steps. Below each of the major jumps in pore fluid pressure is a gas-filled sand. The gamma log indicates there are 40 to 50 transitions from sand to shale in the shale intervals above these gas sands. Shosa and Cathles (in preparation) have shown in laboratory experiments that under basin conditions of pressure and temperature and in the presence of a gas phase, an exit pressure of a few bars can be expected at each sand-shale interface within a basin. Since free gas is clearly present, and since the gamma logs show that there are enough sand-shale interfaces in both pressure transition zones to account for the increase in pressure by gas capillary exit pressure effects discussed by Shosa et. al., the pressure transition zones in the pathfinder well could be gas capillary exit pressure seals. If so, because gas exsolution is controlled by pressure and there is no lack of sand-shale interfaces in the upper part of the SEI minibasin, the position of the pressure transition zone there could have maintained a relatively constant depth, with sediments moving through the seal with time.

Figure V.17 shows that the porosity profile in a basin depends strongly on whether the seal is fixed to a particular strata or migrates through the sedimentary layers as sedimentation progresses. The calculations shown in Figure V.17 are for steady, layer-cake sedimentation. If there is no seal, compaction is linear until the minimum porosity of 0.1 is attained. If there is a seal, overpressuring below the seal decreases the effective stress and inhibits compaction. If the seal is fixed to a particular strata, porosity increases under the seal. Compaction is arrested from shallow depths, and, since the pressure under the seal is limited to 0.8 times the reduced lithostatic load at the seal (e.g., the lithostatic load just under the seal minus the cold-water hydrostatic head there), compaction resumes once a certain amount of burial takes place. For a fixed seal, the porosity under the seal is greater than the porosity just above the seal.

If the seal migrates through the stratigraphy so as to maintain a constant depth (e.g., the "migrating" seal case in Figure V.17), the porosity is arrested at the value just above the seal when the sediments move into the seal. The result is a constant porosity to depths at which the effective stress again attains the values it had just above the seal.

Porosity profiles of both the fixed and migrating style are observed in the Gulf Coast. However, it is clear that the porosity profiles in the SEI 330 study area (Figure 14a.

b) are most similar to the migrating seal profiles. Porosity profiles near the Red Fault show a minor increase in porosity below the top of overpressure in most cases. Thus there is a tendency for seal migration to be more fixed near the Red Fault than further from it. The reasons for this are not clear, but it may be that shearing has disturbed the contiguity of sand-shale interfaces and made it more difficult for the gas-capillary seal to smoothly migrate upward through the section.

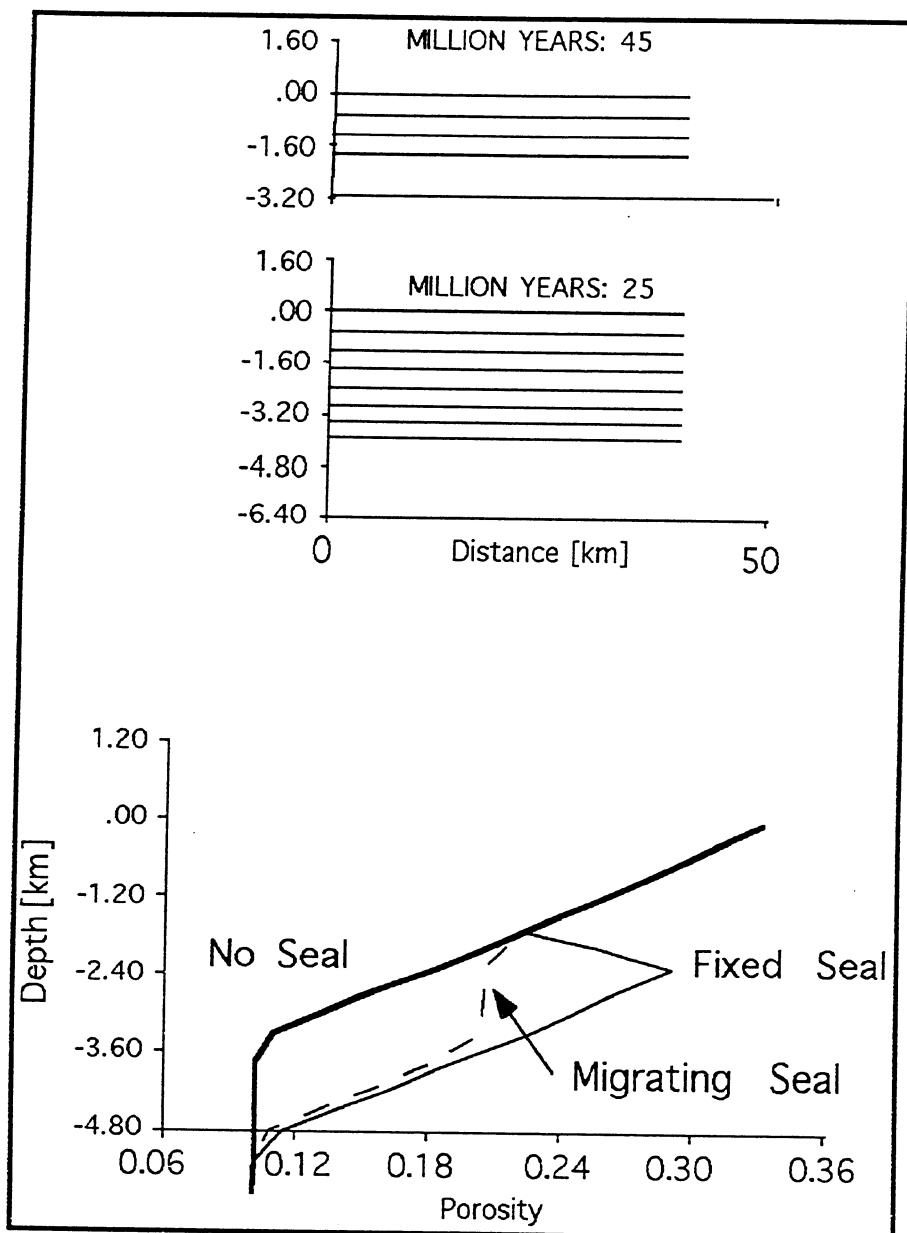
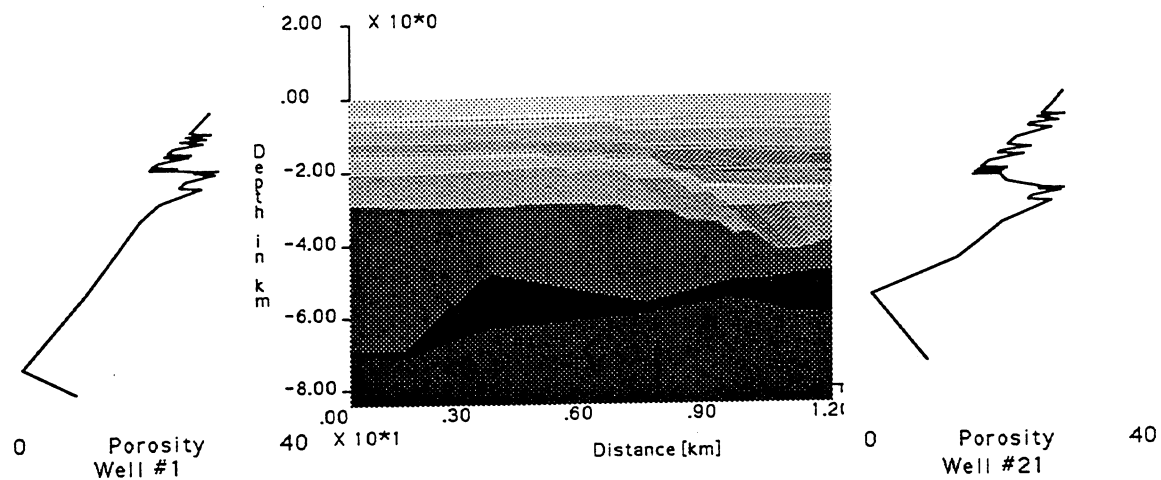


Figure V.17. Porosity profiles produced with the same sediment compressibility for basins with no seal, a seal fixed to a particular strata from the time of its deposition, and a migrating seal which maintains constant depth.

SEI Line 1, Fixed Seal:



SEI Line 1, Migrating Seal:

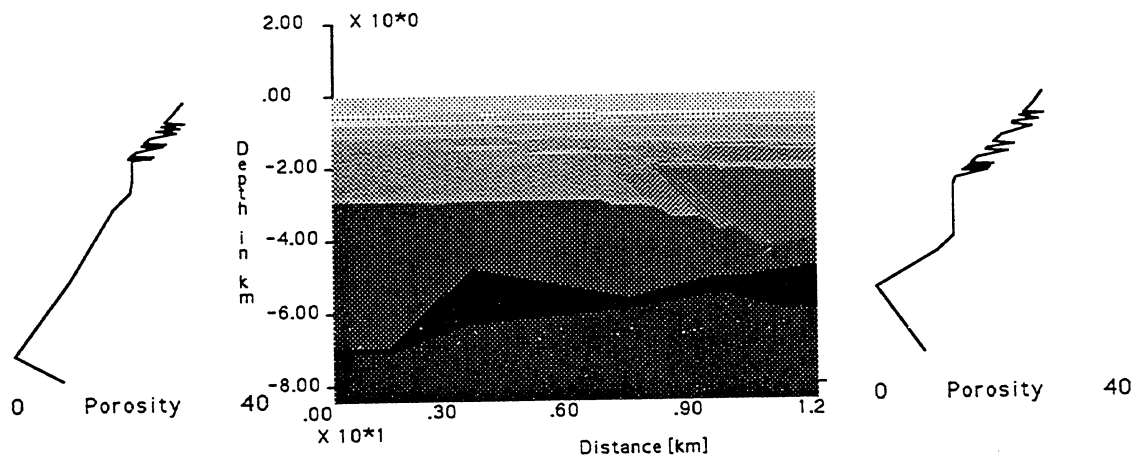


Figure V.18a,b. Calculated porosity distribution for Line 1 for migrating and fixed seals. Porosity is indicated in cross sections by grey scale. Porosity profiles are plotted along each side of each diagram. The increased porosity under the fixed seal and the constant porosity under the migrating seal are clearly indicated.

Figure 18a and b show the full porosity pattern predicted by calculations for Line 1 in the SEI study area (see Figure V.3 for the location of Line 1). Plots of porosity versus depth are shown for the pseudo-wells on the extreme left (north) and right (south) of the section. The porosities are calculated for the material properties calibrated to the SEI 330 area as discussed in section V.b.3.a, and so are slightly different for sands and shales. Thus the sands show up as relatively uncompacted (white) layers on the cross sections. Note that the porosities are calculated for the mid-point of each sedimentary layer.

Comparing the porosity-depth profiles in Figure 18b and the observed profiles in Figure 14a and b, we conclude that at least since 1.5 ma it is likely that the pressure transition in the SEI 330 area maintained a relatively constant depth and thus the pressure transition zone migrated steadily upward through the sedimentary section as sedimentation took place.

2. Temperature Modeling (D. Coehlo, Cornell)

a. Introduction

A large number of 2D temperature simulations have been run for the sections shown in Figure V.3. Most runs were made for Line 6, the line that passes through the center of the minibasin and passed directly under Pennzoil's Block 330 reservoirs. Several 3D simulations have also been made, and results from these runs are presently being analyzed. The thermal modeling proceeded in stages. First sensitivity analyses were carried out to assess the relative importance of variable sedimentation, thermal conductivity, sea level variations, heat generation in the sediments by radioactive decay, etc., and to determine the best base case model. These studies revealed the importance of hydrocarbon-related temperature anomalies and radiogenic heat generation. Consequently hydrocarbons and radioactive heat generation were present in the base-case model.

Temperature in the base-case model was then calibrated to the present day temperatures by varying heat flow. Heat flow was not previously known in the SEI study site. Our calibration indicates that the heat flow at 8.5 km depth is about 1.05×10^{-6} cal/cm²-sec. This is about the value one might have estimated by interpolation from locations in the region where heat flow has been determined.

With the basal heat flow defined, we then calculated the thermal effects of hydrocarbon emplacement between 0.709 and 0.46 ma, and the consequences of this on vitrinite reflectance and other maturity indicators. The emplacement of hydrocarbons produces a thermal blanketing and heating, and this produces a small but potentially measurable vitrinite reflectance anomaly. The anomaly is small compared to that observed in the A6-sidetrack, however.

Table V.2. The impact of various parameter changes on subsurface basin temperature at the level of the Pennzoil reservoirs, ranked in order of magnitude.

	Variable Changed In Test Case	Nature of comparison	Maximum ΔT in Wells 6 and 17
Hydrocarbons	Hydroc. on reservoirs- no hydrocarbons in reservoirs	dipole -5° above reserv.	$+15^\circ$ below
Paleobathymetry	max: always very shallow - very deep probable: always present depth-variable		$+12^\circ\text{C}$ $+2^\circ\text{C}$
Salt	No salt under line 6 reservoirs - obsv sale		3°C
Timing of HC emplatmt	Hydrocarbons from deposition-base case Early plausible emplacement - base case		3°C 1.7°C
Heat Generation	Reasonable maximum - reasonable minimum		$+2^\circ\text{C}$
Solid Advection	Building with hydroc. - steady state w. HC		2°C
Fluid Advection	no flow - steady compactive flow		1.5°C
Thermal Conductivity	all sand - all shale stratigraphy realistic lithologic variations sand best HF changed from 1.05 to 1.25 HFU	from 9.5 to 11.5 TCU shale from 7.4 to 8 TCU	-1.4°C $\pm 0.2^\circ\text{C}$
Seal Position	reasonable high - reasonable low seal		$+0.08^\circ\text{C}$

Hydrocarbon maturation calculations show that significant oil is matured only below the salt weld at the base of the SEI minibasin. Thus the oil in the SEI minibasin cannot have been sourced from within the minibasin, and must have been supplied from greater depths either locally or regionally.

Temperature perturbations produced by rupture of the seal were computed for the models and parameters described above, and much more intensively with a very refined grid and very high temporal resolution in an extensive series of calculations. This modeling shows that thermal anomalies of up to 30°C can be produced by episodic rapid fluid venting. The critical parameter controlling the initial thermal anomalies (first ~100 years of venting) is the fault and sand permeability. The shale permeability is not important at these short timescales.

b. Temperature Sensitivity Analysis

Sensitivity analyses were carried out to assess the relative importance of the various factors that affect subsurface temperature. The impact of variable changes was generally assessed by calculating the difference in temperature between the test calculation and a reference calculation along pseudo wells 6 and 17 of Line 6 located in the upthrown and downthrown blocks respectively. Table V.2 lists the maximum temperature difference between the test and base models and the parameter varied.

Table V.2 shows that, after hydrocarbons which will be discussed below, the next most important factor is historical variations in water depth in the study, and the position of the sediment-water interface relative to the thermocline that this variation dictates. The water depths assumed for the study area are shown in Table V.3. The depths are constrained by paleontologic data reported in Alexander(1994) and Rowan (1994).

Table V.3. Water depths used in the SEI Block 330 modeling as a function of time.

<u>Depth[m]</u>	<u>Time [ma]</u>	<u>Water Depth[m]</u>	<u>Time [ma]</u>	<u>Water</u>
	0		76	2.2 100
	0.46		15	2.6 338
	0.65		37	2.7 381
	0.9		91	3.4 495
	1.1		91	4 495
	1.27		100	10
	610			
	1.5		91	

Other variables affecting temperature have minor impact for various reasons. As can be seen from Table 3, only extreme variations in salt distribution significantly affect subsurface temperatures at 1.5 to 4 km depth. Heat generation is an important effect, but errors here will be transferred to errors in the inferred heat flow. Solid advection affects subsurface temperature but the differences across the faults are negligible at the depths of interest. This contrasts with McKenna's (1994) conclusion that the "Red Fault" temperature anomalies could have been caused by differences in sedimentation on the two sides of the fault. We find no

such effect. Steady fluid advection produces no significant anomalies along the faults. Reasonable variations in the other variables in the Table have a negligible impact on subsurface temperatures.

The sensitivity analysis identified heat generation and hydrocarbons as important variables. Consequently a base case incorporating these variables was established. The base case model is described in Table V.4.

Table V.4. The Base Case Model for the SEI 330 Study Area.

Thermal Conductivity	K(T,f,So,Sg) as described in V.D.4.b.
Compaction	Linear function of effective stress (V.D.4.a.)
Bottom Water T	Function of thermocline and paleodepth (V.D.3.)
Hydrocarbons	0.709 into GA and HB; 0.65 into OI-JD, 0.46 into
DA	
Permeability	Function of lithology and porosity (V.D.4.c.)
Heat Generation	Values determined by McKenna
Sedimentation History	Inferred from 3D seismic interpretation (V.D.1)
Basal heat flux	1.05×10^{-6} cal / cm ² -sec (V.D.5.c)
Hydrocarbon Generation	Modified Burnham and Sweeney (V.D.4.f.)
Maturity Indicators	Burnham and Sweeney, Luo (V.D.4.d,e.)

c. Basal Heat Flow

The basal heat flow in the SEI 330 area was unknown at the start of this study. It was determined by varying heat flow in the base model (Table V.4) and determining the base heat flow that produces present-day temperatures in closest agreement with those observed (V.D.2). The results are shown in Figure V.19. This figure shows that for pseudowell 6 and 17 in Line 6 (see Figure V.20) the present subsurface temperatures are best matched with a heatflow of $1.0 \text{ cal / cm}^2\text{-sec}$ in the downthrown block and a heat flow of $1.1 \text{ cal / cm}^2\text{-sec}$ in the upthrown block. In our base case we use a compromise heat flow of $1.05 \times 10^{-6} \text{ cal / cm}^2\text{-sec}$. These heat flow values are compatible with the regional pattern of heat flow as inferred from measurements at other sites

d. Subsurface T Anomalies produced by Hydrocarbons

The sensitivity analysis shows that the distribution of hydrocarbons is the most important factor affecting subsurface temperatures at 1.5 to 4 km depths in the SEI 330 area. Even the timing of hydrocarbon emplacement can affect subsurface temperatures significantly. Figure V.20 shows

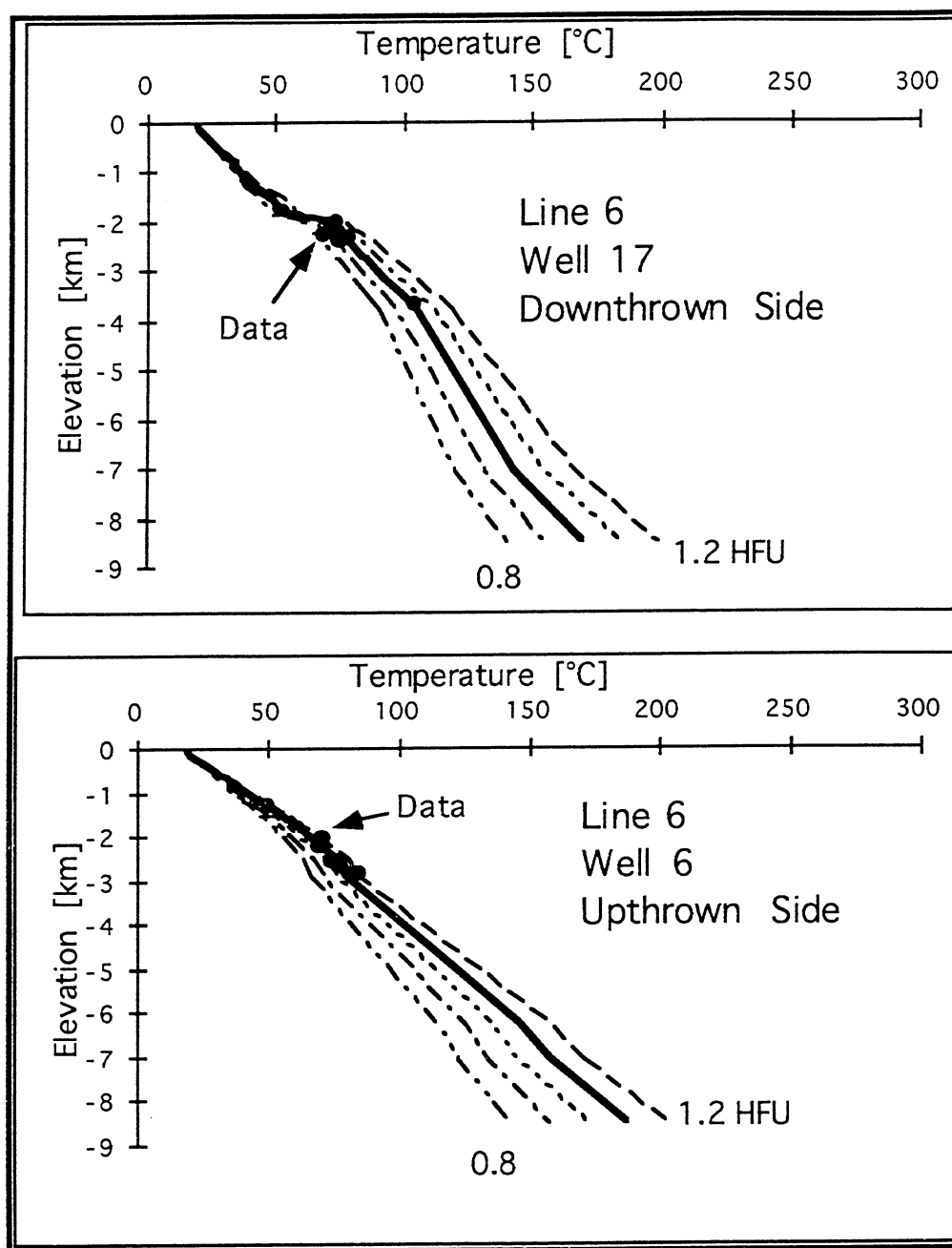


Figure V.19. Calibration of the heat flow in the South Eugene Island study area. Subsurface temperature profiles are compared to measured temperatures along pseudowell 6 and 17 in Line 6. The best match is obtained for a heat flow of 1.1 HFU in the upthrown side, and 1.0 HFU on the downthrown side of the Red Fault.

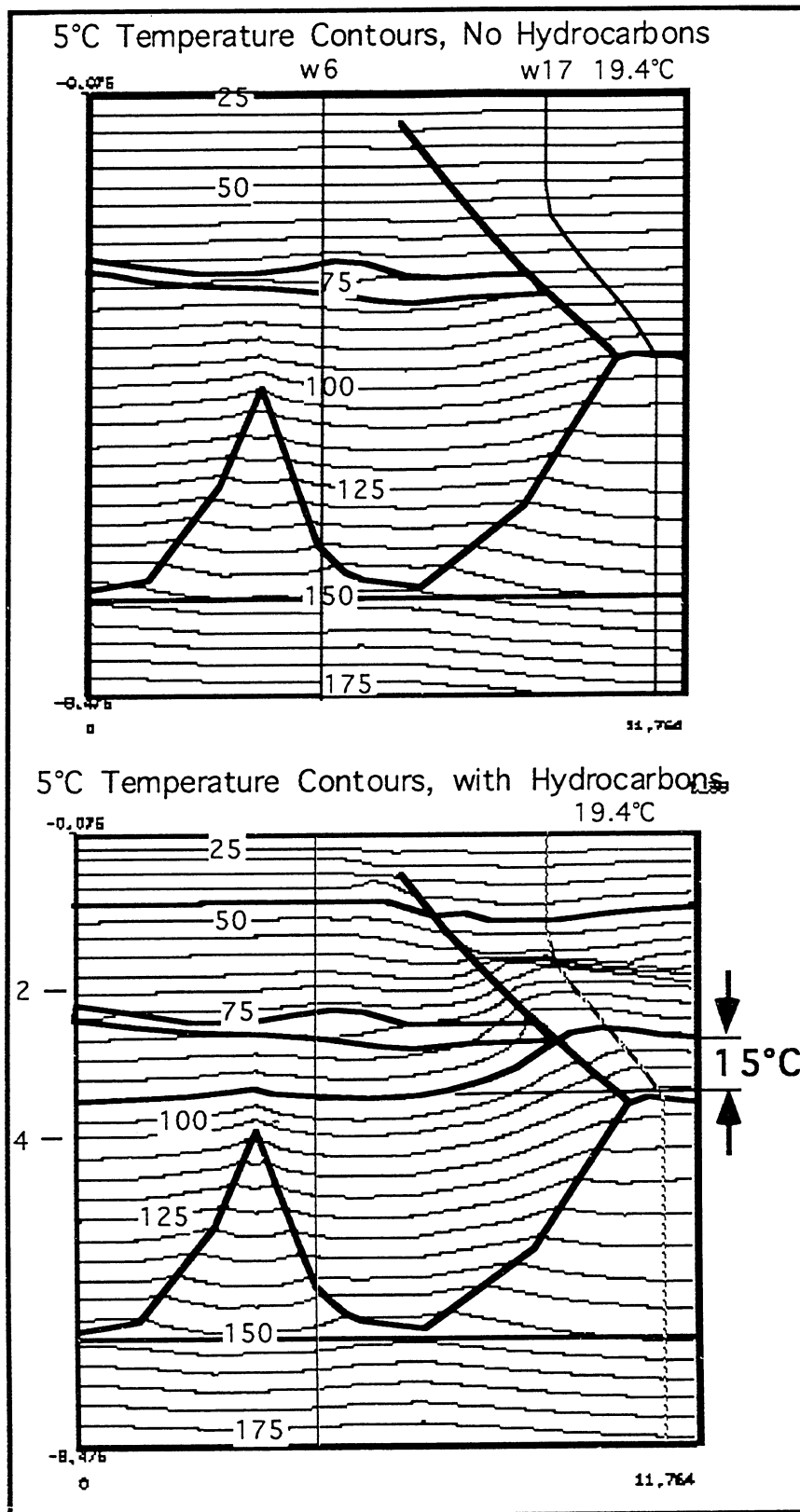


Figure V.20. Calculated subsurface temperatures along Line 6. Hydrocarbons produce steep temperature gradients and T anomalies of +15°C below and - 5°C above the Pennzoil reservoirs.

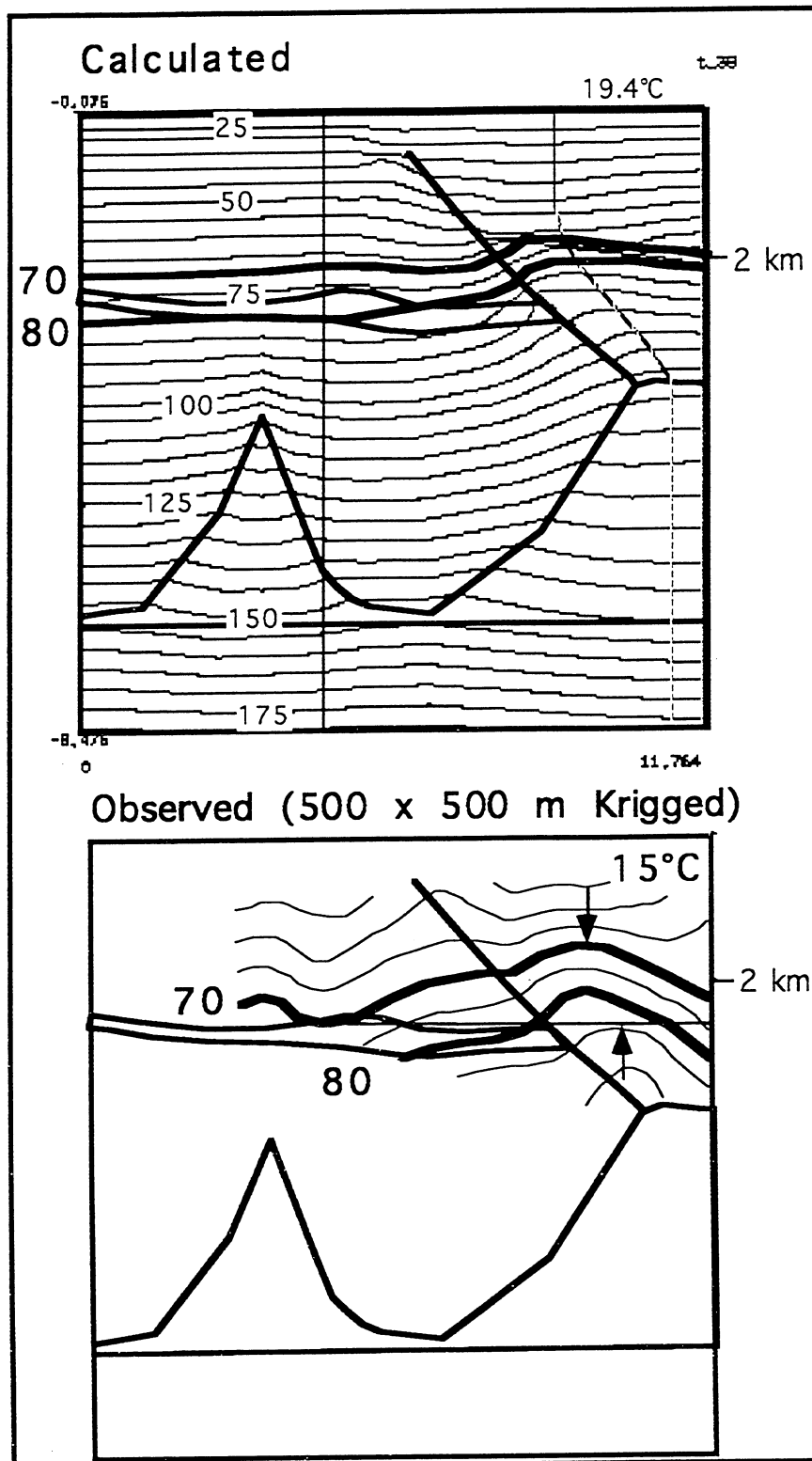


Figure V.21. Calculated and observed (from Figure V.12) patterns of subsurface T are compared. In both cases temperatures of 75°C are achieved in the upper salt sill, and a T anomaly of +15°C underlies and -5°C overlies the Pennsylvanian reservoirs. However, steep T gradients in the hydrocarbon reservoirs are not present in the observed data, probably because of the 500 m Krigging cell size.

the temperature pattern along line 6 with and without hydrocarbons in the Pennzoil reservoirs. Figure V.20 shows that when hydrocarbons are added to the appropriate sands and the impact of these hydrocarbons on thermal conductivity is considered, the subsurface temperature pattern changes significantly. Because the hydrocarbons make the sediments much more thermally insulating, their presence in reservoirs produces a steep temperature gradient in the reservoirs, a negative temperature anomaly (isotherm syncline) above the oil fields and a positive anomaly (isotherm anticline) below them. From the perturbation of the isotherms above and below the hydrocarbon reservoirs in Figure V.20b it can be seen that the positive anomaly below the reservoirs is about 15°C in magnitude, and the negative anomaly above the reservoirs about 5°C in magnitude.

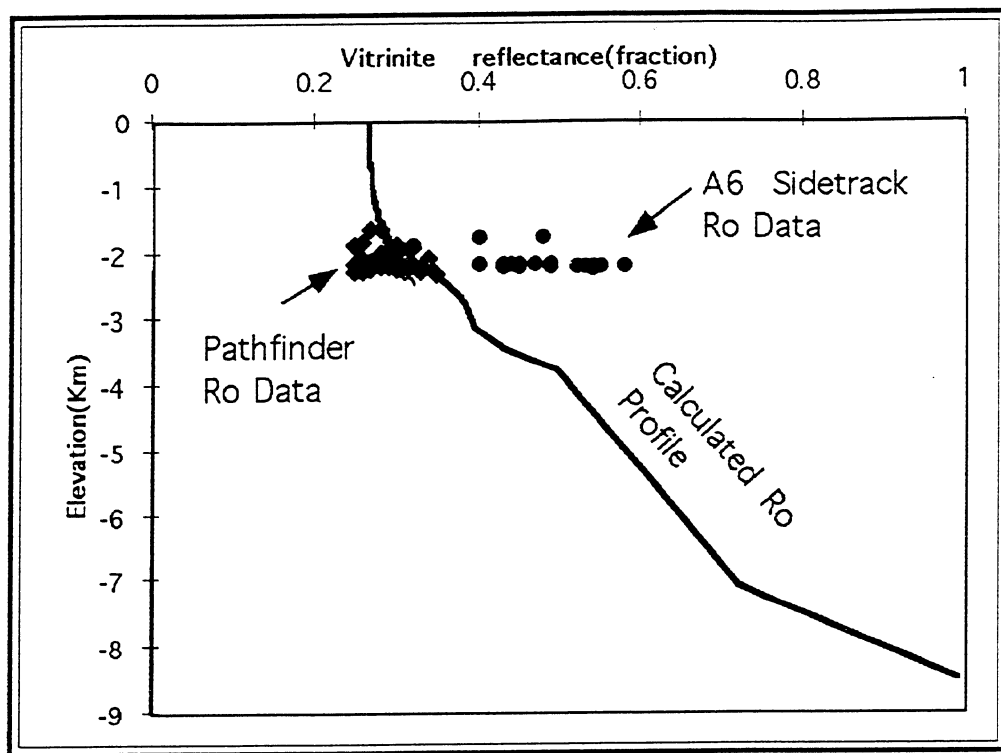
The calculated and observed temperature anomalies are compared in Figure V.21. The form of the temperature distribution is very similar. In both calculated and observed cases the temperature in the upper salt sill is 75°C. The observed positive temperature anomaly along the Red Fault is 15°C, the same magnitude as the calculated, and the negative anomaly above the reservoirs is 5°C in both cases. The observed temperature distribution does not show the strong steepening in temperature gradient in the reservoirs that the calculated pattern shows so clearly, however. This we attribute to the 500 m cell size of the Krigging that was used to interpret the temperature data in three dimensions. When the 3D temperature simulations are run we will be able to compare the observed and calculated data without interpolation of the observed temperature data and make a much better comparison of the two. At this stage of the analysis we conclude that the present subsurface temperature field appears to be well explained by the thermal conductivity effects of the subsurface hydrocarbon distribution. Rapid fluid venting up the Red Fault is not required to explain present day subsurface temperatures.

e. Maturity Indicators

Vitrinite reflectance, illite-smectite, and TTI indices of maturity were calculated. Vitrinite reflectance was measured in the Pathfinder and A6 sidetrack wells. The Pathfinder vitrinite reflectance agree extremely well with the values calculated for our base case model, as shown in Figure V.22. The patterns of calculated vitrinite reflectivity and illite-smectite ratio are shown in Figure V.23. The effect of the differential movement on the Red Fault is clearly reflected in the reflectance R_o , mainly because of the shorter time sediments take to reach equal depths on the high sedimentation side of the fault.

f. Additional Maturity Caused by Introduction of Hydrocarbons

The thermal blanketing initiated with the introduction of hydrocarbons increased temperatures below the Pennzoil reservoirs. Over time this increased temperature can be expected to produce higher vitrinite reflectance in organic material under the reservoirs. The increased vitrinite reflectance due to the introduction of hydrocarbons was calculated and is shown in Figure V.24. The increase is about 0.07%. This is not large enough to account for the 0.3% R_o anomaly observed in the A6 sidetrack (Figure V.22). Thermal blanketing by hydrocarbons cannot explain the A6 sidetrack anomaly. However, the maturity anomalies produced by hydrocarbon blanketing are large enough that there is some hope that their accurate definition might constrain the time of emplacement of hydrocarbons in some instances.



Figure

Figure V.22. Comparison of calculated and observed vitrinite reflectance Ro data for Line 6. Hydrocarbons introduced between 0.709 and 0.46 ma (base case calculation). Ro data are from the pathfinder and A6 sidetrack.

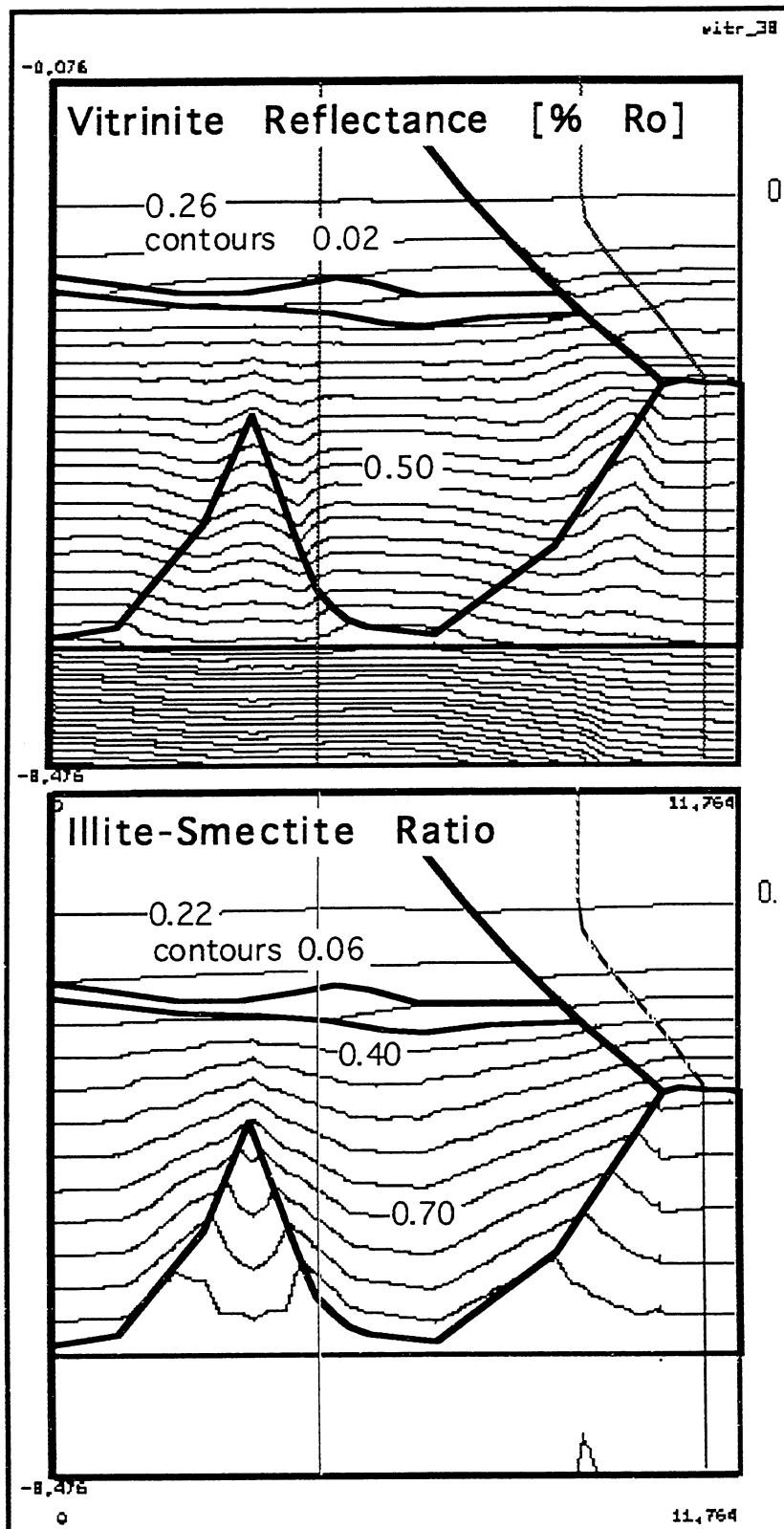


Figure V.23. Calculated vitrinite reflectance and illite-smectite ratios for Line 6.

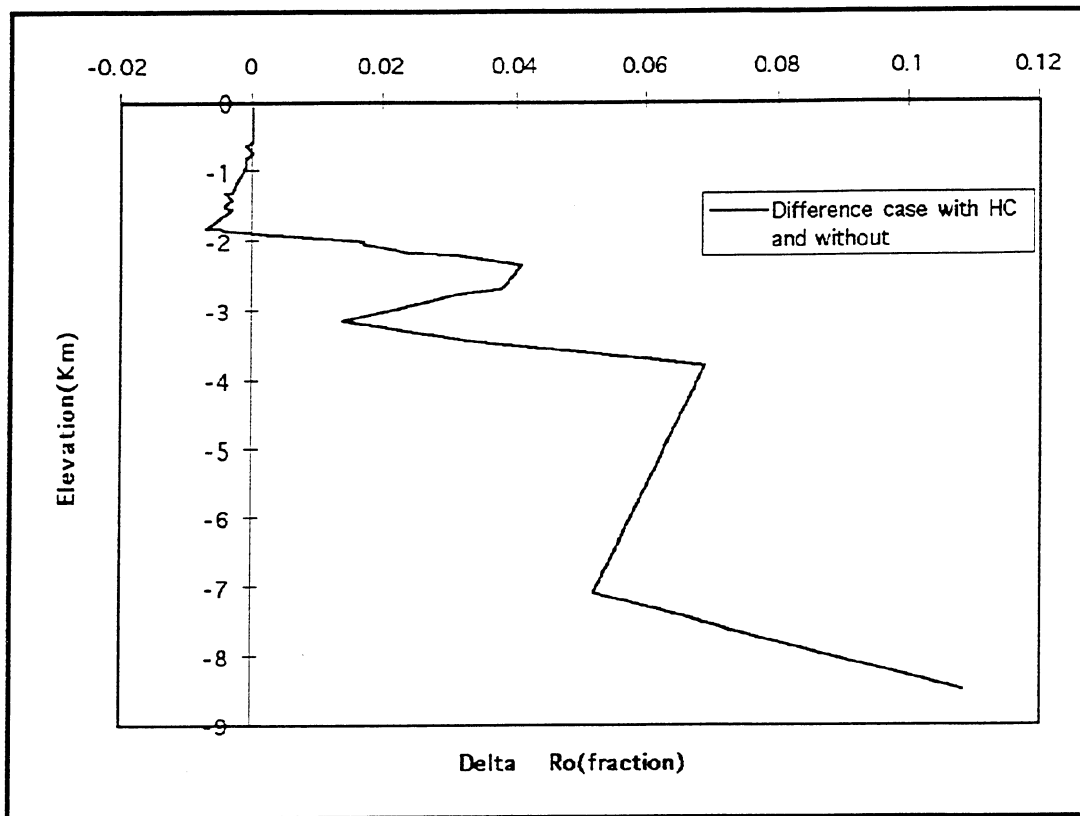


Figure V.24. Introduction of hydrocarbons with timing indicated in Base Case Table V.5 increases sediment maturity under the reservoirs by ~0.1% Ro.

g. Hydrocarbon Maturation

Calculation of hydrocarbon maturation in the SEI data cube shows clearly that there is no hydrocarbon maturation in the minibasin itself. Figure V.25 shows that oil is being generated below the salt weld at the base of the minibasin, but not in the minibasin itself. This is an important result. It shows that the hydrocarbons in Pennzoil's Block 330 fields cannot have been produced in the SEI Block 330 minibasin that hosts them, but must have been produced below the minibasin and introduced when the salt weld opened.

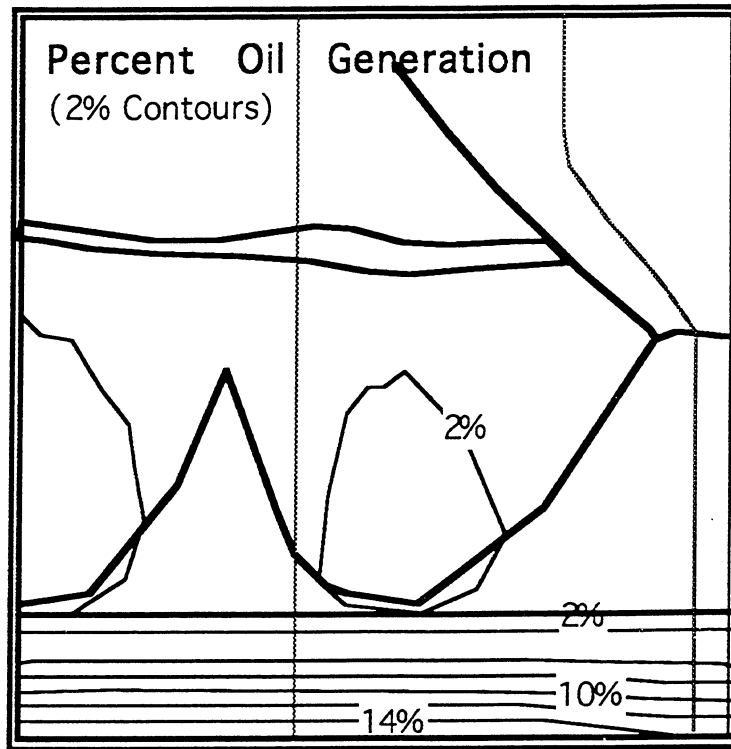


Figure V.25. Percentage of oil conversion in Line 6. Significant oil is generated only below the lower salt sill. Significant oil was not generated within the minibasin or in the Miocene section that lies between the two salt sills. Oil must have entered the minibasin through salt welds.

h. Steady Fluid Flow in the SEI Minibasin

The permeability of the seal is adjusted in nature and in our calculations such that the excess fluid pressures under the seal do not exceed 0.8 reduced lithostatic (lithostatic minus hydrostatic). Fluids leak through the seal where it is topographically highest because it is there that fluid pressures first exceed this fraction of lithostatic. Calculated subsurface fluid pressures agree well with the pressures inferred from mudweights. Figure V.26 compares the two in pseudowell 17 of Line 6.

Because of the interaction of the migrating seal with low permeability faults and salt, there are several fluid compartments in our simulations of the South Eugene island subsurface. The most interesting case is shown in Line 4 where the Red Fault is a nexus of 4 parallel faults. Figure V.27 shows the calculated pressure distribution at the present time for Line 4. Arrows indicate flow. The figure shows flow is occurring into the horse between the two of the faults, and that this focussed leakage is producing a very localized finger of overpressure at shallow depths. Such a finger of overpressure is not observed in the study area, probably because flow leaks across the faults where sands are juxtaposed (a feature not included in the simulation shown in Figure V.27). However, narrow fingers of overpressure are known in the Gulf Coast, and phenomena similar to that illustrated in Figure V.27 may be the cause.

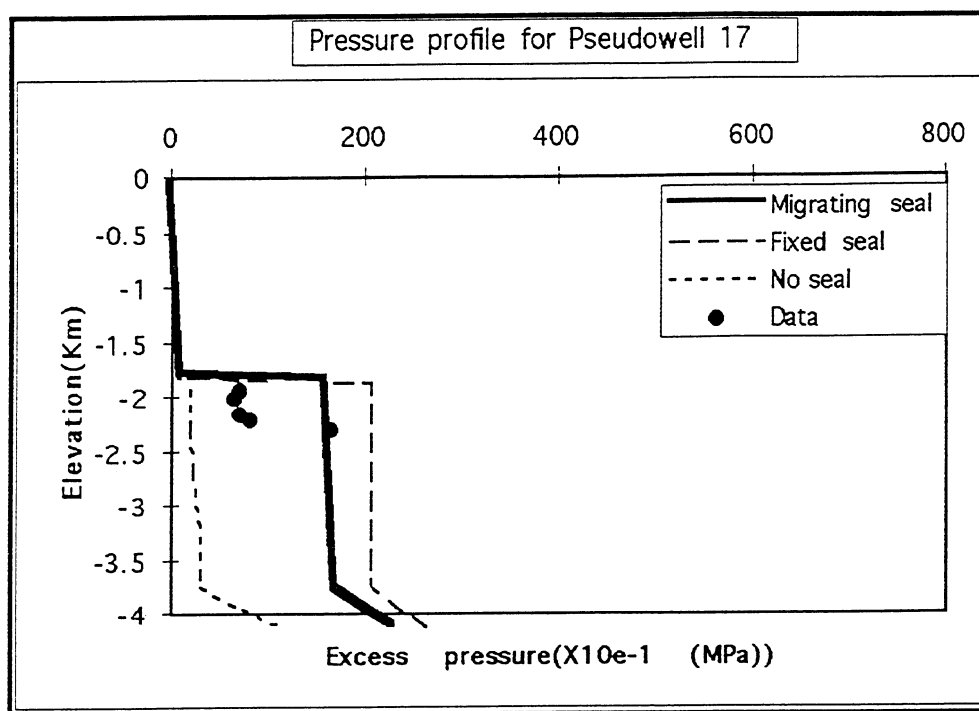


Figure V.26. Pressure Profile along pseudowell 17 in Line 6 compared to mudweight data. Pressure increase at 3.7 km reflects entry into the salt sill. Data indicates there are perhaps two pressure compartments above the salt sill, with the upper compartment (between 1.7 and 2.3 km depth) overlying a lower compartment (between 2.3 and 3.7 km). Our models resolve only one compartment at this location (between 1.7 and 3.7 km depth).

Another feature observed in the simulations is important. Fluids were observed to move horizontally through the sands both to the east and to the west. We are currently addressing this pattern and seeking to simulate Allen-type flow across the faults where sands are juxtaposed. The important point to be made at this stage is that there horizontal fluid flow through sands is intense and the pattern of flow is complex. It is therefore perhaps no surprise that the kinds of rock alteration that depend on fluid flow is complex and difficult to interpret. We hope that despite the complexities modeling can identify the robust aspects of the flow pattern and that these can be verified by alteration data.

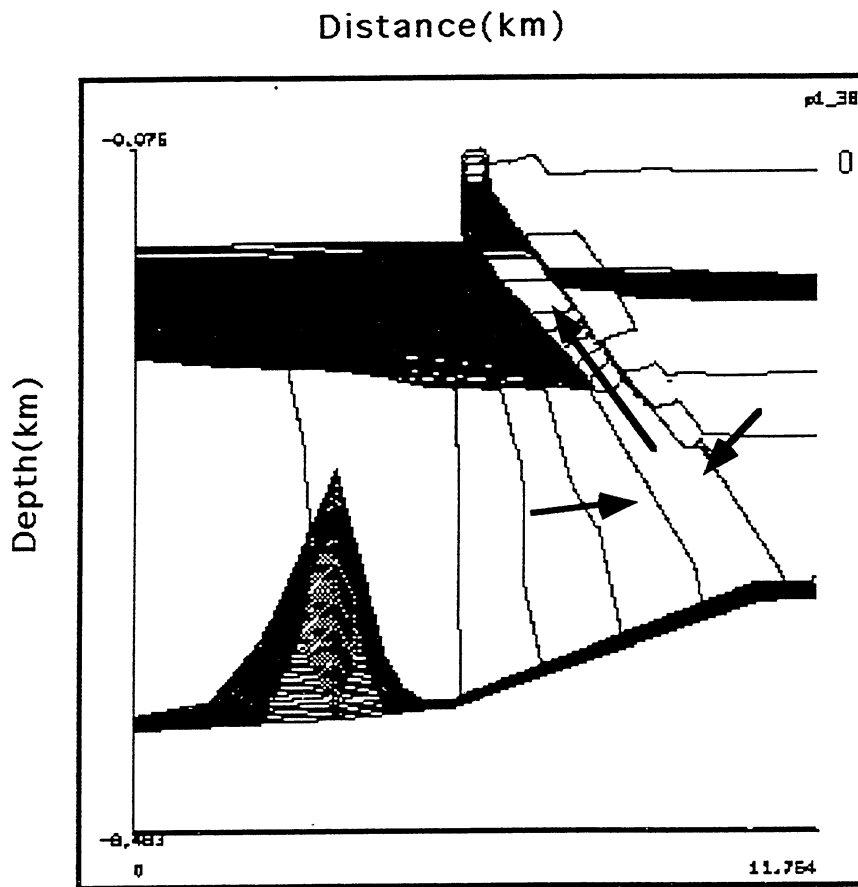


Figure V.27. Pressure compartmentalization and flow in Line 4. In this case flow is channeled around impermeable faults into a horse between two faults. Within the horse this steady leakage produces a narrow finger of shallow overpressure. Pressure is contoured and overpressures indicated also by different shading. Arrows show the general direction of fluid flow.

i. T Anomalies Produced by Pulses of Fluid Flow

Figure V.27 shows the temperature pattern 400 years after the seal on both sides of the Red Fault was ruptured, rapidly venting fluids through the permeable sand network in the section. The sides of the fault were given 5.2 darcy permeabilities, and the sand network had the realistic permeabilities assigned by the porosity-dependent permeability model (section V.D.3.c).

Sudden venting is one possible explanation for the temperature anomalies observed along the Red Fault. However the pattern is not as good a match as the hydrocarbon-generated anomaly pattern. The rapid venting anomaly is not as broad as the observed anomaly, and fluid flow could account for the positive temperature anomaly under the reservoirs and along the Red Fault, but not the negative temperature anomaly above the reservoirs. The temperature pattern produced by hydrocarbons produces the dipolar anomaly pattern observed; rapid fluid venting cannot produce this dipolar pattern.

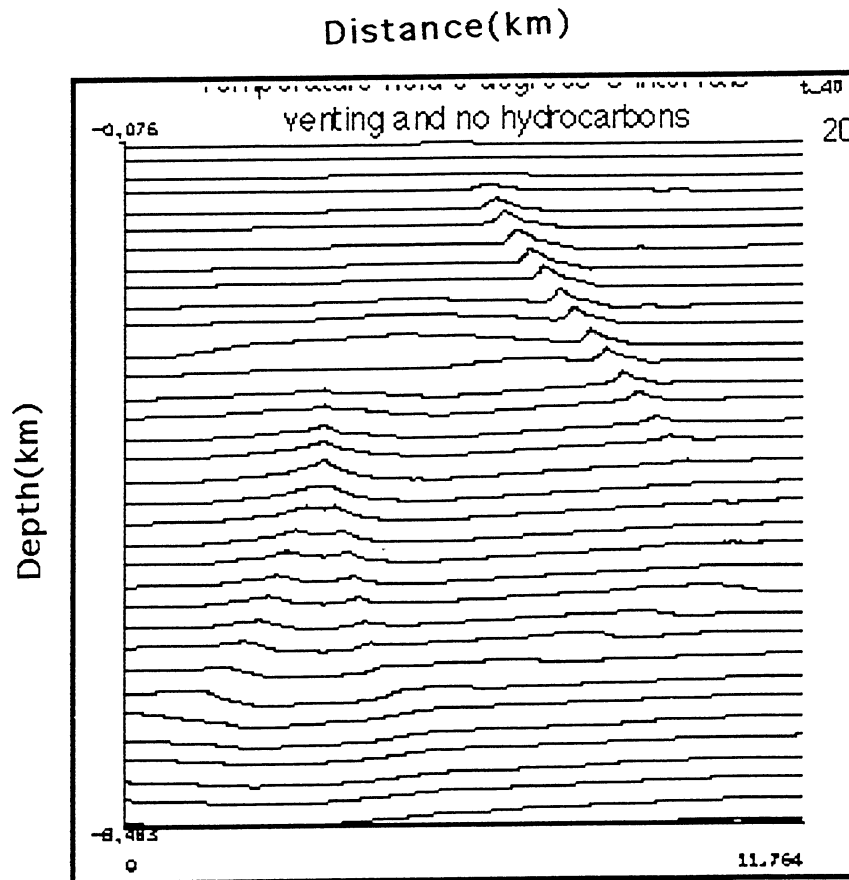


Figure V.28. Temperature anomalies of about 5°C are produced after 400 years after the seal on either side of the Red Fault in Line 4 was ruptured. Section geology is shown in Figure V.26.

j. Analysis of Highly Episodic Fluid Flow(Roberts, Boling Green, Nunn, LSU)

A great deal of modeling attention has been devoted to assessing the magnitude of thermal anomalies that could be produced by episodic rapid venting through ruptured portions of the seal in the Block 330 study area. This work has been accepted for publication in the Journal of Geophysical Research (Roberts et. al., in revision).

The studies that are reported there found that venting from the Red Fault can produce temperature anomalies up to 30°C in magnitude 350 years after a 10 millidarcy fault is opened. The anomalies are localized within 0.5 km of the Red Fault and do not extend more than 0.75 km above the seal because flow is effectively diverted by the overlying sands. The depth extent of those parts of the fault that become permeable during a rupture event is important. If the permeable part of the fault extends 0.5 km rather than 1.5 km below the seal, the maximum temperature anomaly after 100 years of venting is reduced from 24 to 15°C. The permeability of the shale units in the basin does not significantly impact the temperature anomalies produced in the first few hundred years of venting. The permeability of the sands and fault are the important controls. For example, the maximum temperature anomalies calculated for cases where the permeability of the fault is a time-dependent function of fluid pressure (not a constant 10 millidarcies) is 7°C at 100 years after the start of fluid expulsion. All sands were taken to have 1 millidarcy permeability in the simulations. This value is conservatively low (see discussion in V.d.4.c).

These simulations show that temperature anomalies up to 30°C can be produced along the ruptured parts of a fault in and below the seal. With higher sand and fault

permeabilities the episodic flow events could be of very short duration and the temperature anomalies produced along the fault could be extremely local. Very short and intense rupture appear the best candidate to account for the elevated vitrinite reflectance R_o anomalies observed in the A6 sidetrack and the lack of any such anomalies in the Pathfinder 1000 ft away.

k. Vitrinite Reflectance Anomalies in the A6 Sidetrack

Highly episodic fluid venting can account for the vitrinite reflectance R_o anomalies observed in the A6 sidetrack and the curious feature that the same anomalies are not observed in the Pathfinder well only 300 m from the A6. We have calculated the effects of subjecting fault sediments near where the A6 intersects the Red Fault to temperatures to temperatures 10° and 30°C above present ambient for 150 years. These temperature perturbations cause an increase in vitrinite R_o of 0.14 and 0.21%, respectively. Figure V.29 shows that this level of additional maturation can easily account for the vitrinite anomaly observed in the A6 sidetrack. In addition, a thermal perturbation lasting 150 years will only propagate about 140 m on either side of the fault. Thus the lack of a vitrinite reflectance in the Pathfinder well 300 m distant from the A6 sidetrack can be explained providing the duration of the fluid venting episode was short.

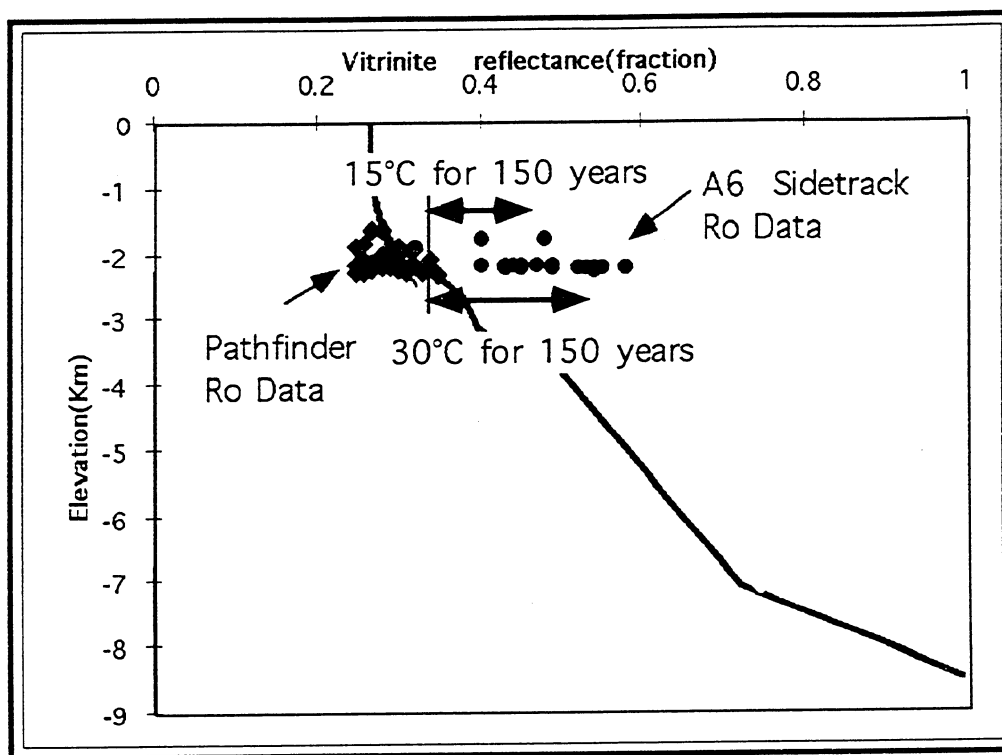


Figure V.29. Calculations show that a heating pulse of 30°C for 150 years could explain the vitrinite reflectance anomaly observed in the A6 sidetrack and its absence in the Pathfinder well 300 m distance from the A6.

l. Fluid Transport in Migrating Fluid-Filled Fractures (Nunn, LSU)

The conclusions of the previous section are very close to a new idea that came out of the DOE project: that upward propagation of water- and hydrocarbon-filled fractures could be a significant mechanism of fluid transport in the overpressured sediments below seals in the Gulf of Mexico and elsewhere. Analysis shows that such fractures could

propagate at 1000 m/yr and could cumulatively accommodate mass flux rates of ~100 kg / m²-yr. This idea is described in Nunn (in press).

m. Thermohaline Convection, Salinity Distribution, and Salt Dissolution

Pore water salinity varies in the SEI 330 study area in ways that suggest fluid movement. Pore water salinities of reservoir sands were estimated from about 50 SP logs. Reservoirs in the SEI study area at <1600 m depth have higher salinities than reservoirs at >2000 m depth. The salinity of the shallower reservoirs has decreased significantly since the 1970's whereas the salinity of the deeper reservoirs has not changed. This may suggest that recent expulsion of low salinity waters from the overpressured zone that have diluted the deeper reservoirs in the recent past are only now diluting the higher reservoirs.

Calculations (Sakar et. al., 1995) show that thermohaline convection can be a significant mechanism of salt dissolution even in sediments with permeabilities as low as 0.01 md. This shows that the high salinities in the upper Block 330 reservoirs could have been produced by convective dissolution of salt domes in the area.

E. CONCLUSIONS

Major conclusions from the modeling are:

(1) The present-day temperature distribution, contrary to the perceptions at the start of the project, is a steady state distribution. Thermal anomalies along the Red Fault are due to the blanketing effects of overlying hydrocarbons, not bursts of rapid fluid venting from the overpressured zone.

(2) Vitrinite reflectance and other maturity indicators in the Pathfinder drill hole are well matched by calculated maturity parameters assuming no rapid fluid venting.

(3) No hydrocarbons have matured in the SEI Block 330 minibasin. However kerogen has matured to oil below the salt weld at the base of the Miocene section. Oils and gases in the Block 330 reservoirs must have come from sources below the minibasin, perhaps when the salt weld opened.

(4) The blanketing effect of oil and gas in the Block 330 reservoirs causes the vitrinite reflectance of organic matter along the red fault to increase about 0.07%. This is a potentially observable increase and suggests that the time of hydrocarbon emplacement might be constrained by maturity anomalies. However the maturity increase by hydrocarbon blanketing is much smaller than the 0.3% anomaly observed in the part of the fault penetrated by the A6 sidetrack, a mere 1000 ft from the Pathfinder well. The Ro anomaly in the A6 is corroborated by conodont color changes and fluorescence data and thus the maturity anomaly thus appears to be real.

(5) The maturity anomaly in the A6 sidetrack could potentially be caused by rapid, episodic fluid venting. Very localized venting up the Red Fault is indicated by the lack of vitrinite anomalies in the Pathfinder well only 1000 ft from the A6 sidetrack. Calculations show that a short lived (few hundred year) pulse of fluid up Red Fault could produce a localized temperature anomaly in the fault up to and perhaps somewhat greater than 30°C in magnitude. This magnitude and duration of thermal pulse would be sufficient to produce an Ro anomaly of 0.2%, nearly the 0.3% recorded by the A6 sidetrack measurements.

E. REFERENCES

- Alexander, L. (1995). Geologic Evolution and Stratigraphic Controls on Fluid Flow of the Eugene Island Block 330 Mini-basin, Offshore Louisiana, Gulf of Mexico. Cornell PhD Thesis, 250p.
- Dowdle, W. L. and W. M. Cobb (1975). "Static Formation Temperature From Well Logs - An Empirical Method." Journal of Petroleum Technology **27**: 1326-1330.
- Guerin, G., Anderson, R. N., He, W. (1994). "3D Temperature Distribution and Heat Flow Analysis for the Eugene Island 330 Area, Offshore Louisiana." AAPG-Abstract:
- Holland, D. S., W. E. Nunan, et al. (1980). "Eugene Island Block 330 Field - USA. Offshore Louisiana." in Halbouty, M. T., ed., Giant oil and gas fields of the decade:1968-1978 AAPG Memoir #30: 253-280.
- Losh, S., L. Eglinton, et al. (1994). "Report on Geologic and Geochemical studies on rocks collected from the Pathfinder well and elsewhere in SEI Block 330." DOE yearly report :
- Luo, M., J. R. Wood, et al. (1994). "Prediction of Thermal Conductivity in Reservoir Rocks Using Fabric Theory." Journal of Applied Geophysics **32**: 321-334.
- McKenna, T. E. (1994). "Evaluation of Subsurface Temperature in Eugene Island Block 330 and Vicinity." AAPG Abstracts:
- McKenna, T. E. and J. M. Sharp (1995). "Thermal Conductivity and Radiogenic Heat Production from South Texas (Gulf of Mexico Basin)." GSA Abstracts **27**(6):
- McKenna, T. E., J. M. Sharp, et al. (1996). "Thermal Conductivity of Wilcox and Frio Sandstones in South Texas (Gulf of Mexico Basin)." Submitted to AAPG Bulletin:
- Mello, U. (1994). Thermal and Mechanical History of Sediments in Extensional Basins, Columbia University PhD thesis, 350p.
- Meulbroek, P. and L. M. Cathles (in Preparation). "Modeling the Effects of Evaporative Fractionation on Bulk Composition." :
- Nunn, J. A. (1996). "Buoyancy-Driven Propagation of Isolated Fluid-Filled Fractures: Implications for Fluid Transport in Gulf of Mexico Sediments." Journal of Geophysical Research In Press:
- Nunn, J. A., S. J. Roberts, et al. (1995). Fluid Migration in Eugene Island Block 330 Area of Offshore Louisiana Archie Visualization Technology Conference, Woodlands, Texas,
- Roberts, S. J. and J. A. Nunn (1995). "Episodic Fluid Expulsion From Geopressured Sediments." Marine and Petroleum Geology **12**: 195-204.
- Roberts, S. J., J. A. Nunn, et al. (1996). "Expulsion of Abnormally Pressured Fluids Along Faults." Journal of Geophysical Research In Revision:

- Sarkar, A., J. A. Nunn, et al. (1995). "Free Thermohaline Convection Beneath Allocthonous Salt Sheets: An Agent For Salt Dissolution and Fluid Flow in Gulf Coast Sediments." Journal of Geophysical Research **100**: 18085-18092.
- Shosa, J. D. and L. M. Cathles (in Preparation). "A Direct Investigation of Capillary Exit Pressure as a Basin Sealing Mechanism." :
- Whelan, J. K., L. B. Eglinton, et al. (1994). "Organic Geochemistry of Fluids and Kerogens from DOE Drilling in Eugene Island 330 Reservoirs Indicators of Fluid Flow Pathways." AAPG Abstracts:

Task Six - Geochemistry

Steven Losh - Task Manager

OBJECTIVE:

The purpose of the geochemical phase of this project was to analyze rock, brine, oil, and gas samples in order to test the hypothesis that oil and gas have recently migrated and are still migrating from depth, along growth faults, into the currently-producing reservoirs in the SEI Block 330 field. To accomplish this, analyses were performed on samples from the Pathfinder well, within and adjacent to the main growth fault abutting the Block 330 field, and compared with data obtained from samples from the reservoirs. For organizational purposes, the data so obtained are divided into two categories and are presented in this order in the report: 1) inorganic geochemistry, which includes: a) geology of the core, b) petrographic, mineralogic, whole rock geochemical, and stable isotopic investigations of rock samples, and c) brine chemistry; and 2) organic geochemistry, which includes a) hydrous pyrolysis experiments in order to evaluate controls on and kinetics of gas generation from sediments, and b) a wealth of analyses (many published separately) pertaining to whole oil, gas, and condensate compositions, compound-specific isotopic composition, and biomarkers. An on-line database (c) has been constructed to allow public access to the data collected as a part of the inorganic and organic geochemical investigations. The inorganic geochemical report (Subtask 6.1) summarizes the work carried out over the duration of the project, whereas the organic geochemical report (Subtask 6.2) summarizes the work accomplished over the past year.

SUMMARY:

Some of the main findings of the geochemical investigation regarding fluid ascent via the growth fault system in SEI Block 330 are:

- Although there is a considerable degree of compositional heterogeneity between reservoirs, the oils, gases, and condensates in SEI 330 appear to have a single source in Mesozoic rocks. The presently-observed variations in composition have resulted from processes that affected the oil and gas during and after migration, such as evaporative fractionation and biodegradation. Gas is characterized via higher thermal maturity than oil, suggesting that the oil is "swept up" by vertically migrating gas. Brine composition, specifically ^{129}I and $^{87}\text{Sr}/^{86}\text{Sr}$, supports the interpretation of large-scale vertical migration of fluid into the reservoirs. Systematic variations in major element, specifically chlorine, composition of brine between reservoirs indicate that brine entered the reservoirs at different times and/or from different directions.

- A variety of data support ongoing filling of the GA sand via rapid injection, and high fluid flux in the fault zone in the past. Repeated sampling of wells over a period of 10 years has led to the finding that unbiodegraded oils are injected into the GA sand on the time scale of years or less. Biodegradation occurs rapidly there, and the presence of unaltered oil is interpreted to reflect rapid influx from depths at which biodegradation does not take place. A variety of other organic geochemical data corroborate this conclusion. In the A6ST well, which penetrates the main growth fault a point 1000 feet from the fault intercept in the Pathfinder well, sediments from within the growth fault are characterized by anomalously high vitrinite reflectances relative to sediments outside the fault, indicating that the fault is locally a paleothermal anomaly. Combined with stable isotopic composition of

minerals from the fault in that well, these data support the conclusion that the fault, at least at some locations, acted as a conduit of relatively high-temperature fluids.

- The Pathfinder core contains three structurally - distinct fault domains, only the deepest of which contains oil. Based on structural and geologic data, this deepest domain is concluded to have been most recently active. Structural and geochemical data indicate the other two fault domains were active prior to oil migration. The oil-barren domains contain fractures that are favorably oriented to transmit oil, and oil is furthermore present in sands in these domains; it is evident that fault zone oil migration took place only within that part of the fault that was active during the time migratable oil was available to the fault. Despite the variability of hydrogeologic characteristics of faults as evident in the core, the geochemical data indicate that none of these cored faults transmitted significant amounts of fluid in the Pathfinder well, indicating the operation of a higher-order control on fluid flow in the growth fault. The same fault in the A6ST well has apparently acted as a fluid conduit, indicating relatively short-range lateral variability in fluid flow behavior in the fault.

Summary of analyses accomplished for Task 6.1, Inorganic geochemistry

Subtask	Contracted	Completed
6.1.1	250	225
6.1.2	100	80
6.1.3.	Omitted	
6.1.4	100	110 ¹
6.1.5.	225	138 ¹
6.1.6.	150	10 ²
6.1.7	150	10 ²
6.1.8.	100	85
6.1.9.	250	81 ²
6.1.10/	10	5
6.1.11.	30	22

1. One analysis was counted as two hours of analysis time.

2. These subtasks were budgeted on the assumption that authigenic phases suitable for analysis would be abundant; this turned out not to be the case. The money not spent on these subtasks was reprogrammed within Task 6.1 for the completion of other essential tasks for which no money was initially budgeted. These tasks include:

- Development of protocol for acquisition, preservation, and complete analysis of core, involving research and meetings in Houston with oil company and service company personnel. The coring procedure was highly successful and has been adopted by Pennzoil and other operators in the Gulf.
- Overseeing coring while on rig. Funds were also redirected to cover cost overruns for core acquisition.
- Logging core in detail while Pathfinder was being drilled.
- Structural interpretation of core.
- Core preservation and curation.

SUBTASK 6.2
ORGANIC GEOCHEMISTRY
Jean Whelan, WHOI
October 9, 1995

I. COMPLETION TASKS IN GANT CHART:

A. Task 6.2.1-a to d: Organic Geochemistry, Hydrous pyrolysis:

Contracted: Completion of eight experiments
Completed: Nineteen experiments (see section II-A below)

B. Task 6.2.2, Organic Geochemistry, petrography, isotopes:

Contracted: Completion of 430 analyses
Completed: 817 analyses as summarized in Table II-B-i including 144 oil and 144 gasoline range hydrocarbon analyses by the GERG group as summarized in Table II-B-ii (see section II-B below).

C. Task 6.2.3, Organic geochemistry, Modeling and technology transfer:

Contracted: Completion paper on GBRN data; completion hydrous pyrolysis paper

Completed:

- GBRN data: Two papers complete; one additional paper in preparation (see attached manuscript); several papers presented at scientific meetings (see abstracts and posters in section II-C below).
- GBRN data (additional): World Wide Web page completed (<http://dynatog.who.edu/>); summary of this work included along with links to other GBRN work and to places where other geochemical research is being carried out, such as Newcastle University in the U.K (See section II-C-ii below).
- GBRN data (additional): Created data base of organic geochemical data (see section II-C-i below for parameters included and layout of data); this will be be made available via our WWW page.
- Hydrous pyrolysis: one paper published (in Nature); a second on the Monterey Shale has been submitted and a third is in preparation. Several papers on this work have been presented at national scientific meetings (see abstracts included in report in section II-C-v).

II. SUMMARY OF TECHNICAL PROGRESS:

A. Task 6.2.1-a to d: Organic Geochemistry, Hydrous pyrolysis:

Introduction

Thermal maturation of sedimentary organic matter involves numerous chemical transformations that result in the production of hydrocarbon and non-hydrocarbon gaseous alteration products. These products play a critical role in the development of overpressure, the transport of petroleum, and sediment diagenesis in sedimentary basins (Hunt *et al.*, 1995; Price *et al.*, 1983; Whelan *et al.*, 1994a,b). Understanding fundamental processes that regulate the generation of gaseous products is essential to constrain factors influencing the accumulation of hydrocarbons in the Gulf Coast, USA. Owing to the extreme complexity of natural systems, key processes that regulate the timing, amounts, and composition of organic alteration products are often obscured. Laboratory heating experiments have proven to be an effective tool for constraining physical and chemical processes associated with the generation of hydrocarbons. In particular, the role of water during organic reactions in geologic environments has received much attention in recent years (Helgeson *et al.*, 1993; Hoering 1984, Lewan 1991, 1993; Seewald 1994; Shock 1988; Siskin and Katritzky, 1991; Stalker *et al.*, 1994). Laboratory experiments have demonstrated that the presence of water during the maturation of sedimentary organic matter significantly influences the amounts and composition of liquid hydrocarbons. It is likely that water may also play an integral role in the generation of volatile hydrocarbons and non hydrocarbon such as carbon dioxide. Except for a few notable exceptions (Lewan 1992; Tannenbaum and Kaplan 1985; Seewald 1994) laboratory studies focusing on the generation and stability of hydrocarbon and non-hydrocarbon gases have been conducted in the absence of added water.

The experiments presented here were conducted to constrain factors influencing the generation of natural gas and carbon dioxide during the thermal maturation of sedimentary organic matter from the Monterey, Smackover, and Eutaw formations. The experimental design reflects our attempts to duplicate natural conditions in the laboratory. Water is ubiquitously present in most sedimentary basins. Accordingly, our experiments involved heating bulk sediments in the presence of liquid water. Experiments were conducted at temperatures ranging from 125 to 360°C at 350 bars pressure, conditions that are similar to those in most sedimentary basins during gas generation.

Methods

Sample Description and Preparation.

Samples of the Monterey, Smackover, and Eutaw Shale were used for the experiments presented here. These samples allow comparison of the gas generation characteristics of a sediment containing sulfur-rich organic matter primarily of marine origin (Monterey Shale), with two sediment samples containing relatively sulfur-poor organic matter primarily of terrestrial origin (Eutaw and Smackover Shale).

The Monterey Shale is a thermally immature (bituminite reflectance = 0.25% expressed as R_o) consolidated sediment sample from the Miocene Monterey Fm. (ML91-17). It was obtained from an outcrop at Naples Beach, CA. The sample was removed from a 10 cm interval at the base of Unit 315, approximately 9 m below the lowest phosphorite horizon (M.D. Lewan, personal communication). The sample comprised a lenticularly laminated claystone and visually appeared fresh (i.e. unweathered) and blocky. The surfaces of the sample were scraped to expose pristine material and remove possible contaminants. This sample is organic rich (20.6 wt. % TOC) and based on petrographic observations and elemental analyses can be classified as a type II-S kerogen.

The Eutaw Shale is a Cretaceous consolidated sediment obtained from core cuttings recovered at a depth interval of 3011 to 320 m from the Hampton/Nelson Ball well in Pike County, Mississippi. It is a relatively organic lean shale (0.97 wt. % TOC) and contains abundant quartz. A measured vitrinite reflectance value of 0.45% R_o indicates that the kerogen has not yet reached the oil window. Petrographic observations indicate that this sediment contains mostly terrestrial derived organic matter that can be classified as type-III kerogen.

The third shale is a sample from the Upper Smackover formation (Jurassic). It is a consolidated sediment obtained from core cuttings recovered at a depth of 3260 m from the Amareda Scotch Well #1 in Clark County, Alabama. This shale is relatively organic-lean (0.917 wt. % TOC), contains abundant quartz, and has a measured vitrinite reflectance value of 0.52% R_o . Petrographic observations indicate that the kerogen in this sample is type-III and characterized by a similar maceral type distribution as the Eutaw Shale.

During this study our primary goal was to constrain chemical processes that regulate the rate and extent of chemical reactions responsible for the generation of gaseous products. Accordingly, to minimize physical processes associated with expulsion of produced gases, the starting sediments were pulverized in a disc mill until the entire sample passed through a <125 μ m sieve. In addition, existing hydrocarbons were removed prior to heating. This was achieved for the Eutaw and Smackover Shale by Soxhlet extraction in a 93:7 $\text{CH}_2\text{Cl}_2/\text{CH}_3\text{OH}$ mixture for 48 h. The Monterey was sequentially extracted by sonic disruption for 9 minutes in CH_2Cl_2 , a 1:1 mixture of $\text{CH}_2\text{Cl}_2/\text{CH}_3\text{OH}$, and CH_3OH . Because we were concerned only with carbon dioxide generated from sedimentary organic matter, the starting sediments were treated with 10% HCl at 40°C for 2 h to remove sedimentary inorganic carbonate minerals that could dissolve during an experiment. For the Monterey Shale experiments at 225 and 275°C, the sediment was not treated with HCl. Thus, generated carbon dioxide for these two experiments almost certainly includes a contribution from inorganic carbonate.

Experimental Apparatus and Conditions

The experiments were conducted in 316 stainless steel tubing reactors with a 20 cm^3 internal volume (Fig. II-A1). The experiments described here are in many ways similar to the hydrous pyrolysis experiments described by Lewan (1991) in that bulk sediments are heated in the presence of excess liquid water, but there are important differences. For example, in our experiments the reactor vessel is filled completely with liquid water precluding the existence of a vapor head space during an experiment. This may be particularly significant for studying volatile products since they effectively partition into a vapor head space at the conditions of an experiment removing them from intimate contact with the water and sedimentary components. In addition the apparatus utilized for this study allows fluid samples to be withdrawn from the pipe-bomb at the temperature and pressure of an individual experiment avoiding potentially ambiguous reactions during a prolonged quench process. Moreover, because the experiments do not need to be cooled to determine the amounts of generated gases, fluid chemistry can be monitored as a function of time during an individual experiment.

During this investigation, it was assumed that all generated gases dissolved into the aqueous phase at the conditions of these experiments. To avoid the formation of a separate gas or oil phase which might represent a sink for gaseous alteration products, relatively high water/sediment mass ratio were used. For each experiment 1.0 g of bulk sediment was loaded into the tubing reactor before sealing. Prior to heating, the air in the tubing reactor was evacuated and partially filled with argon-purged distilled water to ensure that the sediment was in contact with liquid water during heating. The entire reactor was heated to the experimental temperature in a horizontal tube furnace in approximately 30 minutes. Once at the desired temperature, the tubing reactor was completely filled with distilled water and pressurized to 350 bars so that only a single liquid phase was present (i.e., no head-space). Temperature was monitored ($\pm 2^\circ\text{C}$) with a thermocouple at each end of the tubing reactor to ensure there were no thermal gradients. Experiments utilizing the Monterey and

Smackover Shale were conducted isothermally for approximately 170 h. In contrast, the Eutaw Shale investigation was conducted by maintaining the tubing reactor at a constant temperature for a selected period of time before rapidly increasing the temperature to a new value. At each temperature condition gas generation was monitored as a function of time.

During the course of an experiment fluid samples were withdrawn into glass gas-tight syringes and monitored for the concentration of dissolved species. An internal 10 μm steel mesh filter ensured particle free fluids. Pressure was maintained during the sampling process by pumping argon-purged distilled water into one end of the tubing reactor with an HPLC pump while the fluid sample was removed from the other. The sampling process was performed rapidly (1 to 2 minutes) to avoid dilution of the fluid samples with the freshly injected water. All subsequent concentrations of dissolved gases were corrected for the amount of water injected on each sampling occasion.

Analytical Procedures

Fluid samples were analyzed for the dissolved concentrations of CO_2 , C_1 - C_4 hydrocarbons, and for selected samples dissolved organic acid anions, H_2 , and H_2S . The first aliquot of fluid (0.5 ml) withdrawn from the tubing reactor on any sampling occasion was discarded and served only to flush the sampling valve and stainless steel lines. Dissolved CO_2 and C_1 - C_4 hydrocarbons were analyzed in duplicate in subsequent aliquots (0.5 ml) by injecting the sample into a purge and trap apparatus interfaced directly to a gas chromatograph equipped with a flame ionization and thermal conductivity detector connected in series. The fluid samples were acidified with 1 ml of 25 % phosphoric acid in the purge cell to ensure complete evolution of dissolved CO_2 . Separation of gases in the gas chromatograph was achieved with either a porapak-Q packed column or a poraplot-Q megabore capillary column. Authentic standards were used to establish a three level calibration curve for CO_2 and each hydrocarbon. Analytical uncertainties are estimated to be <5 % for these species.

The concentrations of aqueous organic acid anions generated during the experiments were analyzed by ion chromatography on a Dionex DX-300 ion chromatograph equipped with an AS11 column and a conductivity detector. Samples were preserved with 200 ppm mercuric chloride and stored in a refrigerator prior to analysis. Authentic standards were used to establish a three level calibration curve for all acids reported.

Dissolved H_2 concentrations were determined by gas chromatography (thermal conductivity detector and a 5A molecular sieve packed column) following a headspace extraction. Dissolved H_2S was determined gravimetrically by acidifying the fluid sample with 25 % phosphoric acid and precipitating the evolved H_2S as Ag_2S in a 3 wt. % AgNO_3 solution. Estimated uncertainties for the H_2 and H_2S analyses are <5 %.

Careful accounting of all fluid removed and added to the tubing reactor allowed the absolute amounts of generated products to be calculated from the dissolved concentrations, tubing reactor volume, and the mass of sediment in each experiment. The specific volumes of water at the temperature and pressure conditions of each experiment were calculated from the equation of state for water of Haar *et al.*, (1980).

Elemental analyses (CHNSO) of the starting sediments and solid alteration products were conducted on either a Leco 932 or Fisons EA1108 elemental analyzer. Inorganic carbonate (IC) was determined on a Coulometrics carbon analyzer. Total organic carbon (TOC) was determined by difference. The starting sediment and solid alteration products for the Monterey Shale experiments were demineralized by HCl and Hf acid digestions (Eglinton and Douglas, 1988) to isolate the kerogen. Iron sulfides were removed from the kerogen by treatment with CrCl_2 and HCl (Canfield *et al.*, 1986; Acholla and Orr, 1993). The relatively pure kerogen isolate was analyzed for its elemental composition. Similar kerogen isolations for the Eutaw and Smackover Shale were not possible owing to the low organic matter content of these sediments.

Results

Volatile Products

Thermal maturation of organic-bearing sedimentary rocks is characterized by the generation of gaseous alteration products, the extent and rate of which are strongly dependent on time and temperature (Tables IIA-1, 2, and 3; Figs. IIA-2, 3, and 4). For example, during the Monterey and Smackover experiments, methane generation increased by more than three orders of magnitude during heating at 360°C relative to 125°C, while methane generation was almost 3 orders of magnitude greater at 360°C relative to 225°C for similar reaction times during maturation of the Eutaw Shale. The concentrations of ethane and propane showed similar temperature trends although the absolute abundance of these hydrocarbons were substantially less than that of methane (Tables IIA-1, 2, and 3). Although, methane is the dominant hydrocarbon gas generated at all conditions during these experiments, its relative abundance shows a clear trend as a function of temperature (Fig. IIA-5). At 125°C methane constitutes approximately 90 % of the generated hydrocarbon gas while at 360°C its relative abundance has decreased to approximately 40 %. Increasing maturation time results in decreasing relative abundance of methane on the time scale of these experiments (Fig. IIA-5).

In addition to alkanes, significant quantities of alkenes were generated at all temperature for all sediments (Tables IIA-1, 2, and 3). In general the abundance of alkenes increased with increasing temperature. In contrast to the saturated hydrocarbons, however, the abundance of alkenes decreased with continued reaction at constant temperature, except during the 125°C experiments in which their abundance remained effectively constant. These results indicate that ethene, propene, and *n* butene are unstable at temperatures > 150°C. That the alkene abundance at 125°C remained constant while the abundance of alkanes increased may suggest that alkenes were being generated but degradation reactions were occurring at a similar rate. These results confirm the hypothesis of Tannenbaum and Kaplan (1985) who suggested that alkenes are initially produced in small quantities under dry or hydrous conditions but represent an unstable intermediate during the formation of petroleum.

Although the thermal maturation of sedimentary organic matter results in the production of substantial hydrocarbon gases, carbon dioxide was unequivocally the dominant gaseous alteration product (Tables IIA-1, 2, and 3). During thermal maturation at 360°C 312, 337, and 194 mg/g TOC carbon dioxide were produced from the Monterey, Smackover, and Eutaw Shale, respectively, and was still increasing in all experiments, even after heating the Eutaw Shale for 2716 h at 360°C. These quantities are at least an order of magnitude greater than the total amount of hydrocarbon gases produced from each sediment. Carbon dioxide generation increased with increasing temperature, similar to the hydrocarbon generation trends.

Owing to the possibility that carbonate minerals such as calcite or siderite can precipitate during hydrous pyrolysis experiments, carbon dioxide values represent absolute minimums. Evidence for calcite precipitation is provided by the Monterey experiments MS5 and MS13. In contrast to the other Monterey experiments in which the rate of release of carbon dioxide to solution showed continuously decreasing rates with increasing reaction time, MS5 and MS13 were characterized by initially rapid carbon dioxide increases in solution followed by relatively minor increases between the samples at 25 and 70 h. A subsequent rapid release of carbon dioxide was observed between 70 and 170 h (Fig. IIA-2). This trend suggests that carbon dioxide may have been precipitating as a carbonate mineral suppressing the amount observed in solution. The non-systematic increases in carbon dioxide released to solution as a function of temperature during the Smackover Shale experiments (Fig. IIA-2) may also suggest carbonate mineral precipitation since the solubility of carbonate minerals is particularly sensitive to pH and dissolved Ca or Fe concentration in addition to temperature, pressure, and dissolved carbon dioxide concentration. Requisite Ca and Fe for the formation of calcite and/or siderite was likely derived from feldspars,

clays, and/or iron sulfides present in the sediment. Carbonate minerals were not observed petrographically at the termination of each experiment, although mass balance calculations indicate that only trace amounts of carbonate minerals would form unless the majority of carbon dioxide precipitated. Immersion of some of the alteration products in dilute HCl resulted in minor effervescence suggesting the presence of a minor carbonate phase.

Determination of total dissolved H₂S concentrations in the Monterey Shale experiments revealed increasing abundance in solution with increasing temperature in the range 250 to 360°C (Table IIA-1). At temperatures <225°C dissolved H₂S concentrations were too low for gravimetric determination, but H₂S was detectable by odor in all experiments. No attempt was made to determine H₂S abundance in the Eutaw and Smackover Shale experiments but a strong H₂S odor in all fluid samples indicated its presence. The absolute abundance of total dissolved H₂S was likely regulated by the solubility of iron sulfides such as pyrite and/or pyrrhotite owing to the rapid dissolution precipitation kinetics for these minerals under hydrothermal conditions (Seewald and Seyfried, 1990). Pyrite was abundant in the unheated Monterey Shale and persisted along with newly formed pyrrhotite in the thermally altered sediments. Sources of sulfur during these experiments include diagenetic pyrite and organic matter. Although it is not possible to quantitatively determine the relative contributions from these two sources, the amounts of H₂S released to solution at 350 and 360°C, 12.7 and 18.8 mg/g sediment, respectively, exceed the amount of sulfur present as diagenetic pyrite in the starting sediment (10.5 mg/g sediment as H₂S). Thus, these data indicate the release of organically bound sulfur to solution. Because sulfide is likely cycled through the solution into iron sulfide minerals, the amounts of organically bound sulfur indicated here represent minimum values.

Dissolved H₂ concentrations were determined in the final fluid samples from the Monterey Shale experiments at 200, 300, 325, 350, and 360°C and in samples from the 325 and 360°C phase of the Eutaw Shale experiment. During the Monterey Shale experiments the dissolved H₂ concentrations showed a systematic increase with increasing temperature, except for experiment MS5 at 325°C. Experiment MS5 was the first experiment conducted in a new tubing reactor and the relatively high dissolved H₂ concentrations may reflect H₂ released as a result of water disproportionation associated with oxidation of the stainless steel tubing reactor. Similarly, the Eutaw Shale experiment was also conducted in a new tubing reactor. Thus, the relatively high dissolved H₂ concentrations observed at 325°C may reflect oxidation of the reactor walls. Continued reaction at constant temperature resulted in decreasing dissolved H₂ concentrations (Table IIA-3).

Organic Acids

The abundance of organic acid anions were determined in fluid samples from the Monterey and Smackover Shale experiments (Tables IIA-4 and 5). Acetate was the most abundant organic acid anion in all samples. Thermal maturation of Monterey Shale also resulted in the production of formate and propionate and trace amounts of valerate, oxalate, and succinate. In contrast, thermal maturation of the Smackover produced significant formate but did not generate detectable quantities of propionate, valerate, oxalate, and succinate, except for experiments SM6 and SM1 in which trace amounts of oxalate were detected. There is some indication that the abundance of acetate and propionate increased with increasing temperature during Monterey Shale maturation. Continued reaction at constant temperature in the relatively high temperature experiments (>225°C) resulted in decreasing acid concentrations, most likely the result of decarboxylation reactions (Kharaka *et al.*, 1983; Palmer and Drummond, 1986). The abundance of organic acids during the Smackover Shale experiments showed no clear trends with temperature (Table IIA-5).

Solid Alteration Products

The results of elemental analyses of the solid alteration products are presented in Table IIA-6. In general, the bulk sediments were characterized by decreases in TOC contents consistent with the generation of hydrocarbons. The N and S content of the Monterey bulk sediment also decreased.

Analyses of the Monterey Shale isolated kerogen, however, reveals chemical changes directly associated with kerogen maturation. For example, increasing C accompanied by decreasing O and H contents with increasing temperature indicates the residual kerogen was becoming more C-rich., a likely result of the generation of hydrocarbons and carbon dioxide.

Examination of Table IIA-6 reveals a minor initial increase in the TOC content of the solid products during low temperature maturation. Because the sediment represents the only source of C present during the experiments, this increase likely reflects dissolution of the inorganic sediment components. Quantitative determination of the extent of inorganic mineral dissolution is not possible with the data available. However, to produce an increase from 20.6 wt. % TOC in the initial sediment to a value of 23.5 wt. % in the alteration products from experiment MS10 at 150°C requires dissolution of 12.3 wt. % of the inorganic minerals present. This value is an absolute minimum because generation of liquid and gaseous C-bearing alteration products would result in decreasing TOC contents for the solid alteration products. If the amount of liquid and gaseous C-bearing products are accounted for, dissolution of approximately 15.0 wt. % of the inorganic minerals present is required.

Discussion

Generation of gas during the thermal maturation of kerogen involves a diverse and large set of reactions. Formation of low molecular weight hydrocarbons and carbon dioxide can occur as a result of the direct cleavage of functional groups from the kerogen macromolecule and/or secondary reactions involving generated long chain hydrocarbons that compose bitumen. The latter process is commonly referred to as "oil cracking". Current models that constrain the timing and amounts of carbon dioxide and hydrocarbon generation are to a large extent based on compositional trends observed for the maturation of kerogen in response to increased time and temperature. Examination of Figure IIA-6 reveals that early stage maturation results in the loss of oxygen, a likely result of the cleavage of carboxyl, carbonyl, and methoxy functional groups, and little decrease in the hydrogen content of kerogen. Continued heating results in exhaustion of kerogen oxygen and decreases in the hydrogen content of kerogen. It is generally assumed that kerogen represents the only source of oxygen and hydrogen available for carbon dioxide and hydrocarbon generation involving organically derived carbon (Tissot and Welte, 1984; Ungerer 1990; Cooles *et al.*, 1985; Barker, 1990). Accordingly, peak carbon dioxide generation is generally viewed as an early-stage phenomenon that precedes peak hydrocarbon formation (Tissot and Welte, 1984). The results of this study, however, suggest that carbon dioxide generation may be substantially more pervasive. Although, significant quantities of carbon dioxide were generated during sediment maturation at low temperatures, carbon dioxide continued to be the dominant gaseous alteration product at 360°C in all experiments. For the Monterey experiments, carbon dioxide production continued at temperatures significantly higher than those associated with peak bitumen formation which occurs during hydrous pyrolysis experiments at approximately 275°C (Baskin and Peters, 1992; Nelson *et al.*, 1995). Thus, based on experimental evidence carbon dioxide generation occurs before, during, and after peak hydrocarbon generation.

Variations in the compositional evolution of kerogen during the Monterey Shale experiments are consistent with maturation trends observed in nature. Large decreases in the oxygen kerogen content were observed in the relatively low temperature experiments with only a minor decrease in the hydrogen content while maturation at relatively high temperatures resulted in only minor decreases in oxygen content and substantially greater decreases in the hydrogen content (Table IIA-6, Fig. IIA-7).

Possible sources of oxygen during these experiments include H₂O and oxygen bound in inorganic minerals. Considering the low ferric iron content of the Monterey Shale and thermodynamic barriers to reducing ferrous iron and aluminosilicate minerals, oxygen directly from these sources is not available for the formation of oxygen-bearing organic alteration products. Thus,

kerogen and H₂O represent the only additional source of oxygen during these experiments. H₂O has been implicated as a source of oxygen in other hydrous pyrolysis experiments at temperatures $\geq 300^{\circ}\text{C}$ (Lewan 1992; Stalker *et al.*, 1993). Thus, H₂O may represent an important source of oxygen during kerogen maturation in these experiments and in natural systems.

Consumption of H₂O-derived oxygen during the production of oxygen-rich alteration products would necessarily result in the release of hydrogen. Hydrocarbon formation represents a likely sink for excess-hydrogen during the thermal maturation of sedimentary organic matter. Results of redox-buffered hydrothermal experiments have demonstrated the incorporation of water-derived hydrogen during the saturation of ethene to form ethane at 325°C (Seewald 1994). These experiments demonstrated that the relative abundance of ethene and ethane are controlled by a state of metastable redox dependent thermodynamic equilibrium that directly involves water. Similar reactions are likely during the present experiments. Alkenes which are a known product during the pyrolysis of sedimentary organic matter under dry and aqueous conditions (Tannenbaum and Kaplan, 1985; Esser and Schwochau 1991) were abundantly present in the early stages of these experiments and showed decreasing abundance with increasing time, even at temperatures as low as 150°C . This trend is consistent with saturation of alkenes with H₂O derived hydrogen to form alkanes. Alkenes did not completely disappear during any of these experiments even after reaction 2716 h at 360°C suggesting they were likely approaching a state of metastable thermodynamic equilibrium in response to the redox state of the chemical system.

The possibility that H₂O may represent a source of oxygen and hydrogen for the formation of carbon dioxide and hydrocarbons has important implications for the generation of oil and natural gas in sedimentary basins. Presently, most models that predict maximum oil and gas yields during kerogen maturation assume that requisite hydrogen and oxygen are only derived from kerogen only. Owing to the ubiquity of water in most sedimentary basins, these models may underestimate the oil and gas potential of sedimentary organic matter. Predicting maximum yields of organic-derived alteration products is a complicated and difficult task since the reactions involved are a function of numerous parameters including organic matter composition, temperature, pressure, and the chemical environment at the site of generation. It is unlikely that hydrogen availability represents the limiting factor during the initial generation of liquid hydrocarbons since it is generally believed that these products are produced to varying extents by the cleavage of intact fragments of kerogen which retain many of the compositional characteristics of the source kerogen. In addition, because early generated oil is composed of relatively long chain hydrocarbons only minor amounts of hydrogen are required to produce saturated products. With increasing thermal maturation, however, hydrogen demands increase as organic transformations result in a decrease in the average carbon chain length of hydrocarbons and associated increases in the H/C ratio. Thus, it is likely that H₂O-derived hydrogen may represent an important contributor to the overall hydrogen budget under high temperature conditions that result in the extensive cracking of oil to form natural gas.

Catalytic Processes

Reactions responsible for the production of natural gas via the cracking of long-chain hydrocarbons have been viewed as purely thermal processes during which sufficient thermal energy is available to result in cleavage of carbon-carbon bonds (Tissot and Welte, 1984; Barker 1990; Ungerer 1990) or as thermocatalytic processes in which the energy required to break carbon-carbon bonds is substantially lowered due to the presence of a catalyst (Mango *et al.*, 1993). Mango *et al.* (1993) argues that a purely thermal model for the production of natural gas requires temperatures in excess of those found to exist during natural gas production in natural systems and produces a gas that is compositionally distinct. In general, natural gas is composed predominantly of 50 to 100 wt. % methane with lesser amounts of ethane and propane (Fig. IIA-8). In contrast, laboratory experiments have demonstrated that thermal cracking of petroleum and pure hydrocarbons produces a hydrocarbon assemblage that contains significantly lower amounts of methane (Horsfield *et al.*, 1992; McNab *et al.*, 1952; Fabuss *et al.*, 1962; Appleby *et al.*, 1947). Mango (1993) demonstrated in the laboratory the catalytic activity of the Monterey Shale by producing a gas product via the

thermocatalytic cracking of *n*-octadecene-1 in a hydrogen at 1 atm total pressure at 190 to 220°C under anhydrous conditions to produce a gas product with a strikingly similar composition to that of natural gas. He suggests that transition metals present in the sediment represent the catalytically active species.

Reactions occurring during laboratory heating of the Monterey, Smackover, and Eutaw shale results in the production of low molecular weight hydrocarbons whose relative abundance is consistent with those observed in nature. In all the experiments, methane constituted approximately 40 to 90 % of the generated hydrocarbon gas suggesting catalytic activity may be important. The relative abundance of methane varied systematically with temperature and time (Fig. IIA-5). Increasing temperature resulted in decreases in the relative abundance of methane. A possible explanation for this trend is that the selectivity of the operant catalyst varies with temperature. Alternatively, the temperature dependence may reflect a systematic shift in the individual reactions responsible for the production of methane. For example, methane generation at low temperature may reflect production directly from kerogen while high temperature generation may be the result of oil cracking reactions. Regardless of the reactions responsible, the rates of methane production observed during these experiments are sufficiently rapid to produce substantial accumulations of natural gas on a geologic time scale (see below).

Although the results of these experiments appear consistent with those of Mango *et al.* (1993), there are some important differences related to the experimental conditions. The experiments presented here were conducted at 350 bars in the presence of liquid water while those of Mango *et al.* (1993) were at 1 atm in a dry system. Mango *et al.* (1993) observed decreasing selectivity towards methane upon addition of high amounts of water. Perhaps more importantly, however, is the presence of abundant dissolved sulfur species in our experiments which were essentially absent in the Mango *et al.* (1993) study. Sulfur is well known poison for the catalytic activity of transition metals due to the formation of transition metal sulfides. The presence of sulfur notwithstanding, the apparent catalytic activity in our experiments suggests that sediment components other than transition metals may represent the catalytically active species. Possibilities include dissolved sulfur species, inorganic minerals, and organic compounds such as NSO-rich asphaltenes.

Kinetic Modeling

Numerous models have been developed to predict the extent and timing of hydrocarbon generation in sedimentary basins (Sweeney *et al.*, 1995; Hunt *et al.*, 1991; Ungerer 1990; Braun and Burnham, 1990; Lewan 1985; Lopatin 1971, 1976; Karweil 1956; Waples 1980). In general, these models are based on reactions that are governed by first order reaction kinetics and the Arrhenius equation, but vary significantly with respect to the number of reactions that are used to describe the process of hydrocarbon generation. The thermal maturation of kerogen to produce oil and gas is an inherently complex process involving numerous sequential and parallel reactions. Accordingly, even the most complex kinetic models represent gross simplifications of naturally occurring processes. Nonetheless, they represent effective tools for petroleum exploration and predicting the geochemical evolution of sedimentary basins, provided of course that reliable data for activation energies and pre-exponential factors are available.

Laboratory experiments represent a unique opportunity to calibrate kinetic models under controlled conditions of time and temperature. Data from the present experiments are ideally suited to provide kinetic data for the generation of light hydrocarbons and carbon dioxide since gas generation was monitored as a function of time over a wide range of isothermal conditions. For this purpose we used computer code KINETICS (Braun and Burnham, 1990) to analyze the data from the experiments. This code fits an average pre-exponential frequency factor (A_0) and the relative fractions associated with a given activation energy (E_a) for by up to 25 first order parallel reactions. For the present analyses, the absolute amounts of gases generated were converted to fractions

reacted relative to the maximum generated at 360°C. A 2 kcal/mole spacing between consecutive values of E_a was used for all calculations.

Results of the kinetic analyses indicate that the generation of carbon dioxide and methane are characterized by different pre-exponential frequency factors and activation energy distributions that are also dependent on the composition of the source kerogen (Figs. IIA-9 and 10). Methane production from the Eutaw and Smackover Shale (type-III kerogen) is best accounted for by E_a values in the narrow range of 70 to 74 kcal/mole and A_0 values of $1.15 \times 10^{19} \text{ s}^{-1}$ and $3.74 \times 10^{19} \text{ s}^{-1}$, respectively while production from the Monterey shale (type II-s) requires E_a values in the range 66 to 68 kcal/mole and a A_0 value of $6.37 \times 10^{18} \text{ s}^{-1}$.

In contrast to low molecular weight hydrocarbon generation, the E_a distributions for carbon dioxide production are characterized by a wide range of energies that vary from approximately 40 to 64 kcal/mole for both the Monterey and Eutaw shale. This distribution may suggest that a more diverse set of reactions is responsible for the generation of carbon dioxide. For example, it is likely that carbon dioxide production associated with low values of E_a is the result of the cleavage of oxygen-bearing functional groups directly from the kerogen macromolecule while that associated with high values of E_a may reflect reaction of organic compounds with water.

Application of the kinetic parameters retrieved from the experimental data to temperature and time conditions typical of petroleum producing sedimentary basins allows predictions to be made regarding the timing of gas generation. Gas generation curves for a hypothetical basin with a geothermal gradient of 25°C/km that is subsiding at a rate of 2 km/My are shown in Figures IIA-11 and 12. The bulk of methane generation is restricted to a relatively narrow temperature range of 170 to 220°C for the Monterey Shale while generation from the Eutaw and Smackover Shale is shifted to temperatures approximately 20°C higher. Carbon dioxide generation from organic matter, however, is predicted to occur continuously from low temperatures that characterize early diagenesis to temperatures as high as 220°C, reflecting the wide range of activation energies associated with its production. Thus, extrapolation of the experimental results to natural conditions indicates that carbon dioxide production is not restricted to diagenetic processes that proceed peak hydrocarbon generation but can be expected to occur during all phases of kerogen maturation including natural gas formation deep within a sedimentary basin.

Comparison of the kinetic parameters derived here with previous studies shows both agreement and disagreement. Horsfield *et al.* (1992) used the results of confined anhydrous pyrolysis experiments to derive an E_a distribution that ranged from 66 to 70 kcal/mole and a A_0 value of $1.1 \times 10^{16} \text{ s}^{-1}$ for the cracking of a relatively immature crude oil from the North Sea to form C_1 - C_4 hydrocarbons. These values correspond to the bulk of natural gas formation at temperatures of approximately 170 to 220°C in the hypothetical basin described above, consistent with the results of our experiments. Generation of gas during our experiments is likely a two step process involving the initial generation of bitumen followed by thermocatalytic cracking to produce gaseous products. The striking similarity of E_a and A_0 values determined here with those Horsfield *et al.* (1992) for petroleum cracking suggest that generation of bitumen may be a relatively rapid process occurring at relatively low temperatures while the cracking of bitumen represents the rate limiting step that dominates the timing and extent of gas generation in our experiments.

Knaus *et al.* (1992) derived individual Gaussian distributions of activation energies for the generation of methane, ethane propane and butane from hydrous pyrolysis experiments examining the New Albany Shale. Their results indicate E_a distributions centered on a value 55 kcal/mole for the generation of all gases. The significantly lower E_a values may be due to the fact that they assumed a A_0 value determined using a Pyromat II instrument applied to their hydrous pyrolysis experiments. There is no obvious reason to support such an assumption, however, since reactions occurring during open-system anhydrous, high temperature and low pressure pyrolysis are not likely to resemble those during closed system, hydrous, relatively low temperature and high pressure

pyrolysis experiments. Alternatively, the discrepancy between E_a values determined by Knaus *et al.* (1992) may be due to compositional differences between the New Albany Shale and the sediments examined here.

Summary

Laboratory experiments represent an effective means to constrain processes responsible for organic transformations that occur in sedimentary basins. Results of hydrous pyrolysis experiments conducted as part of this project indicate that carbon dioxide is the dominant volatile alteration products generated during thermal maturation of the Monterey, Smackover, and Eutaw Shale. Carbon dioxide formation is not limited to early diagenesis but continues during and after peak hydrocarbon formation. Methane constitutes 40 to 90 % of the generated hydrocarbon gases. This distribution of hydrocarbon gases is consistent with those observed in nature and suggests that thermocatalytic cracking controls the generation of natural gas. Low molecular weight alkenes are generated but rapidly decrease in abundance with continued maturation to a level that may be controlled by metastable thermodynamic equilibrium.

Results of kinetic modeling indicate that E_a for the generation of methane range from approximately 66 to 74 kcal/mole while A_0 values vary from 6.37×10^{18} to $3.74 \times 10^{19} \text{ s}^{-1}$. Calculated E_a and A_0 values for carbon dioxide generation show a much wider range of values varying from 40 to 64 kcal/mole and 1.98×10^{14} to $2.95 \times 10^{17} \text{ s}^{-1}$. Predictions based on these kinetic parameters suggest peak methane and carbon dioxide generation in the range of 200°C while carbon dioxide generation is predicted to occur continuously at both low and high temperatures in a typical sedimentary basin.

B.Task 6.2.2, Organic Geochemistry, petrography, isotopes:

i) summary of biomarker work

All analyses have been completed, as indicated in Table II-B-i, and data is in process of being entered into an on-line data base which will be accessible through the Ethernet (see section C-i below). Two papers have already been published on this work, Whelan *et al.*, 1994 and 1995, and a third manuscript is attached (Appendix A). A fourth summary paper is also planned describing a plausible overall plumbing system for rapid injection of hydrocarbons into EI-330 reservoirs, as outlined below.

On the basis of biomarkers, all EI-330 oils have a common (Jurassic to Early Cretaceous marine) source. The Jurassic is currently estimated to be deeper than 30,000ft. It is assumed to be directly beneath EI-330 or too the south because continental shelf oils to the north are compositionally different. The organic geochemistry is most consistent with the oils from the stacked faulted EI-330 reservoir system having been generated fairly early and then having been expelled into overlying reservoir rocks (Cretaceous, or other rocks which currently lie at 20,000 to 25,000 ft or somewhat deeper). These, in turn, were buried further under impermeable cap rocks, possibly under salt. Later, as the salt receded, the oil remained trapped beneath overpressure until very recently when further gas formation and pressurization either in situ or from deeper formations caused ejection of the deep reservoir oil into modern Pleistocene reservoirs, in some cases through overpressure. This scenario fits the relative oil and gas maturities, with gases in all reservoirs being much more mature than the oil ($R_o = 1.5$ to 1.7% for gas compared to 0.7 to 0.8% for oil, Whelan *et al.*, 1994a; 1995). Figure B-i-1 shows the depths corresponding to these maturities at the present time, along with current best estimates on the limits on the oil and gas generation zones beneath EI-330. We assume that the gases were generated in deeper, more mature formations and have subsequently moved upward to solubilize and pressurize the oil, although a combined marine source/reservoir facies below 25,000 ft is also a possibility. The gas/oil phase is

envisioned as episodically having sufficient pressure to break through the overpressure in order to flow upward into the overlying Pleistocene reservoirs. From an exploration standpoint, this hypothesis is important because it implies deeper reservoirs, below overpressure and below reservoirs which are producing and actively filling today.

This scenario is supported by ages of the inorganic fluids in EI-330 reservoirs. The ^{129}I ages are fairly uniform and are in the range of 35 to 58 Ma. The ^{129}I originates during kerogen maturation and, therefore, roughly reflects the age of sediments from which the oil was generated. These ages are minimum because of potential for contamination with younger fluids during upward migration. It is interesting that ^{129}I ages agree fairly well with those calculated by Qian *et al.* (manuscript attached) based on calculations of Young *et al.*, (1977) using ratios of gasoline range hydrocarbons. The ages calculated from the oil compositions are 12 to 59 million years at 100°C, or 4 to 20 million years at 150°C (Appendix A). The lower temperature gives ages closest to those measured by the ^{129}I data. Considering the numerous processes other than maturity are known to affect the hydrocarbon compositions, the agreement between the two ages is remarkable, particularly when one is made using the oils and the other on the aqueous fluids.

Whatever the exact age, all of the estimations above are consistent in suggesting that EI-330 fluids, both aqueous and organic, have spent considerable time in reservoirs much hotter than the EI-330 reservoirs are today, consistent with contemporary oil/gas migration from much deeper reservoirs.

ii) reproducibility of gas and oil compositions over time.

The manuscript by Qian *et al.*, (attached, Appendix A) also presents additional evidence regarding the temporal changes in oil and gas described previously for EI-330 oils (Schumacher, 1992; Whelan *et al.*, 1994). The new analyses are most consistent with these temporal changes being caused by recent migration for a deeper reservoir or source. Artifacts produced by sampling or storage or the analytical procedures have been pretty well ruled out. Evidence is presented against an alternative hypothesis of lateral migration as the cause of these temporal changes in composition.

iii) TLC-FID (Iatroscan) results

Introduction

Petroleum migration conduits and reservoirs contain molecular records of petroleum as it migrates from source to trap. Compositional changes associated with increasing maturities of the sourcing kerogens and chemical interactions that occur along the migration pathways affect the bulk and molecular compositions of petroleum and rock extracts. Therefore, vertical and lateral differences in the molecular composition of petroleum streams can help identification of migration pathways and field filling directions (Karlsen and Larter, 1991). Bulk compositions of petroleum and the organic fingerprints left behind in the regional rocks through which petroleum has flowed can be used to interpret heterogeneities in reservoir sands and migration pathways (Karlsen and Larter, 1991). Comparison of the compositions of petroleum flowing through more permeable sand vein networks and/or fractured host-rock, in association with biomarker and phenol data (Taylor, 1994) from oils and fluids, may provide further information relating migration pathways and field filling history (Karlsen and Larter, 1989).

Our goal was to reveal compositional information to predict whether migrated hydrocarbons have penetrated host-rock, rock fractures and sandstone veinlets. Host-rock and rock fracture enrichment with saturated hydrocarbons may indicate the presence of lower molecular weight compounds which have faster diffusion coefficients, according to estimations by England *et al.*, (1987) for oil migrating in tortuous media. This diffusion may be further enhanced by the degree of fracturing in the host-rock.

Methods

An Iatroscan TH-10 MK-III, equipped with a flame ionization detector was used to quantify the bulk compositions of oils and core extracts separated by thin layer chromatography on Chromarod-S III silica rods. The solvent system used for separation into saturated hydrocarbons, mono- and di-aromatic hydrocarbons, poly-aromatic hydrocarbons, resins and asphaltenes was as follows:

Compound groups	Elution time	Solvent mixture	Solvent
1). Saturates	27 mins	100%	Hexane
2). Mono-, di- and poly-aromatics	10 mins	100%	Toluene
3). Resins and asphaltenes	3 mins	95:5%	Dichloromethane: Methanol

External standard quantitation was performed using a calibration mixture containing known amounts of:

Surrogate standard	Compound group
n-Eicosane	Saturate response
n-Undecylbenzene	Mono-, di-aromatic response
Phenanthrene	Poly-aromatic response
2,6-Dimethoxyphenol	Resins and asphaltene response

Figure II-B-iii-1 shows examples of standard, host and vein extract chromatograms from Iatroscan analyses.

Samples

The Eugene Island Block-330 Pathfinder (A-20S/T) core provided high quality, contamination free core material ideal for detailed geochemical analysis. Core plugs were collected from the slabbed core, which had been stored in a frozen state, two weeks after core recovery.

To monitor detailed compositional heterogeneities throughout the Pathfinder cored interval, the dominant silty shale lithology was sampled in relation to a number of sand and silty laminae and thin-bedded sandstones. Core photographs in Figure II-B-iii-2 show examples of our sampling strategy. The Pathfinder core logging revealed three distinct major structural zones (Anderson *et al.*, 1994). An upper faulted zone exists between 7670 - 7848' m.d. This zone contains slickensided faults at moderate to high angles. A middle structural zone between 7848-7923' m.d. is relatively unfaulted and unfractured but contains several thin, yellow fluorescing sand beds and laminae. The lower zone between 7923-8053' m.d. is faulted. Silty shales have gouge zones that intersect the well at both low and high angles. Fractures in this zone are fairly persistent and thin hairline faults are often slickensided and occasionally show fluorescence (Anderson *et al.*, 1994).

Samples from all three structural zones were collected from the dominant medium-dark grey silty-shale, termed host-rock, and thin sand laminae and sandstone veins, termed vein-rock. The latter invariably showed fluorescence properties under blue-light excitation. Frozen core sub-samples were defrosted and carefully sectioned to collect vein-rock without interference from host-rock and *vice-versa*. The vein- and host-rock samples were Soxhlet extracted for 48 hours using a 93:7 azeotrope of dichloromethane and methanol. The extracts were all reduced and diluted to a set volume ready for separation by TLC-FID (Iatroscan). Eight rods were spotted and eluted with 2 external standard rods loaded per rack of 10 rods. Data was acquired and quantified using Rainin Dynamax® software. Each sample was analyzed in triplicate and relative abundances calculated. Relative abundance is used in preference to absolute concentrations to counter the effects of porosity changes (Karlsen and Larter, 1989).

Results and discussion

Tables II-B-iii-1 and -2 show data for the relative abundance (%) of saturated hydrocarbons, mono- and di-aromatic hydrocarbons, poly-aromatic hydrocarbons, resins and asphaltenes for host-rock and vein-rock extracts, respectively, for the Pathfinder (A-20 S/T) core.

The sandy and silty vein-rock extracts bulk compositions show a fairly constant predominance (~ 50%) of saturated hydrocarbons (Figure II-B-iii-3). Poly-aromatic hydrocarbons are the second most dominant compound group in these extracts with average abundances of 28%. The polar resins and asphaltenes are present in lower abundances, averaging 14% and 3.5% respectively. The resins show a small increase in abundance with depth below 7858.5' m.d. which lies within the middle, relatively unfaulted structural zone.

Figure II-B-iii-4 shows the percentage distribution of saturate, mono-, di-aromatics, poly-aromatics, resins and asphaltenes in the Pathfinder core host-rock extracts. Polar compounds are enriched in the deeper parts of the host extracts averaging about 75%. There is <5% relative abundance of poly-aromatics and less than 2% of mono- and di-aromatic hydrocarbons which remains fairly constant vertically. However, the saturates show a striking trend. There is a greater relative abundance of saturates (~40%) between 7678.8' m.d. and 7815.5' m.d. in the shallowest, more faulted structural zone followed by a sharp decrease (~8%) to 7893.70' m.d. within a polar enriched zone (89%), with the exception of one sample near 7846.4' m.d. which contains about 60% saturated hydrocarbons. Comparison of the compositions of the faulted host-rock extract and the adjacent vein-rock extract at 7846.4' m.d. (Tables II-B-iii-1 & 2 and Figures II-B-iii-3 & 4) show similar relative abundances of saturates (59% and 62% respectively). Most variance occurs in the amounts of poly-aromatics which are more dominant in the vein-rock extract (18% vein-rock, 2% host-rock). Figure II-B-iii-5 shows this host-rock (7846.4' m.d.) was sampled from a small sub-vertical, sinistral fault zone that had no fluorescence properties, unlike adjacent thin, strongly fluorescing sand laminae. Since contamination can be ruled out, we conclude that detectable volumes of more volatile, saturated hydrocarbons have infiltrated the silty shale along this vertical fault plane. The host extract from 7894.5' m.d. contains ~80% of saturated hydrocarbons and very few resins and aromatics but 16% asphaltenes. This sample was taken from a non-fluorescing zone within a section of core that had several thin fluorescing sand laminae and may indicate minor migration or diffusive action.

The high abundance of polar compounds in most of the host-rock extracts is consistent with other immature rock extracts (bitumens) which tend to be dominated by polar compounds (particularly asphaltenes) (Tissot and Welte, 1978). Figures II-B-iii-6-10 show comparison relative abundances between host and vein samples for each compound group separated.

Summary and conclusions

TLC-FID has shown that vein extracts are compositionally quite distinct from the host-rock extracts in the Pathfinder core. The vein-rock extracts indicate petroleum is present in the sandy migration conduits and that petroleum composition is dominated by saturated hydrocarbons and relatively small abundances of polar compounds and is similar in composition to oils from producing reservoirs. Figures II-B-iii-11 and 12 show ternary plots of the summed aromatics, polars (NSO's) and saturated hydrocarbons for, 47 reservoir and fault zone oils from Eugene Island Block 330 and vein-rock extracts, respectively. These data show a good correlation between the bulk compositions of vein-rock extracts and oils. It is reasonable to conclude that these thin sand and silty laminae form part of complex distributary migration networks, channeling petroleum to shallower, more extensive reservoir sandstones. The ternary plot shown in Figures II-B-iii-13 shows the distribution of host-rock extracts from fractured and unfractured sections and shows that although, saturated hydrocarbons are enriched in some fractured samples, aromatic compounds remain in low relative abundance. One possibility to explain the low abundance of aromatics in

host-extracts may reflect water-washing of the host rock. Since, aromatic hydrocarbons are more water soluble than saturated hydrocarbons they may be preferentially removed by water. Polar compounds are also water soluble but since they are so predominant in immature sediments they may not show such a pronounced loss. However, host-rock samples that transect a fracture or small faulted zone do show evidence for the presence of migrated hydrocarbons. The relative intensity of the compound groups is also higher in fractured and faulted host-rock extracts relative to unfractured and faulted host-rock extracts. Phenol analysis may help to clarify some of these observations.

iv) Phenol analysis

Twenty three representative EI-330 oil and their associated aqueous fluids from each of the stacked reservoirs described in Whelan *et al.*, 1994 and from the Pathfinder well have been sent to Dr Steve Larter at the University of Newcastle for analysis of phenols. If successful, this analysis can potentially distinguish between rapid oil migration up faults versus slower migration through pore spaces. The analysis uses compositional changes in phenols, a polar fractions of oil which partitions between the moving oil and water migrating phases and the solid immobile mineral phase. The partition coefficients for phenol between the three phases are well known from the environmental literature. Measurement of the distributions of phenols between the three phases can then be combined with calculations for partitioning between the various possible phases and reservoirs, developed by Larter. The calculations place limits on the amount of time the oil has "seen" the walls of the migration conduit (Larter and Aplin, 1995; Taylor *et al.*, submitted). Dr Steve Larter from Newcastle University in the U.K., who developed these procedures on fluids from North Sea reservoirs, spent the summer of 1995 at Woods Hole. He has agreed to collaborate with us in applying these procedures to Gulf Coast reservoirs, particularly EI-330. We hope this analysis will allow a distinction between fault-associated migration (fast migration; predicted for some GA and HB and JD and LF reservoirs) versus (predicted) slower migration through the capillary pore system (predicted for many of the shale associated OI oils from the Pathfinder well).

These procedures will also allow us to address several important questions regarding migration in EI-330 - is the migration occurring up fault or through pore space? Figure B-iv-1 shows a 3-D seismic profile of migration of a gas plume in S. South Marsh Island from underneath salt which goes all the way to the surface and appears to be bypassing faults. Such plumes are evidently common in this area of the Gulf Coast.

An alternative migration scenario also consistent with the EI-330 organic geochemical data is that oil is currently being generated and expelled from early Cretaceous (marine) rock already saturated with more mature gas derived from the underlying Jurassic rocks. The additional on-going gas generated from a marine Early-Cretaceous marine source rock is sufficient to move indigenous gas plus oil upward into Pleistocene reservoirs. In this case, the Lower Cretaceous marine oil source and reservoir rocks are the same. In marine carbonate and siliceous formations, source and reservoir rocks are commonly very closely associated, often being the same rock, (*eg.* Hunt & McNichol, 1984). In this case, the whole source/reservoir rock system is carried downward, with efficient oil expulsion being impossible until a depth is reached where sufficient gas can be generated to aid in the expulsion and migration process.

The distinction between these two scenarios is important from an exploration point of view - the first implies deeper conventional reservoirs which could be produced; the other implies a lower porosity marine source/reservoir rock where the producing permeable zones might be much patchier and harder to find.

Limited data suggests that year time scales of oil/gas injection into reservoirs, which appears to be occurring at EI-330, is extremely fast on the scale of normal reservoir mixing processes (Table II-B-3). Therefore, it seems unlikely that rapid time scale injection could be occurring from a source rock. However, because marine rocks can act simultaneously as both a

source and reservoir, it is possible that some sort of combined deeper source/reservoir rock could be providing the "deep holding tank" required for rapid oil injection into shallower reservoirs.

C.Task 6.2.3, Organic geochemistry, Modeling and technology transfer:

i) Description of data base

A data base has been created for all of the geochemical data gathered during the course of this project using commercially available "4D Database" on the MacIntosh. Figures C-i-A1 - A51 show the data base structure and data which they will contain. Entry into a GBRN database folder allows access to other parts of the program, as shown on Figure II-C-i-A1. The data base has input sheets for data as well as for sample inventories. Data sheets and plots can be inserted into the "GBRN share" files for transfer by ftp to any other organization. Currently, GBRN members can access these files via the World Wide Web (<http://pogg@dynatog.who.edu>). This version of 4D replaces an earlier attempt using the same program designed by Charley Rego and Mary Zawoysky.

For plotting, macros are utilized to export the data from the 4D data sheets to Excel which has much more sophisticated plotting routines than are available within the 4D program. This has proved to be very advantageous in plotting the very complex data sets generated by the high resolution gas chromatograph mass spectrometer data (HRGCMS) of the biomarkers in the EI-330 oils. At the present time, loading of the most complex HRGCMS data set is almost complete.

ii) World Wide Web page and plans

A proposal has been submitted to develop the WWW technology for communication of the GBRN results for EI-330 and elsewhere as described below. Even if funding from this particular source is not obtained for all parts of the project, we plan to carry out as many of the parts of the project as possible with funding from other sources. The proposal description is as follows:

Organic geochemistry in cyberspace - development of a virtual coffee hour, discussion group, and electronic journal

Dr. Jean K. Whelan, Principal Investigator
(Cynthia L. Chandler, Associate Investigator)

We propose to explore inexpensive, fast, effective, new methods for sharing scientific data, ideas, and concepts using the software and hardware which has recently become available for the World Wide Web (for more information on cyberspace and the WWW in particular, please see URL, Uniform Resource Locator, <http://www.eit.com/goodies/www.guide>). The Internet offers new, innovative means of communication, utilizing cross-referenced links to facilitate 'visits' to research sites worldwide. The ability to include sound and graphics (including animated video clips) offers tremendous potential for oceanographers. The effective use of graphics makes complex scientific data much clearer to non experts in a particular field.

The idea for this proposal has risen out of our (the Petroleum Organic Geochemical Group, POGG, at Woods Hole, URL <http://dynatog.who.edu>) need to share ideas and data with other academic and research institutions, oil companies and government agencies in a timely and less expensive manner. The worldwide organic geochemistry community which would be served is small and still relatively uncomfortable with computers. Currently, this community relies predominantly on scientific journals to communicate research results. These journals are expensive (some annual subscriptions cost in excess of \$1,000) and slow (minimum of one year from initial),

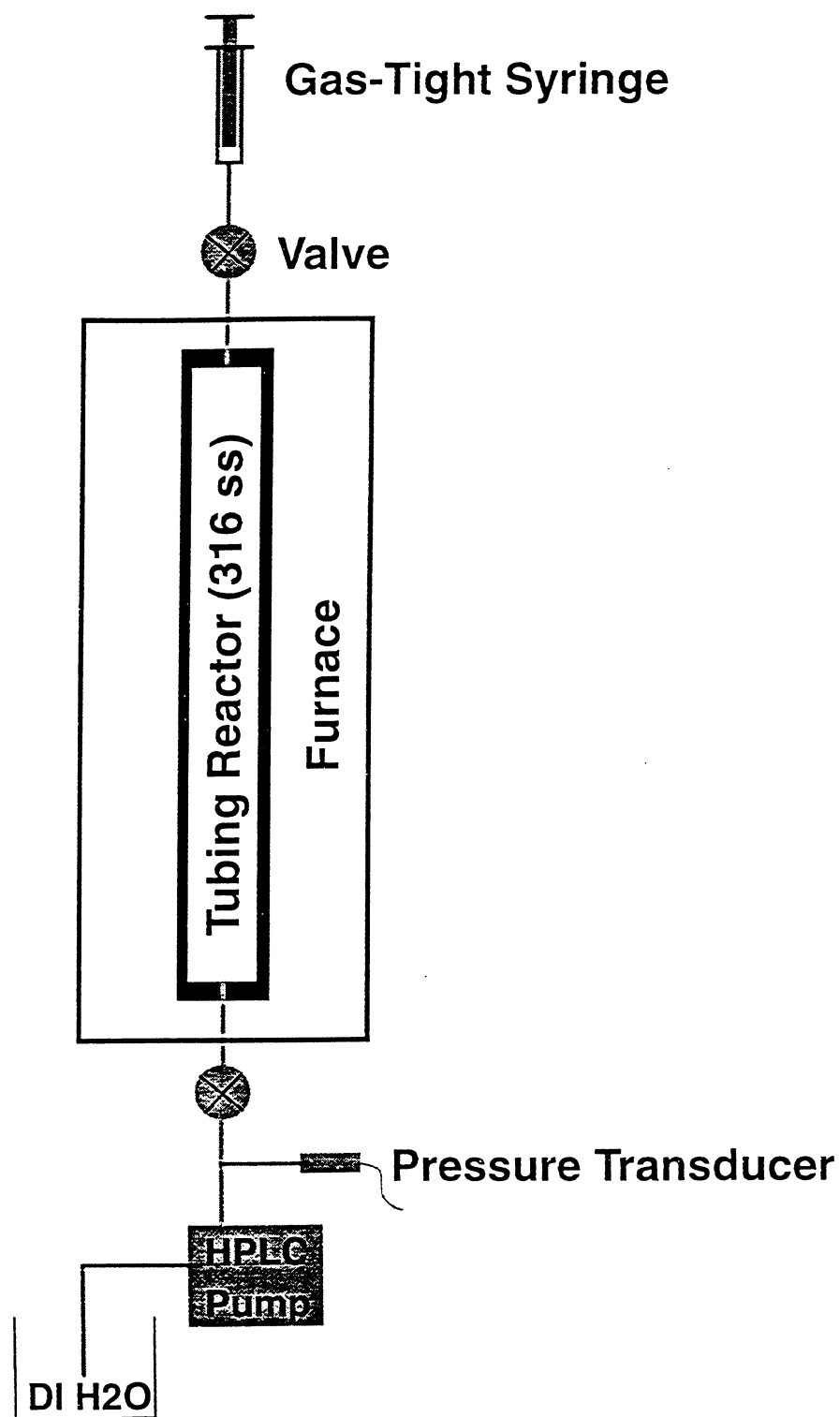


Figure IIA-1. Stainless steel tubing reactor used for hydrous pyrolysis experiments.

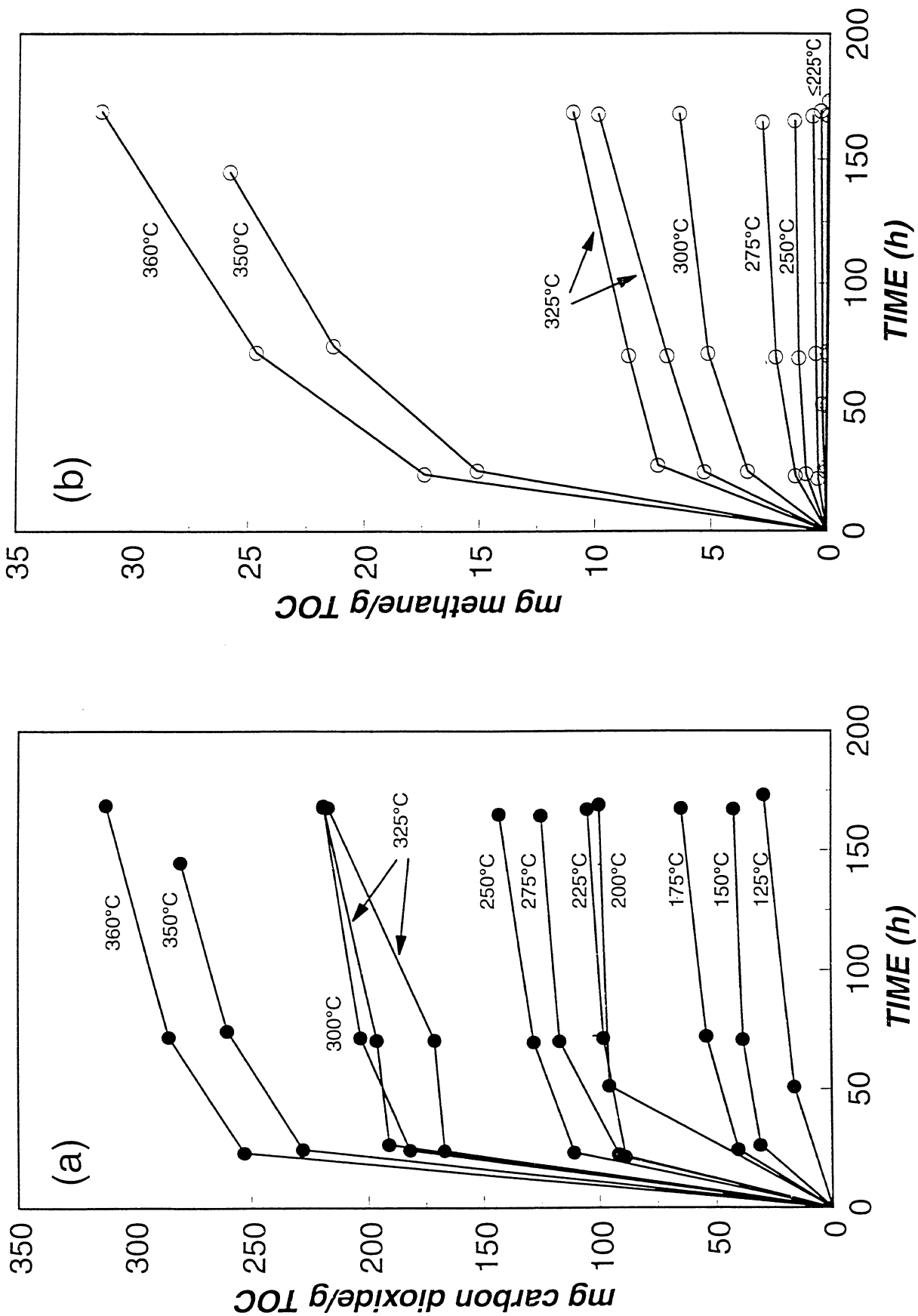


Figure IIA-2. Variations in the absolute amounts of (a) carbon dioxide and (b) methane generated during hydrous pyrolysis of Monterey Shale. The experiments at 225 and 275°C were not decarbonated prior to heating.

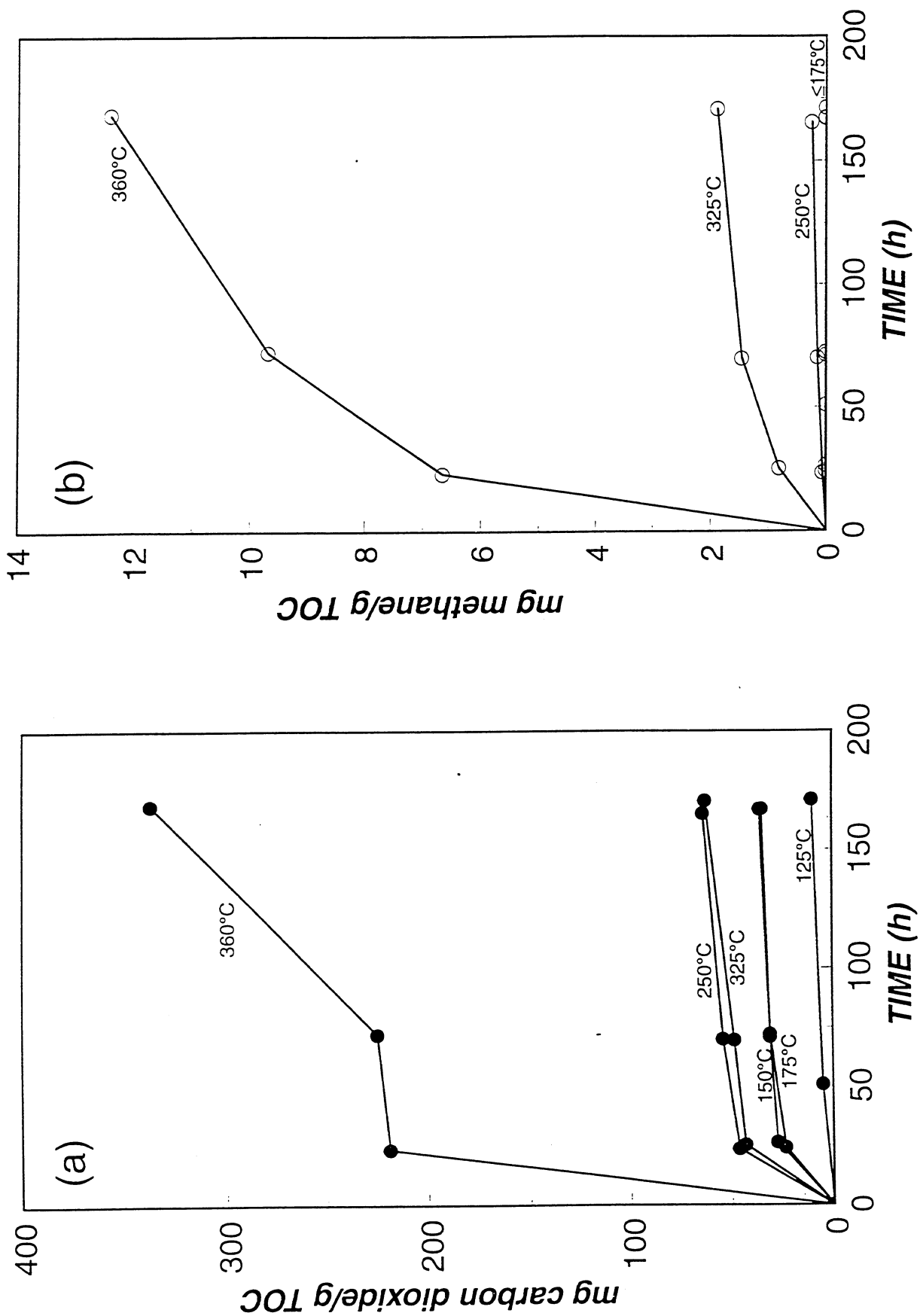


Figure IIA-3. Variations in the absolute amounts of (a) carbon dioxide and (b) methane generated during hydrous pyrolysis of Smackover Shale.

**This page
left blank
on purpose**

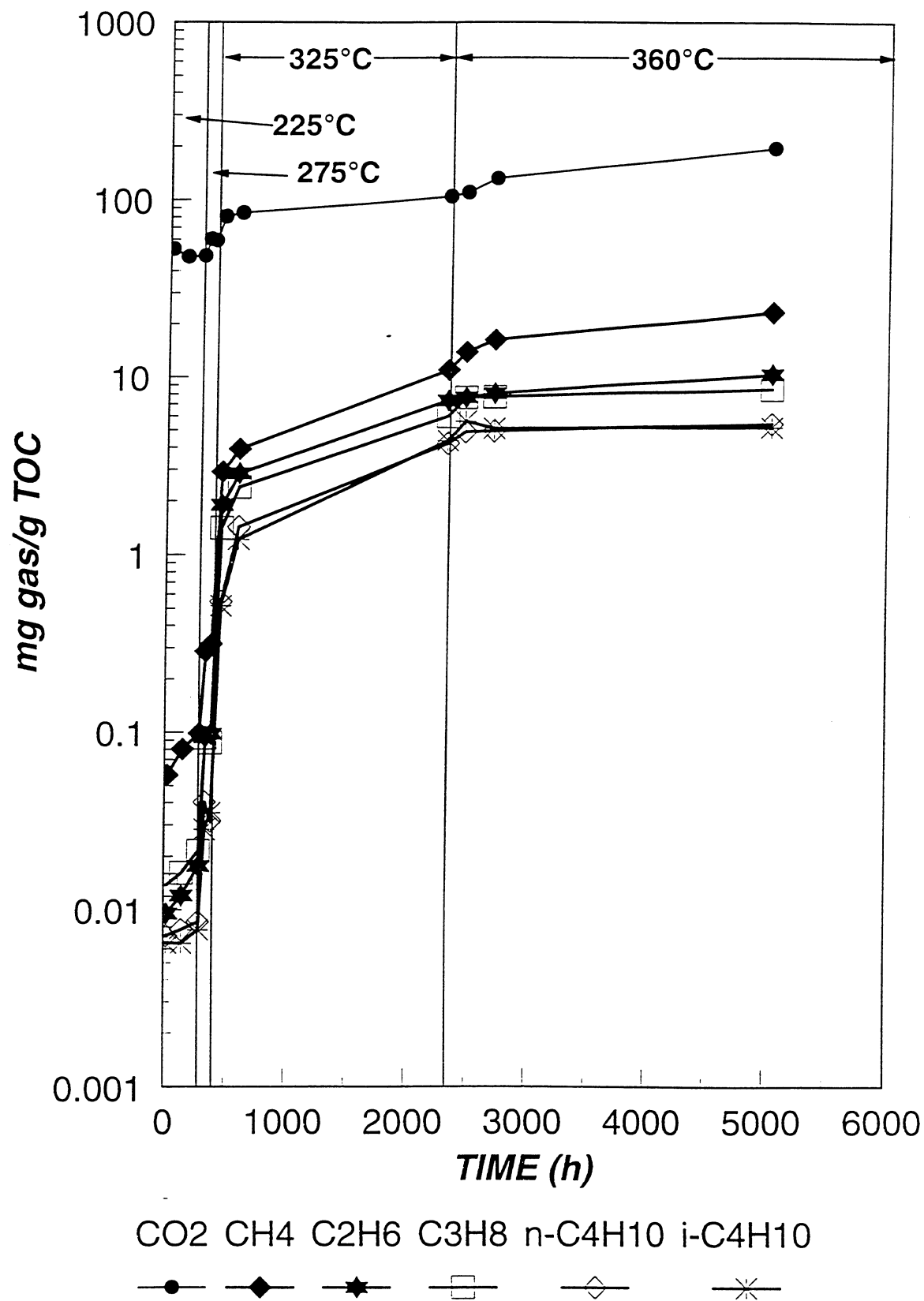


Figure IIA-4. Variations in the absolute amounts of gases generated during hydrous pyrolysis of Eutaw Shale.

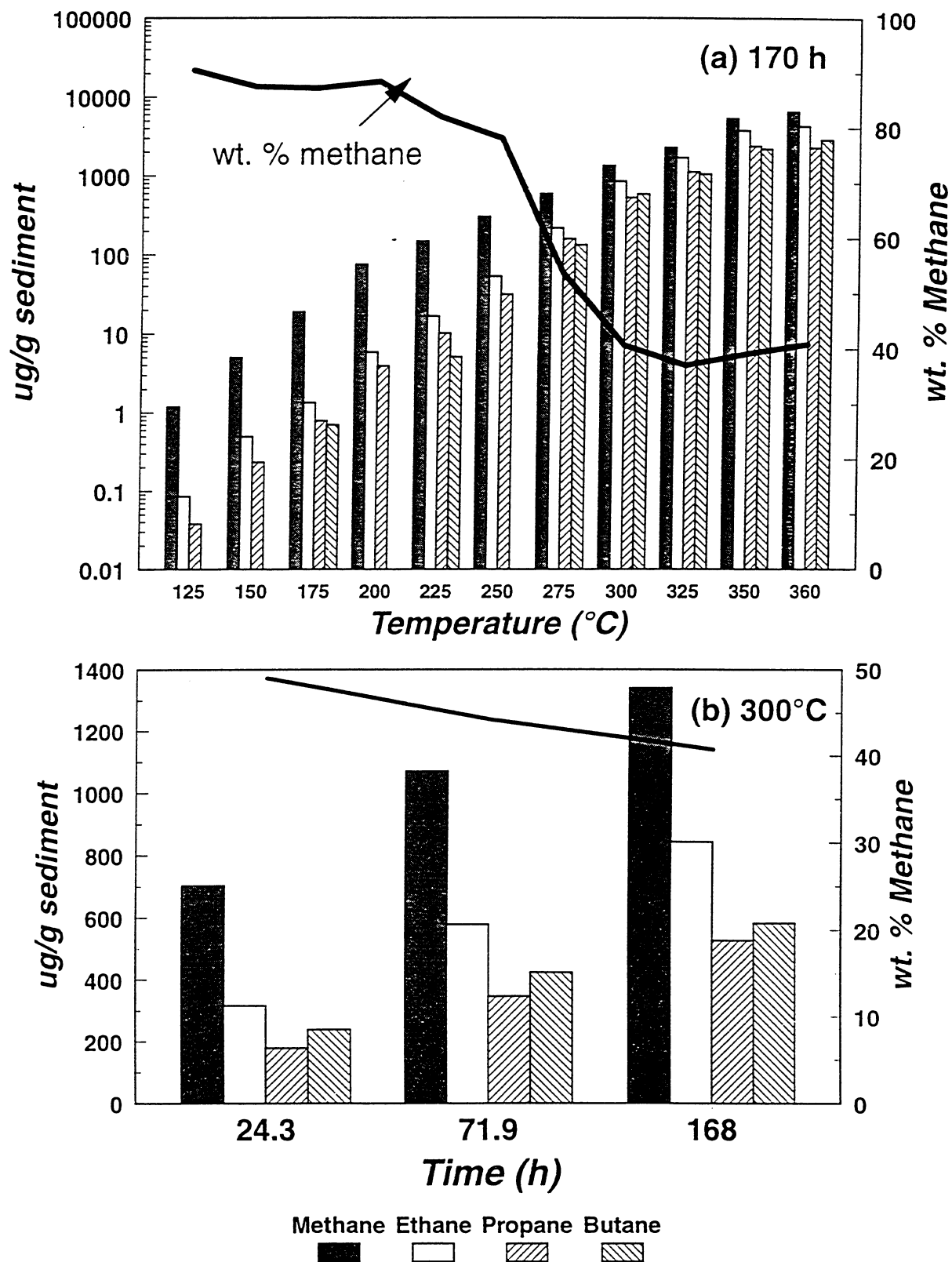
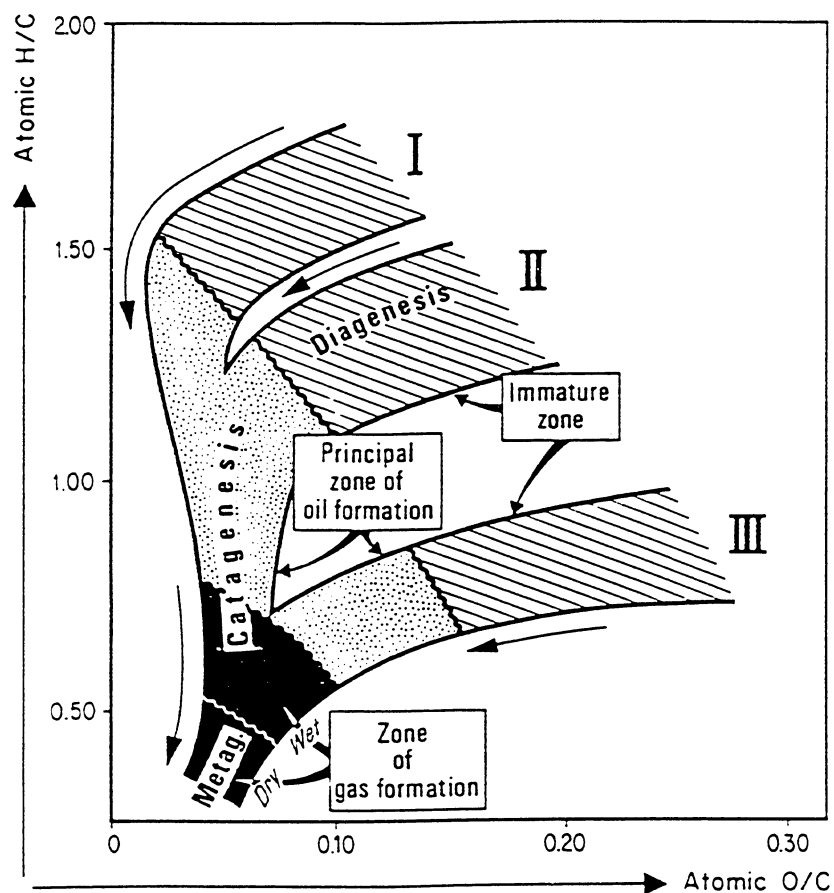

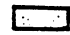



Figure IIA-5. Variations in the amount of generated low-molecular weight hydrocarbons and weight % methane as a function of (a) temperature and (b) time during hydrous pyrolysis of Monterey Shale.

Fig. IIA-6: Van Krevelen diagram of kerogen evolution (Tissot and Welte, 1978).



Principal products of kerogen evolution

-  CO₂, H₂O
-  Oil
-  Gas

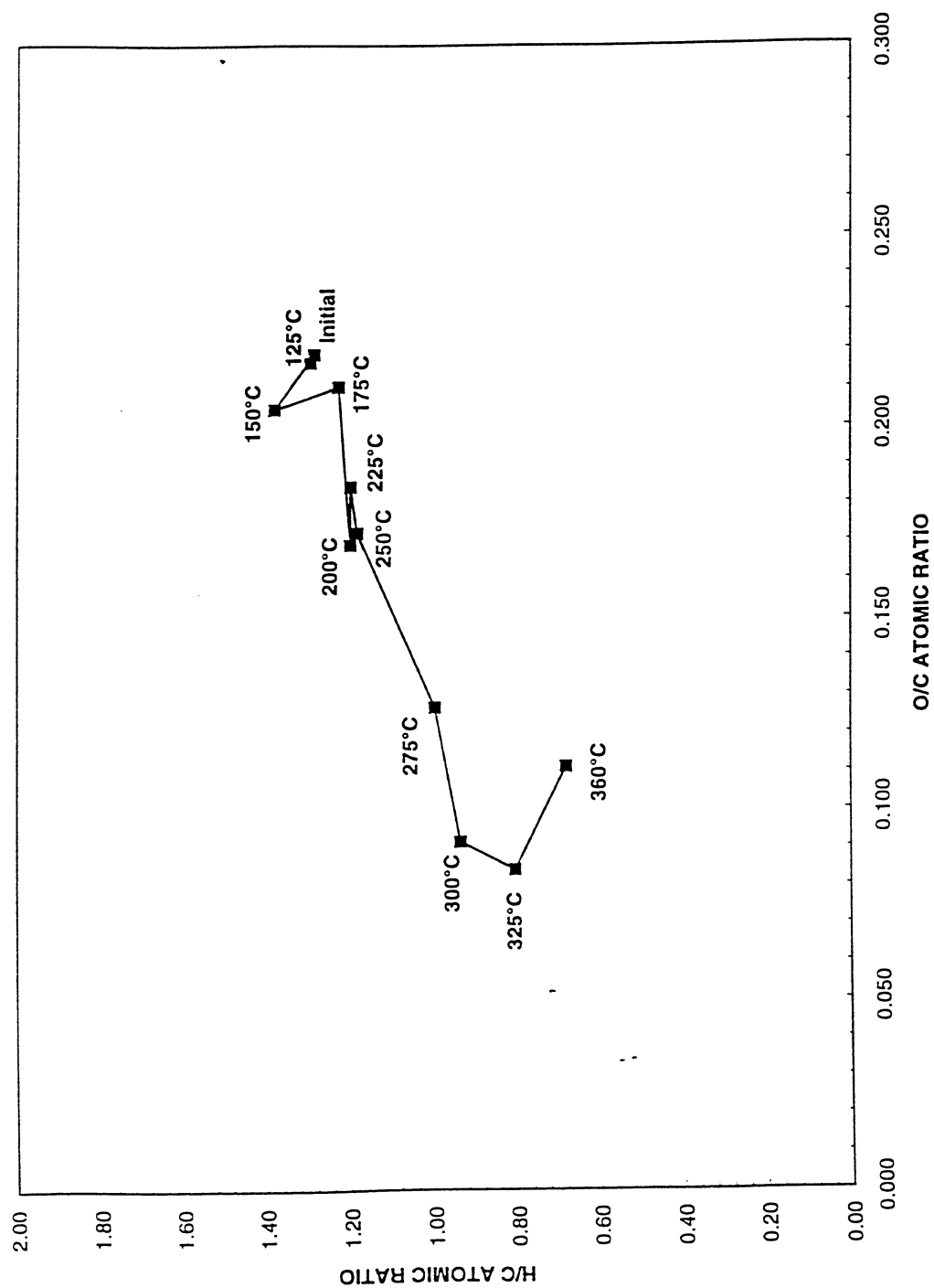
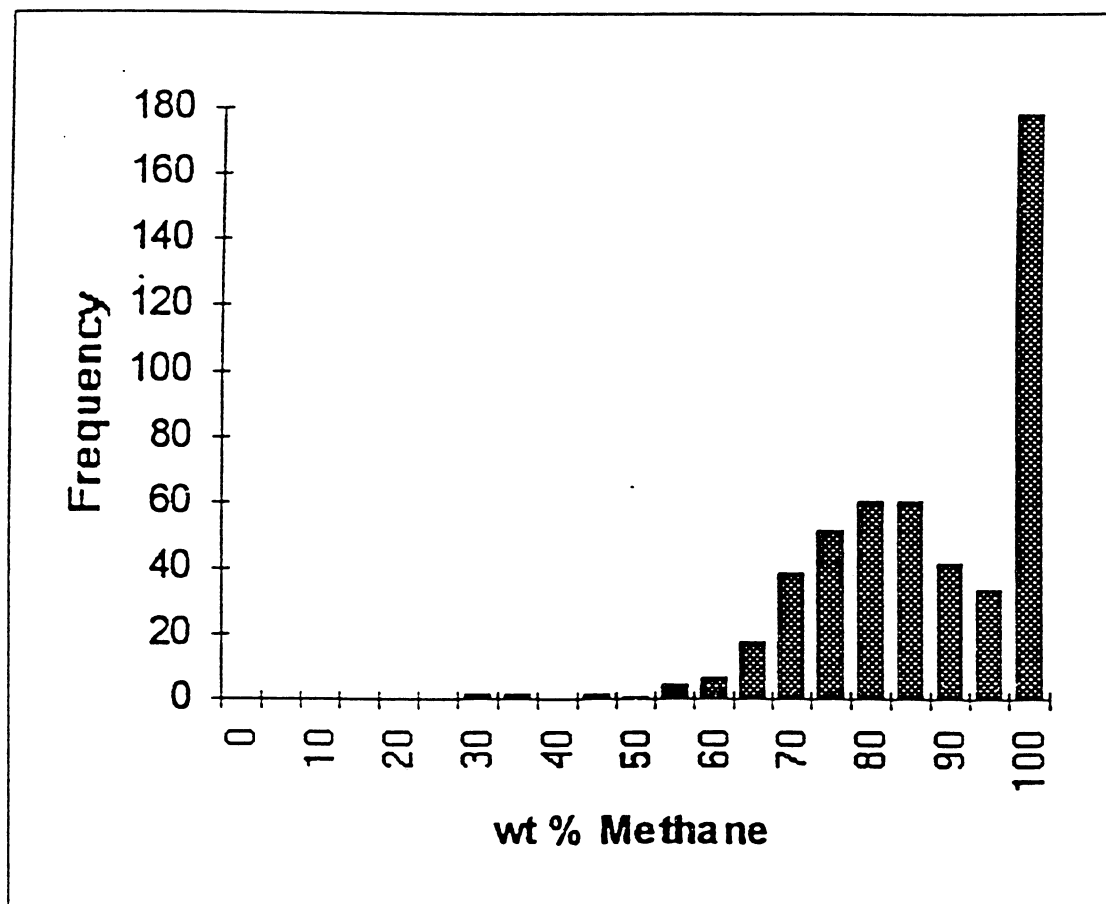


Figure IIA-7. Variations in the H/C and O/C atomic ratio of kerogen isolated from Monterey Shale after heating in the presence of liquid water at 125 to 360°C and 350 bars.

Fig. IIA-8: Histogram of weight % methane concentrations of 500 randomly selected natural gas samples (Mango *et al.*, 1994).



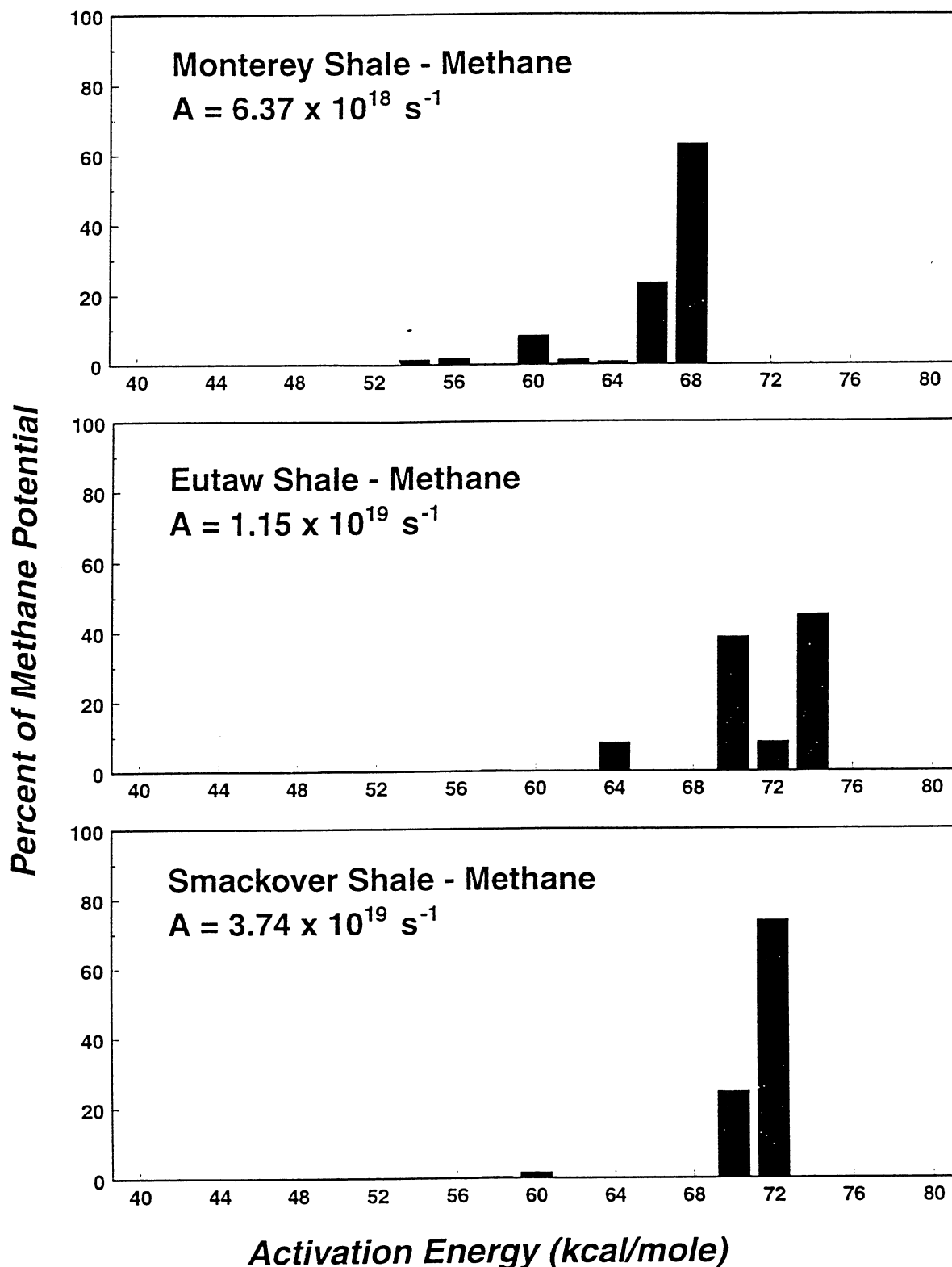


Figure IIA-9. Distributions of activation energies and preexponential factors for methane generation during hydrous pyrolysis experiments. The computer code KINETICS (Braun and Sweeney, 1990) was used to calculate these values.

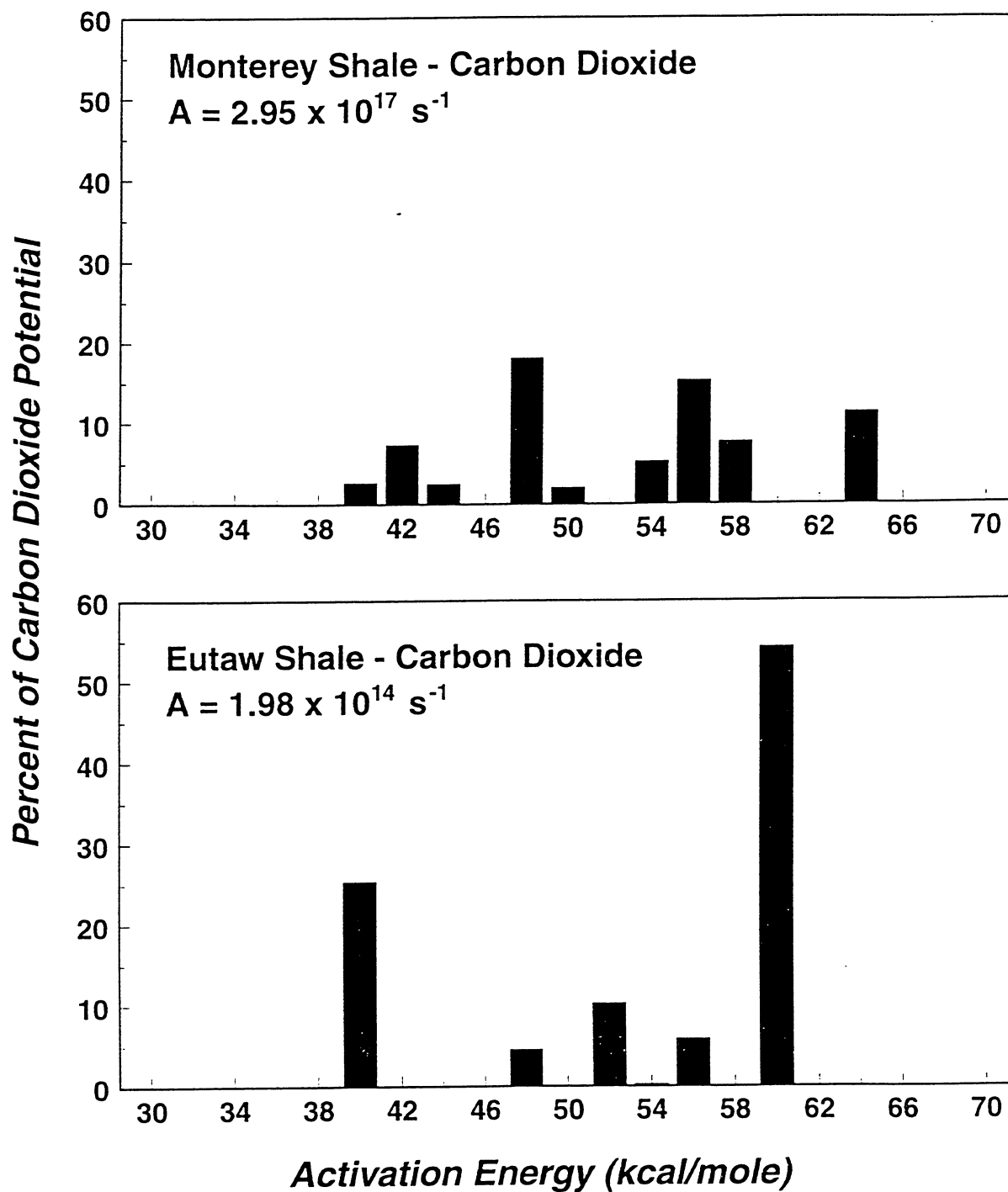


Figure IIA-10. Distributions of activation energies and preexponential factors for carbon dioxide generation during hydrous pyrolysis experiments. The computer code KINETICS (Braun and Sweeney, 1990) was used to calculate these values.

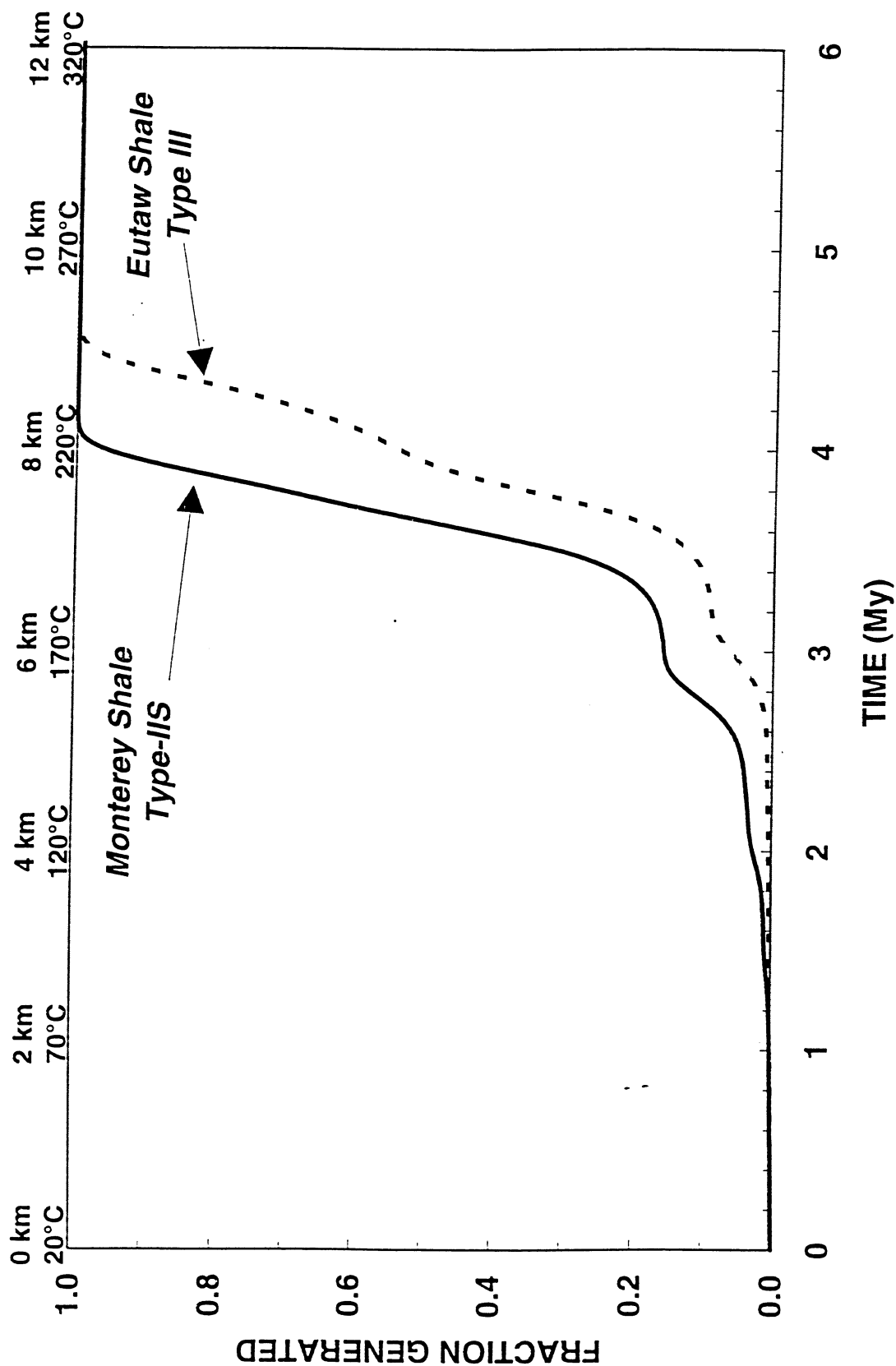


Figure IIA-11. Generation of methane from Monterey and Eutaw Shale in a hypothetical basin with characterized by a geothermal gradient of 25°C/km and a subsidence rate of 2 km/My. The curves were generated by the computer code KINETICS (Braun and Burnham, 1990) from the results of hydrous pyrolysis experiments presented in this report.

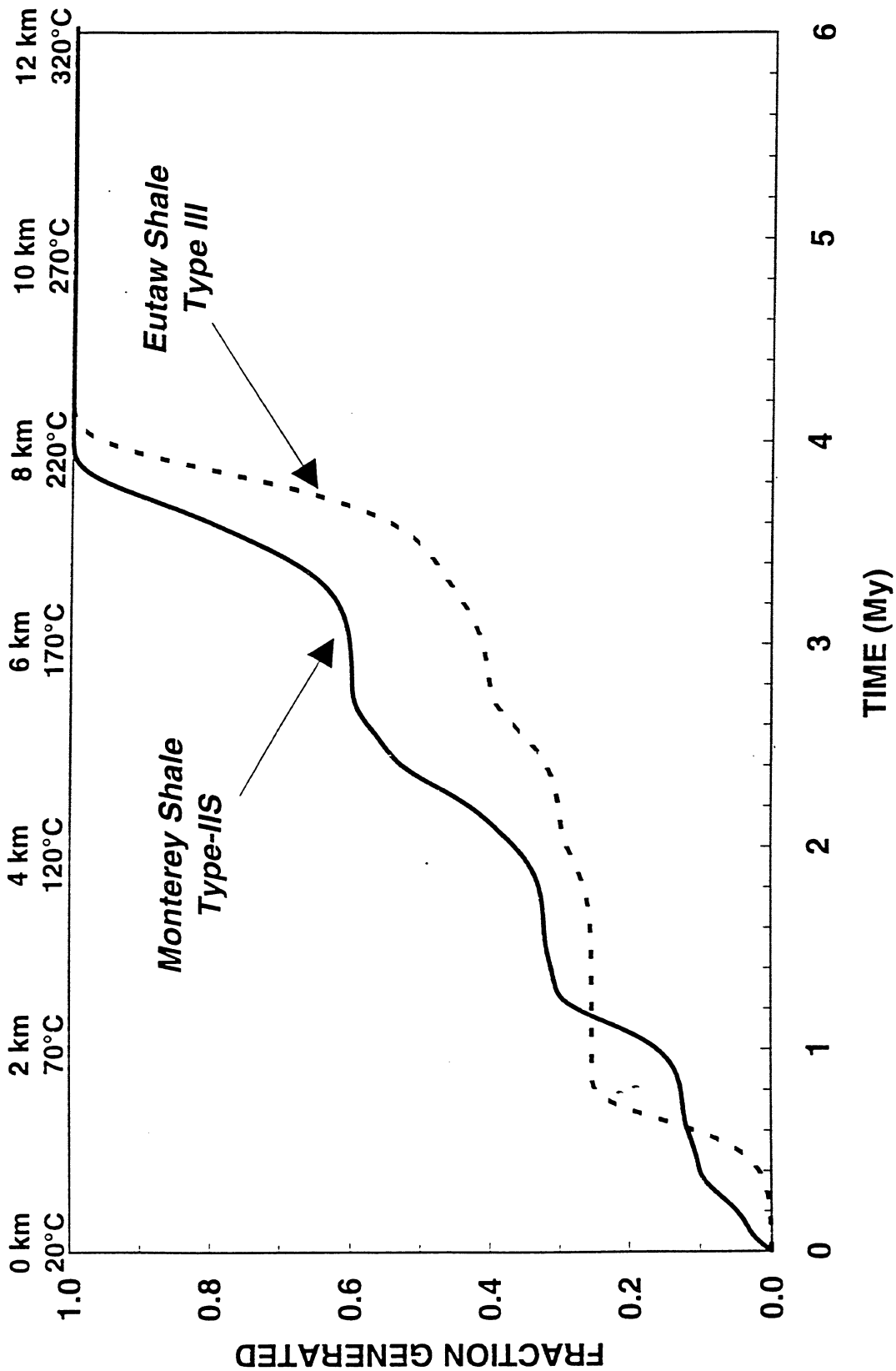
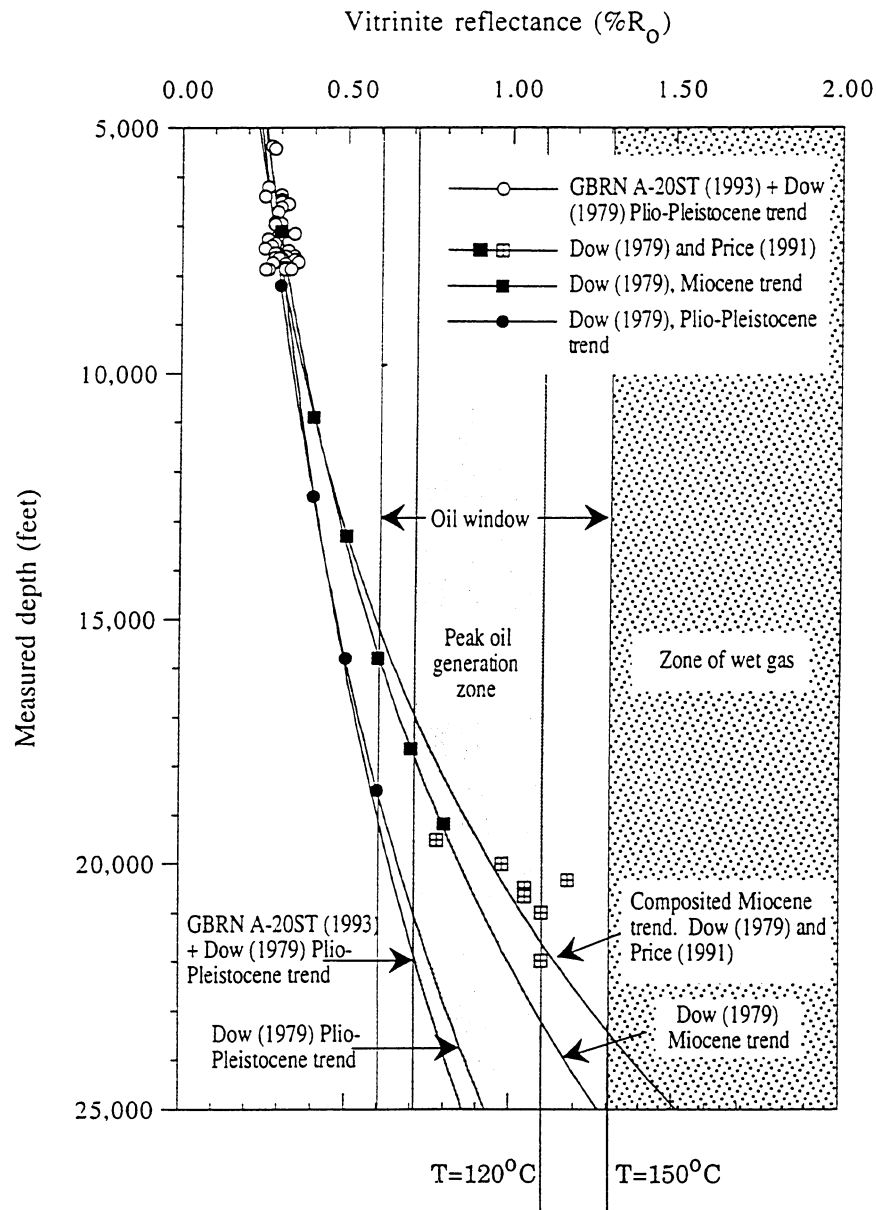


Figure IIA-12. Generation of carbon dioxide from Monterey and Eutaw Shale in a hypothetical basin with characterized by a geothermal gradient of 25°C/km and a subsidence rate of 2 km/My. The curves were generated by the computer code KINETICS (Braun and Burnham, 1990) from the results of hydrous pyrolysis experiments presented in this report.



- 1). Age: EI fluids = 30-55Ma (minimum), (I-129)
- 2). Temperature of reservoirs "storing" oil over long period (since ~ 30Ma).
Therefore, reservoir temperatures = ~120-150°C(!!)
- 3). Estimates via procedures based on light hydrocarbon composition (Young et.al., 1977)
- 4). Jurassic >30,000ft.

Figure B-i-1: Various estimates of maturation vs. depth near EI-330. Estimated temperature exposures for oils and corresponding reservoir depths are shown.

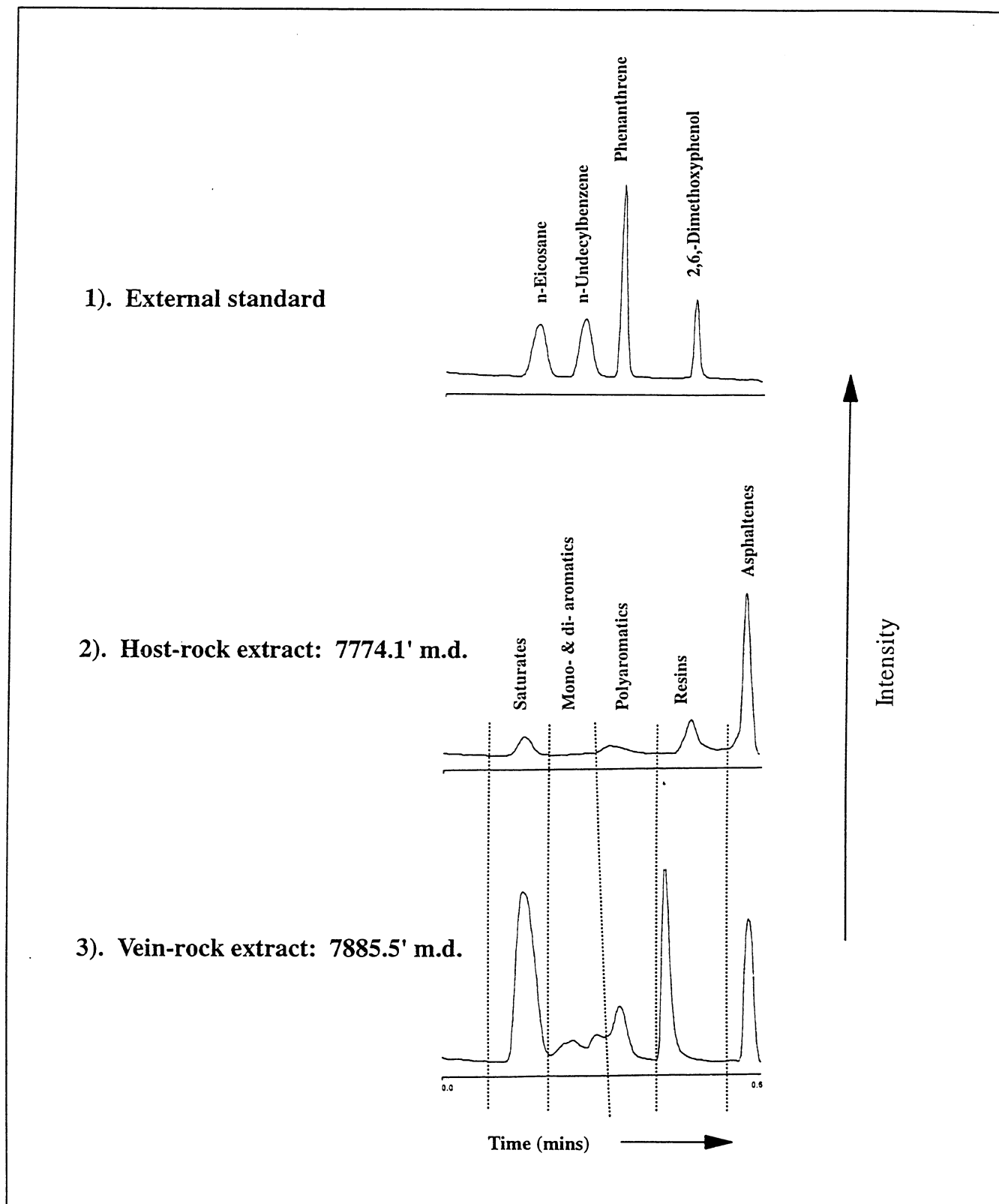
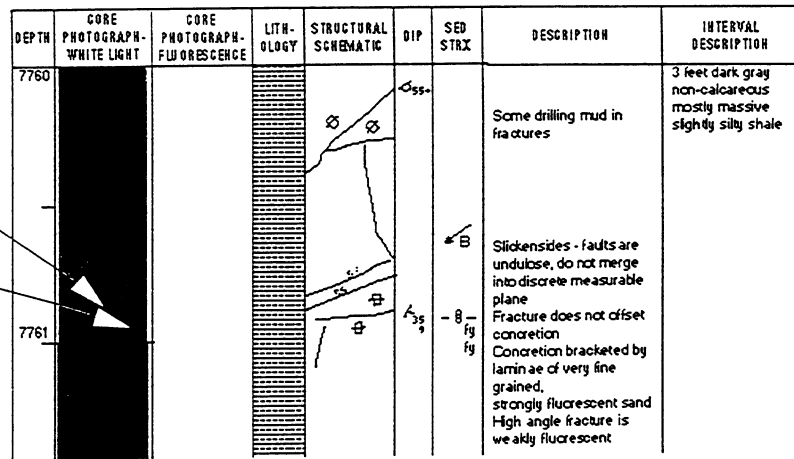


Figure II-B-iii-1: Typical TLC-FID (Iatroscan) chromatographic distributions of major compound groups for an external standard, host-rock extract and vein-rock extract.

Core logs

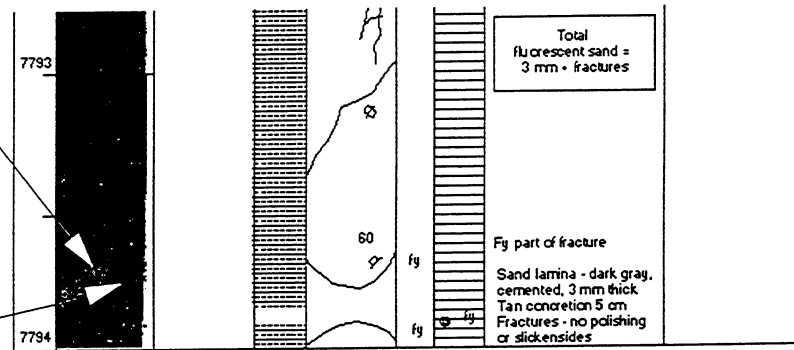
Vein sample 7760.80'

Host sample 7760.80'



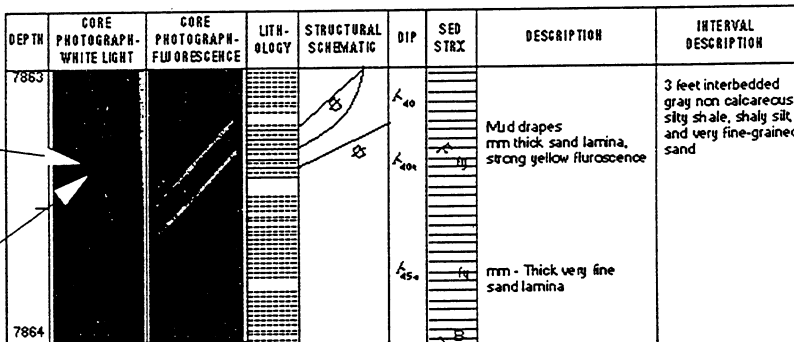
Vein sample 7793.80'

Host sample 7793.80'



Host sample 7863.30'

Vein sample 7863.30'



Vein sample 7885.30' →

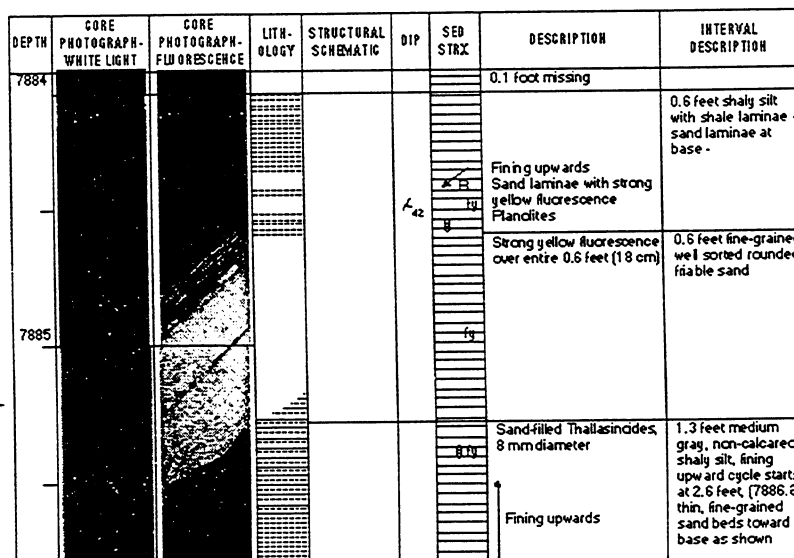


Figure II-B-iii-2: Core logs showing core photographs in white light and fluorescence light (where appropriate), structural details, rock descriptions and showing examples of sampling sites host-rock and vein-rock extracts.

Figure II-B-iii-3: Pathfinder core vein-rock extract bulk compositions

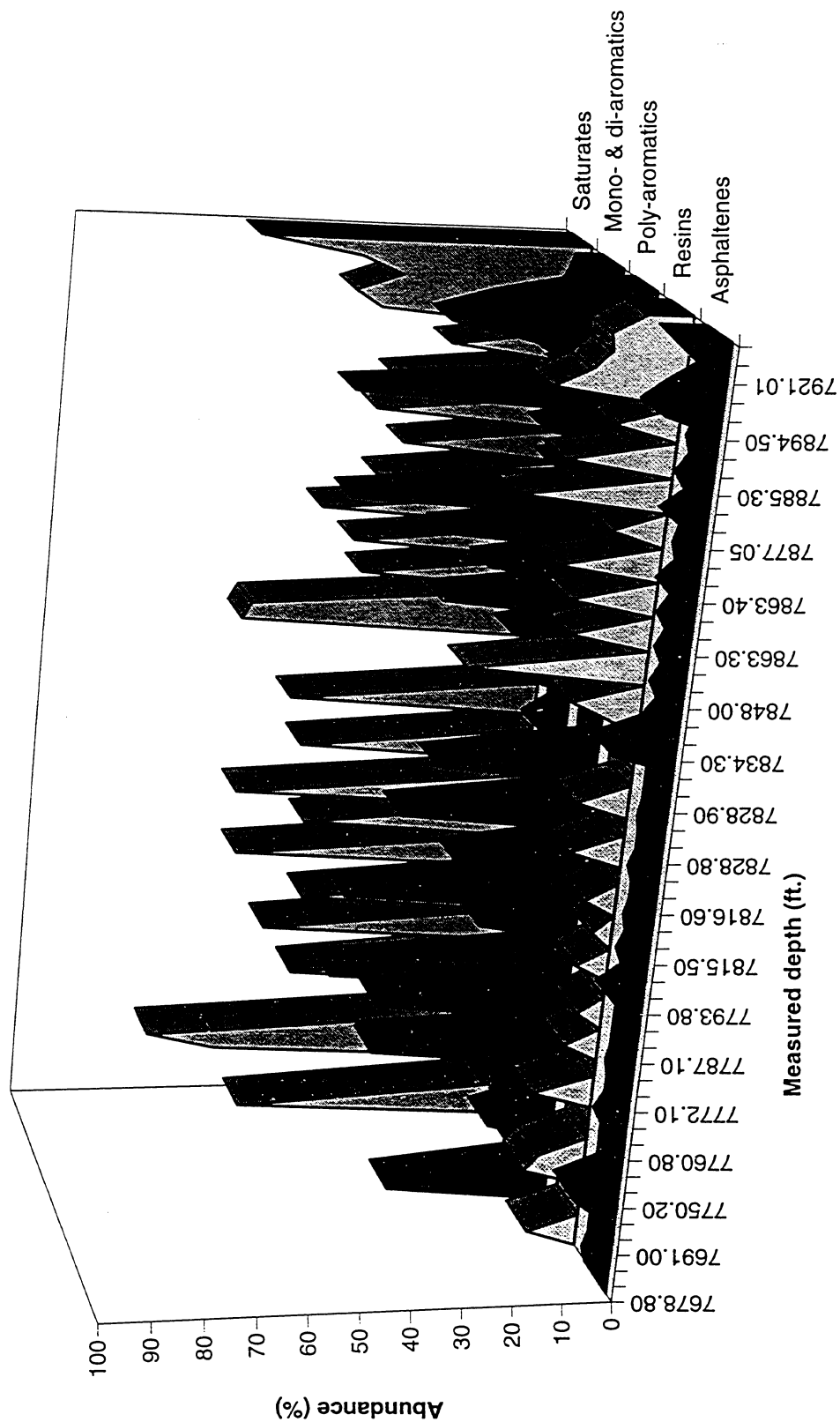
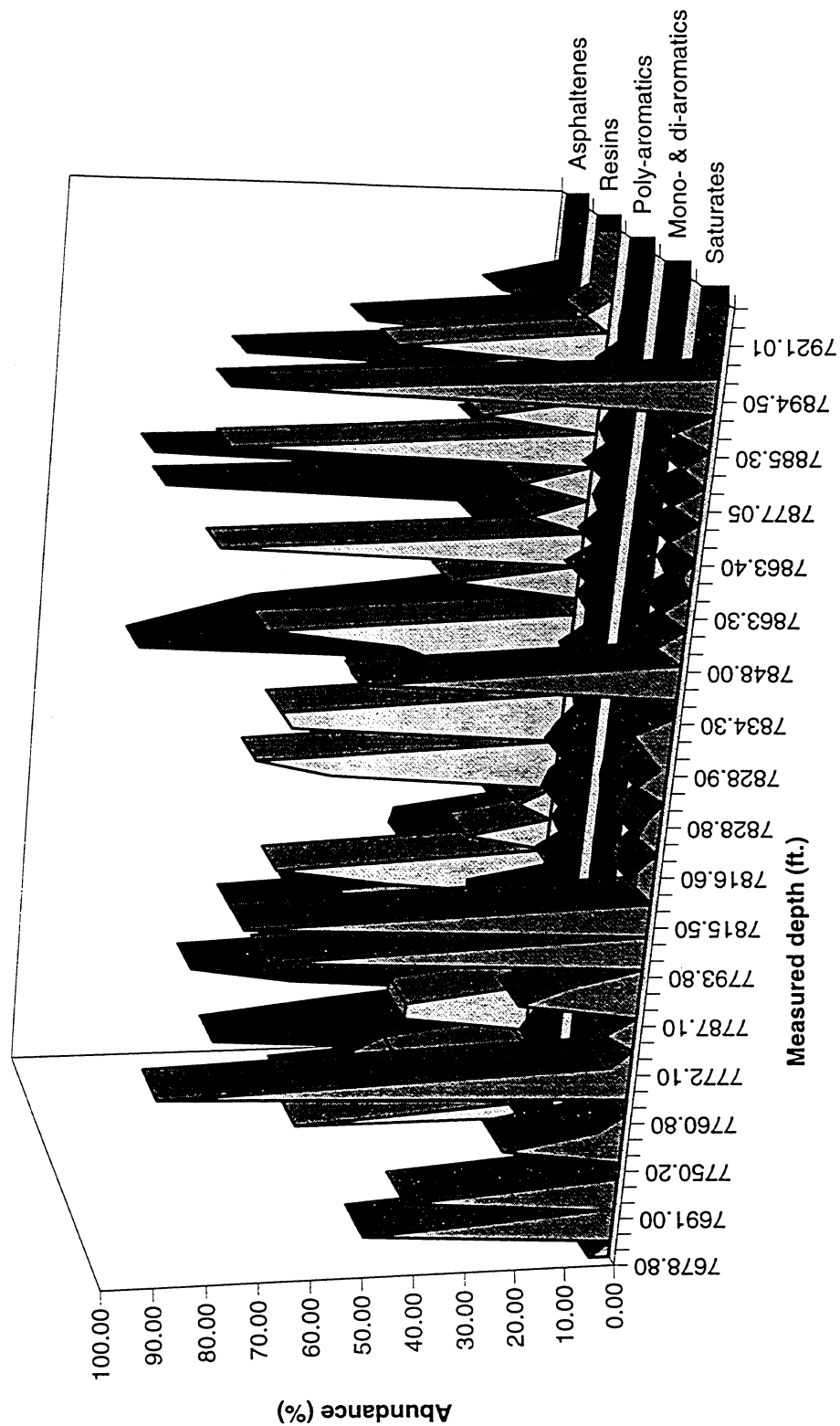
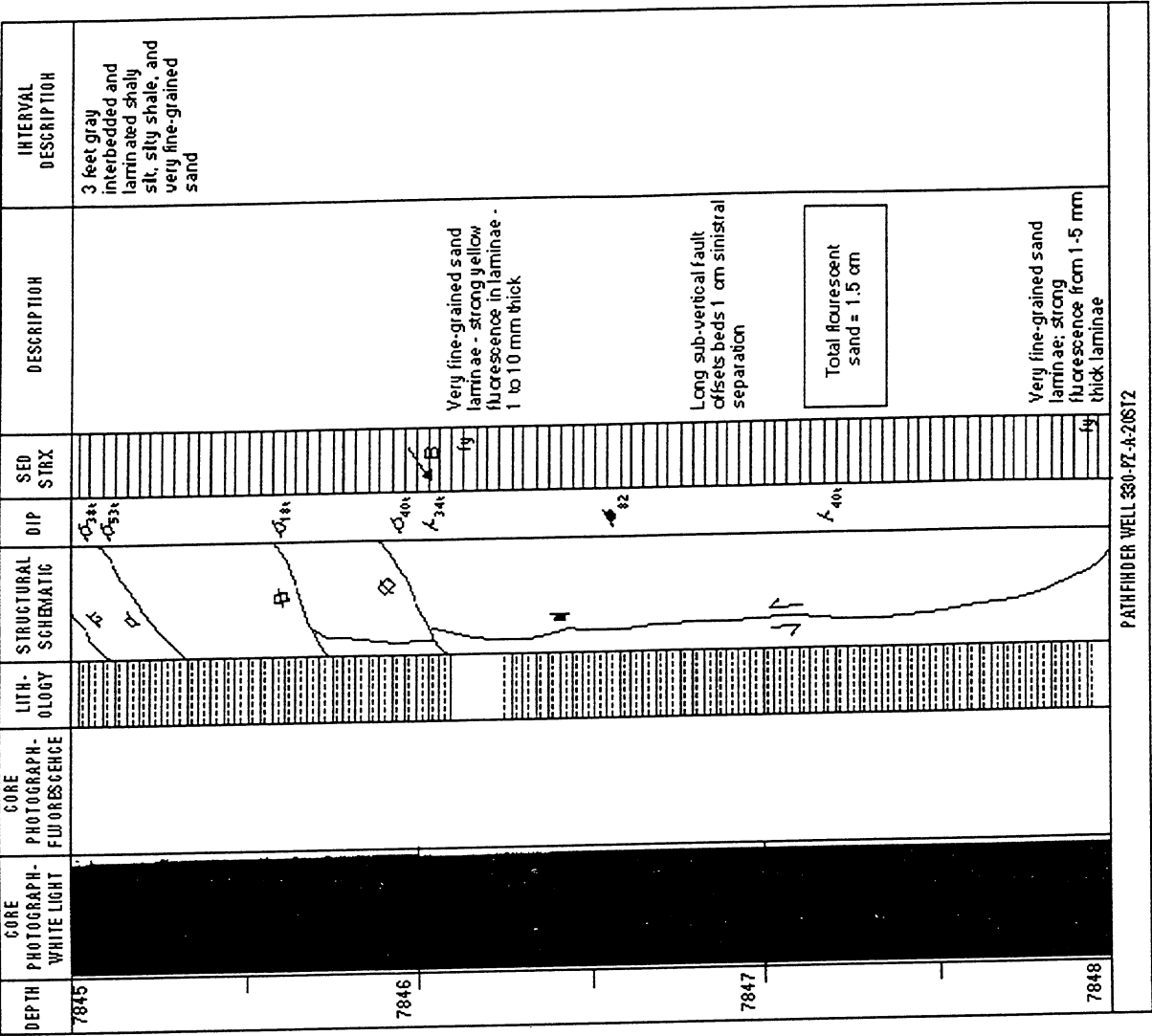


Figure II-B-iii-4: Pathfinder core host-rock extract bulk compositions



Core Log



Host-rock sampled 6" below a 1cm —
thick, strongly fluorescing sand laminae
(7846.4' m.d.) and cutting a long
sinistral, sub-vertical fault that offsets
bedding by ~ 0.5".

Figure II-B-iii-5: Core photograph of the 7846.6' m.d. host-rock extract sampling site showing a sub-vertical, sinistral fault zone.

Figure II-B-iii-6: Comparative distributions of saturated hydrocarbons separated from host- and vein-rock extracts.

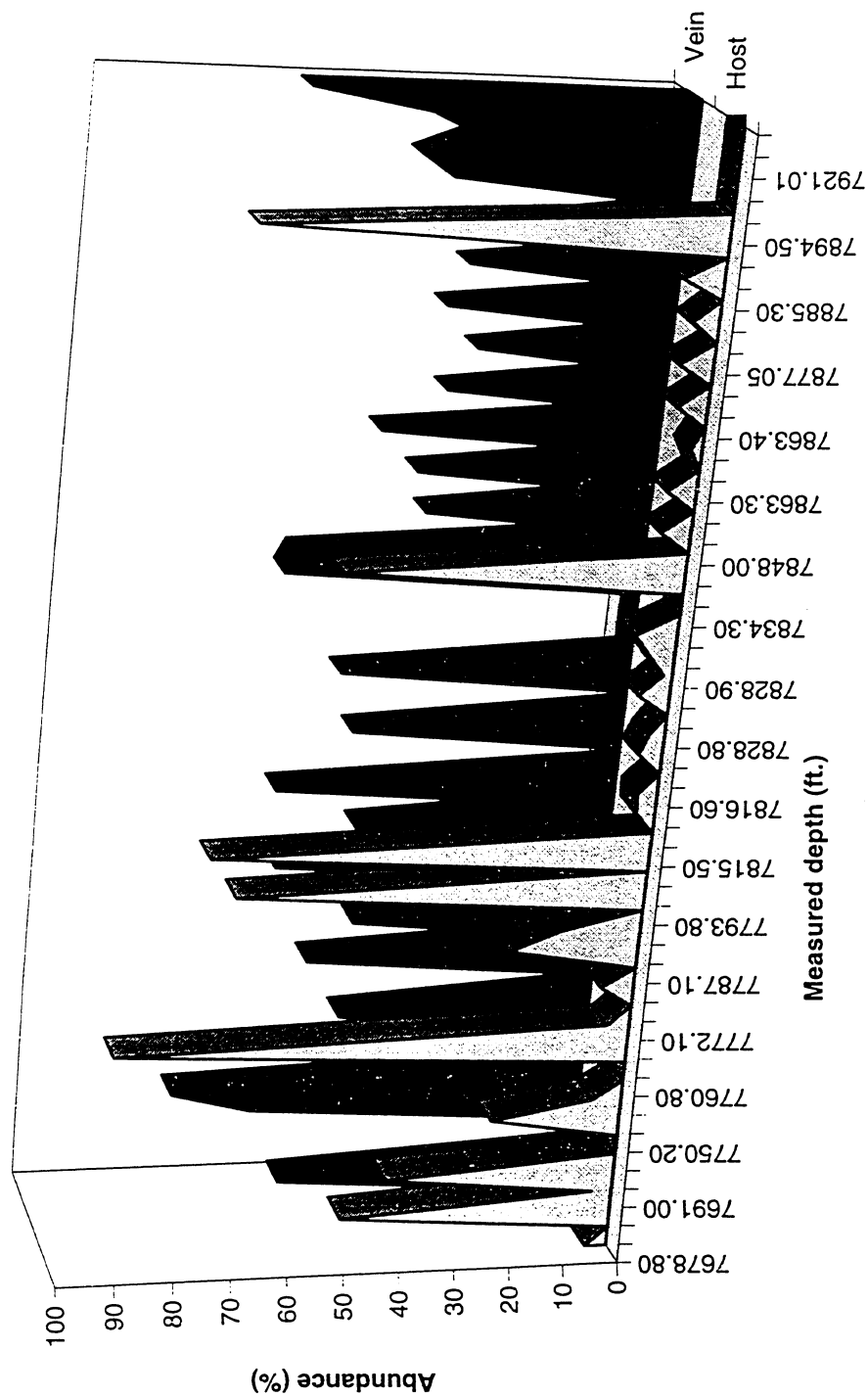


Figure II-B-iii-7: Comparative relative distributions of mono- and di-aromatic hydrocarbons separated from host-and vein-rock extracts.

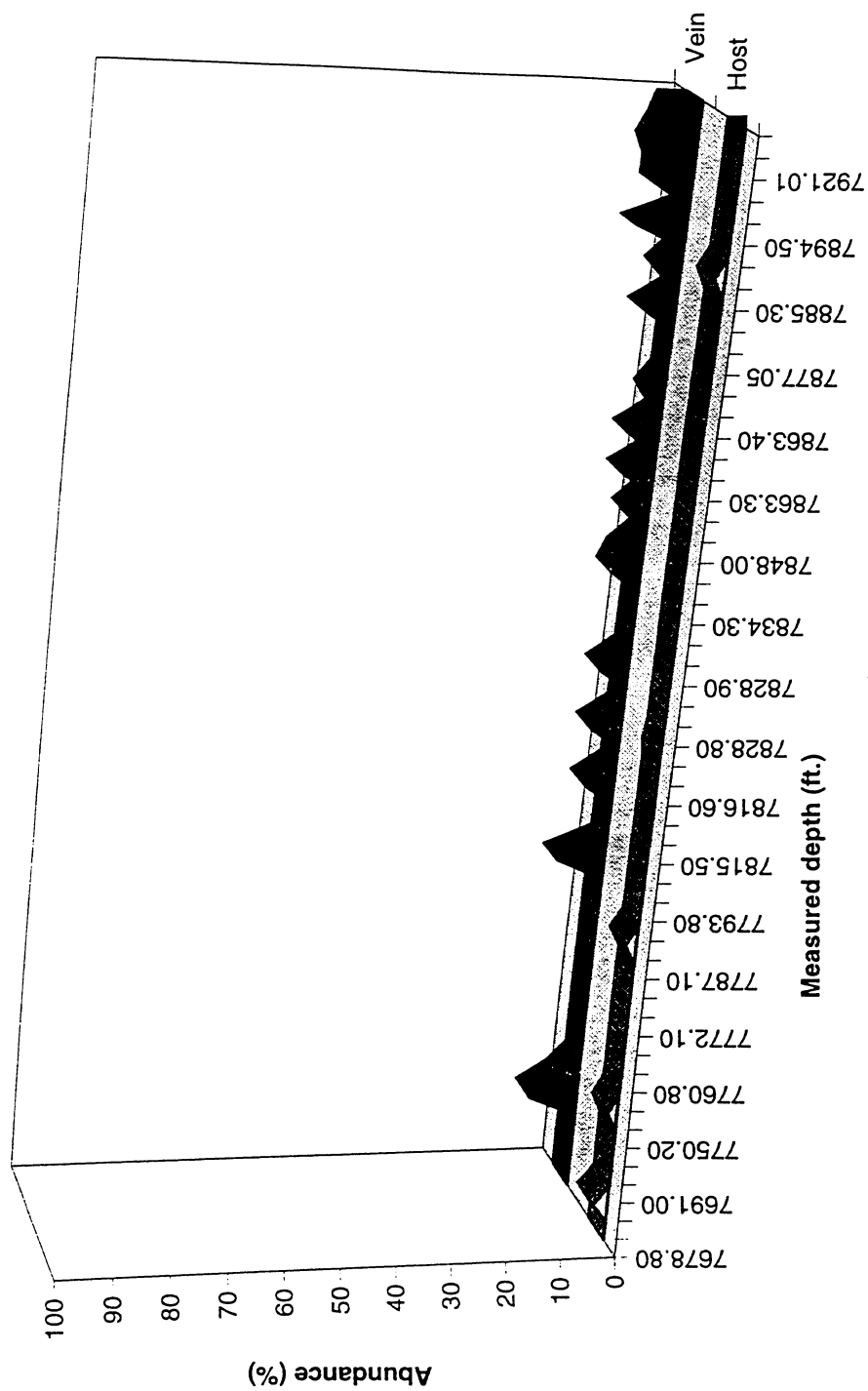


Figure II-B-iii-8: Comparative distributions of poly-aromatics hydrocarbons separated from host- and vein- rock extracts.

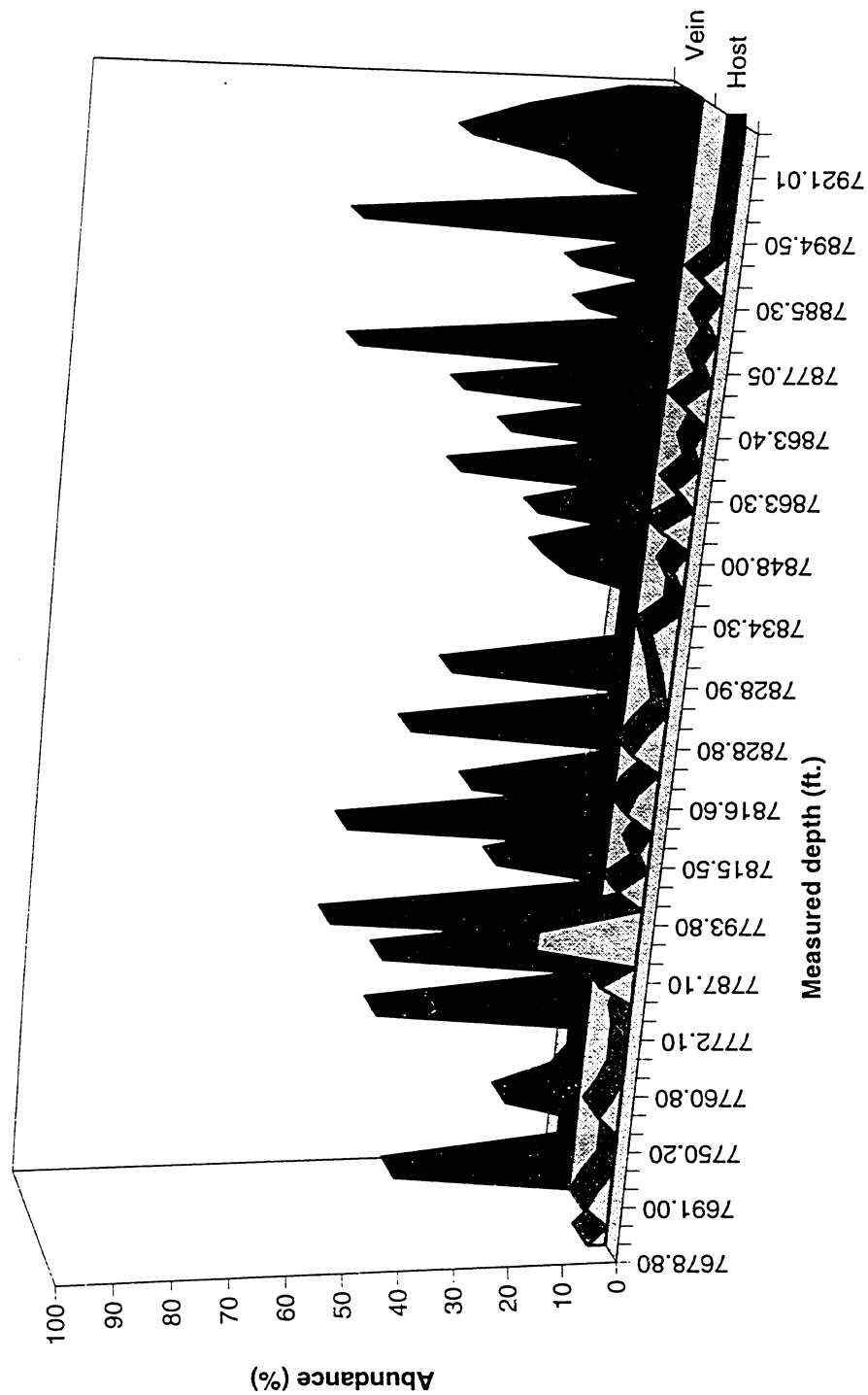


Figure II-B-iii-9: Comparative distributions of polar resins separated from host- and vein-rock extracts.

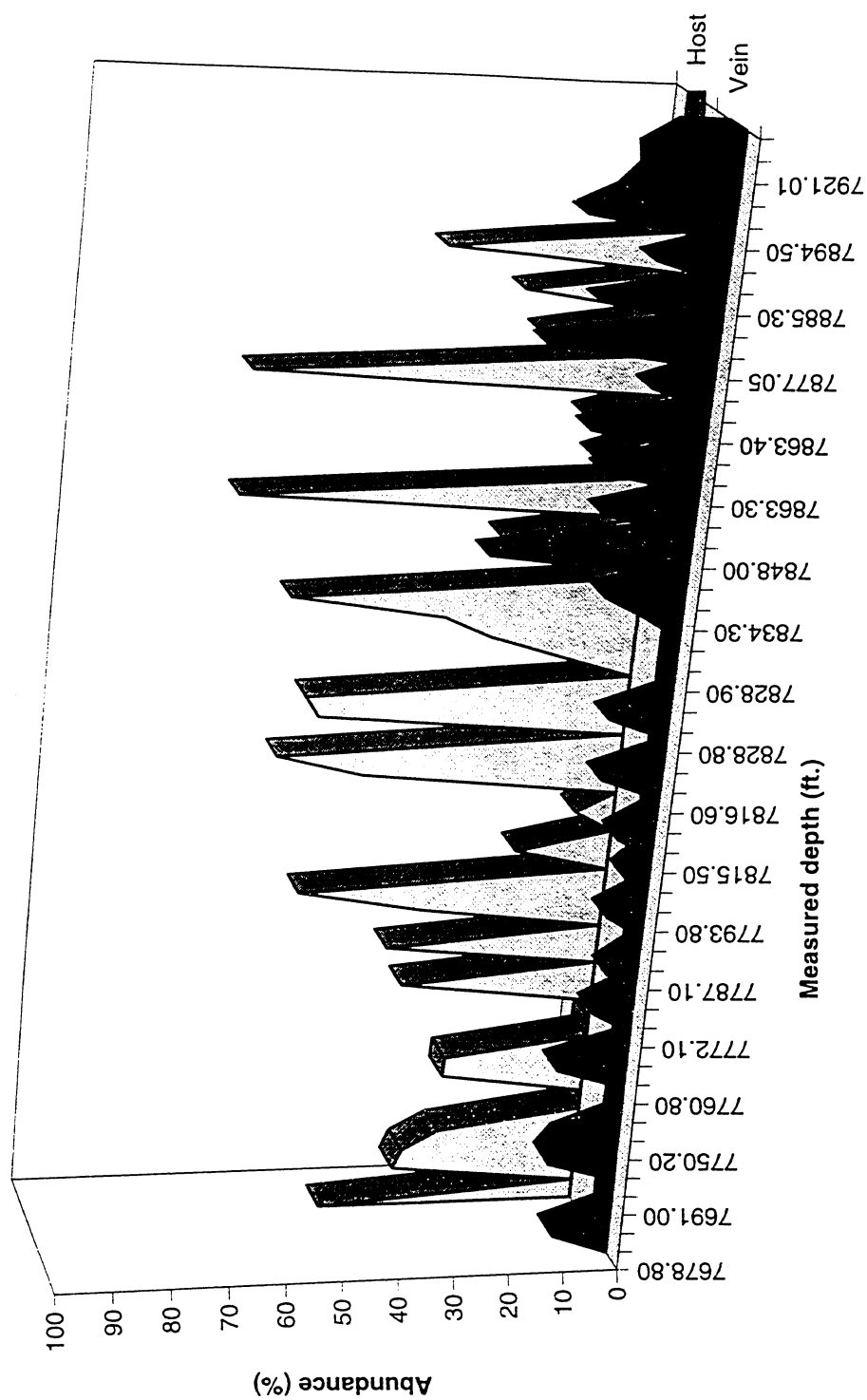
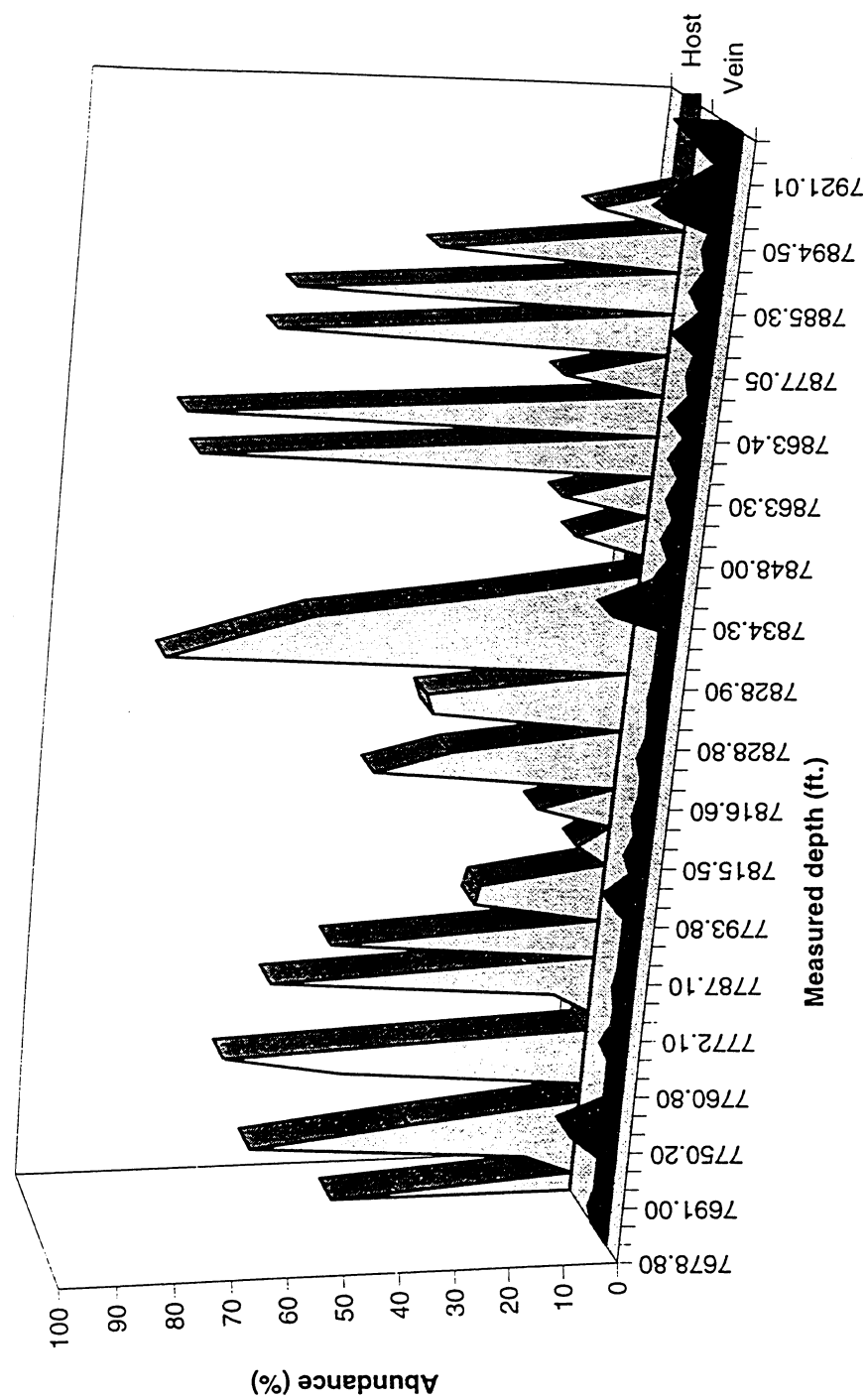
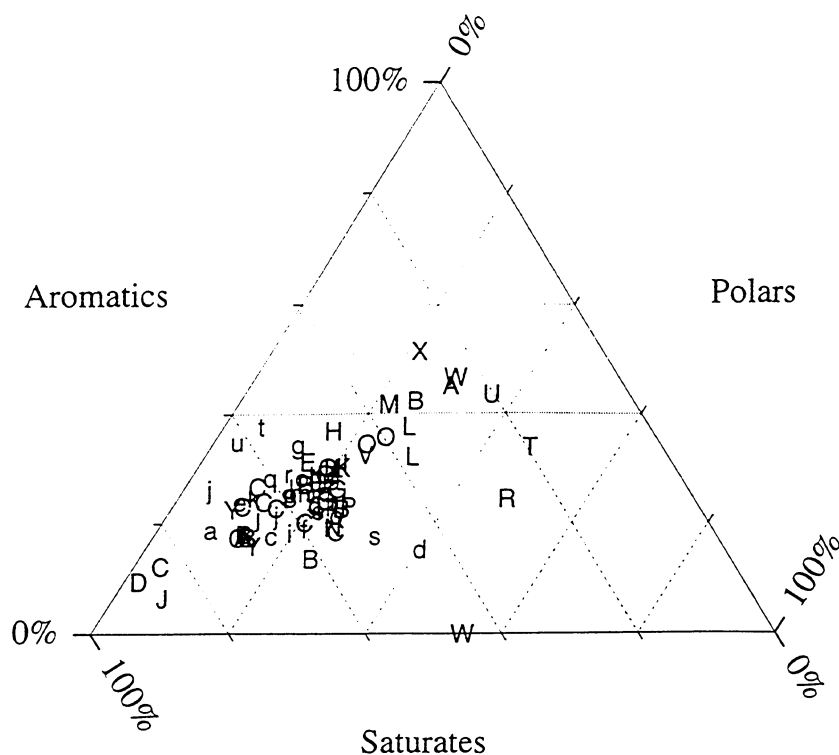


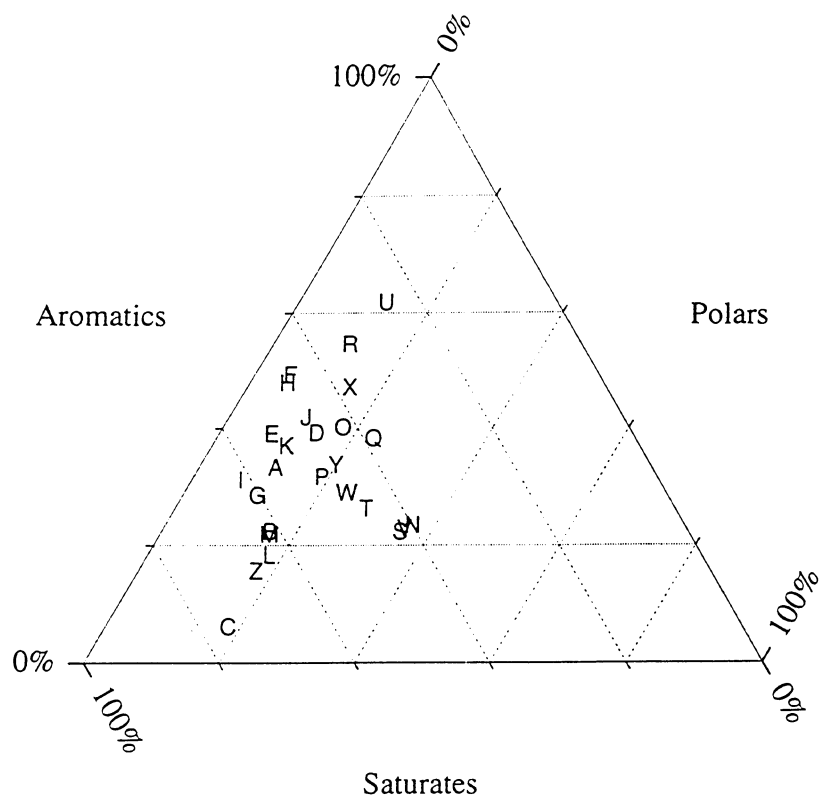
Figure II-B-iii-10: Comparative distributions of polar asphaltenes separated from host- and vein-rock extracts.





A	GBRN-04 Fault	M	B3AST HB-2	Y	A4 L-FB-C	k	A2st OI-5-FB-0
B	GBRN-05 Fault	N	A7st HB-3-FB-E	Y	A8 L-FB-C	l	B11 OI-2-FB-A
C	GBRN-06 Fault	O	C11 IC-4	a	A10 L-FB-C	m	B11D OI-4
D	A20st Fault	P	A8st IC-4	b	B6st LF-FB-A	n	B12D OI-1-FB-A
E	C5 GA-1	Q	A10st IC-4	c	A21 LF-FB-B	o	C14 OI-1
F	C1D GA-2	R	A19st J-1D-FB-D	d	C15 MG-1,2,3,4	p	C19 OI-1
G	C7st GA-2	S	B7AST JD-FB-A Unit	e	A9 MG-FB-A-1	q	C21 OI-1
H	C13D GA-2	T	A1B JD-FB-B	f	A3 N.I.	r	C4E OI-1
I	C20 GA-2	U	A5 JD-FB-B	g	C18 NH	s	C9d OI-1
J	D2 GA-5	V	A11D JD-FB-C	h	B10st NH-FB-A1	t	Texaco Res ?
K	C3D HB-1	W	C17 KE-2	i	A14 OI-1-2-3-FBV-B	u	Texaco Bleed Off
L	C10st HB-1B,2	X	A6st KE-FB-E	j	A23 OI-4		

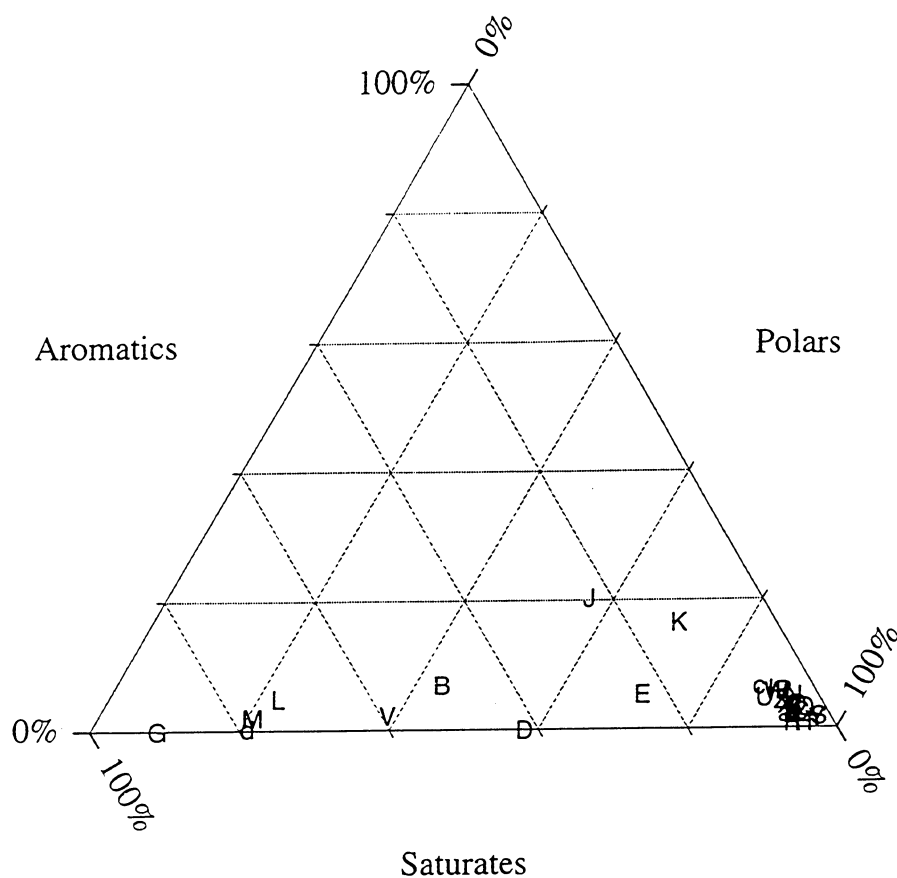
Figure II-B-iii-11: Ternary diagram showing the buk compositions 47 oils from Eugene Island Block 330, Louisiana Gulf Coast, based on saturated, summed aromatic and summed polar relative abundances (%).



Measured depth (ft.)

A	7679.5	F	7787.1	K	7828	O	7858.5	S	7877.05	W	7919.08
B	7750	G	7793.8	L	7834.3	P	7863.3	T	7885.3	X	7921.01
C	7750.2	H	7805.85	M	7846.4	Q	7863.4	U	7893.7	Y	7971
D	7760.8	I	7815.5	N	7848	R	7865.7	V	7894.5	Z	7978.3
E	7786.11	J	7816.6								

Figure II-B-iii-12: Ternary diagram showing the bulk compositions of Pathfinder core vein-rock extracts based on saturated, summed aromatics and summed polar relative abundances.



Measured depth (ft.)

A	7678.8	F	7751.25	K	7793.8	P	7828.8	U	7834.3	Z	7865.7
B	7679.5	G	7760.8	L	7805.85	Q	7828.8	V	7846.4	a	7877.05
C	7691	H	7772.1	M	7815.05	R	7828.9	W	7858.5	b	7877.1
D	7750	I	7786.11	N	7816.6	S	7828.8	X	7863.3	c	7893.7
E	7750.2	J	7787.1	O	7816.6	T	7834.3	Y	7863.3	d	7894.5

Figure II-B-iii-13: Ternary diagram showing the bulk compositions of Pathfinder core host-rock extracts based on saturated, summed aromatics and summed polar relative abundances.

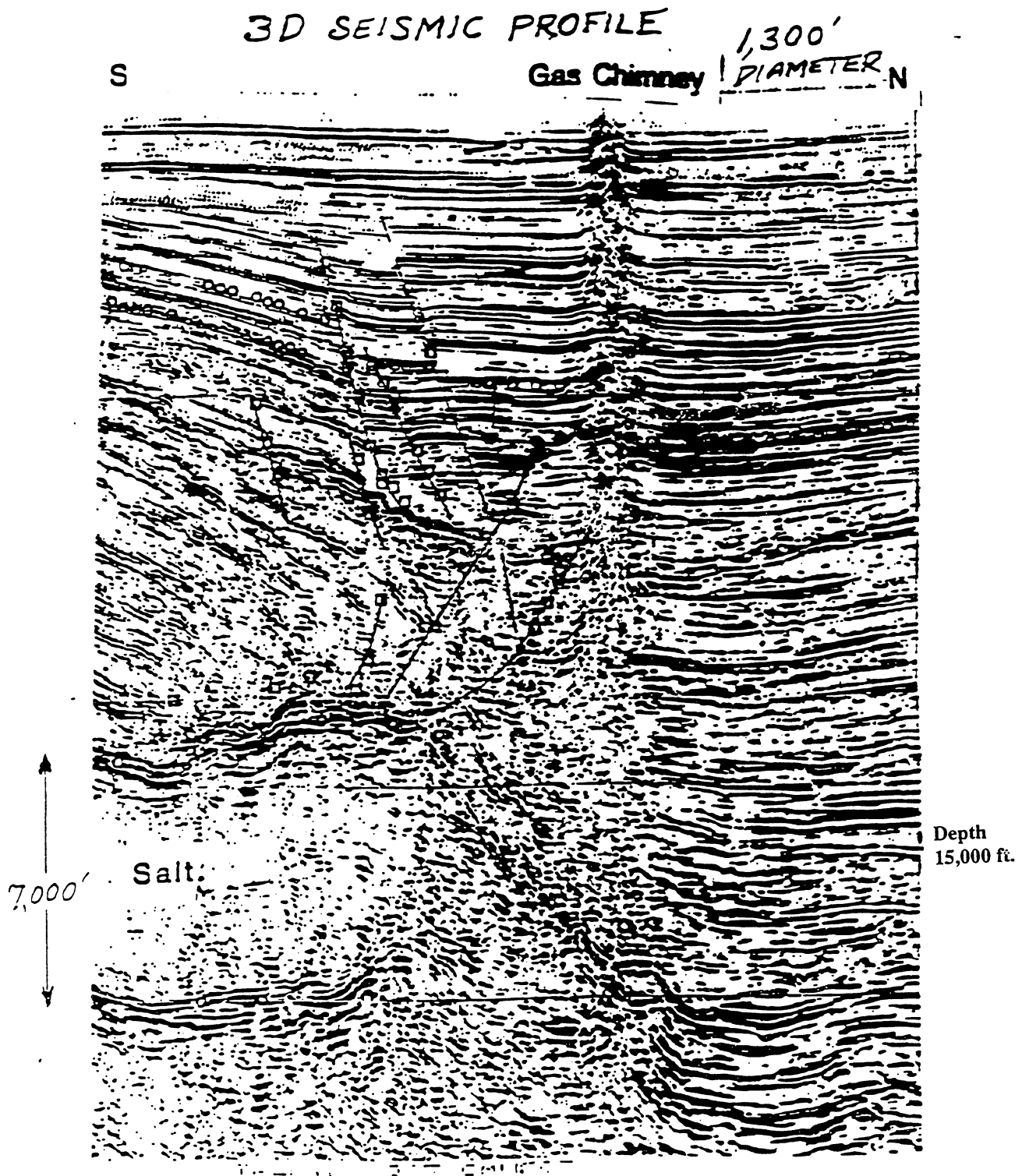


Figure II-B-iv-1: Seismic profile of gas plume - S. Marsh Island. From Hunt *et al.*, (in Press).

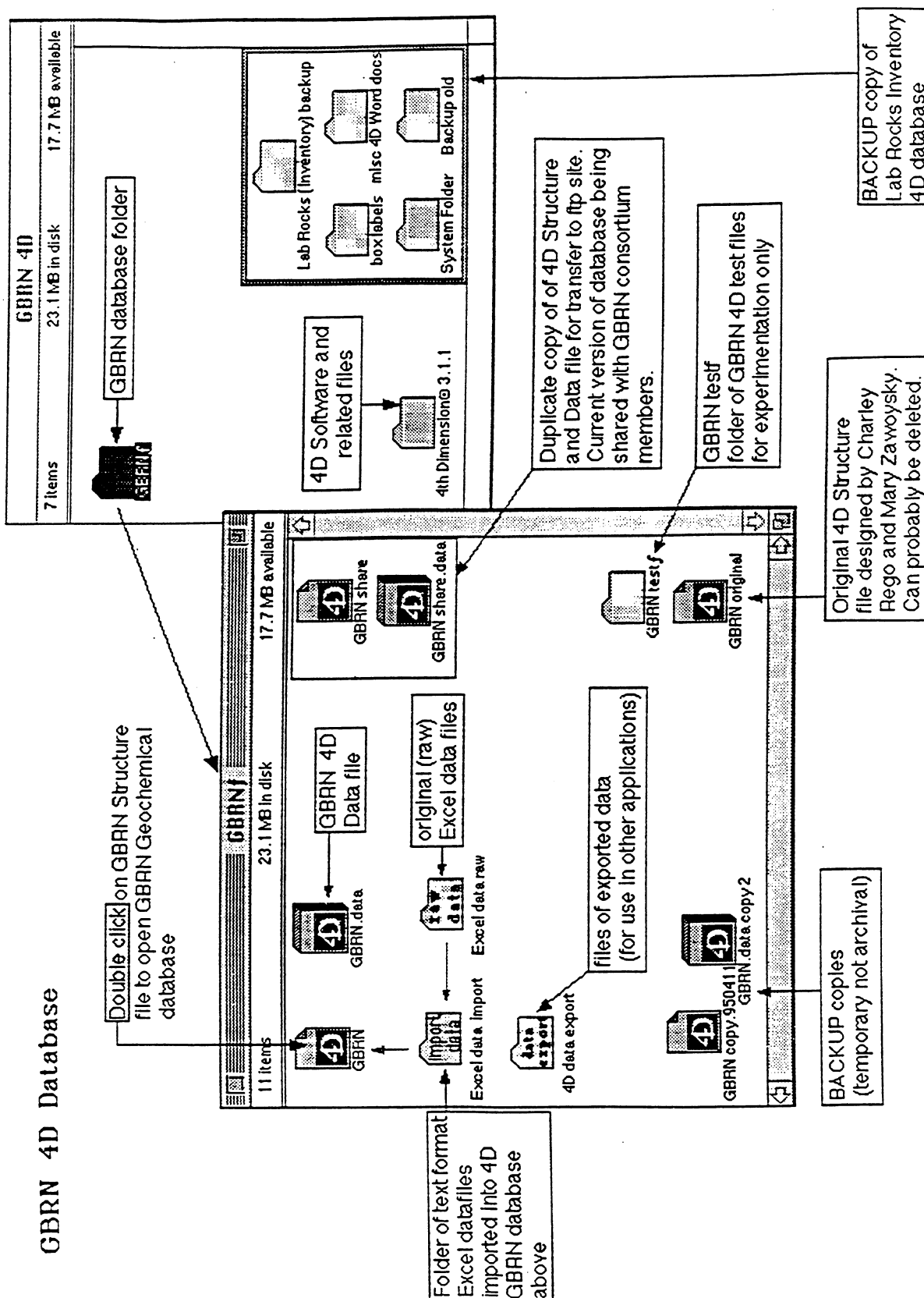
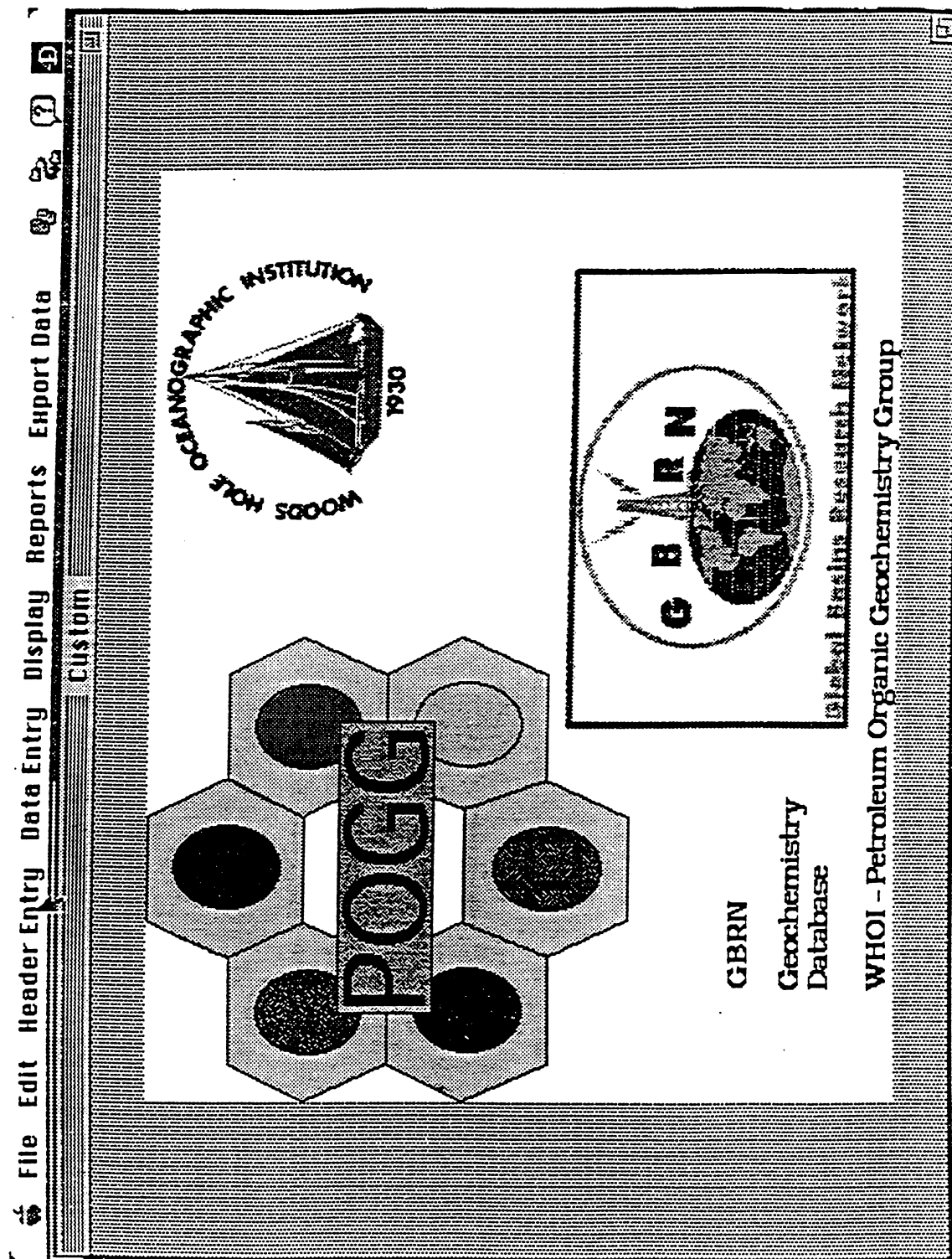


Figure II-C-i-A1: Mac screen shot of GBRN 4D database folder

Figure II-C-i-A2: Mac screen shot of GBRN 4D database menu driven runtime application

GBRN 4D Database Runtime Application



Oil Migration in a Major Growth Fault: Structural Analysis of the Pathfinder Core, South Eugene Island Block 330, Offshore Louisiana

Steven Losh

Dept. of Geological Sciences, Cornell University

ABSTRACT

The Pathfinder core, taken in the South Eugene Island field, offshore Louisiana, provides an outstanding sample of structures associated with a major growth fault that abuts a giant oilfield and which is thought to have acted as a conduit for hydrocarbon migration into the producing reservoirs. Where cored, the growth fault zone cuts semi-consolidated Plio-Pleistocene mudstone and is over 100 meters wide. The fault zone in the core consists of three structural domains, each characterized by distinct rock type, distribution of fault dips and dip azimuths, and distribution of spacing between adjacent faults and fractures. Although all of the domains contain oil-bearing sands, only faults and fractures in the deepest domain contain oil, even though the oil-barren fault domains contain numerous faults and fractures that are parallel to those which contain oil in the deepest domain, and are thus favorably oriented for transmitting oil. This deepest domain is also distinguished from the other two by a greater degree of structural complexity and by a well-defined power-law distribution of fracture spacings. The departure of the fault spacings in the upper two domains from a power-law distribution, combined with stable isotope data that point to low-temperature water-rock interaction within a gouge zone that separates these two fault domains, indicates that the faults in those domains may have been active only in the early stages of the growth fault zone. These faults may thus predate oil migration. In contrast, the faults in the oil-bearing domain may have been active later in the fault zone's history, when geologic and organic geochemical investigations indicate oil migrated into the Block 330 reservoirs. Even though oil was present in sands throughout the core, its restriction to faults in the probably-youngest portion of the fault zone implies that oil migrated only through that part of the fault that was active during the time when oil was available. The absence of oil in favorably-oriented fractures in the other, probably-older fault domains indicates that the oil was never sufficiently - pressured to hydraulically fracture its way up the fault zone, and instead migrated along faults and fractures that were opened primarily by tectonic stresses.

Introduction

High-angle faults in sedimentary basins should logically play a significant role in hydrocarbon migration from deep, overpressured reservoirs and "kitchens" to shallower reservoirs from which they can be economically produced. A number of studies have documented indirect and direct evidence of large scale, cross-formation fluid flow along growth faults (Jones and Wallace, 1974; Weber et al, 1978; Hippler, 1993; Galloway et al, 1982, review of Hooper, 1991). While these examples provide valuable information about processes that affect such flow and also give permissive evidence that large volumes of hydrocarbons may migrate in such a fashion, there has remained a large uncertainty as to the actual connections between fault-conduit fluid flow and the filling of economically-producible oil and gas reservoirs. A clear understanding of fault charging could be extremely valuable as a prospect evaluation criterion. Although many reservoirs are spatially associated with faults, what role do the faults really play in charging of the reservoirs? Do some faults, or portions of faults, act as hydrocarbon migration conduits, while others do not? If fault charging does occur, what controls fluid migration up such faults and into the reservoirs?

In order to develop and test answers to these questions, the Global Basins Research Network, a consortium of universities and industry affiliates, undertook a multifaceted U. S. Department of Energy - funded project in South Eugene Island Block 330, offshore Louisiana, having the goal of simultaneously drilling and sampling a large, active growth fault and carrying out a variety of analyses of rocks, brines, and oil and gas from reservoirs adjacent to the fault. This particular location was selected because of a variety of evidence supportive of recent (even ongoing) reservoir filling linked to the bounding fault system (Anderson, 1993; Anderson et al, 1994). The fault was drilled and cored as an extension of a Pennzoil development well (the A20 sidetrack; figure 1) in the fall of 1993, a variety of logs were run and measurements made, and the fault was drill-stem tested as a potential reservoir (Anderson et al, 1994).

The purpose of this paper is to present a structural description of the core that was taken from the well. Particular attention is paid in this study to understanding why, although a wide fault zone was cored, only a discrete portion of it contained oil.

Core acquisition and processing

Because of the need to continuously sample the fault zone in order to fully characterize it, we utilized a whole-coring system designed to maximize recovery in the semi-consolidated sediments typical of the SEI Block 330 field. The bottom-hole assembly (BHA) consisted of the following:

Bit: Baker-Hughes INTEQ prototype RC 425 anti - whirl PDC bit. The cutters were asymmetrically placed around the the bit in order to minimize "walking" of the bit in the hole.

Core barrel: 18.3 meter x 0.1 meter (60-foot x 4 - inch) barrel with 6 - millimeter (1/4 inch) aluminum liner, with pressure release valves. Barrel was equipped with full-closure "clamshell" type doors just above the bit. Closure of these was activated from the surface before pulling out of the hole.

Coring was done at a mudweight of 1.97 kg/liter (16.3 pounds per gallon). There was no appreciable fluid pressure gradient associated with the fault in this well.

We anticipated that the core would be taken primarily in semi-consolidated smectite-rich mudstone. Industry experience with whole coring in this type of sediment led us to use an experimental mud formulation in order to stave off "balling", or adhesion of clay to the bit, which typically slows penetration rates to 60 centimeters an hour or, usually, less. The requirement that we use a water-based mud constrained us to utilize an environmentally-safe synthetic additive; we used a poly alpha olefin (Friedheim et al, 1991), such that it constituted 3% of the mud. This substance does not fluoresce, it is chemically distinct from nearly all of the organic compounds we anticipated finding in the core, and, at the low concentrations used, it did not interfere with sensitive electrical resistivity measurements

required for the Formation MicroImager (FMI) log. We also used an additive to inhibit clay swelling which could have led to jamming in the core barrel.

The combination of the above enabled us to obtain unprecedented penetration rates with the core bit in the semi-consolidated mudstones, averaging 21 meters/hour, ranging as high as 52 meters/hour. We retrieved 104.6 meters of core out of 109.8 meters attempted, for a recovery rate of 95%.

Because we initially anticipated slow (30 to 60 cm/hour) penetration rates during coring, we expected to retrieve perhaps 25 meters of core in the time available to us. Thus, we opted not to put on the coring BHA until we had drilled to within 12 meters of the fault, as determined from seismic data. Unfortunately, the uncertainty in picking the fault and converting time to depth for the seismic data resulted in our drilling through the upper bounding fault of the growth fault zone, which was marked by a gas show of 360 units (compared to a background of about 75 units), before changing to the coring BHA: this fault zone later produced several barrels of oil in a drill stem test (Anderson et al, 1994). The top of the core is thus about 8 meters below the first main fault in the growth fault zone.

On the rig, the core was marked with orientation stripes as it was pulled out of the core shuttle, then cut into 91-cm (three-foot) sections, or tubes. Every other tube, beginning with the second one, was placed in dry ice on the rig, and has been continuously frozen since, in order to preserve organic compounds for geochemical analysis. The unfrozen tubes were placed on a tilted table in order to drain the drilling mud, and then capped and filled with non-fluorescing epoxy in order to stabilize the core in the liner and thus prevent damage during transport and storage.

In Houston, the cores were logged for spectral gamma radiation, oriented for slabbing by means of X-ray radiography, and logged on site at a scale of 1:5 as soon as they were slabbed. Wherever possible, tubes were slabbed perpendicular to the predominant set of fractures in order to facilitate sampling of them; where no fractures were present, tubes were cut perpendicular to bedding. The cores are presently stored at Pennsylvania State University: frozen cores are kept at -15 C, the unfrozen ones are waxed and stored in a humidified room at 3 C.

Methods

All observed faults and fractures were recorded on the core logs, and their geometries in three dimensions were verified using X-ray fluoroscopy. A feature was considered a fault if it displayed gouge, breccia, pervasive slickensides, or offset beyond that which accompanied breakage of core in the inner tube (figure 3). A disproportionately large share of faults are perpendicular to the long axis of the core, and at least some could represent breakage and rotation of core in the barrel as it was drilled (Kulander et al, 1990). However, many of these faults experienced only translational offset, with no evidence of rotation either in the form of differences in apparent bedding dip across the fault or of circular grooves or slickensides on the fault surface. Where such evidence of coring-induced faulting was lacking, the fault was recorded as a natural feature. In contrast to faults, a fracture was indicated by a planar break across which no offset was observable, or which did not display any other fault characteristics.

Except for the fault at 2325 meters DD, faults and fractures were generally not detectable in the FMI log, perhaps owing to their tightness, so their orientations in real space had to be obtained indirectly. Structures in the core were oriented by the following procedure: 1) the core was co-registered with the FMI log by comparing the core gamma log with the downhole gamma ray log that was run with the FMI, as well as utilizing log header information. The depths recorded on the core (driller's depths) are 4.6 meters less than those recorded on the FMI log (logger's depths); this magnitude of discrepancy is not unexpected. 2) Places were identified where the bedding dip in the core matched the apparent bedding dip in the Formation MicroImager log. In those instances, the apparent azimuth of the bedding dip in the FMI and that of the slabbed face of the core were

identical. 3) The apparent orientation of the stripes on the core inner tube was computed. It is assumed that this orientation does not vary over the length of a given 9.1 - meter (30-foot) core, as care was taken to maintain the core orientation when pulling it out of the shuttle on the rig. 4) The apparent azimuth of the slab face for each section was then computed, according to the angle between the orientation lines on the inner tube and the slab face. The azimuth was uniquely constrained by the direction of bedding dip in the core. 5) Apparent dip and dip azimuth were measured for all faults whose dip azimuth lay in the plane of the slab face. Because the slab faces were oriented to be cut parallel to the apparent dip azimuth of the majority of faults in a given section, the overwhelming majority of faults in the core were measured. However, the dataset of oriented faults and fractures does not contain planes that were oblique, rather than perpendicular, to the slab face: these account for about 20% of all observed planar features. 6) The apparent dip and dip azimuth data so obtained were then rotated to account for the hole deviation, which in the cored interval was 22 degrees to the vertical in the 038 direction. Over four hundred data points were obtained in this fashion.

GEOLOGIC SETTING AND DESCRIPTION OF FAULTS

Geologic setting of the Pathfinder Well

The DOE-Pennzoil well in SEI Block 330, the Pathfinder, was drilled in a fault-bounded salt withdrawal minibasin of Plio-Pleistocene age (Holland et al, 1990; Alexander and Flemings, 1995). This minibasin hosts the giant South Eugene Island field, presently the largest producing field in offshore Gulf of Mexico and the largest Pleistocene oil field in the world. Production is primarily from rollover anticlines in a section of deltaic and fluvial sands, and the reservoirs are segmented into a number of fault blocks (op cit). This sequence of sands, interbedded with mudstones, overlies a thick (600-meter) mudstone and, below that, turbidite/slope fan deposits (Alexander and Flemings, 1995).

The main growth fault zone penetrated by the Pathfinder well (the 'A' fault zone) is seismically imaged from > 5 seconds to approximately 0.4 seconds; at shallower depths, it is not resolvable in the data (figure 2). The 'A' fault zone has a throw of approximately 600 meters at the level of the OI sand, just above where the Pathfinder intersected it, and displacement decreases approaching the surface. Based on stratigraphic evidence, the fault experienced its highest slip rate during deposition of the deltaic sand - shale sequence, between 1.8 and 1.2 Ma (Alexander and Flemings, 1995), but current activity of the fault is implied by its presence at the shallowest resolvable depths in seismic data and by oil seeps along its trace on the seafloor. The geometry of the fault and hangingwall deformation in SEI Block 330 are consistent with dip-slip normal movement, and preliminary data on well-bore breakouts from the Pathfinder well indicate a minimum horizontal compressive stress direction nearly perpendicular to the fault trace (Peter Flemings, Penn State Univ., 1995, oral comm.), again consistent with normal faulting with no discernible strike-slip component.

Fault zone geometry and displacement in the Pathfinder well

In the Pathfinder well, the upper bounding fault for the 'A' fault zone was intersected at 2325 meters driller's depth (DD), just below the OI-5 sand and 23 meters below the first appearance of the foraminifera *Robulus* 64 (1.8 Ma). This bounding fault has a dip of 53 degrees in the 213 (southwest) direction, according to the Formation MicroImager, and is about one meter thick in the well. Below this fault is a thick (>244 meters, to the bottom of the well at 2563 meters) section of variably faulted calcareous and non-calcareous silty mudstone, shaly silt, and rare sand, mostly as laminae but also, in one instance, in beds up to 25 cm thick. Using the paleontological picks (Table 1) and assuming a sedimentation rate of 1.3 mm/year for the *D. brouweri* - *Robulus* 64 interval (cf. Alexander and Flemings, 1995), an omission of about 67 meters of section across the

upper bounding fault at 2325 meters DD can be calculated, taking true bed thickness into account. The first appearance of *G. miocenica* (2.0 m.y.) at 2476 meters DD, below the bottom of the core, is consistent with an apparent sedimentation rate of 1.04 mm/yr in the *D. brouweri* - *G. miocenica* interval, which is within the range of expected sedimentation rates, thus implying a small net throw on all of the cored faults. In contrast, *D. pentaradiatus* (2.2 m.y.) appears at 2503 meters DD, consistent with an omission of about 240 meters of section between that marker and the *G. miocenica* marker just 27 meters higher in the well, again assuming that a sedimentation rate of 1.3 mm/year applies to this interval. Additional faults may lie below this depth, but are not discernible from the paleontological, FMI, or seismic data.

In contrast to the gentle northeast bedding dips determined from seismic data and well intercepts for strata above the main fault zone, the FMI log shows consistent moderate (20-40 degrees) north to northwest bedding dips below the main fault. Seismic and well top data from the upthrown block to the northeast of the fault zone indicate horizontal to gentle southwest dips. Thus, the cored portion of the Pathfinder well is best interpreted as a rotated horse between two or more faults, only the top one of which is evident on the seismic section (figure 2). The northwest component of dip azimuth observed on the FMI in the cored interval could be accounted for by a modest counterclockwise rotation (looking northeast) about an axis perpendicular to the plane of the upper bounding fault at 2325 meters; the northerly dips may be the result of rotation related to cross-faults that may lie within the faulted rock below the 'A' fault.

Nature of faults in core

Although we had drilled past the upper bounding fault before beginning to core, the core contains over 500 faults and provides much information about the nature and geometry of faults in the growth fault zone. In terms of physical appearance, there are two main types of faults logged in the core. The predominant type is a very thin to hairline slickensided fault across which displacement or truncation of beds can be observed in many cases (figure 3a). The slickensided fault surface is polished, and the slickenlines are very fine parallel grooves. Much less abundant than the "hairline" faults are gouge/breccia zones, which are up to 15 centimeters across in the core (figure 3b). In these, mudstone has been reconstituted into slickensided gouge that is slightly lighter colored than the adjacent mudstone and supports clasts of relatively undeformed mudstone up to 1.5 cm across, typically elongated parallel to the gouge foliation. A number of faults comprise zones up to 1 cm wide, mainly containing brecciated mudstone clasts with minor clay gouge infilling the interstices; these faults may represent a gradation between the two types above. No consistent cross-cutting relationships between sets of "hairline" faults is observed: shallowly-dipping faults cut steeply-dipping ones and vice versa, although the former situation is more common. However, the gouge zones, which typically dip shallowly to moderately to the southwest, are almost never cut by any later structures in the core and in fact truncate more steeply-dipping faults and fractures.

Several faults and fractures in the core are mud-filled, but no natural fracture fillings or mineralized fault breccia were observed, and few open fractures or faults were detected in situ on the FMI log. However, about 25 faults and fractures in the core fluoresced strong gold, indicating the presence of oil (figure 3c), and will be described later. In addition, a weak gas show (increase of 70 units above background) was recorded in faulted mudstone at the bottom of the core.

Orientation of faults in core

Three structural "domains" can be identified in the core on the basis of plots of depth vs fault dip and dip azimuth (figure 4). The upper and lower thirds (more or less) of the core contain faults having a wide range of dips, and their dip azimuths nearly span the compass. The middle third, in contrast, lacks shallow-dipping faults and faults whose dips

lie in the northeast quadrant; southeast-dipping faults are present but rare. The boundary between domains 1 and 2 in the core corresponds to a 15-cm wide gouge zone that dips shallowly to the southwest and separates calcareous mudstones above from non-calcareous mudstones below. This fault zone is also marked by a high density of fractures and faults. Within domain 2, faults are scarcer and the rocks are siltier progressing downhole; the few notable sand beds in the core lie in the interval of minimal fault/fracture density. Although no distinct fault boundary was observed between domains 2 and 3, the rocks of domain 3 are much shalier than those immediately above, the faults typically contain more gouge than those in domains 1 and 2, and the fault+fracture density is also much higher. All but one of the 25 oil-bearing faults and fractures lie in domain 3.

Utilizing the above breaks, the fault data were analyzed separately for each domain. Dip/dip azimuth lines were plotted on an equal-area lower hemisphere stereographic projection (figures 5a, b, c). The number of lines per 1% area was then corrected for the angle between the line and the borehole orientation (Terzaghi, 1965; Barton and Zoback, 1992), and the resultant dip-corrected dataset was contoured using spherical Gaussian statistics (Kamb, 1959). Each domain is characterized by a distinctive concentration of fault orientations. The faults in domain 1 are predominantly shallowly to moderately southwest dipping, although a weakly-developed set of east-dipping faults is also present (figure 5a). Domain 2 (figure 5b) consists predominantly of moderately- west to west-northwest-dipping faults. Domain 3 contains two well-developed populations of faults, one moderately to steeply west-dipping, the other shallowly dipping to the southwest (figure 5c). A lesser population of northeast-dipping faults is also present. The dip/dip azimuths of oil-bearing faults are also plotted individually on figure 5c: they do not appear to have an affinity for any particular population.

In contrast to the fault domains, fracture orientations do not appear to show systematic variations with depth (figure 6a). A stereographic projection of the total population of fracture dip/dip azimuth data, corrected for the angle between the diplane and the drillhole, as done for the fault data above, shows a single broad maximum dipping steeply to the west-northwest (figure 6b).

Geometric distribution of fault/fracture spacings

As a way of evaluating each domain with respect to its propensity to act as a fluid conduit, some simple analyses of fracture/ fault spacing in each domain were carried out. The depth of every planar discontinuity that intersected the centerline of the core was recorded, including those for which orientations were not derived; spacings between immediately adjacent structures were figured directly from these depths. Log-log plots of fracture/fault spacing vs the cumulative frequency of fractures/faults at or greater than a given spacing are, like the stereonet plots, distinctive for each domain. A plot of data using this transformation would be expected to yield a straight line for a power-law distribution of fracture/fault spacings (Gillespie et al, 1993). The data from domain 1 (figure 7a) cannot be well-fitted with a straight line over any significant range of spacings. Domain 2 spacings (figure 7b) can be fitted with a straight line if the spacings below 10 centimeters are considered to be under-sampled and thus dropped from the dataset; the correlation coefficient (r^2) for the remaining data is then 0.96, with a slope of 1.00. The validity of considering fracture/fault spacings under 10 centimeters to be under-represented is questionable, however, as the practice during logging of this core was to record all distinguishable fractures and faults. Even in massive mudstones, fractures or faults 10 centimeters apart are readily distinguishable from one another. The lower threshold of spacing resolution for the core as a whole is on the order of 5 cm: in well-laminated intervals, fractures and faults as closely spaced as 5 mm were mapped as separate features. Including fractures and faults as closely-spaced as 5 cm in the domain 2 dataset results in a poorer straight-line fit to the data, with a correlation coefficient of .926. Thus, the data for domain 2 do not appear to be well-characterized by a power-law distribution, or the

closely-spaced fractures and faults are characterized by much different statistics than are the more widely-spaced ones.

Fracture/fault spacing data from domain 3 (figure 7c) are well-fit by a straight line on a log-log cumulative frequency plot, using a lower spacing cutoff of 3 cm. The correlation coefficient for a straight line of slope 1.59 is 0.98, over a range of 1-1/2 orders of magnitude. The fracture/fault spacings in domain 3 clearly follow a power-law distribution.

The same data were also analyzed using an interval counting method. Intervals of varying sizes (d) were imposed on the core log, and the number of intervals (N) containing at least one fracture or fault was counted. Plots of $\log N$ vs $\log (1/d)$ yield linear slopes for power-law distributions (Barton, 1995). The data for domains 1 and 2 (figures 8a, 8b) are moderately characterized by such a distribution, having correlation coefficients of 0.98 and 0.97, respectively, for interval sizes greater than 30 cm; however, the data also show a weak but continuous curvature. The data for domains 1 and 2 depart significantly from a power-law distribution at sampling intervals less than 30 cm. This departure is not believed to be an indication of a lower limit of perceptibility, as fractures much closer than 30 cm apart were logged routinely, as noted above. Thus, the fracture spacing data from these two domains are not characterized by a power-law distribution. In contrast to domains 1 and 2, and consistent with conclusions drawn from the cumulative frequency vs spacing plots above, data for domain 3 (figure 8c) are well-fit by a straight line on a plot of $\log N$ vs $\log (1/d)$, yielding a slope of 0.88, with r^2 equal to 0.995 over 1-1/2 orders of magnitude of interval sizes. Analysis of residuals (Brooks, 1995) and incremental slopes between adjacent data points (Gillespie et al, 1993; Walsh and Watterson, 1993; Manning, 1995) corroborate the validity of a straight line fit to the domain 3 data.

Discussion

The above data demonstrate the structural complexity of a typical young growth fault zone in a mudstone-dominated section offshore Louisiana. Any conclusive interpretation for the cause of the uneven distribution of oil within the cored faults, as envisaged in the introduction to this paper, is greatly hindered by the fact that the drill hole is a one-dimensional sample of what is clearly a three-dimensional system. For instance, the presence of oil within domain 3 faults could be simply due to the proximity of an oil-charged sand in or adjacent to that particular fault zone near the Pathfinder well or to a locally complex fault pattern related to a nearby subsidiary fault. In fact, the structural data for domain 3 demonstrate the presence of two distinct fault sets, one of which is oblique to the main growth fault trend. The interaction of these fault sets would be expected to result in an interconnected set of fractures that could constitute a permeable pathway for fluid flow.

Overlaid on the structural complexity, however, the analysis of fault spacing data indicates there may also be intrinsic differences in fault mechanics between the three structural domains in the core, in that the oil-barren domains are also characterized by a "deficiency" of closely-spaced faults and fractures relative to a power-law distribution, in contrast to domain 3. Because it is unlikely that this behavior is an artifact of a lower limit of perceptibility, this geometric difference may in fact reflect a difference in the mechanics of faulting. As shown above, fault/fracture spacings of domain 3 are well-characterized by a power-law distribution, typical of "tectonic" faults/fractures documented elsewhere in consolidated rocks (Velde et al, 1991; Barton and Zoback, 1992; Gillespie et al, 1993; Barton, 1995). Departure from this behavior in domains 1 and 2 may reflect deformation of sediments whose material properties during faulting differed from those of consolidated rock, as suggested by Gillespie et al (1993). In this case, the faults in domains 1 and 2 may have been active earlier in the consolidation history of the sediment than were the faults of domain 3; the domain 3 faults could even be presently active.

Oxygen isotope data, from which one may derive temperature and thus depths at which water-rock interaction took place, were collected for calcite from two faults,

including the low-angle gouge zone that separates domains 1 and 2 (Table 2). This gouge zone contains an unusually high amount of calcite (up to 9 weight %, determined by X ray diffraction; Losh et al, 1994), which is primarily diagenetic in origin. The $\delta^{18}\text{O}$ values of this calcite are consistent with isotopic exchange with pore fluid having oxygen isotopic composition of 0 permil SMOW at temperatures of 14 to 22 C (fractionation equation of O'Neil et al, 1969). The fluid that circulated through the gouge zone precipitated calcite at temperatures not much higher than those that probably prevailed at the seafloor at the time, thus indicating isotopic exchange took place at shallow burial depth, early in the fault's history. Oxygen isotopic equilibration between calcite and fluid at present-day temperatures in the cored portion of the fault zone (about 65 C) would have produced distinctly-different calcite $\delta^{18}\text{O}$ values on the order of 21 permil, which are nowhere in evidence in the sampled faults in the core. Thus, the sampled faults in domains 1 and 2 have served as fluid conduits only early in the history of the growth fault zone, a finding consistent with the above interpretation of fault spacing data.

The coupling of relative timing of fault movement with the distribution of oil in faults, fractures, and sands in the core provides some insight into the timing and controls of oil migration relative to faulting. As was noted earlier, oil is present in all sands in the core, regardless of structural domain, but is (with one exception) present only in faults and fractures in domain 3. Furthermore, the stereograms illustrate the presence, in all three domains, of faults having "favorable" orientations for being oil-filled. The attitudes of faults that contain oil, a *de facto* indicator of favorable orientation, in domain 3 generally lie well within the population of fault orientations deduced for domains 1 and 2 (figure 5), but these features are barren of oil in those domains. Taken together, the above observations and interpretations indicate that: 1) faulting in domains 1 and 2 took place before the sands in those domains were charged with oil, 2) faults in domain 3 have been active more recently than those in domains 1 or 2, and may be active now, and 3) oil migration in the fault zone took place relatively late in the evolution of the growth fault, and may be occurring now. The relatively recent timing of oil migration into Block 330 reservoirs is indicated by organic geochemical and geologic studies (Whelan et al, 1994; Alexander, 1995). Thus, oil migration appears to have taken place within the same time interval as activity of faults in domain 3. The mere presence of favorably-oriented breaks, as defined above, did not appear to have enhanced oil migration in the upper two domains (cp Barton and Zoback, 1995). Rather, oil and gas migration in the fault zone probably took place only in those faults that were active when migratable hydrocarbons were available.

If fault-hosted oil migration was in fact restricted to the active part of the fault, some inferences may be made with respect to mechanisms of fluid migration within the fault zone. In particular, Anderson et al (1994) hypothesized that fluid ascent within the fault zone was described in terms of cycles of fluid pressure build-up followed by hydraulic fracturing, rapid fluid migration, fluid pressure dissipation, and ultimate closure of the fracture. In this interpretation, fluid migration up the fault is not directly linked to fault activity. However, the temporal linkage between oil migration and tectonic activity as described above, and the lack of migration via faults that were evidently inactive when oil flushed through the sediments, implies that deviatoric tectonic stress sufficient to produce failure was a major control on fracture and fault permeability in the Pathfinder core, and that fluid pressures alone were never sufficient to hydraulically open fractures.

Conclusions

The Pathfinder core provides a detailed traverse through much of a major growth fault which is believed to have played a significant role in migration of hydrocarbons from deep to shallower levels. Detailed logging of the core shows that this growth "fault" is a zone at least 100 meters thick and that it consists in the core of three distinct domains, each characterized by its own distribution of fault orientations and fault/fracture spacings. Except for the upper bounding fault, only the faults in the lowest of the domains are known to

contain oil. This domain is also characterized by a more complex fault pattern and is well-described by a power-law distribution of fault/fracture spacings, in contrast to the other domains whose faults contain no oil. Both faulting and oil migration appear to have taken place in the same relatively recent time interval in domain 3, whereas faulting probably preceeded oil charging of sands in the other two domains. The restriction of oil-bearing faults to the youngest portion of the fault zone, and their absence from portions of the fault that were active before migration, points toward fault activity as a major controlling factor on oil migration in the faults sampled by the Pathfinder core.

Acknowledgements

Funding for this work was provided by the Global Basins Research Network and Dept. of Energy grant DC-FC22-93BC14961 to Roger Anderson, Lamont-Doherty Earth Observatory. I especially thank Pennzoil Exploration and Production Co, without whose involvement the Pathfinder Well would not have been drilled. Paleontological analysis was carried out by Ardy Callender and Bernie Shaffer, Applied Biostratigraphix, Houston, and elucidated by Denise Butler, Pennzoil. Formation MicroImage interpretation was performed by Laura Foulk, Schlumberger, and Bruce Hart assisted with core logging. I thank Bruce Malamud, Ben Brooks, and Prof. Don Turcotte for assistance with statistical analysis. Any shortcomings in interpretation are my own.

REFERENCES

- Alexander, L., 1995, Ph.D. thesis, Cornell University
- Alexander, L., Flemings, P., 1995, Geologic evolution of a Plio-Pleistocene salt withdrawal mini-basin, Eugene Island South Addition, Block 330, offshore Louisiana; Amer. Assoc. Petrol. Geol. Bull.
- Anderson, R., 1993, Recovering dynamic Gulf of Mexico reserves and the U.S. energy future; Oil and Gas Jour., April 26, p. 85-91
- Anderson, R., Flemings, P., Losh, S., Austin, J., Woodhams, R., 1994, Gulf of Mexico growth fault drilled, seen as oil, gas migration pathway; Oil and Gas Jour., June 6, pp. 97-103
- Barton, C.C., 1995, Fractal analysis of scaling and spatial clustering of fractures, in Barton, C.C., and LaPointe, P., eds., Fractals in the Earth Sciences, Plenum Press, New York, pp. 141-178
- Barton, C.A., Zoback, M.D., 1992, Self-similar distribution and properties of macroscopic fractures at depth in crystalline rock in the Cajon Pass scientific drill hole; Jour. Geop. Res., vol 97, pp. 5181-5200
- Barton, C.A., Zoback, M. D., Moos, D., 1995, Fluid flow along potentially active faults in crystalline rock; Geology vol. 23, pp. 683-386
- Brooks, B., 1994, Fractal clustering of metamorphic veins: Comment; Geology, v. - pp. 1147-1148
- Friedheim, J., Hans, G., Park, A., Ray, C., 1991, An environmentally superior replacement for mineral-oil drilling fluids; Soc. Petrol. Eng. preprint SPE 23062, pp. 299-312
- Galloway, W., Henry, C., Smith, G., 1982, Depositional framework, hydrostratigraphy, and uranium mineralization of the Oakville Sandstone (Miocene), Texas Coastal Plain. Univ. of Texas at Austin Bur. of Econ. Geol. Rept. of Investigations 113, 51 pp.
- Gillespie, P., Howard, C., Walsh, J., Watterson, J., 1993, Measurement and characterisation of spatial distributions of fractures; Tectonophysics, vol. 226, pp. 113-141
- Hippler, S., 1993, Deformation microstructures and diagenesis in sandstone adjacent to an extensional fault: Implications for the flow and entrapment of hydrocarbons; Amer. Assoc. Petrol. Geol. Bull., vol. 77, pp. 625-637.
- Holland, D., Leedy, J., Lammlein, D., 1990, Eugene Island Block 330 field - U. S. A., offshore Louisiana; in Beaumont, E., and Foster, N., eds., Structural Traps III: Tectonic Fold and Fault Traps; Amer. Assoc. Petrol. Geol. Treatise of Petroleum Geology, pp. 103-143
- Hooper, E. C. D., 1991, Fluid migration along growth faults in compacting sediments; Jour. Petrol. Geol. vol 14, pp. 161-180
- Jones, P., Wallace, R., Jr., 1974, Hydrogeologic aspects of structural deformation in the northern Gulf of Mexico basin; Jour. Res. U.S. Geol. Surv., vol 2, pp. 511-517
- Kamb, W., 1959, Ice petrofabric observations from Blue Glacier, Washington, in relation to theory and experiment, Jour. Geop. Res., vol. 64, pp. 1891 - 1910
- Kulander, B., Dean, S., Ward, B., Jr., 1990, Fractured Core Analysis: Interpretation, Logging, and Use of Natural and Induced Fractures in Core; Amer. Assoc. Petrol. Geol. Methods in Explor. Series, vol. 8, 88 pp.
- Losh, S., Eglinton, L., Wood, J., 1994, Coring and inorganic geochemistry in the Pathfinder Well, in Anderson, R., Billeaud, L., Flemings, P., Losh, S., and Whelan, J., Results of the Pathfinder Drilling Program into a Major Growth Fault: Part of the GBRN/DOE Dynamic Enhanced Recofery Project in Eugene Island 330

- Field, Gulf of Mexico; Annual Report (CD-ROM) to DOE, contract no. DE-FC22-93BC14961, pp. 183-249.
- Manning, C., 1994, Fractal clustering of metamorphic veins: Reply; *Geology*, vol. - , pp. 1148-1149
- O'Neil, J., Clayton, R., Mayeda, T., 1969, Oxygen isotope fractionation in divalent metal carbonates; *Jour. Chem. Phys.*, v. 51, pp. 5547-5558
- Terzaghi, R., 1965, Sources of error in joint surveys; *Geotechnique*, vol. 15, pp. 287-304
- Velde, B., Dubois, J., Moore, D., Touchard, G., 1991, Fractal patterns of fractures in granites; *Earth Planet. Sci. Lett.*, vol. 104, pp 25-35
- Walsh, J., Watterson, J., 1993, Fractal analysis of fracture patterns using the standard box-counting technique: Valid and invalid methodologies; *Jour. Struct. Geol.* v. 15, pp. 1509-1512
- Weber, K., Mandl, G., Pilaar, W., Lehner, F., Precious, R., 1978, The role of faults in hydrocarbon migration and trapping in Nigerian growth fault structures; Tenth Annual Offshore Technology Conference Proc., vol 4, pp. 2643-2653 (OTC 3356)
- Whelan, J., Eglinton, L., Requejo, R., Kennicut, M., 1994, Pathfinder Well organic geochemistry: Indicators of oil source and maturity and fluid flow mechanisms, in Anderson, R., Billeaud, L., Flemings, P., Losh, S., and Whelan, J., Results of the Pathfinder Drilling Program into a Major Growth Fault: Part of the GBRN/DOE Dynamic Enhanced Recovery Project in Eugene Island 330 Field, Gulf of Mexico; Annual Report (CD-ROM) to DOE, contract no. DE-FC22-93BC14961, pp. 616-662.

FIGURES

- Figure 1. Location of Pathfinder Well. Structure contours are on top of OI-1 sand (from Holland et al, 1990).
- Figure 2. Seismic dip line including trace of Pathfinder Well, showing selected reservoir sands and faults intersected by well path. Coring began just below 'A' fault.
- Figure 3. Faults in core: a) planar "hairline" faults offsetting laminated mudstone at 2442 - 2442.3 m (8010-8011 ft) DD, b) clay gouge zone at 2425.8 m (7956.7 ft) driller's depth, c) faulted interval at 2421.6 - 2422 m (7943-7944) ft in ordinary (left) and ultraviolet (right) light. Oil-bearing sand is nearly horizontal in photo; fluorescent fractures cross bedding and contain oil. Rulers to left of each core are in 0.1-foot increments.
- Figure 4. Structural variations in cored interval as a function of depth. From left to right: bedding dip and dip azimuth; gamma ray log, showing predominantly mudstone; fault azimuth and dip amount; and fault/fracture density expressed as number of features per five-foot interval. Three structural domains are delineated on the basis of well-defined breaks in the fault dip/dip azimuth vs depth plots.
- Figure 5. Lower-hemisphere Kamb plots for data from a) domain 1, b) domain 2, c) domain 3. Stereonet program of Rick Allmendinger, Cornell University.
- Figure 6. a) Fracture dip azimuth vs depth. No breaks in these data correlative to the fault domains are seen. b) Kamb plot of fracture dip/dip azimuth data (program of Rick Allmendinger, Cornell University).
- Figure 7. Log - log plots of spacing between adjacent faults/fractures vs cumulative frequency of spacings equal to or greater than a given value for a) domain 1, b) domain 2, and c) domain 3.
- Figure 8. Log (number of filled intervals) vs. log of inverse of interval width for a) domain 1, b) domain 2, c) domain 3, d) total core.

Table 1. Summary report of paleontological analysis from cuttings for Eugene Island Block 330 A20ST (Pathfinder) well

Sample range 1259 - 2563 meters
 Foram analysis by Ardy Callender
 Nannofossil analysis by Bernie Shaffer

1259 meters	First sample analyzed
1268	In small Gephyrocapsa (abundant cement)
1287	First Trim A
1314	Large Gephyrocapsa
1424	Stilostemella antillea (deeper water equivalent to Trim A)
1524	Hyalinea balthica with Globigerina. incisa (planktic equiv. to Hyal B.)
1524	Scyphosphaera pulcherrima
1534	H. sellii
1561-1854	Zone of low abundance and diversity
1854-1890	Moderate abundance still in H. sellii
1890-2018	Low abundance
1863	First Angulogerina B (rare)
2018	Significant fauna increase and the first slope deposits
2027	C. macintyreii
2046-2073	Zone of very abundant shell fragments/mollusk hash and abundant Amphistegina deposited into a mid-outer shelf environment
2302	First Rob 64 (rare)
2329	Faunal change with sudden increase in Rob 64 likely top of fault)
2348	Abundance peak with Discoaster brouweri "A". Significant increase in pyrite with an increase of fauna by 2-3x
2476	Globorotalia miocenica
2503	Discoaster pentaradiatus (rare)
2563	TD

Table 2. Selected oxygen isotope data, Pathfinder Well

Sample depth (DD)	$\delta^{18}\text{OSMOW}$	Comments
2352.18 m (7717.79 ft)	29.1	Gouge/breccia zone, dips 30-40 SE
2352.92 m (7717.6 ft)	29.0	Do.
2358.41 m (7735.6 ft)	30.8	Gouge, dips 25-40 SW, boundary
2358.51 m (7735.9 ft)	30.7	Between fault domains 1 and 2
2358.57 m (7736.1 ft)	30.9	Do.

Water - Rock Interaction in a Large Growth Fault, South Eugene Island Block 330 Field, Offshore Louisiana

Steven Losh

Dept. of Geological Sciences, Cornell University, Ithaca, NY

Lorraine Eglinton

Dept. of Chemistry, Woods Hole Oceanographic Institution, Woods Hole, MA

James Wood

Dept. of Geological Sciences, Michigan Technological University, Houghton, MI

ABSTRACT

We examined whole core, sidewall core, and cuttings from seven wells that penetrated a large growth fault abutting the Plio-Pleistocene South Eugene Island Block 330 field, offshore Louisiana, for evidence that the fault acted as a conduit for fluid flow into the prolific reservoirs. The analytical program was designed to deduce mass and heat flux within the fault zone, and focused on comparing a variety of measurements on faulted and unfaulted rocks. Data include vitrinite reflectance and spore fluorescence measurements, standard petrographic and cathodoluminescence techniques, Rock-Eval pyrolysis, oxygen and carbon isotopic analysis, determination of bulk mineralogy and illite/smectite ratio by X-ray diffraction, and whole-rock major element and trace element geochemical determinations.

Rocks within and adjacent to the fault zone in the D.O.E.-Pennzoil Pathfinder well, taken at about 2226 - 2317 meters (7300 - 7600 feet) TVD, were characterized by low vitrinite reflectances, averaging 0.3%Ro, yellow to yellow-green spore fluorescence colors, moderate to high $\delta^{18}\text{O}$ and $\delta^{13}\text{C}$ values ($\delta^{18}\text{O}$ of calcite in faulted rocks ranged from 28 to 31 permil SMOW, with $\delta^{13}\text{C}$ from 0.8 to -3.1 permil PDB), and, except for slight increases in K_2O , CaCO_3 , and Zn in some faulted samples, no differences in major or trace element composition between deformed and undeformed sediments. The lowest $\delta^{18}\text{O}$ value, 21.8 permil, was from a calcite-cemented siltstone 11 meters above the fault. The rocks were characterized by illite/illite+smectite ratios between 40% and 60%, unexpectedly high considering the low maturity of organic matter, and in most cases, there is no distinction between faulted and unfaulted rocks in terms of mineral assemblage or relative abundance. One gouge zone contained calcite in excess of that in the average mudstone, but oxygen and

carbon isotopic data, noted above, indicate the calcite precipitated at shallow burial depth.

Rocks from the A6ST well, which intersects the 'A' fault about 300 meters northwest of the Pathfinder at 1980 meters (6500 feet) TVD, exhibit higher vitrinite reflectances, averaging 0.55% Ro in the 'A' fault decreasing to 0.4%Ro at a distance of 50 meters (160 feet) above the top of the fault, yellow-orange to orange spore fluorescence colors, a distinct $\delta^{18}\text{O}$ and $\delta^{13}\text{C}$ shift to lower values (22.4 and -9 permil, respectively) at the top of the fault, and, like the Pathfinder, little evidence of mass influx into the sampled fault rocks. There are no observed mineralogical differences between faulted and unfaulted rocks, and the illite/illite+smectite ratios are a subject of dispute: one laboratory obtained a range of 40-55%, averaging 44%, whereas another obtained a range of 23-35%, averaging 27%, from samples from the same interval within the fault zone.

Based on the existing data, the 'A' fault in the Pathfinder is concluded to have transmitted little fluid from depth, whereas the same fault in the A6ST well appears to have been a conduit for ascent of a substantial amount of fluid.

Introduction

High-angle faults in sedimentary basins may be expected to play a significant role in hydrocarbon migration from deep, overpressured reservoirs and "kitchens" to shallower reservoirs from which they can be economically produced. A number of studies have documented indirect and direct evidence of large scale, cross-formation fluid flow along growth faults (Jones and Wallace, 1974; Weber et al, 1978; Hippler, 1993; Galloway et al, 1982, review of Hooper, 1991). While these examples provide valuable information about processes that affect such flow and also give permissive evidence that large volumes of hydrocarbons may migrate in such a fashion, there has remained a large uncertainty as to the actual connections between fault-conduit fluid flow and the filling of economically-producible oil and gas reservoirs. A clear understanding of fault charging could be extremely valuable as a prospect evaluation criterion. Although many reservoirs are spatially associated with faults, what role do the faults really play in charging of the reservoirs? Do some faults, or portions of faults, act as hydrocarbon migration conduits, while others do not? If fault charging does occur, what controls fluid migration up such faults and into the reservoirs?

In order to develop and test answers to these questions, the Global Basins Research Network, a consortium of universities and industry affiliates, undertook a multifaceted U. S. Department of Energy - funded project in South Eugene Island Block 330, offshore Louisiana, having the twin goals of simultaneously drilling and sampling a large, active growth fault and carrying out a variety of analyses of rocks, brines, and oil and gas from reservoirs adjacent to the fault. The centerpiece of this project was the Pathfinder well, drilled into the main fault bounding a salt withdrawal minibasin of Plio-Pleistocene age (Holland et al, 1990; Alexander and Flemings, in press). This minibasin hosts the giant South Eugene Island field, presently the largest producing field in offshore Gulf of Mexico and the largest Pleistocene oil field in the world. Production is primarily from rollover anticlines in a section of deltaic and fluvial sands, and the reservoirs are segmented into a number of fault blocks (op cit). This sequence of sands, interbedded with shales, overlies a thick (600-meter) shale and, below that, turbidite/slope fan deposits (Alexander and Flemings, in press). This particular location was selected because of a variety of evidence supportive of recent (even ongoing) reservoir filling linked to the bounding fault system (Anderson, 1993). The fault was drilled and cored as an extension of a Pennzoil infill development well (the A20 sidetrack: figure 1) in the fall of 1993, a variety of logs were

run and measurements made, and the fault was drill-stem tested as a potential reservoir (Anderson et al, 1994, 1995).

Geochemical research on rocks from Block 330 has focused on ascertaining chemical and thermal signatures of fluid thought to have ascended the main growth fault (the 'A' fault) and flowed into reservoir sands. This paper presents petrographic, mineralogic, stable isotopic, and bulk geochemical data from fault zone samples from the Pathfinder well, the A6ST well, which also penetrated the 'A' fault, and several other wells along the 'A' fault (figure 1). Whole coring was carried out in the Pathfinder well in order to continuously sample a major growth fault abutting the Block 330 reservoirs. Continuous sampling, as opposed to sidewall coring, across the fault zone was considered important in that many features related to fluid flow in fault zones typically vary greatly over distances of centimeters. Thus, we attempted to obtain as much whole core as was practical, and recovered 109 meters (343 feet) of 10.2-cm (4-inch) diameter core in unfaulted to highly faulted rock, primarily mudstone. Sidewall cores were taken above the cored interval in order to evaluate evidence for fluid flux within the main 'A' fault, which was not cored, as well as in the downthrown block to the fault zone.

Analytical procedures

Vitrinite reflectance measurements were carried out on three different types of samples: 1) kerogen concentrate samples, cold set in epoxy resin and polished in accordance with ICCP protocol (1963, 1971); 2) thin sections, prepared in accordance with the methods of Stach (1982), and 3) polished blocks of sediment. In whole-rock samples, an "operator selective approach" ("European method" of Mukhopadhyay, 1992) is used, whereby morphology, color, relief, quality, internal structure and other characteristics are used to identify vitrinite particles indigenous to the sediment (Plates 1 and 2). The whole rock approach is preferred for Gulf Coast sediments since one can distinguish autochthonous vs. allochthonous vitrinite, bitumen populations, cavings, and drilling contaminants. Rather than measuring a wide range of reflectances on a variety of macerals and then selecting the dominant or lowest-reflectance population as indicative of vitrinite maturity, as is frequently done for kerogen concentrates, we believe that more-reliable results can be obtained from these organic-lean, immature sediments by measuring fewer but better-characterized vitrinite particles in whole-rock mounts (Barker and Pawlewicz, 1993).

Vitrinite reflectance was measured using a Zeiss standard universal research microscope-photometer system (MPM01K) equipped with a tungsten-halogen lamp (12V, 100W), a x40 Epiplan oil immersion objective, filtered 546 nm incident light, and Zeiss immersion oil (n_D 1.517 @ 23C). Three standards are measured in triplicate before analysis and every 30 minutes once analysis commences. Blue light fluorescence observations on spores (Mukhopadhyay, 1992) was performed on the same microscope fitted with a high-pressure mercury lamp (HBO100) for autofluorescence and an LP520, BP450-490 filter system.

Illite/smectite ratios were determined at Michigan Technological University on the <2 μ m fraction, with selected samples further separated to <1 μ m. Samples from each size fraction were mounted on ceramic plates using a vacuum pump apparatus, with XRD analysis carried out on an automated Dapple/Norelco machine using $\text{CuK}\alpha$ and 1 degree slit size at a counting time of 2 seconds per step. Samples were then solvated with ethylene glycol in a desiccator for 24 hours at room temperature. Identification of I/S and estimation of percent expandables were made from techniques described by Moore and Reynolds (1989). A similar procedure was followed at Exxon Production Research for samples analyzed there.

Sample preparation and analysis for carbon and oxygen isotopic analysis of whole-rock carbonate was carried out by Krueger Enterprises, Cambridge, Mass. Carbon dioxide

was liberated from the calcite by reaction with phosphoric acid at 90 C. Several calcite+dolomite samples were analyzed by timed extraction: a CO₂ sample was taken from the reaction vessel at 20 minutes, and is taken as representative of the isotopic composition of calcite, and a second sample was collected at 3 hours after initiation of reaction, and is taken to represent dolomite.

Whole - rock multielement geochemical analyses of whole core and sidewall core samples were obtained by X Ray Assay Labs, in Don Mills, Ontario. Major elements, Cl, Cr, Sn, Rb, Sr, Y, Zr, Nb, Ba, and LOI were analyzed by X-ray fluorescence, rare earths by neutron activation, S by LECO, and Li, Be, B, V, Co, Ni, Cu, Zn, Ge, Mo, Ag, Cd, Pb, and Bi by ICP spectroscopy. Gold, platinum, and palladium were analyzed by fire assay with DCP spectroscopy finish, but were found to be below the detection limits of 1, 1, and 10 ppb respectively. Major element oxides are computed without consideration of LOI or H₂O⁺/H₂O⁻. For all plots, BaSO₄, taken as a tracer of drilling mud, is corrected for in samples having greater than 10,000 ppm Ba

THE PATHFINDER WELL

General geology

In the Pathfinder well, the first detectable fault in the 'A' fault zone was intersected at a measured driller's depth (DD) of 2325 meters (7625 feet), after drilling through a 15-meter thick section of tilted sands and shales of the OI-5 sand. According to the Formation MicroImager, the main fault has a dip of 53 degrees in the 213 (southwest) direction, and is about 120 centimeters thick in the well. Below this fault is a thick (>245 meters, to the bottom of the well at 2563 meters (8405 feet) DD) section of faulted and unfaulted calcareous and non-calcareous silty mudstone, shaly silt, and rare sand. In contrast to the gentle northeast bedding dips determined from seismic data and well intercepts for strata above the main fault zone, the FMI log shows consistent moderate (20-40 degrees) north to northwest bedding dips below the main fault. Seismic and well top data from the upthrown block northeast of the fault zone indicate horizontal to gentle southwest bedding dips. Thus, the cored portion of the Pathfinder well is best interpreted as a rotated horse between two or more major faults, only the top one of which is evident on the seismic section.

The core was taken from 2332 - 2442 meters (7650-8012 feet) DD, within the interval defined by Robulus 64 (1.8 Ma), first encountered at 2303 meters DD, and Globorotalia miocenica (about 2 Ma), first encountered at 2476 meters. The average sedimentation rate of 0.7 mm/yr calculated for the above faulted interval is about half the 1.3 mm/yr rate calculated by Alexander and Flemings (in press) for unfaulted shales of this age elsewhere nearby in the minibasin, and is consistent with a stratigraphic omission on the order of 120 meters due to faulting in this interval.

Lithology and structure

The core consists of three lithologic "domains" that correspond to structural domains in the core, described elsewhere (figure 2; in review). The uppermost 26.2 meters of core consists primarily of slightly to moderately calcareous, predominantly medium gray laminated to massive silty shale (mudstone) to shaly silt, also sampled by sidewall cores above the fault. The next 47 meters of core are significantly siltier but non-calcareous, and the thickest sand beds, up to 22 centimeters, are found in this interval. The bottom 36.6 meters comprise laminated, non-calcareous silty shale with only a paucity of sand. Siderite concretions to 4 cm in diameter are common. The boundary between domains 1 and 2 is a low-angle gouge zone at 2358.5 meters (7736 feet) DD that was sampled as part of this study. Oil was found almost exclusively in faults and fractures in the deepest structural/lithologic domain in the core.

The fault zone partly sampled by the core is believed to have a total throw on the order of 600 meters at the depth of the core (Alexander and Flemings, in press). The FMI log shows faults both above and below the cored interval, and paleontological data suggest that the cumulative throw on faults in the core is relatively minor. Nonetheless, the core contains over 500 faults and fractures, which are of two types: very thin slickensided, polished "hairline" faults that display mm to tens of cm of offset in the core and that have a range of orientations, and slickensided gouge/breccia zones to 15 cm thick that are of indeterminate offset and that have low to moderate dips to the southwest.

Petrography, Mineralogy, and Vitrinite Reflectance

Petrographic examination of faulted shale from the whole core and sidewall cores shows a variety of structures: microshears defined by bands of rotated clay from tens to a couple of hundred microns wide, rotated blocks bounded by microshears, and microduplex structures. In terms of cathodoluminescence, calcite/dolomite in these rocks comprises two populations: angular, bright red-orange luminescing calcite and redder dolomite grains that appear to be detrital, and subangular to subhedral dull red-orange luminescent ferroan calcite grains that are disseminated throughout the rock and in some instances lie in fractures. This latter type of calcite is believed to be authigenic. Foraminiferal calcite tends to be non-luminescent.

X-ray diffraction of shales from the core and sidewall cores was carried out at Exxon Production Research and Shell's Bellaire Laboratory, with one sample analyzed by Fourier Transform Infrared spectroscopy (FTIR) at Core Labs (figure 3). The eleven shales consist primarily of clay (42 to 71%) and quartz (21 to 37%), and contain between 6 and 17% combined feldspars and a few percent calcite (0-9%). Clay and K-feldspar are negatively correlated. Only one sample had detectable dolomite, and one had detectable pyrite. Samples from within or near fault zones (7631, 7635-7636.1, 7734.9) tended to have more calcite than samples farther than a few feet from a known fault (7612, 7657), although the sidewall core at 2317.4 meters (7601 feet) consists largely of authigenic calcite. The fault at 2358.5 meters (7736 feet) separates calcareous rocks above from non-calcareous ones below, and no sample below 2358.5 meters has more than trace amounts of calcite, regardless of position with respect to faults.

Clay mineralogy has been determined for a number of samples, both in terms of bulk mineralogy and smectite-illite ratios in the mixed-layer clays. The former was primarily performed at Exxon Production Research, Houston, with one sample analyzed at Shell Bellaire Labs, Houston. Smectite-illite ratios (Table 1) were determined primarily at Michigan Technological University, with four samples analyzed at Exxon Production Research. Clays are predominantly mixed-layer smectite-illite (60-69%; four samples), with lesser detrital illite (16-22%), kaolinite ((14-17%), and chlorite (1-2%). Overall, smectite/(smectite+illite) ratios in the <2 micron glycolated fraction from cuttings, sidewall cores, and the whole core show an gradual increase in I/S from about 30-40% at depths of 1200-1500 meters (4000 to 5000 feet) to 45-60% deeper in the hole (figure 4). The shift to intermediate I/S ratios at depth is permissible given the bottom-hole temperature on the order of 70 to 75 degrees C (Abercrombie et al, 1994; J. Boles, oral comm., 1994)), although these ratios are not normally observed in rocks below temperatures on the order of 100 C (Hower et al, 1976; Milliken, 1985). However, the relatively high I/S ratios higher in the well (most published profiles for Plio-Pleistocene rocks show I/S ratios on the order of 20-30% at the depths of the Pathfinder well) suggest the initial composition of the smectite may favor transformation at lower temperature than usually observed. The elevated I/S ratio is probably not an effect of pore fluid chemistry, if the brine samples (Losh and Wood, 1995) are representative of fluids that interacted with the fault rocks. If anything, the potassium concentration is low (on the order of 300 mg/L), and the Na and Mg concentrations are high (ca 40,000 and 1500 mg/L, respectively), which should

suppress the smectite to illite transformation rather than enhance it (Huang et al, 1993). Work is continuing on this issue.

Vitrinite reflectance measurements (table 2) were made at Woods Hole Oceanographic Institute (WHOI); details concerning sample preparation and analysis procedure are provided in Appendix 1 and examples of material analyzed are shown in Plate 1. Reflectance measurements were made on a variety of macerals, allowing distinction to be made between reworked and "indigenous" vitrinite, with indigenous vitrinite reflectance measured on telocollinite.

In the Pathfinder well, indigenous vitrinite reflectance ranged from 0.25%Ro to 0.47%Ro (figure 5). The highest-reflectance sample comprised 2 readings: excluding this sample, the maximum reflectance was 0.37% Ro. Reflectance increases slightly with depth, and shows no increase relative to known faults at 2325 meters (7625 feet DD) (A fault) and 2055 meters (6741 feet) (B fault). In addition, no petrographic evidence of oxidation or bitumen impregnation was observed. The vitrinite reflectance values are in accord with burial along a normal (20-25 C/km) geothermal gradient and do not allow for anomalous heating related to the fault zones. Yellow and yellow-green spore fluorescence colors corroborate the low thermal maturity of the sediments indicated by the vitrinite reflectance data.

Pyrolysis

Pyrolysis Tmax data were also obtained at Woods Hole on some of the same samples analyzed for vitrinite reflectance, using a Chemical Data Systems pyroprobe system interfaced for computer data acquisition and processing. Tmax data in general covaries with vitrinite reflectance, although they indicate a somewhat higher thermal maturity in terms of equivalent vitrinite reflectance than do the actual reflectance measurements (figure 6). Elevated Tmax values for the Pathfinder well are commonly associated with organic assemblages containing greater than 60% reworked vitrinite and inertinite particles, and so may not be indicative of actual thermal maturity of the rocks themselves. In addition to providing evidence concerning thermal maturity, the pyrolysis measurements give evidence of migrated hydrocarbons in the form of P1 peaks on pyrograms from the sidewall and whole core samples (figure 7). Nearly all sidewall cores from the reservoirs penetrated by the Pathfinder well show enhanced P1 peaks indicative of migrated hydrocarbon; however, the fault zone samples show no such peaks.

Stable isotopes

Oxygen and carbon isotope data have been obtained from whole-rock shale samples taken from fault zones and undeformed shales near the faults (table 3). As expected, the $\delta^{18}\text{O}$ values of dolomite and calcite from the same samples differ by several permil, but the minimum $\delta^{18}\text{O}$ value of the calcite obtained in this manner is virtually the same as that of the lowest - $\delta^{18}\text{O}$ calcite + dolomite sample, indicating that the $\delta^{18}\text{O}$ values of the calcite + dolomite mixtures are reasonably representative of the calcite $\delta^{18}\text{O}$. Because of the extremely fine-grained, disseminated nature of the calcite, separate samples of distinct cathodoluminescent character cannot be made. However, the isotopic composition of a shale containing both types of calcite and dolomite must be a mixture of the two end-point compositions of detrital and diagenetic carbonate, and thus useful information about the isotopic composition of diagenetic calcite + dolomite (which is of the greatest interest) can be obtained from the presence or absence of an isotope shift from values in equilibrium with seawater at seafloor temperatures. Re-equilibration with higher-temperature fluid during burial would produce a shift to lower $\delta^{18}\text{O}$ values, which, even in a mixed sample, will be observable in the data.

In the case of samples from the Pathfinder whole core and sidewall cores, oxygen isotopic composition of calcite and calcite + dolomite mixtures ranges from 21.8 to 31.1 permil relative to SMOW, with no observable distinction in calcite $\delta^{18}\text{O}$ between undeformed and highly sheared samples at a given location (figure 8a). Calcite from sidewall cores near or in the 'A' fault at 2325 meters (7625 feet) DD yield $\delta^{18}\text{O}$ values between 26.3 and 28.2 permil, slightly shifted to lower $\delta^{18}\text{O}$ values relative to the deeper fault zone and to undeformed shales above and below the fault. Calcite from undeformed calcite-cemented shale around 2317 meters (7600 feet) (logger's depth) yields the lowest $\delta^{18}\text{O}$ values of all, at 21.8 permil. Calcite-cemented intervals are commonly known above fault zones in the Gulf of Mexico, and these samples probably represent such an occurrence. Carbon isotopic composition of calcite ranged from -0.7 to -9.5 permil relative to PDB; the low- $\delta^{13}\text{C}$ value for the sample having $\delta^{18}\text{O}$ of 31.1 permil may reflect contamination from epoxy, owing to the non-reproducibility of the value (a second analysis of this sample gave a $\delta^{13}\text{C}$ value of -8.2 permil), or, less likely, it may indicate some of the calcite in that sample was precipitated from water containing oxidized methane or "kerogenic" CO_2 at or near the seafloor. Generally, the carbon isotopic composition of the calcite is typical of normal marine shell and foraminiferal material, and is largely independent of $\delta^{18}\text{O}$ (figure 8b). On average, calcite $\delta^{13}\text{C}$ in faulted rocks is slightly higher than in undeformed ones (-1.7 permil vs -2.5 permil).

In a well-developed gouge zone at 2358.5 meters (7736 feet) (data in figure 8a), both $\delta^{18}\text{O}$ and $\delta^{13}\text{C}$ of calcite are typical of values in equilibrium with seawater at seafloor (10-20 C) temperatures, and, particularly in the case of the oxygen isotope data, do not reflect re-equilibration with, or precipitation from, higher-temperature fluids during burial. Even if the sediment were buried as a closed system, with only pore fluid available to exchange with calcite as temperature increased, an ^{18}O shift would be observed as a result of moderate to high water-rock ratio: volumetrically, pore fluid occupies about 25% of the rock, whereas calcite + dolomite, considered to be the only phases to exchange significantly (by recrystallization) with fluid at these low temperatures, comprise only 2 to 3% of the rock, leading to a volumetric water/rock ratio (W/R) on the order of 10, or an oxygen water/rock ratio of about 7. Even if clays were considered to exchange freely with water, the W/R would on the order of 0.5, still sufficient to produce a significant shift in calcite $\delta^{18}\text{O}$ during closed-system exchange during burial. At 70 C and W/R of 0.5, equal to an oxygen W/R of 0.35, calcite initially at 30 permil in the closed system described above would exchange with pore fluid and equilibrate to a $\delta^{18}\text{O}$ value of 27.4 permil (fractionation of O'Neil et al, 1969). As the calcite $\delta^{18}\text{O}$ values from the fault at 2358.5 meters show no shift away from "pristine", seawater-equilibrated values, even resulting from closed-system exchange with pore fluid, they are interpreted to have been precipitated at low temperature, thus, at shallow burial depth. Since calcite is easily exchanged under ambient conditions by recrystallization, its high $\delta^{18}\text{O}$ indicates a lack of influx of even locally-derived fluid, which implies inactivity, in this fault during most of its burial history.

Along similar lines, calcite in the sidewall cores taken near the 'A' fault is only weakly shifted in $\delta^{18}\text{O}$ from unexchanged values of about 30 permil (figure 8a), and reflects minor interaction with fluid during burial and/or faulting. The lowest- $\delta^{18}\text{O}$ samples, from 2317.4 meters (7601 feet), reflect interaction with aqueous fluid at or near present-day temperatures, as indicated by their near-agreement with the modeled ^{18}O equilibrium trend for burial diagenesis at a geothermal gradient of 22 C/km, comparable with that observed presently in the Pathfinder well. As will be shown in the next section,

the calcite $\delta^{18}\text{O}$ values appear to correlate with "sandiness" of the sediment rather than with proximity to shear zones. In no case do the oxygen isotopic data reflect equilibration with ambient pore fluid at temperatures higher than those attributable to a normal geothermal gradient; if that were the case, the $\delta^{18}\text{O}$ values would lie to the left of the "equilibrium line" in figure 8. However, it is possible that, because the isotopic values were measured on whole-rock samples that include a mixture of detrital and diagenetic carbonate, a low- $\delta^{18}\text{O}$ authigenic population exists and that it is masked by the presumably higher - $\delta^{18}\text{O}$ detrital component. It is also possible that a fluid ascending rapidly from depth would have a $\delta^{18}\text{O}$ value higher than the ambient static values assumed in calculating the "equilibrium curve", resulting in anomalously high-temperature calcite lying on the high- $\delta^{18}\text{O}$ side of the curve. The data are insufficient to address these possibilities, and the simpler interpretation - that of an absence of thermally anomalous fluids affecting the oxygen isotopic composition of calcite in the Pathfinder well samples - remains.

Bulk chemistry

Bulk chemical analysis was performed on 69 samples from the core, including all samples for which stable isotope data were obtained. Samples were collected every 60 centimeters (two feet) over a 30-meter (100-foot) interval in the relatively unfaulted middle of the core. Samples were also collected from gouge, fault breccia, sidewall cores within and above the 'A' fault at 2325 meters (7625 feet) DD, and nearby undeformed rocks elsewhere in the core for the purpose of evaluating element flux in the fault zones.

Crossplots of typically immobile phases and elements, such as Al_2O_3 , Zr, and Sc show high correlation coefficients (figures 9a, 9b), indicating their usefulness as monitors of element flux in fault zones sampled in the Pathfinder well. Zirconium and Al_2O_3 are inversely correlated (figure 9a): Zr (from zircon) tracks the sand fraction, as indicated by the strong, positive correlation between Zr and SiO_2 (figure 9c), whereas Al_2O_3 tracks the clay fraction determined by XRD (figure 9d). These elements are less well-correlated with other elements considered to be immobile in the sedimentary environment, such as Ti (figure 9e) and Yb, but the correlations are sufficient to warrant the conclusion that these elements are immobile as a group. For the purposes of gauging mobility of other elements such as potassium, silica, and sodium, Al_2O_3 and Zr are used as references.

The bulk geochemical data indicate little or no difference in chemical composition between faulted and unfaulted rocks in the Pathfinder well. Furthermore, the data indicate that many normally-mobile components, such as K_2O , SiO_2 , Zn, and Cu, are largely immobile in these rocks, even in samples characterized by a pronounced ^{18}O shift (ex., sample 7593): Zn shows a slight increase in gouge samples from the lowest of the three fault domains in the core. A plot of K_2O vs Al_2O_3 (figure 9f) shows a strong correlation ($r^2=0.85$) and a trend having a slope of 0.15, dominated by the stoichiometry of mixed layer smectite-illite clays. Potassium content in the samples is consistent with XRD data indicating the shales consist of approximately 30 to 45 weight percent I/S clay, compared with at most 11 percent K-feldspar in addition to kaolinite and detrital illite. However, a small group of samples from the fault zone at 2358.5 meters (7736 feet) DD plots at slightly elevated $\text{K}_2\text{O}/\text{Al}_2\text{O}_3$ ratio. XRD analysis of one of these samples (7736.4) shows a relatively high I/S ratio of 57%, implying that the increase in K_2O content could be due to illitization of I/S clays. Addition of pure illite ($\text{K}_0.5\text{Al}_3\text{Si}_3.5\text{O}_{10}(\text{OH})_2$) would produce a trend having a slope of 0.3 on this plot, and addition of 11 weight percent illite to the I/S phase of these shales, which average 40% I/S clay by weight, could account for the observed departure from a linear trend; as noted, one gouge sample shows an elevated I/S ratio. Growth of potassic feldspar would be represented as a line having a slope of 1.7 on

this plot, and addition of 0.7 weight percent K-spar could also account for the observed slight K₂O increase; this increase would not be resolvable by XRD and would barely be perceptible by petrographic analysis.

Other frequently mobile components show strong correlation to immobile components in the Pathfinder rocks. SiO₂ shows no departure from immobility in faulted samples (figure 9c), and FeO and MgO correlate well with Zr (figures 9g and 9h respectively). Similarly, zinc and copper, both soluble as chloride complexes at pressure and temperature conditions prevailing in the cored interval, show surprisingly good correlation with alumina (figure 9i), implying that even these elements were not introduced into the Pathfinder rocks by throughgoing fluids. In contrast, $\delta^{18}\text{O}$ of whole-rock calcite is positively correlated with percent clay (3 data points) and negatively correlated with Zr (figure 9j), which tracks sand content. This relationship is interpreted to reflect the control of bulk permeability of rocks in and near the fault zone on calcite $\delta^{18}\text{O}$.

Na₂O in both faulted and unfaulted rocks is essentially independent of K₂O and Al₂O₃ (figure 9k), implying that variations in sodium concentration in these samples is not due to mineralogy, but rather may be due to contamination. Assuming a pore fluid having 50,000 mg/l Na, similar to brines taken from the OI sands nearby, and a shale porosity of 25%, the deposition of salt in pore spaces due to evaporation is calculated to increase Na₂O by as much as 0.9% of the total rock mass, or, equivalently, by as much as 40% over the Na₂O content of the rock itself. A number of samples were washed prior to analysis in order to circumvent this source of contamination, and generally show lower Na₂O content than do unwashed samples, but no quality control was carried out at the lab in order to ascertain that all of the salt had indeed been washed away. Thus, none of the Na₂O values should be considered accurate.

Some of the above samples show elevated CaO content relative to Al₂O₃ (figure 9l), indicating mobility, particularly in the fault zone at 2358.5 meters (7736 feet). Samples from that interval contain as much as 9% calcite, as determined by X-ray diffraction. As discussed above, the oxygen isotope data indicate that this calcite exchanged with fluid only at low temperature; thus, the calcite was precipitated at shallow burial depths.

Gas geochemistry

Martin Schoell, of Chevron Petroleum Technology Company, La Habra, California, collected 15 gas samples during drilling of the Pathfinder well by means of "...splicing a "T" into the gas stream of the mudlogging unit and transferring the gases with a hand pump into aluminum-coated gas bags at ambient pressure. The samples were analyzed for ¹³C₁ and ¹³C₂ using the newly developed Rapid Gas Isotope Analyzer (RGIA) (table 7). A temperature programmable GC (equipped with a 30 m GS-Q megabore column), is on-line connected with a mass spectrometer via a combustion furnace. The mud gases were sampled with a gas tight syringe from the gas bags that were filled at the mud logging unit. Every unknown and standard (NGS-2) was injected at a 6:1 split ratio. The reproducibility of the NGS-2 values is +/- 0.25 permil...Our values were on average 0.9 permil more positive than the accepted value of the standard. Daily correction factors determined from the gas standards were applied to the methane and ethane isotope values...

"The methane isotope values become increasingly more negative with depth (Table 4, figure 10). The value of -47.8 permil above the fault zone in a reservoir sand that will be likely a producer is fairly typical for gases in the Gulf of Mexico. The systematic trend to more negative values in the fault zone indicates two interesting aspects: 1) gases in the fault zone are not homogeneous and 2) the gases are mixtures of bacterial gas and thermogenic gas. Taken at face value, the data are in many aspects surprising. Firstly,

bacterial gas in the fault zone suggests that gases of thermogenic and bacterial origin migrate as mixtures in the migration conduits. Secondly, the systematic trend within the fault zone would suggest unmixed discrete zones of compositionally different gases within the fault. This is difficult to rationalize as one would assume that the fluids are homogeneous in an active feeder fault..." (taken from Schoell and Haught, 1994)

DISCUSSION: Implication of geochemistry for fluid flow in the Pathfinder fault zones

The evidence concerning fluid flow can be divided into two categories: that bearing on thermal imprint of fluids on rocks (smectite-illite ratio, oxygen isotopes, vitrinite reflectance), and that bearing on chemical imprint of fluid (also smectite-illite ratio, oxygen isotopes, mineralogy, bulk chemistry). The former type of data are useful only in determining whether fluid may have ascended the shear zone rapidly enough to produce thermal anomalies, whereas the latter type of data are sensitive to the passage of fluid from any source, at any flux, provided that major or trace elements are transported and precipitated. Thus, the first type of data may yield negative conclusions for the same rocks that are shown by the latter type to have hosted fluid flow. Such appears to be the case for the fault zone rocks studied in the Pathfinder core.

Vitrinite reflectance measurements indicate the fault zones in the Pathfinder well do not represent measurable thermal anomalies relative to unfaulted rocks or rocks at similar depths and geothermal gradients elsewhere in the region. These data yield a more definite insight into thermal maturity of fault rocks than do smectite-illite ratios in that the latter are highly susceptible to a variety of influences, such as fluid chemistry and initial clay composition. While the smectite-illite data may equivocally be interpreted as reflecting unusually high temperatures (as discussed above), the vitrinite reflectance measurements, corroborated by spore fluorescence colors, preclude such a thermal anomaly in faults encountered in the Pathfinder well, including the main 'A' fault zone at 2325 meters (7625 feet) DD. Oxygen and carbon isotopic composition of calcite in and near fault zones in the Pathfinder well do not support throughgoing fluid flow in the sampled shale-dominated portions of the faults, and, if anything, point to fluid focusing into sandier sediments adjacent to the main 'A' fault. These data are in accord with carbon isotopic composition of gas samples collected and analyzed by Martin Schoell of Chevron, which indicate that the biogenic component of the fault zone gases has not been swept out by migrating thermogenic gases during burial.

As noted, scant data indicate flux of some elements in some fault zones in the core. In particular, calcite has been precipitated and illite appears to have formed from smectite in a gouge zone at 2358.5 meters (7736 feet), although this particular mass flux is interpreted on the basis of stable isotope compositions to have taken place early in the burial history. The main 'A' fault at 2325 meters (7625 feet) DD is inferred to have hosted fluids on the basis of a modest calcite ^{18}O shift from unexchanged shale values; however, there is no evidence of mass gain or loss in the sidewall cores taken within or near this fault. The strongest evidence for fluid influx in the form of an ^{18}O shift is from a calcareous shaly silt some 11 meters above the main fault zone, indicating that, on the basis of the available samples, fault-related fluid flow at the location of the Pathfinder well may have been focused in permeable rocks adjacent to the fault rather than within shale gouge zones of the fault itself. The fluid responsible for the ^{18}O shift in calcite did not introduce or remove mass from the affected rocks, implying either that the actual volume of fluid was small or that it in any event was in chemical equilibrium with the bulk shale mineralogy. Much or all of the observed ^{18}O shift in mudstone calcite could have been produced by water-rock interaction in a closed system undergoing burial. This stands in marked contrast to fault rocks from the A6ST well, which penetrates the same fault as does the Pathfinder about 300 meters to the northwest.

The A6ST Well

The A6 sidetrack well was drilled in 1991 to test a target in the KE sand at a TVD of approximately 1890 meters (6200 feet). A rat hole was drilled through the 'A' fault, and a pressure surge was encountered, with oil-cut mud coming to the shaker. Pennzoil shot about 45 sidewall cores in the fault, but cased it off as reservoir dimensions could not be assigned to it. The sidewall cores form the basis of this investigation, which consists of petrographic and cathodoluminescence observations, stable isotope analysis of calcite, X-ray diffraction analysis, smectite-illite ratio determinations, and vitrinite reflectance measurements.

Petrography, Mineralogy, and Vitrinite Reflectance

Petrographic observations indicate the rocks are pervasively faulted, displaying numerous microshears characterized by rotated clays (Plate 3), in some instances showing coarser grain size than in the matrix, as well as rotation of clasts, duplex structures, and drag folding (Plate 4). As with the sidewall cores from the Pathfinder well, these fault structures are believed to represent in situ deformation not associated with the process of collecting the cores. At the outer edge of most cores, a band of clay on the order of 1/4 mm wide has been rotated into parallelism with the core margin (Plate 5): this deformation, and associated fracturing near the core margin, is related to the coring procedure. However, the penetrative structures listed above show consistent displacement sense throughout the entire sidewall core; this, coupled with the observation that measured displacement on some of the faults is greater than that which would be expected on faults produced during the coring operation, implies a tectonic origin for the structures.

The A6ST samples contained essentially the same mineral assemblage as reported for the Pathfinder well (table 5). As is the case for the Pathfinder samples, there are two general types of carbonate with respect to cathodoluminescence: a bright red-orange, angular population, and a dull orange-red to red, subrounded to subhedral group that in some instances occurs as isolated grains in fractures. Both types of grains are disseminated throughout the rocks, are between 10 to 20 microns across, and are not mechanically separable. Calcite comprises an estimated 3 to 5 percent of the shale. As was the case with the Pathfinder samples, dolomite is not detectable in XRD scans made at Cornell University, but was detected in trace amounts in samples analyzed at Exxon Production Research Co, Houston. Electron microprobe analysis indicates dull-luminescent calcite in these rocks contains 2 to 3 percent iron as FeCO_3 .

Smectite/illite ratios in rocks from the A6ST well varied considerably according to the laboratory carrying out the analyses (table 6; figure 11). The first samples were analyzed at Michigan Technological University, and were concluded to have I/I+S ratios in rocks from within and just above the fault zone between 40% and 55% (table 9), averaging 44%, significantly higher than "background" I/I+S ratios of 20-30% reported for Plio-Pleistocene rocks in the area by Milliken (1985). A second group of ten samples from the same interval was analyzed at Exxon Production Research (EPR) in Houston, and found to have I/I+S ratios between 23% and 35%, averaging 27%, lying within the "normal" range as defined above. All samples are characterized by $\text{Reichweite} = 0$. The difference in reported values from the two laboratories could simply be due to different methods of interpreting the X ray spectra. It must be noted that the two laboratories did obtain similar I/S ratios for samples from the Pathfinder well, but also that the A6ST and Pathfinder I/S determinations at MTU were carried out by different researchers, whereas they were carried out by the same personnel using the same techniques at EPR. In view of the above considerations, the lower EPR numbers are taken as accurate. Their I/S determinations show a modest correlation with semi-quantitative degree of deformation in the fault rocks (figure 12). Application of illite-smectite data to paleothermometry of the fault rocks awaits

resolution of two issues: 1) the I/S ratios in the Pathfinder well are significantly *higher* than expected given the low vitrinite reflectance values and spore fluorescence colors; they also show no relation to the fault, and 2) if the EPR I/S determinations for the A6ST well are indeed accurate, and there is no known reason to believe otherwise, the I/S ratios there are significantly *lower* than expected when compared with the vitrinite reflectance values and spore fluorescence colors.

Vitrinite reflectance measurements were made on polished thin sections and whole-rock blocks from fault rocks in the A6ST (table 7, figure 13). Five epoxy mounts of kerogen from fault rocks yielded an average reflectance of indigenous telocollinite, using the same apparatus as described above, of 0.55%Ro, with a standard deviation of 0.08 (79 measurements); an example of these data, from sample 7348, is given in figure 14. Reflectances of other macerals were also measured; typically these were higher than those of the indigenous material and defined discrete populations on histograms. The relatively high reflectance of rocks from the fault zone in the A6ST well identifies that zone as a thermal anomaly with respect to rocks outside the fault zone, and to rocks elsewhere in the fault zone (i.e., the Pathfinder well). The relatively higher reflectance is corroborated by yellow-orange to mid-orange spore fluorescence colors in the same samples; these indicate higher thermal maturity than do the green-yellow, yellow, and yellow-orange colors observed in the Pathfinder samples.

Stable isotopes

As is the case with the Pathfinder samples, dolomite in the samples is volumetrically minor in comparison to calcite and its presence does not appear to affect the $\delta^{18}\text{O}$ of the calcite + dolomite mixture to any significant extent. Oxygen isotopic composition of calcite (+ dolomite) shows a pronounced shift to lower $\delta^{18}\text{O}$ values, as low as 23.4 permil (table 8). The ^{18}O shift actually involves unfaulted rocks just above the fault zone: calcite in rocks at the "top" of the fault shows a reverse ^{18}O shift, back to higher $\delta^{18}\text{O}$ values with depth. Faulted rocks well below the top of the fault (for example, samples at 2269 meters (7443 feet) DD) lie at high, unexchanged $\delta^{18}\text{O}$ values (figure 15a). These data suggest that, if the observed ^{18}O shift is related to fluid flow in the fault, that fluid preferentially flowed along the "top" of the fault.

As noted for the Pathfinder samples, the ^{18}O shift observed in the data may represent a mixing trend between low- $\delta^{18}\text{O}$ diagenetic calcite and high - $\delta^{18}\text{O}$ detrital and foraminiferal calcite, present in samples above and within the fault zone, and the low- $\delta^{18}\text{O}$ endpoint may lie to the high-temperature (low- $\delta^{18}\text{O}$, or left) side of the "equilibrium line". However, there does not appear to be a relationship between abundance of dull-luminescent calcite and whole-rock calcite $\delta^{18}\text{O}$. Alternatively, the calcite $\delta^{18}\text{O}$ values may simply be partially "frozen in" by partial equilibration with pore water during burial. The data are inconclusive in this regard: they permit, but do not unequivocally support, the interpretation of thermally-anomalous fluids in the fault zone.

Calcite $\delta^{13}\text{C}$ values are correlated with the $\delta^{18}\text{O}$ values (figure 15b), such that the lowest- $\delta^{18}\text{O}$ samples also have the lowest $\delta^{13}\text{C}$, between -4 and -9 permil, whereas the highest- $\delta^{18}\text{O}$ samples have normal marine foraminiferal $\delta^{13}\text{C}$ values of around 0 permil. The ^{13}C depletion in the lower- $\delta^{18}\text{O}$ calcites may be due to incorporation of some carbon related to hydrocarbon maturation and/or organic acid decarboxylation, supporting a relatively deep source for the diagenetic fluid.

Whole rock geochemistry

The combined vitrinite reflectance, stable isotopic, and initial smectite-illite data lead us to conclude that at least part of the 'A' fault encountered in the A6ST well acted as a fluid conduit, and that at least some of the fluids were hotter than ambient temperatures. We then sought to corroborate the above evidence for fluid flow with whole rock geochemistry (table 12), anticipating that we might be able to determine the flux of major and trace elements into fault rocks.

As in the case of the Pathfinder well, Zr, Al_2O_3 , and Sc are correlated with one another (figure 16a), although the correlation coefficients are lower than for Pathfinder samples; Al_2O_3 was selected as a "reference" immobile component against which the behavior of other components can be measured. In terms of their geochemistry, the A6ST samples are nearly identical to the Pathfinder samples reported above, and can be plotted together with them (for example, figure 9b). However, to facilitate analysis of the A6ST samples as a group, they are considered independently from the Pathfinder analyses.

Plots of normally-mobile elements, such as SiO_2 , K_2O , Zn, and CaO versus Al_2O_3 indicate little to no mass influx into the fault zone samples. SiO_2 shows a negative correlation with Al_2O_3 (figure 16b) and K_2O is positively correlated with it (figure 16c); the former relationship indicating that SiO_2 content is controlled by abundance of detrital quartz (r^2 of SiO_2 vs Zr, which tracks zircon and thus tracks the coarser detrital fraction, is 0.75), and K_2O is controlled by abundance of clay. The slopes of the K_2O vs Al_2O_3 plots for the A6ST and Pathfinder well samples are nearly the same, 0.13 and 0.15, indicating, as noted for the Pathfinder well samples, that K_2O occurrence is described by mixed-layer I/S stoichiometry. Unlike the Pathfinder samples, rocks from the A6ST well do not show even a weak relationship between K_2O content and extent of faulting. Zinc shows no enrichment in faulted versus unfaulted rocks (figure 16d). CaO does show possible weak enrichment in some weakly to moderately deformed rocks relative to undeformed ones (figure 16e), and the lack of correlation of CaO with Al_2O_3 indicates it is largely in the form of carbonate minerals rather than plagioclase or Ca-montmorillonite. $\delta^{18}\text{O}$ of calcite and mixed calcite+dolomite from these rocks is weakly inversely correlated with CaO content (figure 16f), suggesting that CaO, hence carbonate, in these rocks may be at least partly of diagenetic origin.

DISCUSSION: Thermal anomaly in the fault penetrated by the A6ST well

Modeling based on vitrinite maturation in the fault rocks, as described above, requires a significant thermal pulse in order to produce the average 0.55% Ro vitrinite reflectance at the depths from which these samples came. For this study, the first-order, distributed activation energy model of Burnham and Sweeney (1990) was used. In the simple situation shown in figure 17, rocks now in the fault zone are modeled as being buried along a constant, present-day, geothermal gradient of 30 C/km (present day temperature is about 80C in the fault zone), with a pulse of instantaneous peak temperature of 120 C, or about 45 C above the ambient temperature, being required to produce the measured reflectance values. Longer-duration pulses (i.e., 20-30Kyr) need not have such high temperatures, but still are on the order of 35 degrees hotter than ambient temperature. The same burial history, without a temperature pulse, produces a calculated vitrinite reflectance of 0.27% Ro.

The combined vitrinite reflectance and stable isotope data support the interpretation of thermally anomalous fluid flow in the fault zone at the A6ST well. Large volumes of fluid would be required in order to produce the interpreted thermal anomaly. Furthermore, if fluids are responsible for the thermal anomaly, they must have sourced below the massive shales that lie below the OI sands: only there are the temperatures sufficient to produce the thermal maturation recorded by the vitrinite. However, other interpretations

for a temperature anomaly, such as influence of salt in the past, are possible. Further study is required regarding the detailed history of salt movement in this area, as well as the distribution and nature of other thermal anomalies, if any, within and outside of the fault zone in block 330.

Vitrinite reflectance measurements elsewhere in Block 330

Vitrinite reflectance was measured from cuttings from five other wells in Block 330 (table 9). In most cases, the samples were of only fair to poor quality, and yielded only a few measurements; thus any conclusions drawn from these data must be considered tentative. That said, the data, taken at face value, highlight the Pathfinder well as a "cold spot" in the 'A' fault zone (figure 18). The data imply that the imprint of an anomalous heating event or events, perhaps related to ascent of fluid in the 'A' fault, decreases to the southeast. Additionally, Rock-Eval pyrolysis data were obtained from a suite of cuttings through the fault in the C-7 well, Block 330, in order to evaluate thermal maturity and evidence for migrated hydrocarbons (figure 19). The data show a migrated hydrocarbon peak (P1) in the 5650-5680 sample, which corresponds to the 'B' fault intercept at 1732 meters (5680 feet) DD, no P1 peak in the sample taken below that fault, and weak P1 peaks in the 5980-6010 and 6010-6040 intervals, corresponding to the 'A' fault intercept at 1828 meters (5997 feet) (fault picks based on marked logs provided by Pennzoil Exploration and Production Co.).

In order to address the question of whether the fault represents a paleothermal anomaly and thus may have acted as a conduit for hot fluids, vitrinite reflectance measurements were made on four samples from the KE sand (1.5 My), of approximately the same age and depth as the fault samples, at varying distances from the fault system. Thin sections from these samples yielded significantly lower average vitrinite (telocollinite) reflectance, between 0.25 and 0.3% Ro (figure 18), than did most samples from the fault zone.

CONCLUSIONS: Comparison of fluid flow between the Pathfinder and A6ST wells

Data in hand indicate the main ("A") fault zone is heterogeneous with respect to fluid flow, as is typically the case with fault zones. The evidence is against significant throughgoing fluid in the fault zone encountered in the Pathfinder well, while it supports the interpretation of such flow in the fault drilled in A6St well, only 300 meters away. Specifically, the elevated vitrinite reflectances and spore fluorescence colors in the A6ST fault rocks and the well-constrained extrapolation of vitrinite reflectances to "normal" values 100 meters above the fault identifies the fault as a paleothermal anomaly relative to rocks just above it. A thermal model for the vitrinite reflectance anomaly, while not a unique solution, implicates fluids at temperatures compatible with oil generation.

Furthermore, the low $\delta^{13}\text{C}$ values, combined with low $\delta^{18}\text{O}$, of fault zone calcite combined with early- to mid-Tertiary brine Iodine-129 ages (Losh and Wood, 1995) point to fluid that interacted with rocks at temperatures at which kerogen maturation was taking place (Udo Fehn, Univ. of Rochester, 1994, oral comm). As the maximum ambient temperature at the A6ST well fault intercept was probably no greater than its present-day value of 80 C (and even this value is unusually high for this depth in this area), fluids of these temperatures and/or from these sources must have ascended from depth. Extrapolation of the 30C/km geothermal gradient in the A6ST well indicates such fluids must have migrated a kilometer or more vertically: the brines have migrated considerably more than that since they first interacted with rocks undergoing kerogen maturation in the early to mid-Tertiary.

The lateral variability in fault-hosted fluid flow may result from lithologic and concomitant permeability variations along the fault zone: sandy intervals in the "massive shale" may have smeared out along the fault, providing channelways for fluid to ascend

from depth. Along the same lines, structural anisotropies in the fault, such as dilatant bends acting in concert with oblique slip, may produce fractured channelways. In the Pathfinder well, the deepest of the three fault domains in the core is interpreted to be the best-suited to have acted as a fluid conduit and, as stated above, is the only portion of the cored fault that contained oil. However, even samples of oil-bearing fault rocks from this domain did not yield geochemical or mineralogical evidence for significant mass influx, nor did samples taken in or near the main 'A' fault. Unlike the A6ST well samples, there is no mitigating evidence for fluid flow: vitrinite reflectance values are uniformly low, and calcite $\delta^{13}\text{C}$, which is unfortunately obtainable only in the upper, calcareous portion of the core, is almost uniformly unaffected by products of kerogen maturation. Thus, even though oil is present within some of these deeper faults, indicating that they were capable of transmitting fluid to some extent, it is evident that some factor beyond local fault complexity or geometry of fault/fracture spacings controls large-scale fluid ascent in the 'A' fault. Both the Pathfinder and A6ST wells are distant from intersections of the 'A' fault with subsidiary structures as shown on structure contour maps interpreted from seismic and well data (ex., figure 1), and the 'A' fault has approximately the same trend and, probably, relationship to the stress field at both locations. Thus, a complete answer to the question of which factors exert control on fluid flow in the fault zone does not present itself on the basis of the above data alone. Considering that seismic data and maps derived from them may not be of sufficient resolution to allow distinction of features that could indicate the propensity of the fault to transmit fluid, answers to this question will probably be best derived from integrated geologic and geochemical studies at a number of points along the fault.

Acknowledgements

Funding for this research was provided by the Global Basins Research Network and Department of Energy grant DC-FC22-93BC14961 to Roger Anderson, Lamont-Doherty Earth Observatory. We are deeply grateful to Pennzoil Exploration and Production Co. for their matchless cooperation and generous access to samples and data; without their support, this entire project would not have been possible. SL also acknowledges the valuable help of Peter Vrolijk and Michael Wooten, Exxon Production Research, and the participants in the coring strategy meetings. MTU smectite-illite analyses were performed by Ahn Tu (Pathfinder samples) and Kirsten Price (A6ST), with the knowledgeable help of Prof. Doug McDowell. Biostratigraphic analysis was performed by Applied Biostratigraphix, Houston, and elucidated by Denise Butler, Pennzoil.

REFERENCES CITED

- Abercrombie, H., Hutcheon, I., Bloch, J., DeCaritat, P., 1994, Silica activity and the smectite-illite reaction; *Geology* vol 22, p 539-542
- Alexander, L., Flemings, P., in press, Geologic evolution of a Plio-Pleistocene salt withdrawal mini-basin, Eugene Island South Addition, Block 330, offshore Louisiana; *Amer. Assoc. Petrol. Geol. Bull.*
- Anderson, R., 1993, Recovering dynamic Gulf of Mexico reserves and the U.S. energy future; *Oil and Gas Jour.*, April 26, p. 85-91
- Anderson, R., Flemings, P., Losh, S., Austin, J., Woodhams, R., 1994, Gulf of Mexico growth fault drilled, seen as oil, gas migration pathway; *Oil and Gas Jour.*, June 6, pp. 97-103
- Galloway, W., Henry, C., Smith, G., 1982, Depositional framework, hydrostratigraphy, and uranium mineralization of the Oakville Sandstone (Miocene), Texas Coastal Plain. Univ. of Texas at Austin Bur. of Econ. Geol. Rept. of Investigations 113, 51 pp.
- Hippler, S., 1993, Deformation microstructures and diagenesis in sandstone adjacent to an extensional fault: Implications for the flow and entrapment of hydrocarbons; *Amer. Assoc. Petrol. Geol. Bull.*, vol. 77, pp. 625-637.
- Holland, D., Leedy, J., Lammlein, D., 1990, Eugene Island Block 330 field - U. S. A., offshore Louisiana; in Beaumont, E., and Foster, N., eds., *Structural Traps III: Tectonic Fold and Fault Traps*; *Amer. Assoc. Petrol. Geol. Treatise of Petroleum Geology*, pp. 103-143
- Hooper, E. C. D., 1991, Fluid migration along growth faults in compacting sediments; *Jour. Petrol. Geol.* vol 14, pp. 161-180
- Hower, J., Eslinger, E., Hower, M., Perry, E., 1976, Mechanism of burial metamorphism of argillaceous sediment I: Mineralogical and chemical evidence; *Geol. Soc. Amer. Bull.*, vol 87, p. 725-737
- Huang, W.-L., Longo, J., Pevear, D., 1993, An experimentally-derived kinetic model for smectite-to-illite conversion and its use as a geothermometer; *Clays and Clay Minerals*, vol 41, p. 162-177
- International Committee for Coal Petrology (ICCP): *International handbook of coal petrology*. Centre Nat. Resch. Sci. (Paris), 2nd ed 1963, 164 pp., 1st suppl. 1971, 400 pp.; 2nd suppl. 1975, 68 pp.
- Jones, P., Wallace, R., Jr., 1974, Hydrogeologic aspects of structural deformation in the northern Gulf of Mexico basin; *Jour. Res. U.S. Geol. Surv.*, vol 2, pp. 511-517
- Land, L., MacPherson, G., 1989, Geochemistry of formation waters, Plio-Pleistocene reservoirs, offshore Louisiana; *Gulf Coast Assoc. Geol. Socs. Trans.* vol. 39, p. 421-430
- Land, L., Lynch, F., Mack, L., Milliken, K.L., 1995, Regionally inhomogeneous potash metasomatism, Paleogene mudrocks, Texas Gulf Coast; *Amer. Assoc. Petrol. Geol. Abstr. w/Prog.*, vol 4, p. 53A
- Losh, S., Wood, J., 1995, Brine chemistry, SEI Blocks 316 and 330; in Anderson, R., ed. *Results of the Pathfinder Drilling Program into a Major Growth Fault; Part of the GBRN/DOE Dynamic Enhanced Recovery Project in South Eugene Island 330 Field, Gulf of Mexico*, CD-ROM available from Geosciences Dept., Lamont-Doherty Earth Observatory, Palisades, NY 10964
- Milliken, K., L., 1985, Petrology and burial diagenesis of Plio-Pleistocene sediments, northern Gulf of Mexico; unpub. PhD thesis, Univ. Texas at Austin, 112 pp.
- Moore and Reynolds, 1989

- Mukhopadhyay, R., 1992: In *Diagenesis III. Developments in sedimentology*, 47 ; pp. 435-510. Eds. K. H. Wolf and G.V. Chillingarian. Elsevier Science Publishers
- O'Neil, J., Clayton, R., Mayeda, T., 1969, Oxygen isotope fractionation in divalent metal carbonates; Jour. Chem. Phys., v. 51, 5547-5558
- Schoell, M., Haught, M., 1994, Preliminary report on mudgas isotope analyses, GBRN well EI330 A20ST; Chevron Petroleum Technology Company, La Habra, CA. internal report TM94000051, 7 pp.
- Stach, E., Mackowsky, M-Th., Teichmuller, M., Taylor, G., Chandra, D., and Teichmuller, R., 1982, Textbook of Coal Petrology, 3d ed. 536 pp. Gebruder Borntraeger
- Sweeney, J., Burnham, A., 1990, Evaluation of a simple model of vitrinite reflectance based on chemical kinetics; Amer. Assoc. Petroleum Geol. Bull., vol 74, p. 1559-1570.
- Weber, K., Mandl, G., Pilaar, W., Lehner, F., Precious, R., 1978, The role of faults in hydrocarbon migration and trapping in Nigerian growth fault structures; Tenth Annual Offshore Technology Conference Proc., vol 4, pp. 2643-2653 (OTC 3356)

APPENDIX

Methodology for analyzing smectite-illite ratios, Michigan Technological University

Samples from the Pathfinder and Texaco wells located within the northern Gulf Coast Basin cover a stratigraphic range from Pliocene to Pleistocene. X-ray diffraction techniques were used to analyze clay-size fractions from sidewall core samples to determine clay content

Size separation

The Eugene Island Pathfinder samples were ultrasonically disaggregated in distilled water using a Branson ultrasonic cell disrupter. In a 100 ml graduated cylinder, Stokes Law settling techniques were used to obtain $<2\mu\text{m}$ separates from each sample (Moore and Reynolds, 1989). Selected samples were further separated to $<1\mu\text{m}$ fraction in an attempt to obtain clearer illite/smectite peaks

Preparation of the Texaco samples required an additional procedure. These samples were washed and sieved in order to eliminate any drilling muds, which would produce poor diffraction patterns, preventing acceptable interpretation. Remnants of the country rock left in the sieve were crushed with a mortar and pestle. Size separation was performed using the above procedure.

X-Ray Diffraction Analysis

Samples from each $<2\mu\text{m}$ and $<1\mu\text{m}$ size fraction at each depth were mounted on ceramic plates using a vacuum pump apparatus. Each sample was air-dried and XRD analysis was carried out on a automated Dapple/Norelco X-ray diffraction machine using $\text{CuK}\alpha$ radiation and 1 degree slit size. X-ray diffractograms were run from 2 degrees to 35 degrees 2θ with a counting time of 2 seconds/step. After obtaining diffraction patterns for air dried samples, all samples were ethylene glycol solvated in a glass desiccator for 24 hours at room temperature (Moore and Reynolds, 1989). Identification of illite/smectite and estimation of percent expandables were made from techniques described by Moore and Reynolds (1989).

Plates

1. Stringer of indigenous vitrinite, shaley siltstone from KE-1 reservoir, B-2 well, SEI Block 330
2. Small indigenous vitrinite particle (left) and a recycled vitrinite particle (right) in faulted silty shale, A6ST well, SEI Block 330
3. "Microshears" in silty shale, sample 7434, A6ST well (photo taken under x-nicols). Bedding is east-west in photo, with faults cutting shale from upper right to lower left. The faults are marked by bands of rotated clay (light color in photo) on the order of 5 to 10 microns across. Long dimension of photo is 2.5 mm
4. Gouge zone, sample 7329, A6ST well (Plane polarized light). Main shear (arrow) and subsidiary anastomosing shears transect photo west to east; splay (arrow) cuts shale to lower right. Overall shear sense is top to right. Long dimension of photo is 2.5 mm
5. Undeformed silty shale, sample 7313, A6ST well (photo taken under x-nicols). Most of sample is near extinction (bedding runs east-west in photo), but clays near the edge of sidewall core in upper right have been rotated into parallelism (lighter color, not at extinction) with the margin of the sidewall core (arrow). The 1/4-mm width of this rotated zone at the edge of the plug is typical of the A6ST sidewall cores. Sidewall coring does not in itself produce penetrative deformation of these shales. Long dimension of photo is 2.5 mm.

TABLES

- Table 1. Vitrinite reflectance and spore fluorescence color data, Pathfinder well
- Table 2. Oxygen and carbon isotope data for whole-rock calcite and calcite+dolomite samples from the Pathfinder well.
- Table 3. Carbon isotopic composition of C₁ and C₂ fractions of gas collected from Pathfinder Well.
- Table 4. Minerals present in A6ST well sidewall core samples, determined by X ray diffraction at Exxon Production Research
- Table 5. Illite/(illite+smectite) for sidewall cores from the A6ST well, comparing MTU and EPR determinations.
- Table 6. Vitrinite reflectance measurements from A6ST well samples within and above the 'A' fault.
- Table 7. Oxygen and carbon isotopic values for whole rock calcite and calcite+dolomite samples from the A6ST well. Deformation extent as defined in caption for figure 12.
- Table 8. Vitrinite reflectance data for cuttings from five wells intersecting growth fault system in Block 330

FIGURES

- Figure 1. Location map, Pathfinder and A6ST wells, South Eugene Island Block 330
- Figure 2. Downhole gamma ray log (curve on right), bedding dip and dip azimuth (curve on left) for cored interval. Gross lithologic domains and locations of recovered core (gray) shown in columns to right of logs.
- Figure 3. Mineralogy of shale samples from the whole core and sidewall cores. Data are from the following sources: shales 7612 through 8400, Exxon Production Research; shale 7957.9, Shell Bellaire Lab; shale 7849.5, Core Laboratories (FTIR "Mineralog" analysis).
- Figure 4. Illite/(illite+smectite) ratios for samples from the Pathfinder well. All samples were analyzed at MTU with the exception of 7631 (I/S = 52%), 7736.5 (57%), 8010.8 (47%), and 8400 (57%), which were analyzed at Exxon Production Research.
- Figure 5. Vitrinite reflectance vs depth for the Pathfinder well, showing locations of B and D faults, as well as the "main" A fault zone.
- Figure 6. Pyrolysis Tmax and vitrinite reflectance data vs depth for the Pathfinder well. The two parameters co-vary, but the pyrolysis measurements point to a higher thermal maturity than does the vitrinite reflectance, perhaps owing to incorporation of reworked macerals.
- Figure 7. Pyrograms for sidewall cores from various reservoirs intersected by the Pathfinder well; also shown are pyrograms for fault rocks at 7637' and 7653'. P1 peaks, indicative of migrated hydrocarbons, are absent in fault rock pyrograms.
- Figure 8. a) Oxygen isotopic composition of calcite from sidewall cores from the 'A' fault and from whole core, plotted against depth. "Equilibrium" $\delta^{18}\text{O}$ line assumes isotopic equilibration with pore fluid that varies in $\delta^{18}\text{O}$ from 0 permil at the sediment-water interface to 2 permil at 3 kilometers depth, consistent with published work in Plio-Pleistocene sediments in the Gulf of Mexico (Land and MacPherson, 1989). Calcite -water fractionation is from Clayton et al (1969). b) Calcite and calcite+dolomite $\delta^{13}\text{C}$ vs $\delta^{18}\text{O}$.

Figure 9 a). Al_2O_3 vs zirconium, Pathfinder and A6ST well samples. Omission of A6ST well samples from this plot only increases coefficient of correlation to 0.86. The two components track one another, and are immobile. b) Al_2O_3 vs scandium, Pathfinder well samples. c) Zr vs SiO_2 , Pathfinder and A6ST well samples. d) Al_2O_3 vs clay percent, determined by XRD, showing control of clay on Al content. e) Al_2O_3 vs TiO_2 , Pathfinder well samples. f) Al_2O_3 vs K_2O . Gouge and fault rock points lying at relatively high K_2O give evidence of growth of a potassic phase, modeled by illite and K-feldspar lines on the plot. "Upper gouge" is that at 7736 feet, "gouge" is that at 7950-7970 feet. The two are distinguished because the upper fault zone is interpreted as having experienced movement only at shallow burial depth, whereas the lower one contains oil and is believed to have been active as a fluid conduit much more recently. g) Zr vs FeO , Pathfinder and A6ST samples. h) Zr vs MgO , Pathfinder and A6ST well samples. i) Zinc and copper vs Al_2O_3 . j) Clay, Zr, and SiO_2 vs whole rock calcite (+dolomite) $\delta^{18}\text{O}$. $\delta^{18}\text{O}$ varies with "shaliness" (or the inverse of "sandiness", as indicated by Zr and SiO_2), implying control of lithology-dependent permeability on fluid flow. k) Na_2O vs Al_2O_3 , Pathfinder samples. Sodium in these samples is probably contaminated by briny pore fluids. l) CaO vs Al_2O_3 , Pathfinder samples. The bulk of samples contain less than 1.5% CaO ; samples from within and next to the fault at 2358.5 m (7736 ft) contain up to 4.2% CaO , corroborating the abundance of calcite determined by XRD. For the most part, the higher- CaO samples are the ones that also show K_2O enrichment.

Figure 10. $\delta^{13}\text{C}$ of methane vs depth, Pathfinder well. Fault gases are isotopically light and heterogeneous, indicating variable mixtures of biogenic (shallow) and thermogenic gases in the fault zone.

Figure 11. Illite/Illite+smectite vs depth, A6ST well, comparing MTU and EPR determinations.

Figure 12. Extent of deformation vs Illite/(illite + smectite), A6ST well, as determined by Exxon Production Research. Deformation on the scale of the thin section is defined semi-quantitatively as: 0 = no deformation in thin section, 1 = weak deformation, < 5 microshears in transect across sidewall core, 2 = moderate deformation, 5 to 20 microshears in transect, with block rotation, incipient gouge zones, 3 = strong deformation, gouge over 1 mm wide, micro-duplex structures, brecciation

Figure 13. Depth vs vitrinite reflectance, A6ST well. Best-fit line is drawn through data; "Normal" profile is taken from Pathfinder well and is typical of sediments of this age in the Gulf of Mexico. Curve fit to $\delta^{18}\text{O}$ data is also shown for comparison to vitrinite reflectance data, and defines a possible zone of high fluid flux in the 'A' fault at this location.

Figure 14. Histogram of reflectances of various macerals from a polished slab, sample 7348, A6st well. Indigenous vitrinite grains define a distinct, well-defined population on this plot, illustrating the usefulness of the "operator selective" approach in determining %Ro in these organic-lean, immature sediments.

Figure 15. a) $\delta^{18}\text{O}$ of calcite (+/- dolomite) vs depth, A6ST well. "Equilibrium" $\delta^{18}\text{O}$ line shown for comparison to data, as discussed in text, and is based on same assumptions as described in caption for figure 8. b) $\delta^{13}\text{C}$ vs $\delta^{18}\text{O}$, calcite (+/- dolomite) samples from the A6ST well.

Figure 16. a) Zr and Sc vs Al_2O_3 , A6ST well samples. b) SiO_2 vs Al_2O_3 . c) K_2O vs Al_2O_3 . d) Zn vs Al_2O_3 , showing lack of relationship of zinc content to

deformation as well as general immobility of zinc in the fault. e) CaO vs Al₂O₃. f) CaO vs whole-rock calcite (+dolomite) $\delta^{18}\text{O}$.

Figure 17. Thermal model compatible with vitrinite reflectance, using first-order kinetic equation and the parameters of Sweeney and Burnham (1990).

Figure 18. Vitrinite reflectance means from cuttings from seven wells in Block 330, plotted relative to growth fault. Map is at the level of the KE sand. Sand name in parentheses is that of the last sand drilled through, if other than the KE sand, before the fault was encountered. A6ST and Pathfinder data also shown for comparison, as are four mean Ro values from the KE sand outside the fault.

Figure 19. Pyrograms for cuttings samples taken from depths as shown, C7 well.

Table 1. I/S ratios, Pathfinder well

Meas. depth (ft)	% Illite - Pathfinder well
4220	10
4310	40
4340	15
4730	40
4760	5
4970	5
5000	30
5110	35
5330	45
5390	30
5800	50
5960	30
6070	45
6290	50
6380	42
6440	40
6860	35
6890	51
7360	55
7460	55
7490	55
7550	55
7631*	52
7736.5*	57
7880	60
8010.8*	47
8060	55
8270	45
8390	50
8400*	57
8405	60

*Analyzed at Exxon Production Research Co., Houston

Table 2. Vitrinite data, Pathfinder well

Sample type	Meas. depth (ft)	TVD (ft)	Spore fluorescence color	Reworked spore fluor. color	Vitrinite reflectance (%Ro)	No. readings	s.d	Coeff. of variation
SW core	5387	5371	yellow	lt. orange	0.27	19	0.06	0.2
SW core	5436	5417	yellow	lt. orange	0.28	24	0.05	0.2
SW core	6200	6089	yellow?	-	0.26	3	0.01	0.0
SW core	6359	6215	yellow	-	0.30	19	0.05	0.2
SW core	6389	6239	yellow	-	0.25	7	0.07	0.3
SW core	6449	6287	yellow	mid. orange	0.30	21	0.05	0.2
SW core	6503	6330	green-yellow	dk. orange	0.30	13	0.04	0.1
SW core	6546	6364	yellow/yel.-orge.	-	0.32	16	0.05	0.2
SW core	6613	7417	yellow	-	0.30	19	0.06	0.2
SW core	6715	6497	yellow/yel.-orge.	-	0.29	6	0.03	0.1
SW core	6840	6597	yellow	-	NDP	NDP	NDP	-
SW core	6906	6650	yellow	mid. orange	0.28	3	0.05	0.2
SW core	6947	6683	NDP	-	0.30	11	0.05	0.2
SW core	6956	6691	NDP	mid. orange	0.28	4	0.05	0.2
SW core	7157	6859	yellow?	mid. orange	0.34	6	0.06	0.2
SW core	7202	6898	yellow	-	0.29	19	0.06	0.2
SW core	7256	6945	yellow/yel.orge.	-	0.26	3	0.03	0.1
SW core	7350	7029	yellow	-	0.28	6	0.05	0.2
SW core	7406	7081	yellow	-	0.27	9	0.05	0.2
SW core	7449	7120	yellow	-	0.25	5	0.03	0.1
SW core	7495	7163	yellow	-	0.32	2	0.09	0.3
SW core	7550	7214	yellow	lt. orange	0.28	7	0.05	0.2
SW core	7599	7260	yellow/yel.-orge	-	0.34	5	0.07	0.2
SW core	7601	7262	yellow/yel.-orge.	-	0.31	12	0.05	0.2
SW core	7611	7271	yellow?	mid. orange	NDP	NDP	NDP	-
SW core	7625	7284	yellow	-	NDP	NDP	NDP	-
SW core	7633	7291	yellow	-	0.30	9	0.06	0.2
SW core	7636	7294	yellow	-	0.29	7	0.04	0.1
SW core	7637	7295	yellow/yel.-orge.	-	0.28	7	0.06	0.2
SW core	7639	7297	yellow	-	0.30	13	0.05	0.2
SW core	7641	7299	yellow	-	0.28	10	0.05	0.2
SW core	7653	7310	yellow	lt. orange	0.30	13	0.05	0.2
Core	7654.4	7311	yellow	lt. orange	0.29	8	0.05	0.2
Core	7666.4	7322	yellow	t.-mid orange	0.34	9	0.07	0.2
Core	7690.5	7345	green-yel.	mid-dk orge.	0.34	4	0.01	0.0
Core	7726.3	7738	yellow?	mid-dk orge.	0.35	5	0.08	0.2
Core	7750.9	7401	yellow	mid. orange	0.27	12	0.07	0.3
Core	7755.2	7405	yellow?	- 0.31	11	0.05	0.2	
Core	7823.9	7468	yellow?	mid. orange	0.31	9	0.04	0.1
Core	7834.1	7478	yellow	mid. orange	0.31	14	0.05	0.2
Core	7864.1	7506	yellow	mid. orange	0.31	9	0.09	0.3
Core	7871.1	7512	yellow/yel. orge	mid. orge.	0.26	12	0.05	0.2
Core	7874.6	7515	yellow	mid orange	0.25	7	0.09	0.3
Core	7875	7516	yellow	mid orange	0.33	12	0.08	0.2
Cuttings	8090-8120				0.31	3	0.13	
Cuttings	8270-8300				0.34	7	0.09	
Cuttings	8330-8360				0.47	2	0.01	
Cuttings	8360-8390				0.37	3	0.00	

* (Barker and Pawlewicz, 1993: 0-0.2, reliable; >0.2 less reliable/unreliable); NDP - No Determination Possible; orge = orange, ? = yellow, lt = light, mid = middle, dk = dark. ? = tentative color assignment often based on spore fragments

Table 3. Carbon and oxygen isotopic composition of carbonates, Pathfinder well

Measured depth (ft)	$\delta^{13}\text{C}$	$\delta^{18}\text{O}$	Rock type
7716.700	-2.900	29.400	Undeformed
7717.150	-3.300	29.100	Fault
7717.600	-2.100	29.000	Fault
7722.400	-2.300	28.300	Undeformed
7724.910	-8.900	31.100	Undeformed
7728.500	-1.300	30.600	Undeformed
7730.900	-2.200	30.500	Undeformed
7734.700	-.900	30.700	Undeformed
7735.600	-2.800	30.800	Fault
7735.900	-3.100	30.700	Fault
7736.100	-1.600	30.900	Fault
7617.000	-3.800	26.300	Undeformed
7631.000	-.800	27.900	Fault
7636.000	-.700	28.200	Fault
7653.000	-3.300	26.800	Fault
6742.000	.200	30.800	Fault
6746.000	.100	30.600	Fault
7585.000	-2.900	27.000	Undeformed
7587.000	-3.900	26.800	Undeformed
7595.000	-1.600	26.900	Undeformed
7599.000	-2.400	27.100	Undeformed
7601.000	1.600	23.000	Undeformed
7601.000	1.400	21.900	Undeformed
7611.000	-3.900	27.100	Undeformed
7625.000	-.400	29.900	Undeformed
7633.000	-.800	28.400	Undeformed
7545.000	-1.700	29.000	Dolomite - undeformed
7551.000	-4.600	30.000	Dolomite - undeformed
7593.000	-.400	28.700	Dolomite - undeformed
7545.000	-6.500	27.600	Calcite - undeformed
7551.000	-9.000	22.800	Calcite - undeformed
7593.000	-3.900	21.900	Calcite - undeformed

Table 4. Gas geochemistry, Pathfinder Well

Depth	$\delta^{13}\text{C}_1$	$\delta^{13}\text{C}_2$	Show units
6420	-47.75	-29.34	600
7100	-52.1		20
7160	-51.71		200
7180	-51.67	-30.21	350
7375	-51.63		250
7680	-56.27		30
7740	-56.46		30
7790	-56.87		30
7850	-57.05		35
7905	-57.72	-29.95	75
7990	-58.54		90
8000	-58.92		100
8270	-58.25		75
8330	-55.63	-28.86	75
8405	-57.71		70

Table 5. Mineralogy, A6ST Well

Depth	7317	7321	7324	7328	7329	7349	7351	7437	7439	7445
Minerals										
Quartz x	x	x	x	x	x	x	x	x	x	
Kspar x	x	x	x	x	x	x	x	x	x	
Plag	x	x	x	x	x	x	x	x	x	x
Calcite x	x	x	x	x			x			
Dolomite	x	x	x	x	x	x	x	x	x	
Siderite	x	x	x	x	x	x	x	x	x	x
Pyrite		x	x	x	x	x	x			
Apatite							x			
Ill/Sm x	x	x	x	x	x	x	x	x	x	
Kaolinite	x	x	x	x	x	x	x	x	x	x

Table 6. I/S determinations, A6ST well

Depth (MD, ft)	%I(MTU)	%I(EPR)
5801	10	•
5803	10	•
6827	20	•
6833	20	•
6843	20	•
7107	50	•
7269	50	•
7279	40	•
7283	40	•
7289	40	•
7313	40	•
7315	40	•
7316	40	•
7317	40	30
7319	45	•
7321	45	27
7323	50	•
7325	45	•
7327	45	•
7329	40	•
7313	40	•
7323	40	•
7329	40	35
7341	45	•
7343	50	•
7345	45	•
7347	45	•
7349	45	28
7349	40	•
7351	40	24
7353	45	•
7355	45	•
7357	50	•
7433	45	•
7435	50	•
7437	45	24
7439	45	23
7441	45	•
7443	40	•
7445	45	30
7324	•	22
7328	•	30

Table 7. Vitrinite reflectance data, A6ST well.

Depth (ft)	%Ro	No. readings	Mount type
5801	0.4	1	Thin section
5801	NDP		Whole-rock block
5803	0.48+/-0.05	6	Whole rock block
5803	NDP		Thin section
6233	0.32	1	Whole rock block
7104	0.43+/-0.18	2	Whole rock block
7104	0.44+/-0.05	3	Thin section
7107	0.49+/-0.10	5	Thin section
7114	0.40+/-0.08	4	Whole-rock block
7114	0.45+/-0.14	3	Thin section
7114	0.47+/-0.07	6	Whole-rock block
7269	0.43+/-0.14	5	Whole-rock block
7269	0.49+/-0.06	4	Thin section
7279	0.54	1	Whole rock block
7279	0.52+/-0.07	3	Thin section
7283	0.45+/-0.06	10	Thin section
7289	0.45+/-0.07	18	Whole-rock block
7327	0.58+/-0.05	22	Whole-rock block
7340	0.55+/-0.11	13	Whole-rock block
7344	0.54+/-0.13	13	Whole-rock block
7348	0.53+/-0.04	18	Whole-rock block
7440	0.54+/-0.08	13	Whole-rock block
NDP: No Determinations Possible			

Table 8. Carbon and oxygen isotope data, A6ST well

Depth (ft)	$\delta^{13}\text{C}$ (PDB)	$\delta^{18}\text{O}$ (SMOW)	Rock type
7107	-2.16	31.3	Undeformed
7114	-.66	30.4	Undeformed
7269	-5.39	27.5	Undeformed
7279	-5.29	26.1	Undeformed
7283	-4.76	23.8	Undeformed
7313	-2.46	23.4	Whole rock - fault
7321	-4.66	26.9	Whole rock - moderate deformation
7323	-5.25	24.5	Whole rock - fault
7434	-2.53	30.8	Whole rock - fault
7439	-2.45	29.4	Undeformed
7316	-4.03	25.6	Whole rock - fault
7319	-5.54	25.5	Whole rock - fault
7320	-5.42	25.3	Whole rock - fault
7437	-.12	31.0	Whole rock weak deformation
7317	-7.1	23.3	Calcite - moderate deformation
7320	-4.6	23.0	Calcite - moderate deformation
7324	-8.5	25.2	Calcite - moderate deformation
7328	-7.6	24.2	Calcite - weak deformation
7329	-8.2	23.2	Calcite - moderate deformation
7349	-5.9	25.3	Calcite - weak deformation
7351	-5.9	27.1	Calcite - undeformed
7445	-5.9	28.5	Calcite - weak deformation
7317	-3.9	30.6	Dolomite - moderate deformation
7320	-5.0	29.0	Dolomite - moderate deformation
7324	-1.8	29.3	Dolomite - moderate deformation
7328	-1.7	28.5	Dolomite - weak deformation
7329	-3.3	27.2	Dolomite - moderate deformation
7349	2.2	29.1	Dolomite - weak deformation
7351	1.0	30.7	Dolomite - undeformed
7445	.5	33.0	Dolomite - weak deformation
5801	-.27	30.1	Undeformed
5803	.69	30.4	Undeformed
6027	-3.07	26.5	Undeformed

Table 9. Vitrinite reflectance data, Block 330 wells.

Well Name	Interval (MD)	%Ro (+/- s.d.)	No. Readings
No. 5	6850-6880	0.41+/-0.05	4
	6880-6910	0.38	1
No. 7	6650-6680	0.37	1
	6680-6710	0.27+/-0.00	2
	6710-6740	0.45+/-0.05	2
C7	5650-5680	0.51+/-0.00	2
	5680-5710	0.45+/-0.05	6
	5710-6010	0.48	1
	6010-6040	0.44+/-0.07	5
A16	5450-5480	0.55+/-0.00	2
	5480-5510	0.46+/-0.07	2
A5	6920-6950	0.33+/-0.06	5
	6950-6980	0.52+/-0.01	2
	6980-7010	0.39+/-0.06	12

Brine Chemistry, Blocks 330 and 316

Steven Losh

Cornell University; Jim Wood, Michigan Technological Univ.

Twenty two samples of brine were collected from producing wells in South Eugene Island Blocks 330 and 316 (figure 1) by Dr. Lynn Walter and Anna Martini (University of Michigan) over a three-day period during January, 1994. Seventeen phases were analyzed at the University of Michigan (table 1), in addition to temperature at the wellhead, pH, density, and Sr isotopic composition (Table 2). Chemically, the brines are similar to those documented in nearby Plio-Pleistocene reservoirs by Land and MacPherson (1989). They are NaCl waters that exhibit a sizeable range of chloride content, from 19,900 to 103,100 mg/L (however, the low-salinity sample from the A10ST well is probably contaminated by completion fluid, as that well has only recently gone into production), but lie on a seawater-halite dissolution line (figure 2). Calcium concentration is somewhat higher than would be expected from dissolution of halite (figure 3), but may reflect dissolution of gypsum associated with salt. Sulfate concentration is unusually low, in most cases below the detection limit, and may reflect ongoing sulfate reduction. The brines appear to be seawater mixed with varying proportions of halite-saturated fluid, or seawater that has simply dissolved varying amounts of salt as it migrated. These fluids have been further modified by limited fluid-silicate interaction.

Iodine-129 dating has been carried out at the University of Rochester, under the direction of Dr. Udo Fehn, on nearly all brines collected during this study (table 3 and figures 7 through 10). This method yields apparent brine ages between 31 and 61 Ma considering only a cosmogenic source of ^{129}I . However, even when accounting for likely fissiogenic contributions, an early Cenozoic age of the brine is indicated, and significant vertical fluid flow is implied. It is not anticipated that dissolution of Gulf Coast evaporites would significantly affect the measured brine age, as these materials contain very low concentrations of iodine (U. Fehn, 1994, oral comm.); indeed, no correlation between iodine age and chloride concentration is present (figure 4). The brine age is likely strongly affected by the age of maturing kerogen from which much of the brine's iodine was derived, but even so, the ages imply that at least a component of the brines was present in rocks of at least mid-Cenozoic age.

Chloride concentration of the brines shows no systematic variation with depth (figure 5), nor does it appear to vary with respect to distance from faults, with one notable exception; however, it does show sizeable differences between reservoirs. It is highest in the shallowest reservoir, the GA (figure 6), about half as high in the underlying HB sand (figure 8), and high but variable in the deeper sands (figures 9 and 10). Chloride concentration also shows no noticeable change from upthrown to downthrown blocks (figure 9). As noted, chloride concentration in brines near faults is similar to that in brines far from faults, with the exception of the sample from the A2 well (OI-5 sand), which is unusually dilute for waters at this depth. This fluid may represent incorporation of water from shales undergoing dewatering below the OI sands. However, other brines collected near faults (the A6ST sample, for example, was taken from the KE sand, immediately above the 'A' fault) show no such decrease in chloride concentration. In a manner

analogous to the distribution of chloride concentrations, ^{129}I ages show no systematic variation with respect to faults (although the range of ^{129}I concentrations is small), nor do there appear to be significant age variations between reservoirs (figures 7 through 10).

The pronounced variations in brine chemistry between reservoirs and the evident compositional homogeneity within a reservoir, using chloride as a monitor, indicate that the brine entered the reservoirs at different times and/or from different directions, as opposed to a model in which a single stream of fluid migrated up the fault and leaked into each reservoir it passed by. For example, the GA2 sand contains the highest - salinity brines in the dataset, yet is the shallowest reservoir sampled. Brines that entered that reservoir necessarily bypassed the HB1 sand, in which brines have only half the salinity of the GA2 sand a few hundred feet above it. If $^{87}\text{Sr}/^{86}\text{Sr}$ ratios are interpreted as indicative of brine source (that is, neglecting water-rock interaction), comparison with the DSDP seawater Sr isotope curve (figure 11) implies that the least radiogenic brine with respect to Sr isotopes originated in 30 Ma sediments. This brine is also characterized by the lowest $1/\text{Sr}$ value in the dataset; other brines have higher $^{87}\text{Sr}/^{86}\text{Sr}$ and lower $1/\text{Sr}$ (figure 12) and thus appear to have been contaminated by a radiogenic component of sediment-derived strontium. The mid-Tertiary age deduced from Sr isotope ratios is consistent with the above iodine- ^{129}I data, and points to large-scale vertical migration of brine to its present location in the Pleistocene reservoir sands.

REFERENCE CITED

Land, L., MacPherson, G, 1989, Geochemistry of formation water, Plio-Pleistocene reservoirs, offshore Louisiana; Gulf Coast Assoc. Geol. Socs. Trans. vol 39, p 421-430.

TABLES

- Table 1. Brine chemical analyses, carried out at University of Michigan.
Table 2. Strontium isotope analyses, Block 330 brines, performed at University of Michigan
Table 3. Iodine-129 data for brine samples, analyzed at University of Rochester. Depth for the three samples from Block 316 are estimated at 7500 feet for the A4 and A8 samples, and 6700 feet for the A9.

FIGURES

- Figure 1. Location map for wells sampled in this study. Bottom-hole locations are shown. Structure contours are on the OI-1 sand (all structure contour maps in this report are from Holland et al (1990)).
Figure 2. Na⁺ vs Cl⁻ for brine samples, showing relationship to seawater evaporation trend. Samples plot on trend, implying dissolution of halite as the primary control on Na and Cl in these samples.
Figure 3. Ca⁺⁺ vs Cl⁻ for brine samples.
Figure 4. Cl⁻ vs Iodine-129 age for brine samples. Iodine age is not correlated with salinity, indicating it is not affected by extent of halite dissolution.
Figure 5. Cl⁻ vs depth for brine samples. Chloride concentration shows no correlation with depth per se, although it is correlated with particular reservoir sands, which, owing to folding and faulting, have overlapping depths in Block 330. The highest-salinity fluids are in the GA sand, indicating they have undergone a significantly different evolution with respect to interaction with salt than have brines in the deeper reservoirs.
Figure 6. Structure contour map on top of GA sand, showing chloride concentrations of brine samples from the GA sand.
Figure 7. Structure contour map on top of GA sand, showing iodine-129 ages of brine samples from the GA sand.
Figure 8. Structure contour map on top of HB sand, showing chloride concentration (large number) and iodine-129 age (small number) of brine samples from the HB sand.
Figure 9. Structure contour map on top of KE sand, showing chloride concentrations (large numbers) and iodine-129 ages (small numbers) for brine samples from sands as indicated next to the data points.
Figure 10. Structure contour map on top of OI-1 sand, showing chloride concentrations and iodine-129 ages of brine samples taken from the OI sand.
Figure 11. Brine ⁸⁷Sr/⁸⁶Sr vs time, showing DSDP seawater Sr isotope curve for the last 100 Ma. Block 330 samples shown in filled circles at 0 Ma. Lowest-⁸⁷Sr/⁸⁶Sr brine could have been derived from sediments of at least 30 Ma age
Figure 12. Brine ⁸⁷Sr/⁸⁶Sr vs 1/Sr, indicating mixing of less-radiogenic, low Sr (seawater) and more-radiogenic, high Sr (sediment) endmembers.

Table 2. Strontium isotopic ratios, Block 330 brine samples

Sand	Well	$^{87}\text{Sr}/^{86}\text{Sr}$
GA2	C2	0.71000
GA2	C13	0.70875
HB1	C3	0.70820
OI	A14	0.70833
OI5	A2	0.70804

2s for all analyses is 0.00002

Reservoir Diagenesis, SEI Block 330

Steven Losh

Cornell University, with contribution from Jim Boles, Univ. Calif. Santa Barbara

The diagenesis of Pennzoil's Block 330 reservoir sediments has been studied in order to assess the possible relationship of cementation and alteration of these rocks to the fault that has presumably provided a conduit for diagenetic fluids. Approximately 200 thin sections from sidewall cores of reservoir rocks throughout Block 330 have been examined for diagenetic effects; the GA, HB, JD, and OI reservoirs in particular have been studied in terms of cementation and grain alteration. In general, cement is sparse, less than 2 percent of the rock (in many cases, much less), and consists of calcite, ferroan dolomite, and siderite. Diagenetic pyrite, usually framboidal, is also present, whereas silica overgrowths are rare. Organic matter is scattered but ubiquitous, typically being found within foraminifera, as layer-parallel stringers in shale (especially in the KE sands), and as discrete bitumen "patches" in sands.

These observations were made as a complement to the petrographic analysis of sediments from the same reservoirs carried out by David K. Davies Associates for Pennzoil. It was originally anticipated that cementation or grain alteration may be more intense as the fault is approached, and this study focused on obtaining samples in traverses across faults and examining for grain alteration, specifically albitization and plagioclase dissolution. Diagenetic minerals as determined both by Davies Associates and in this study show no apparent relationship with distance from the fault in terms of their abundance or type (figure 1).

GA sands

Most of the sections are of sandy or silty shale to shaly silt; clean sand is not well-represented in this suite, probably in part because sidewall cores of sand disaggregate very easily. Calcite cement in silty rocks is sparse (up to 3%) and extremely fine-grained. Plagioclase commonly shows weak to moderate pitting, but in any given sample, most plagioclase grains show no albitization. It is likely that any albitized plagioclase in these sands has been reworked from an older sand. Detrital carbonate grains are common, in many cases comprising 5-20% of the grain population.

Dr. Jim Boles, University of California, Santa Barbara, concluded his examination of selected sidewall cores from the GA sand, Block 330, wells B16, A19ST, and B3ST. His report is as follows. Photographs are not included here.

"A petrographic study of 17 sidewall core samples of the "GA sand", Block 330 was undertaken to look for evidence of diagenesis resulting from fluid movement along faults. Results indicate that very little diagenesis has occurred.

The samples were received as loose particles and thus were prepared as grain mounts. Overall, samples are very fine to fine grain size sand with varying proportions of silt and clay matrix. Porosity could not be estimated from these samples due to their disaggregated condition.

The detrital components are quartz, K-feldspar, plagioclase, siliceous rock fragments, detrital carbonate shell material, micas, and trace minerals including glauconite, green hornblende, and garnet. A notable feature of some samples is the presence of zoned plagioclase feldspar indicating a hypabyssal or volcanic source component and rare volcanic rock fragments. No systematic changes in detrital or diagenetic mineralogy were noted with depth in the wells nor in comparison between wells.

Diagenetic smectite and illite are the most abundant authigenic phase but even these minerals do not exceed 10% by volume in the samples. The clays occur as thin rims on detrital grains and as a pore-filling cement. In many cases, diagenetic clay appears admixed with detrital clay matrix and it is difficult to distinguish the detrital from the authigenic phase. The samples with the most abundant, what is clearly authigenic clay, are B16@5074' which has up to 10% of small scattered lath-shaped birefringent illitic clay particles. Curiously, these crystals are length fast, whereas typical illite is length slow. Other examples of diagenetic clay are in the A19ST well where a birefringent (illitic?) clay forms thin rims about detrital grains or in some cases, pores are partially filled with a yellowish-green to yellowish-brown clay.

Diagenetic carbonate occurs in trace amounts in some samples. Typically it occurs as scattered subeuhedral to euhedral grains or in some cases as grain coatings. In some cases, such as B3ST @5917' and 5930', the yellowish-brown color or the carbonate indicates it is probably siderite. Similar appearing siderite is found in Cretaceous sands from the Alaska North Slope and in this case they can be shown to have formed near the sediment-water interface.

Syntaxial quartz overgrowths are very rare in these samples, indicating that they have not undergone silica cementation due to upwelling hot fluids. The few samples with quartz overgrowths occur as incipient syntaxial overgrowths on a few grains in a few samples. The rarity of the overgrowths indicates that they could be reworked.

Feldspar diagenesis is a sensitive indicator of changing burial conditions. Neither dissolution of feldspar nor *in situ* albitization of detrital plagioclase can be demonstrated in these samples. Albitized feldspar occurs in the samples but is in a mixed population with fresh plagioclase. This suggests that albitization is not an *in situ* process. In addition, zoned plagioclase, typically some of the most unstable feldspar, appears unaltered.

In summary, these samples are not extensively cemented. Clay minerals, which appear to be the dominant diagenetic phase, appear similar to those found in incipient diagenesis. The most compelling evidence for upwelling hot fluids from deep in the basin would be the presence of abundant authigenic silica. Such evidence is not found in these "GA" sand samples."

HB sands

Most sections are of moderately sorted shaly silts and shaly sands. Detrital calcite is common, in many cases comprising 10-20% of the rock. Authigenic calcite and ferroan dolomite occurs as ragged overgrowths on the detrital grains, and is thus more abundant in rocks containing more detrital carbonate. Aggregates and disseminations of extremely fine-grained siderite are common, comprising perhaps 2% of many sands. At most, diagenetic carbonate comprises 10% of the rock, and is always extremely fine-grained. Plagioclase dissolution is minor to non-existent in many of the silts, but is moderately advanced in others. Michel-Levy analysis of albite twin angles for unaltered plagioclase indicates the feldspars may be as calcic as An₆₀.

Diagenesis of the 70 examined HB sand samples (wells B16, B3ST, A7ST, C15ST, C13, C11, C9, C21, C2, #3, #4 (A1), A23, A19ST, C20, A6ST, A13, B12, C3, #1, #6; figures 2 - 12) is largely similar to that observed in the GA sand, except that carbonate (both detrital and authigenic) is slightly more abundant, and that dissolution of plagioclase, K feldspar, and in some cases quartz, is more common, in some cases involving all of the plagioclase and a significant percentage of other grains in a sample (particularly samples from C2, C9, and C13). The dissolution is manifest both in the forms of uncommon skeletal grains and as microporosity, which may affect up to 15-20% of the quartz and feldspar grains in a sample. Skeletal grains are interpreted as reflecting *in situ* dissolution, whereas the intensely-pitted grains are similar in

appearance to pitted grains described from the vadose zone (i.e., soil profiles) in humid regions. In at least one case (B16, 6144'), dissolution is inversely correlated with carbonate cement: where cement is abundant, feldspars are fresh, whereas uncemented zones contain pitted and rare skeletal plagioclase and K feldspar. This type of relationship indicates the dissolution is at least partly in situ, and that the carbonate cement in this sample predates at least some of the dissolution. Pronounced variations in proportion of pitted grains to unpitted ones exist over short vertical distances in the wells. Intergrown fine-grained calcite and dolomite were noted in two samples from the B16 well; these were analyzed for carbon and oxygen isotopic composition (dolomite: $\delta^{18}\text{O} = 26.0\text{-}26.6$ permil SMOW, $\delta^{13}\text{C} = 1$ to 1.9 permil PDB; calcite $\delta^{18}\text{O} = 23.1\text{-}23.4$ permil, $\delta^{13}\text{C} = 0.3$ to 0.5 permil). These diagenetic indicators show little to no apparent spatial relationship between extent of diagenesis and proximity to faults (figure 12); however, samples above the oil/water contact on the north side of a nearly east-west fault traversing the southern part of Block 330 have more carbonate cement and a higher proportions of pitted to unpitted grains than do samples south of this fault or samples below the O/W contact. There does not appear to be any correlation between abundance of pitted grains or authigenic carbonate and stratigraphic position within the HB "sand". More work is being done to assess the possibility of in situ dissolution; if such a process were occurring, it would be unusual given the relatively low temperature of the HB sand. In situ dissolution generally begins at about 80-100 C, whereas the HB sand is at temperatures closer to 60 C.

JD sands

These are mostly clean sand, with high porosity. Calcite cement is sparse, at most 3-4 modal percent in rocks containing detrital carbonate, and is absent in many cases. Plagioclase is pitted to varying extent in the sections: nearly all rocks show some pitting, and in some cases, up to half of the plagioclase shows weak to moderate dissolution. Clay coatings on sand grains are very rare; no pore-filling, authigenic clay has been noted.

OI sands

Clean to shaly silt and sand. Calcite cement is absent in most rocks, and is scarce (1%) at best. Several of the sands have clay coatings on sand grains or rare pore-filling "felted" clays. Plagioclase dissolution and pitting is weak, typically affecting 10 - 25% of the plagioclase grains in a given section.

FIGURES

Figure 1. Dissolution and carbonate cementation in sidewall cores of HB sands. Symbols for alteration type and degree as shown. Dissolution (called "albitization" on the figure): weak - 50% of plagioclase grains in sample show pitting, moderate - ca. 75% of plagioclase grains are affected; strong - virtually all grains are albitized. Carbonate cement: weak - 2-5%, moderate - 5 - 20%, strong - > 20%. Some samples consist of at least 50% mixed calcite and dolomite. Carbonate cement is always extremely fine-grained in these sediments. Symbols indicate a qualitative average of alteration observed in samples from a given well.

Figure 2. Well log for HB sand, C21 well. Symbols as for figure 1. Tick marks on depth axis indicate location of sidewall cores subjected to petrographic analysis. Absence of symbols next to a tick mark indicates alteration was of a lesser degree than that defined as "weak" in figure 1 caption.

Figure 3. Well log for HB sand, C9 well. See figure 2 caption.

Figure 4. Well log for OI sand, A23 well. See figure 2 caption.

Figure 5. Well log for HB sand, A19ST well. See figure 2 caption.

Figure 6. Well log for MG(?) sand, C20 well.

Figure 7. Well log for HB sand, A7ST well.

Figure 8. Well log for HB sand, B3ST well.

Figure 9. Well log for HB sand, B16 well

Figure 10. Well log for HB sand, C13 well.

Figure 11. Well log for HB sand, C15ST well.

Figure 12. Well log for HB sand, C2 well.

Temporal Variability in the Composition of Some Petroleum Fluids from Eugene Island Field-330 Over Short Time Scales

Mahlon C. Kennicutt II, Yaorong Qian and Adolfo G. Requejo
Geochemical and Environmental Research Group
Texas A&M University
College of Geosciences and Maritime Studies
833 Graham Road
College Station, TX 77845

Jean Whelan and Lorraine Eglinton
Department of Chemistry
Woods Hole Oceanographic Institute
Woods Hole, MA 02543

Introduction

While petroleum is often perceived as a rather uniform fluid, its composition, even within a field, can be quite heterogeneous (Baily et al. 1973; Milner et al. 1977; Hunt 1979; Tissot and Welte 1984; Connan 1984; Leythaeuser and Rückheim 1989). Variations in the composition of petroleum can occur due to many factors including source rock composition, thermal maturity, migration alteration, in-reservoir alteration, and mixing of fluids from multiple sources. The chemical characteristics of petroleum often provide clues for deciphering the evolution of a fluid in regard to temperature history, age of source rock, migration pathways, and the effects of post-generation alteration processes such as biodegradation, evaporative fractionation, water washing, in-reservoir maturation and gravity segregation. It has also been demonstrated that low rates of in-reservoir mixing of multiple charges of petroleum can lead to inhomogeneities (England et al. 1987; England and Mackenzie 1989; Karlsen and Larter 1989; Larter et al. 1989). These variations can be assessed on a variety of vertical and horizontal spatial scales. Regional (kilometers) trends in petroleum compositions provide insight into variations in organic facies, thermal maturity, reservoir filling history, and viable source horizons (England and Mackenzie 1989). Observations within a field can provide insight into post-generation alteration as well as communication amongst reservoirs, sands, and/or across fault blocks.

In contrast to spatial variations, temporal changes in fluid compositions have received little attention (**Table A. Time Scales - Jean Whelan**). Recent observations have led to the hypothesis that in certain geologic settings oil and gas may be migrating into producing reservoirs relatively recently compared to geologic time scales (Anderson et al. 1991a,b; Anderson 1993; Schumacher 1993; Whelan et al. 1994). A variety of circumstantial geological, geophysical and geochemical evidence has been presented in support of the "dynamic fluid injection" hypothesis. The evidence includes slower than

predicted rates of reservoir fluid depletion, coherence of pressure and temperature profiles, the existence of deep seated conduits for fluid migration, displacement of heat flow anomalies away from salt features, intense present-day surface hydrocarbon seepage, temporal changes in oil and gas compositions, and secondary injection of non-biodegraded fluids into reservoir biodegraded fluids (Whelan et al. 1994; Anderson 1993; Schumacher 1992, 1993; Holland et al. 1990; Barnard and Bastow 1991; Anderson et al. 1991a,b; Kennicutt 19__ (seepage)). To further define the origins of temporal variations in fluid compositions, the present study compares and contrasts the composition of fluids collected over an eight-year period at the site where "dynamic fluid injection" was first suggested, the Eugene Island-330 Field in the northwestern Gulf of Mexico.

The geologic setting and chemistry of fluids recovered from the EI-330 field have been discussed in detail elsewhere (Holland et al. 1990; Kennicutt et al. 1992; Whelan et al. 1994). More than 25 Pleistocene sandstones are produced at depths from 701 to 3658 meters (Holland et al. 1990). The EI-330 field consists of more than 100 oil and gas reservoirs that are separated by faults and permeability barriers. The field is considered to be one of the giant oil and gas fields of the world (Carmalt and St. Johns 1986). Fluid compositions are highly variable and different sands produce a variety of admixtures of gas, condensate, and oil. Differences in oil compositions are apparent vertically within the section as well as between fault blocks and within single reservoirs (Schumacher 1993; Whelan et al. 1994, 1995). Despite these variations in composition it has been argued on the basis of biomarker data, that the majority of fluids at EI-330 are derived from the same or similar source facies (Whelan et al. 1994). However, it has been recognized that different molecular weight ranges (boiling points) exhibit characteristics typical of a range of thermal maturities suggesting more than one infusion of fluids (Thompson and Kennicutt 1990). Reservoir petroleum across the Gulf of Mexico exhibits a high incidence of alteration due to non-thermal processes such as biodegradation, evaporative fractionation, migration contamination, and extraction by water (Thompson and Kennicutt 1990).

The objective of this study was to evaluate intra-field fluid compositions to document changes in fluid compositions over short-time scales (months to years). The first goal of the study was to minimize variations due to non-geochemical processes. Variations in fluid composition due to collection, storage and analytical methodologies must be carefully considered. Most surface collection techniques do not recover fluids in their natural state in the reservoir. Physical alterations due to depressurization and cooling are expected. Partitioning of compounds among phases upon depressurization has been demonstrated in the laboratory (Thompson 1987, 1988, 1990). Long-term storage of collected fluids can result in the loss of the more volatile fractions. Gas chromatographic data are strongly influenced by the conditions of the analysis. Operating conditions such as the gas stream split between the vent and the column can lead to significant fractionation of volatile compounds. Differences in the liquid phases of chromatographic columns determine the elution order and the degree of resolution of components in complex mixtures. Chromatographic temperature programs and column gas flows effect the detector response of analytes. Effects related to variations in apparent fluid composition due to analytical conditions, storage, and the method of sample collection must be clearly delineated if variations in reservoir fluid compositions are to be attributed to natural processes occurring over short-time scales (months to years).

Variability Due to Analysis, Storage, and Sampling Conditions

Oil (including condensate) samples were collected from the producing sands of EI-330 in 1985, 1988, and 1993 (Table 1). Oil and condensate samples were analyzed by high resolution capillary gas chromatography (GC) to quantify the percent composition of each fluid from propane to n-C₃₄ (Kennicutt et al. 1992). Samples were also analyzed using a second gas chromatographic column to provide confirmation of peak identities.

Comparison of the results for samples collected and analyzed in 1988 and re-analyzed in 1994 provide an assessment of storage effects on fluid compositions and a comparison of analytical methodologies. An oil sample was also analyzed six times and then re-analyzed six months later to assess the reproducibility of successive injections and the effects of storage.

Replicate analyses were highly reproducible from one injection to the next. For the majority of the compounds the integrated peak areas exhibited less than $\pm 5\%$ coefficient variation for six replicates (Figure 1A). As expected, the coefficient of variation is directly related to the concentration of the compound being analyzed. Compounds accounting for less than 0.5% of the mixture exhibited larger coefficients of variation due to the precision of integrating small chromatographic peaks. However, a coefficient of variation of less than $\pm 10\%$ was obtainable even for minor oil components. When the average results of six replicate analyses were compared to the results of an analysis conducted six months earlier, most compounds, with the exception of C3-C4 compounds, were within $\pm 5\%$ of the mean area of the later analyses (Figure 1B). The C3 and C4 compounds were reduced by 20 to 30% in the later analyses. This suggests that under these storage conditions, gases dissolved in the oil were partially lost. However, for compounds with five or more carbons the reproducibility over time approached that of replicate injections.

Comparison of the analyses of forty-two EI-330 oil samples analyzed in 1988 and then re-analyzed in 1994 showed significant variations in composition (Figure 1C). On average, the C3-C5 compounds had greater relative abundances in the 1994 analysis than in 1988. Intuitively, the C3 and C4 compounds might have been lost during storage as already demonstrated for a six month storage period. On the contrary, the most volatile components accounted for more of the gas chromatographically resolvable compounds after storage for six years. Variations in compositions between the two analyses were also apparent as over- and under-estimates (Figure 1C). The most likely explanation is that gasoline range compounds were significantly effected by the chromatographic conditions, especially the split ratio which is known to fractionate compounds based on boiling point or volatility. The over- and under-estimates can be partially attributed to the improved resolution of components using later analytical methodologies. Peaks occurring as shoulders in the 1988 analysis were either merged or more completely separated depending on the particular analyte. These differences in compositions suggest that variations due to analytical technique must be minimized to ensure comparability of results. Therefore all samples were reanalyzed within as short a period of time as possible under nearly identical chromatographic conditions. The following comparisons only utilize the later analytical results thus minimizing variations due to analytical conditions.

The effect of sampling technique on fluid chemistries is uncertain. Sampling which involves depressurization and cooling is known to cause changes in fluid chemistry (Price et al. 1983). Single step depressurization experiments produced relatively small variations in composition, whereas multiple episodes of depressurization are believed to cause fairly dramatic shifts in chemical composition (Thompson 1987, 1988, 1990; Larter and Mills 1991; Whelan et al. 1994). However, changes due to sample collection in this study equally affect all samples and only one episode of depressurization occurred during sampling. Larter and Mills (1991) reported little change in gasoline range hydrocarbon compositions during a single stage depressurization and phase separation at STP.

(Any other evidence or arguments to support our case?)

Origins of Fluids in EI-330 Field

Identical biomarker distributions and stable carbon isotope values (Holland et al. 1990; Kennicutt et al. 1992; Whelan et al. 1994) indicate that the fluids in the various reservoirs of EI-330 field have a common source.

(Rick - biomarkers/also gas data, etc.?)

Even though hydrocarbons in the GA and HB sands are relatively depauperate of C₉₊ n-alkanes, these fluids contain large amounts of hydrocarbons with three to eight carbons. The API gravities (23-25° API) of the fluids from the GA and HB sands are in the range of a normal oil (Holland et al. 1990) despite the abundant light hydrocarbons. The co-occurrence of these light hydrocarbons with low API gravity fluids and the reduced C₉₊ aliphatic hydrocarbons suggests that the light hydrocarbons were added to these reservoirs after biodegradation had proceeded to an advanced stage (Whelan et al. 1994). This process has also been described for Trinidad Basin and Ecuadorian Oils (Requejo 19__; Sofer 19__). **(Rick--references and other examples.)**

Spatial Variations in Fluid Compositions

Vertical spatial variations in hydrocarbon compositions are significant amongst producing sands in the EI-330 field. The heterogeneity in fluid compositions among sands is believed to be primarily caused by post-generation alteration processes such as re-migration, biodegradation, and phase separation (Whelan et al. 1994). Among these processes, biodegradation causes some of the most dramatic changes in fluid compositions.

Variability within a sand (GA-2) and a block (A) are compared in Figure 2A. Variability within the sand and the block are similar and significantly greater than analytical variability. However increased variability in normal alkanes with 9 to 12 carbons, isoprenoids with 11 and 13 carbons, and the low molecular weight aromatics benzene and toluene in the GA-2 sand is apparent (Figure 2A). It is known that in this shallow sand reservoir biodegradation is quite common. The observed lateral variability in the GA sand fluids is most likely the result of variations in the degree of degradation. Degradation has been observed to be most rapid in alkanes with 9-10 carbons (Thompson 19__). The variability in benzene and toluene content is most likely related to the intensity of water washing. These two aromatic compounds are more water soluble than aliphatic hydrocarbons of similar molecular weight. Individual locations within a sand have been subjected to differing intensities of biodegradation and water washing.

A more detailed look at variability between sands and between fault blocks confirm these interpretations. Deeper in the section degradation decreases and the fluids within a given sand are more uniform (Figure 2B). Therefore spatial variability can be most closely linked to in-reservoir alteration processes. The greatest variability in a fluid is in the shallowest sand (GA-2) which also contains the most altered fluids. Samples from other sands are less degraded or undegraded. Variability within a fault block reflects vertical spatial variability in fluid compositions (Figure 2C). The characteristics of fluids within a fault block are controlled by the distribution of samples among the producing sand. For example, the fault block B sample collection contains a large number of samples from the GA-2 sand and thus the observed variability is primarily related to shallow reservoir alteration processes. However, it should be noted that fluids from the same sand but from different wells show variations on the order of ~25-50%.

Another cause of spatial heterogeneity of hydrocarbon compositions in reservoirs is differences in the permeability of the reservoir sands (England et al. 1987; Leythaeuser and Rückheim, 1989; Horstad et al. 1990; Hillebrand and Leythaeuser, 1992). Low permeability can restrict the lateral diffusion and mixing of hydrocarbon fluids. The porosity and permeability of sands in the EI-330 field are high, with an average porosity of 30% (Holland et al. 1990). Permeability is in the range of 6 md to 6 darcys, with 80% of the sands having permeability of greater than 100 md (Holland et al. 1990). The heterogeneity in compositions within sands may be partially the result of restricted diffusion and mixing however the difference between sands is most likely related to the history of hydrocarbon charge.

Temporal Variability in Fluid Compositions

The amount of low molecular weight to high molecular weight hydrocarbons in fluids from the same well and sand within the EI-330 field increased with time over an eight year period (Figure 3). Gasoline hydrocarbon concentrations were highest during the latest samplings in many samples. Specifically, examining the GA-2 sands between 1988 and 1993 an envelope of compounds is recognizable as an addition. The additions include cyclohexane and a range of hydrocarbons with 7 and 8 carbons. The normal alkanes are particularly enhanced. These differences are most clearly apparent in the GA sand since most of the compounds in this carbon range were greatly reduced in the original charge due to biodegradation and water washing. The additional fluid is of a composition typical of a condensate.

The hydrocarbon ratios proposed by Thompson (1983; 1987) varied consistently from 1985 to 1993 (Table 2). The H, I, and F parameters are believed to reflect fluid maturity (Thompson 1983; 1987). These ratios increased from mature in 1985 samples to super-mature for most of the samples in 1993. The presence of abundant light hydrocarbons in the biodegraded GA and HB sands, the increase in the amounts of light hydrocarbons relative to the higher molecular weight compounds in the later samplings, and the increase in the maturity of light hydrocarbons in the latest samplings all point to a systematic variation in the light hydrocarbon compositions over a period of years.

The Origins of "Injected" Hydrocarbons

The variation in the chemical composition of fluids from the sands of the EI-330 field over short-time scales indicates an influx of fluid into these reservoirs in the past several years. The observed temporal changes could be explained by including localized and lateral migration, migration from deeper intervals, and/or production induced depletion of the reservoir.

An influx of fluids from adjacent less permeable sands to the primary reservoir bodies as the field was depleted has been suggested. The concept of "feeder pays" was suggested by Holland et al. (1990) to explain the overproduction for the GA sands. It was suggested that even though adjacent sandstones had little capacity for significant lateral flow they may recharge the more permeable productive zones. However, the temporal change in fluid chemistry on the EI-330 field was characterized as an increase in fluids of higher maturity. In contrast, Leythaeuser and Rückheim (1989) observed that fluids in high porosity/high permeability sand intervals bear a higher proportion of saturated hydrocarbons and have a higher apparent maturity compared to fluids from lower porosity/lower permeability zones. Therefore it would appear that adjacent "feeder pays" cannot be attributed with recharging the adjacent high porosity zones since it would be hypothesized that less mature fluid would arise from the lower permeability zones with time. Another words, the initial maturity of the fluids charging the sands could not be exceeded and yet maturity increases far beyond that documented throughout the field.

If the change in fluid composition was due to injection from much deeper strata, the latest influx of hydrocarbons would be expected to have had a more advanced thermal history different than the fluids originally emplaced. As well, the apparent age of the latest arriving hydrocarbons would be different from those of the originally reservoirized hydrocarbon. Young et al. (1977) used the relative molar concentrations of paraffins, naphthenes, and aromatics in the light hydrocarbon range (C₅-C₇) and the relative concentrations of the naphthenes with different numbers of rings in higher molecular weight (C₁₅+) hydrocarbons to calculate the ages of these hydrocarbons. The rationale was that the chemical composition of an oil from a single source is determined by the combined effects of time and temperature. With increased time and temperature, the chemical composition of the oil gradually shifts according to chemical kinetics. Based on this rationale the ages of several hundred oil samples were calculated.

Based on the equations and constants given by Young et al. (1977), the relative concentrations of naphthenes (C_n , relative to paraffins and aromatics) and the mean thermal history of light hydrocarbons in EI-330 field were calculated (Table 2). Assuming that the thermal history during and after the generation of hydrocarbons is mostly responsible for the variation of the C_n values observed in the oils and assuming the temperatures of the reservoirs have not changed after the emplacement of oil in these sands, the apparent ages of the light hydrocarbons were calculated using the current reservoir temperatures and the C_n values.

The relative concentrations of naphthenes decreased uniformly from 0.35 in 1985 samples to about 0.25 in 1993 samples for all the reservoirs with the exception of GA-2 sand where the C_n value decreased from 0.4 to 0.34 over the same time period (Table 2). This rapid diminishing of naphthenes might be the result of a temperature-time effect. With increased exposure to high temperature, the oil would become more mature (more paraffinic). However, if the C_n values had decreased from 0.35 to 0.25 within only 8 years at the current reservoir temperatures (55 to 86°C) solely by the effect of temperature, then the C_n values of all of the fluids now in reservoirs should be much lower and the hydrocarbons should have been extensively cracked to gases. A more plausible explanation of the high C_n values of the hydrocarbon fluids at 1985 (0.35) and the rapid decrease to lower values (0.25) over the eight year period is that highly mature hydrocarbons have been added lowering the C_n values of the original hydrocarbon charge. Based on the analyses of several hundred different-aged oil samples, a decrease in C_n value from 0.40 to 0.25 should be expected to take millions of years, depending on the temperatures experienced (Young et al. 1977).

The calculated ages of these oils lie between 8 and 133 million years (Table 2). Given the age of the reservoir sands of 1 to 2 million years (Pleistocene), the calculated ages of the hydrocarbons are substantially older than the age of the reservoir sands. However, the age of the hydrocarbons was calculated based on current reservoir temperatures. Petroleum must have been generated at higher temperatures in deeper sources than the present day reservoirs of EI-330. Young et al. (1977) and Quigley and Mackenzie (1988) concluded that temperature is the most critical factor that influences the generation, maturity, and compositions of oils and time is believed to be less influential than temperature (Quigley and Mackenzie, 1988, Mango, 1990, 1991). If the hydrocarbons were indeed derived from deeper sources (either from source rocks or deeper reservoirs), then higher temperatures should be used in the age calculations. Using the minimum hydrocarbon formation temperatures of 100°C to 150°C (e.g. Quigley and Mackenzie, 1988) and assuming a constant thermal history, the calculated ages are substantially lower than the ages summarized in Table 2. The ages range from 12 to 59 million at 100°C and 4 to 20 million years at 150°C, respectively. This wide variation in the calculated ages of the light hydrocarbons might indicate the presence of hydrocarbons of different ages in these reservoirs. The variation is most prominent among different sampling periods. The ages of the hydrocarbons at the same sampling times are similar between reservoirs. One exception is the GA sands where biodegradation may have obscured the age calculations. In addition, the ages of the hydrocarbons during the earlier sampling period, particularly 1985, are low ranging from 22 to 42 million years based on the current reservoir temperature. The ages are 15 to 21 millions years if 100°C is used in the calculation. These two groups of values are similar to the values reported by Young et al. (1977) for Eugene Island. The calculated ages of the light hydrocarbons are much older for samples from 1993 than those from 1988 and 1985 suggesting a further influx of highly mature (older age and/or higher temperature) hydrocarbons. The source of these hydrocarbons must be substantially deeper in the section and at much higher temperatures. If this is the case, the C_n values and their changes over the past several years in all the reservoirs

(including GA-2 sand) could be explained by the ongoing process of "dynamic fluid injection".

Assuming the hydrocarbons were generated and emplaced in these reservoirs at similar time (i.e. the age of these fluids are similar) their thermal history should also be similar, or more precisely, the hydrocarbons in the shallow reservoirs should have experienced slightly less thermal stress than the deeper ones because the temperature of the shallow reservoirs are lower. The difference in the calculated mean thermal history (mean temperatures) between the shallow reservoirs at each using the OI from that time as a reference sampling is listed in Table 3. For fluids in the OI sand, the deepest sand, secondary processes such as biodegradation are minimal. With the exception of the GA-2 sand and the HB sand, the difference in the temperatures between each reservoir and that in the OI sand at each sampling is small, suggesting that the thermal history of the fluids was similar. This conclusion agrees with oil maturities calculated from biomarkers and aromatic hydrocarbons (Whelan et al. 1994, 1995).

The calculated temperatures in GA and HB sands are substantially lower than the others. Several possible mechanisms can result in these lower calculated temperatures. The amounts of light hydrocarbons that were injected into the GA and HB sands might be small, whereas the amount of injection into the OI sand might be large. As a result, the calculated thermal histories of GA and HB sands relative to the OI sand are low. Alternatively, light hydrocarbons in GA and HB sands have experienced biodegradation (Whelan et al. 1994) because of the lower reservoir temperatures and shallower depth. Biodegradation selectively removes n-alkanes leading to higher naphthene concentrations relative to paraffins and aromatics (higher C_n values). If this second interpretation is correct, the light hydrocarbons in GA and HB sands would appear to be less mature and have lower apparent temperature histories. The calculated temperatures and ages would also be biased on the low side.

The ages of the hydrocarbons in all of the reservoirs are assumed to be similar and the average thermal history of the hydrocarbons in the OI sand over their life time is 86°C (the current reservoir temperature, the actual thermal history of the hydrocarbons in OI sand might be slightly higher than this value), then the mean temperatures of the hydrocarbons in other reservoirs at different sampling periods can be calculated based on the measured C_n values for each reservoir at each sampling (Table 4). These calculated temperatures are substantially higher in the 1988 and 1993 samplings than temperatures during the 1985 sampling. In addition, the calculated temperatures are substantially higher than the current reservoir temperatures for all the samples collected in 1988 and 1993. This higher temperature (higher thermal history) indicates that the light hydrocarbons were injected into these reservoirs recently from a deep, high maturity sources. As a result, the calculated thermal history (time-temperature effect) is higher in 1988 and in 1993 due to a continuing input of highly mature fluids. The increased calculated temperatures of GA sand in 1988 and 1993 is consistent with the injection of high maturity (high temperature or old aged) fluid into the GA reservoir in recent years, in spite of biodegradation which lowered the calculated apparent temperature. The calculated temperatures for the hydrocarbons in most of the reservoirs in 1988, and particularly in 1993, are close to the temperatures of the proposed source rock currently generating hydrocarbons (150 to 170°C; Holland et al. 1990).

The H (heptane ratio), I (isoheptane ratio), and F (paraffinity parameter) values in all the samples show a consistent increase from 1985 to 1993 sampling period for each reservoir. Thompson (1983; 1987) proposed that these parameters reflect the maturity levels of oils, although Mango (1990) disputed this interpretation by arguing that the ratios might be controlled by kinetic mechanisms during the formation of hydrocarbons.

(Jean Whelan - Mango/Thompson controversy)

With an increase in maturity, these parameters should increase (Thompson, 1983, 1987). The consistent, large increases in these parameters from 1985 to 1993 in all samples (Table 2) is consistent with fluid injection during that period. Such an input of high maturity, low carbon-number hydrocarbons derived from deep sources into these reservoirs would cause a rapid and concordant increase in these parameters. The relatively low values of H, I, and F parameters in GA and HB sands as compared with those of deeper reservoirs are probably the result of incipient biodegradation (Thompson, 1983; 1987; Whelan et al. 1994).

In contrast to EI-330, the C_n values from nearby South Marsh Island Block 128 (SMI-128) are nearly constant for all the sands, ranging from 0.32 to 0.34. The calculated ages of the hydrocarbons are in the range of 40 to 50 million years using the current reservoir temperatures. The H, I, and F parameters are also constant for all producing sands, with values of 22 to 25, 0.4 to 0.6, and 0.6 to 0.8, respectively. However, the SMI-128 field was not sampled at different production periods, as was EI-330.

Conclusions

Systematic changes in fluid chemistry have occurred over the time-scales of years at the EI-330 field. The changes are consistent with an on-going infusion of a relatively high maturity condensate fluid. Most evidence suggests that this change is a direct result of the influx of mature fluid from deep in the subsurface. One unknown is whether continued production of a field over long periods of time is sufficient to deplete the reservoir fluid to a degree that a compositional shift is observed. The EI-330 field is a mature field and believed to be in its decline, however less than 50% of the estimated reserves will be produced over the life-time of the field. The large amounts of unrecoverable fluids might argue against a shift in composition due to production. Intuitively it might be argued if anything was depleted over the lifetime of a field it would be the most volatile gaseous compounds that would be preferentially removed. This trend is contrary to the observed compositional variations where apparent maturity increases with time.

A range of observations suggest that fluids are being injected into the petroleum system of the EI-330 field at the present day causing measurable changes in fluid composition. If production induced changes in fluid composition are negligible, additions of highly mature fluids must be moving into the shallower reservoir sands from deeply seated horizons that are generating hydrocarbon fluids today or in the recent past. This "dynamic injection" has resulted in compositional variations in fluids reservoir in the EI-330 field that occur on time-scales as short as months.

REFERENCES

- Anderson, R.N. 1993. Recovering dynamic Gulf of Mexico reserves and the U.S. energy future. *Oil and Gas Journal*, 26 April: 85-91.
- Anderson, R.N., M.A. Hobart, C.R. Wilkinson, and H.R. Nelson. 1991a. Active fluid flow in the Eugene Island area, offshore Louisiana. *Geophysics: the Leading Edge of Exploration*, April: 12-17.
- Baily, N.J.L., A.M. Jobson, and M.A. Rogers. 1973. Bacterial degradation of crude oil: comparison of field and experimental data. *Chem. Geol.* 11: 203-221.
- Barnard, P.C. and M.A. Bastow. 1991. Hydrocarbon generation, migration, alteration, entrapment and mixing in the Central and Northern North Sea. In: W.A. England and A.J. Fleet, eds., *Petroleum Migration*. Geological Society Special Publication No. 59: 167-190.
- Carmalt, S.W. and B. St. John. 1986. Giant oil and gas fields. In: M.T. Halbouty, ed., *Future petroleum provinces of the world*. American Association of Petroleum Geologists Memoir 40: 11-54.
- Connan, J. 1984. Biodegradation of Crude Oils in Reservoirs. In: J. Brooks and D.H. Welte, eds., *Advances in Petroleum Geochemistry*. Academic Press, London, pp. 299-335.
- England, W.A. and A.S. Mackenzie. 1989. Some aspects of the organic geochemistry of petroleum fluids. In: H.S. Poelchau and U. Mann, *Evolution of Sedimentary Basins*. *Geol. Rdsch.*
- England, W.A., A.S. Mackenzie, D.U. Mann, and T.M. Quigley. 1987. The movement and entrapment of petroleum fluids in the subsurface. *J. Geol. Soc. London* 144: 327-347.
- Hillebrand, T. and D. Leythaeuser. 1992. Reservoir geochemistry of Stockstadt oilfield: compositional heterogeneities reflecting accumulation history and multiple source input. *Advances in Organic Geochemistry* 19: 119-131.
- Holland, D.S., J.E. Leedy, and D.R. Lammlein. 1990. Eugene Island Block 330 field—U.S.A., Offshore Louisiana. *AAPG Treatise of Petroleum geology, Atlas of Oil and Gas Fields, Structural Traps III*, pp. 103-143.
- Horstad, I., S.R. Larter, H. Dypvik, P. Aagaard, A.M. Bjørnvik, P.E. Johansen, and S. Eriksen. Degradation and maturity controls on oil field petroleum column heterogeneity in the Gullfaks field, Norwegian North Sea. *Advances in Organic Geochemistry* 16: 497-510.
- Hunt, J.M. 1979. *Petroleum Geochemistry and Geology*. Freeman, San Francisco.
- Karlsen, D.A. and S. Larter. 1989. A rapid correlation method for petroleum population mapping within individual petroleum reservoirs—application to petroleum reservoir description. In: R. Steel, ed., *Correlation in Hydrocarbon Exploration*. Graham and Trotman, London.
- Kennicutt II, M.C., T.J. McDonald, P.A. Comet, G.J. Denoux, and J.M. Brooks. 1992. The origins of petroleum in the northern Gulf of Mexico. *Geochim. Cosmochim. Acta* 56: 1259-1280.
- Larter, S.R., K.O. Børlykke, D.A. Karlsen, T. Nedkvitne, T. Eglinton, P.E. Johansen, D. Leythaeuser, P.C. Mason, A.W. Mitchell, and G.A. Newcombe. 1989. Determination of petroleum accumulation histories. Examples from the Ula field, Central Graben, Norwegian North Sea. In: A.T. Buller, ed., *North Sea Oil and Gas Reservoirs*. Graham and Trotman, London.
- Leythaeuser, D. and J. Rückheim. 1989. Heterogeneity of oil composition within a reservoir as a reflection of accumulation history. *Geochim. Cosmochim. Acta* 53: 2119-2123.

- Mango, F.D. 1990. The origin of light hydrocarbons in petroleum: a kinetic test of the steady-state catalytic hypothesis. *Geochim. Cosmochim. Acta* 54: 1315-1323.
- Milner, C.W.D., M.A. Rogers, and C.R. Evans. 1977. Petroleum transformation in reservoirs. *J. Geochem. Explor.* 7: 101-153.
- Quigley, T.M. and A.S. Mackenzie. 1988. The temperatures of oil and gas formation in the sub-surface. *Nature* 339: 549-552.
- Schumacher, D. 1993. Eugene Island Block 330 Field, Offshore Louisiana: Geochemical Evidence for Active Hydrocarbon Recharging. AAPG Ann. Convention Abstracts, New Orleans, April.
- Thompson, K.F.M. 1983. Classification and thermal history of petroleum based on light hydrocarbons. *Geochim. Cosmochim. Acta* 47: 303-316.
- Thompson, K.F.M. 1987. Fractionated aromatic petroleum and the generation of gas-condensates. *Org. Geochem.* 11: 573-590.
- Thompson, K.F.M. 1988. Gas-condensate migration and oil fractionation in deltaic systems. *Marine Petrol. Geol.* 5: 237-246.
- Thompson, K.F.M. 1990. Contrasting characteristics attributed to migration in petroleum reservoirs in clastic and carbonate sequences in the Gulf of Mexico region. Petroleum Migration Symposium, 1989. Special Publication. Geological Society of London.
- Thompson, K.M. and M.C. Kennicutt II. 1990. Nature and frequency of occurrence of non-thermal alteration processes in offshore Gulf of Mexico petroleum. In: D. Schumacher and B.F. Perkins, eds., *Gulf Coast Oils and Gases*, Proc. Ninth Ann. Research Conf., pp. 199-218. SEPM.
- Tissot, B.P. and D.H. Welte. 1984. *Petroleum Formation and Occurrence*. Springer-Verlag, Berlin.
- Whelan, J.K., M.C. Kennicutt II, J.M. Brooks, D. Schumacher, and L.B. Eglinton. 1994. Organic geochemical indicators of dynamic fluid flow processes in petroleum basins. *Org. Geochem.* 22: 587-615.
- Young, A., P.H. Monaghan, and R.T. Schweisberger. 1977. Calculation of Ages of Hydrocarbons in Oils—Physical Chemistry Applied to Petroleum Geochemistry. AAPG Bull. 61: 513-600.

Table 1. List of the samples analyzed in the present study

No. of samples	No. of wells	Producing sand	Depth range (ft)	Fluid type	Fault block
1985					
2	2	GA-2	4317-5044	oil	B
3	3	HB-1	5380-5722	oil	B
1	1	KE-2	9113-9138	gas/oil	B
1	1	LF	8332-8410	gas/oil	B
2	2	OI-1	8643-8653	gas/oil	A, B
1988					
11	11	GA-2	4317-5509	oil	B
9	9	HB-1	5266-6342	oil	B
1	1	HB-1B,2	6064-6117	oil	B
1	1	HB-3	6980-7026	oil	B
5	5	JD	6616-7278	gas	A, B, C, D
2	2	LF	7750-7881	gas/oil	A, B
2	2	MG-1,2	7920-8165	gas/oil	B, C
1	1	MG-4	8268-8286	gas/oil	B
1	1	NH	8348-8479	gas/oil	A
7	7	OI-1	7450-8480	gas/oil	A, B
2	2	OI-1,2	8840-8873	gas/oil	B
1993					
10	5	GA-2	4317-5805	oil	B
1	1	GA-5	5802-5856	oil	A
3	2	HB-1	5380-5720	oil	B
2	1	HB-1B,2	5194-5224	oil	B
1	1	HB-2	6892-6918	oil	B
1	1	HB-3	6594-6608	gas/oil	B
4	4	IC-4	5798-7588	gas/oil	A
4	4	JD	6508-7278	gas	A, B, C, D
4	3	KE-2	6704-7150	gas/oil	A, B, C
3	3	LF	7734-8104	gas/oil	A
2	1	MG-1,2,3,4	6850-6974	gas/oil	A
4	3	NH	7361-8479	gas/oil	A, B, C
10	5	OI-1	7412-8130	gas/oil	A
2	2	OI-2	7958-8756	gas/oil	A, B
1	1	OI-5	7646-7671	gas/oil	D

Table 2. The relative molar concentrations of naphthenes, maturity level and calculated ages of light hydrocarbons in EI-330 reservoirs

Sand	Year ¹	C _n ²	H ³	I ³	F ³	Age ⁴
GA-2	1993	0.337	18.5	1.9	0.6	70
	1988	0.375	16.2	1.7	0.5	38
	1985	0.409	13.1	1.6	0.4	8
HB-1	1993	0.284	21.9	1.8	0.9	116
	1988	0.306	17.8	1.8	0.7	93
	1985	0.348	16.5	1.7	0.6	42
HB-1,2	1993	0.294	19.1	1.7	0.8	105
	1988	0.315	15.4	1.5	0.6	85
IC-4	1993	0.264	28.3	2.1	1.2	133
JD	1993	0.262	35.3	2.5	1.7	128
	1988	0.280	37.4	2.5	1.7	110
KE-2	1993	0.254	35.2	2.6	1.7	118
	1985	0.355	20.2	2.2	0.8	39
LF	1993	0.242	30.5	2.2	1.4	120
	1988	0.258	32.6	2.5	1.5	106
	1985	0.357	22.6	2.1	0.8	35
MG-1,2,3,4	1993	0.263	38.3	2.6	1.8	94
MG-1,2	1988	0.275	33.2	2.4	1.4	85
NH	1993	0.264	29.7	2.2	1.2	89
	1988	0.295	28.0	2.0	1.1	67
OI-1	1993	0.257	29.1	2.2	1.2	73
	1988	0.271	28.8	2.1	1.1	65
	1985	0.362	22.0	2.2	0.7	22

1. Date of sampling (1985 is actually over the time of 1985 to 1988).
2. Relative molar concentration of naphthenes (Calculated by the formula of Young et al. 1977).
3. H, I, and F are the parameters of Thompson (1983), which were proposed to reflect maturity level of hydrocarbons.
4. Ages calculated by Eq. 3 (in million year) using current reservoir temperature.

Table 3. The difference (°C) in the calculated temperatures of light hydrocarbons among the reservoirs (relative to OI sand at each sampling) based on the assumption that the hydrocarbons have similar ages at each sampling period.

Sand	1985	1988	1993
GA-2	-43	-48	-33
HB-1	-1	-13	-9
HB-1,2	-- *	-16	-13
IC-4	-	-	-2
JD	-	-3	-2
KE-2	+6	-	+1
LF	+4	+4	+4
MG-1,2,3,4	-	-	-2
MG-1,2	-	-1	-
NH	-	-11	-2
OI	0	0	0

*. Sample not available.

Table 4. The mean temperature (°C) that the hydrocarbons have experienced, assuming the ages of the hydrocarbons are similar to that of the hydrocarbons in OI sand at 1985 sampling.

Sand	1985	1988	1993	Current Temp ¹
GA-2	23	76	101	55
HB-1	85	121	132	60
HB-1,2	-- ²	116	127	60
IC-4	–	–	141	61
JD	–	133	141	63
KE-2	92	–	144	68
LF	90	143	150	71
MG-1,2,3,4	–	–	141	74
MG-1,2	–	136	–	74
NH	–	126	141	76
OI	86	137	144	86

1. Current reservoir temperature. If there was no secondary processes, the calculated temperatures should be similar among the sampling periods.
2. Sample not available.

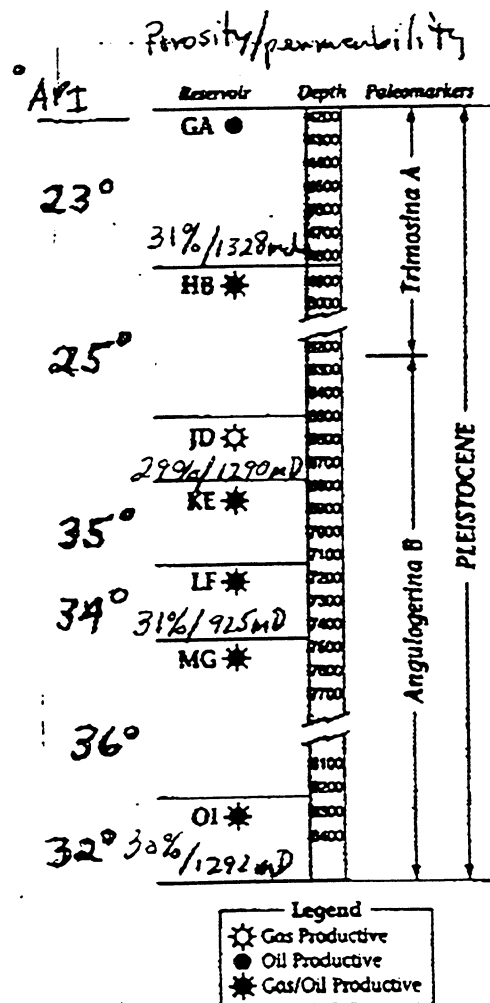
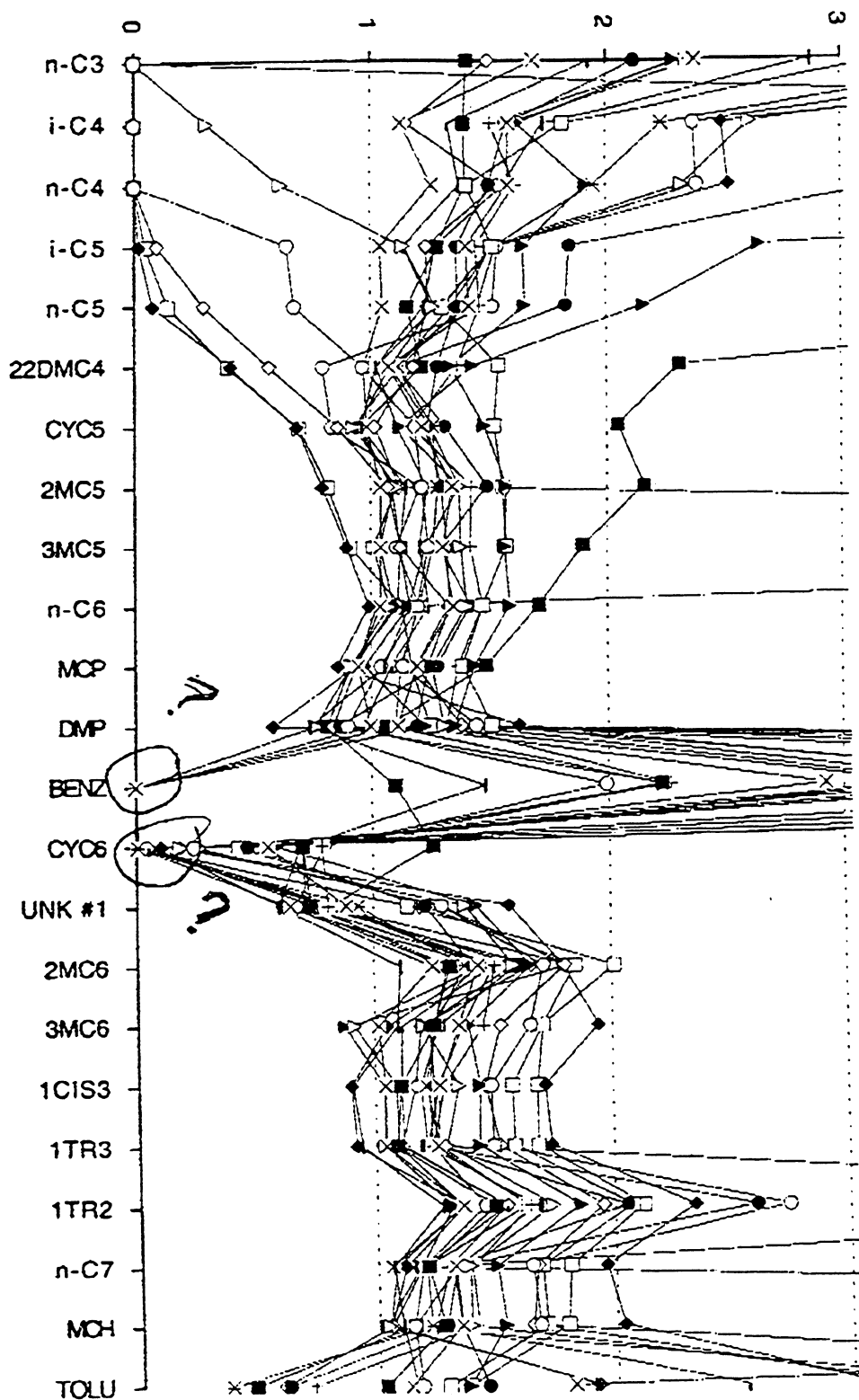
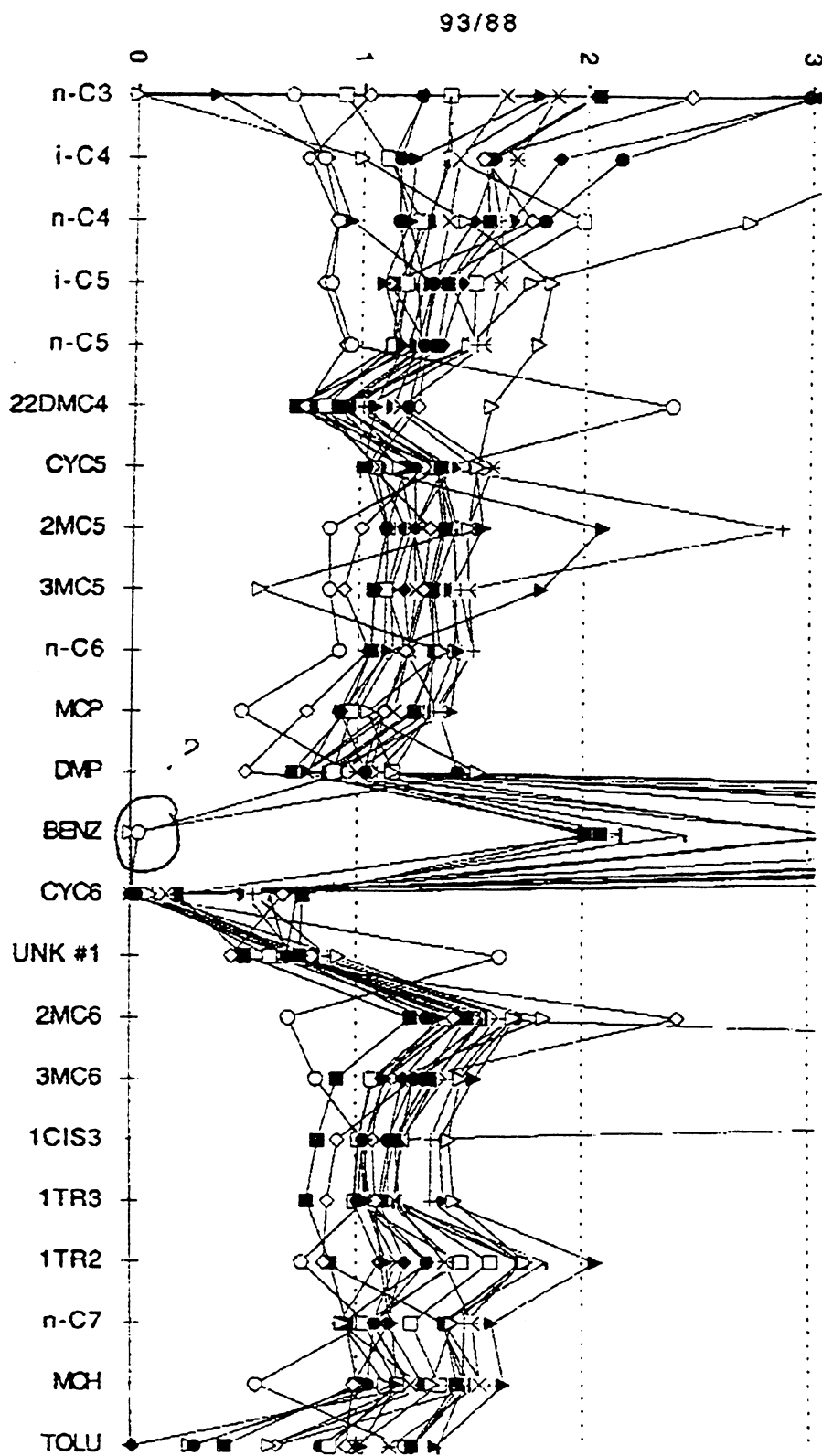
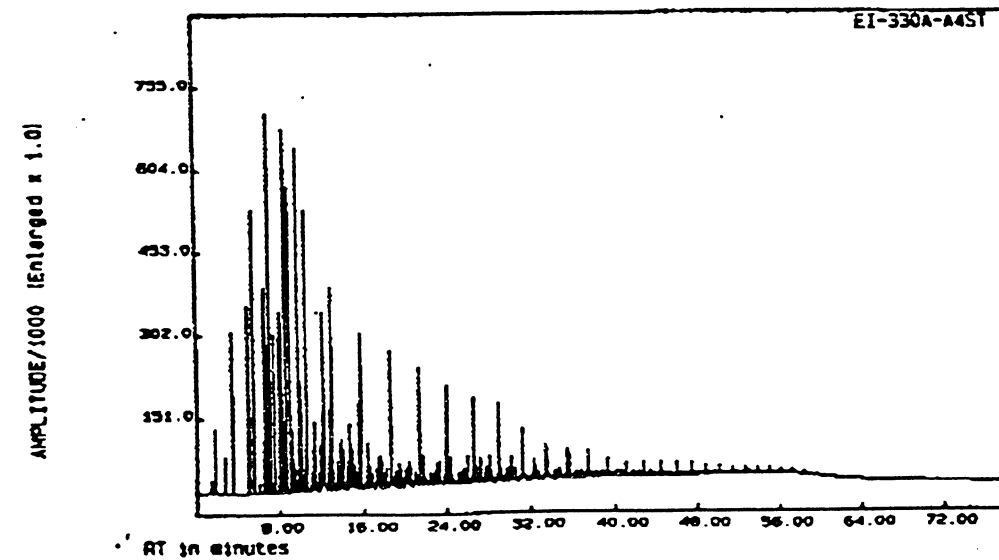
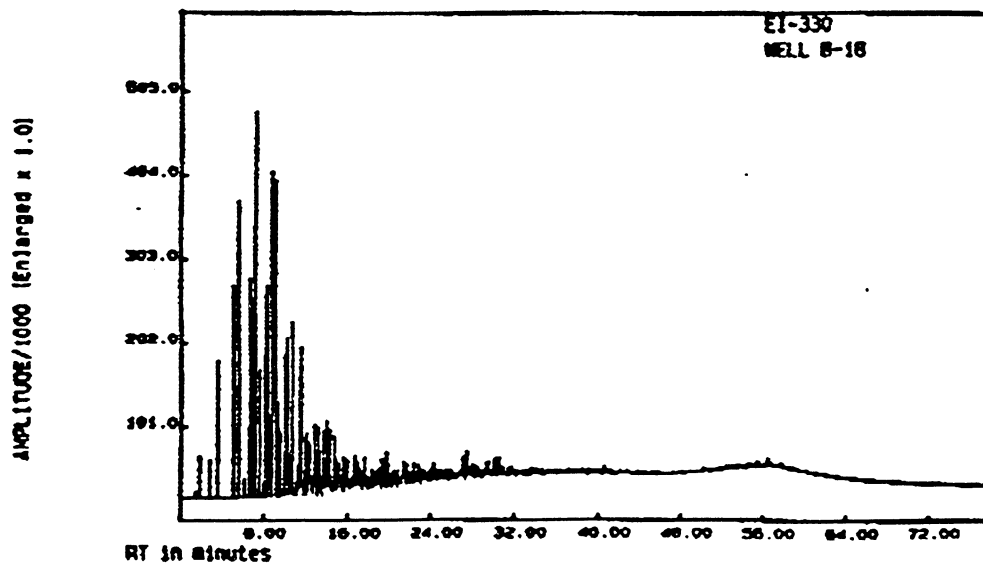
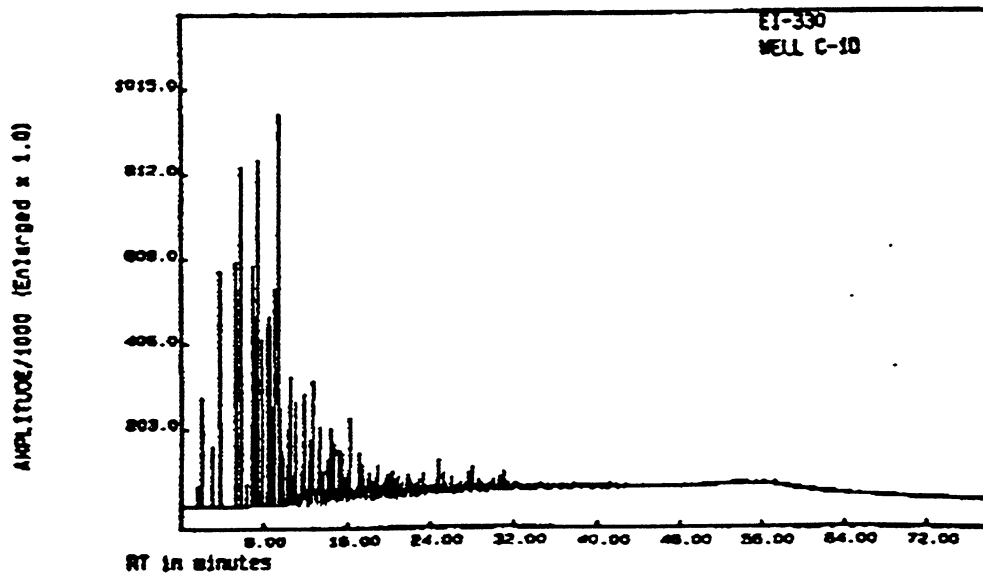


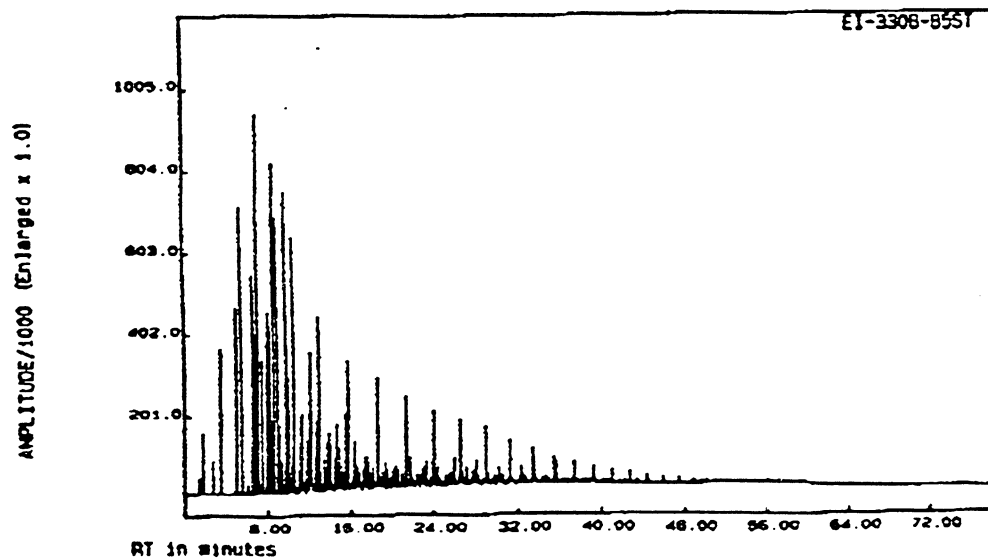
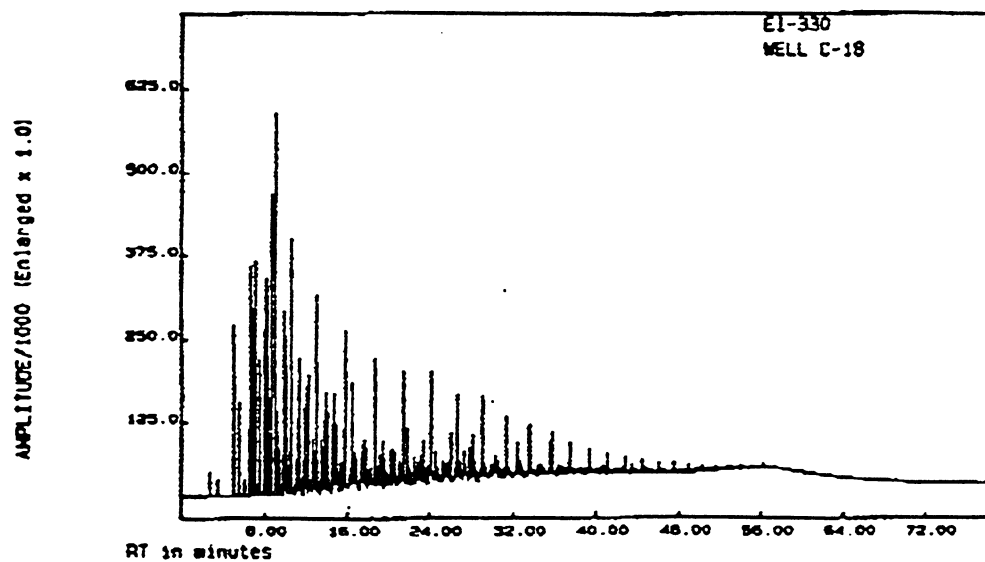
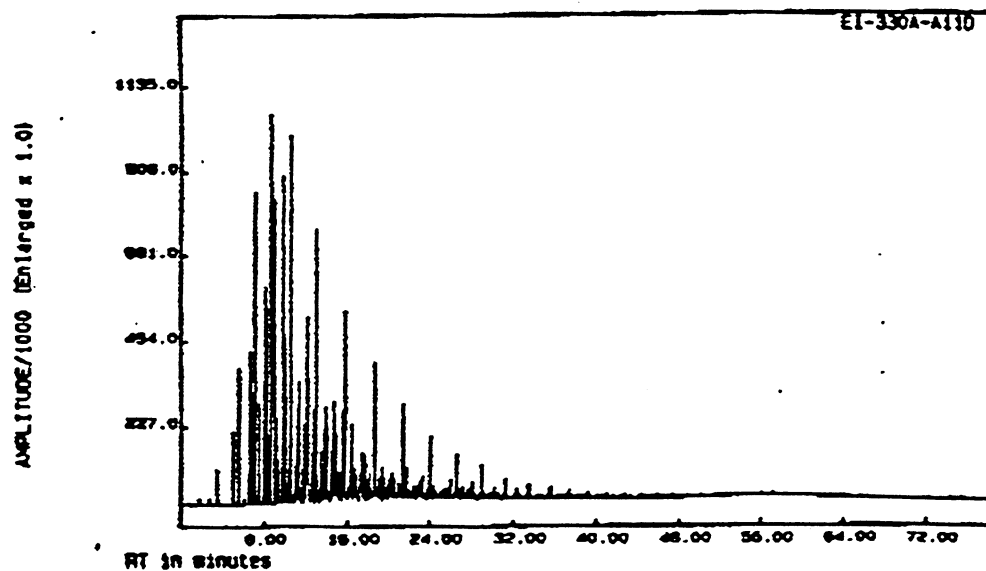
Fig. 1. Oil, gas, and condensate reservoirs in Eugene Island Block 330 field, their stratigraphic ages, and gas/oil productivities (from Holland, 1990).

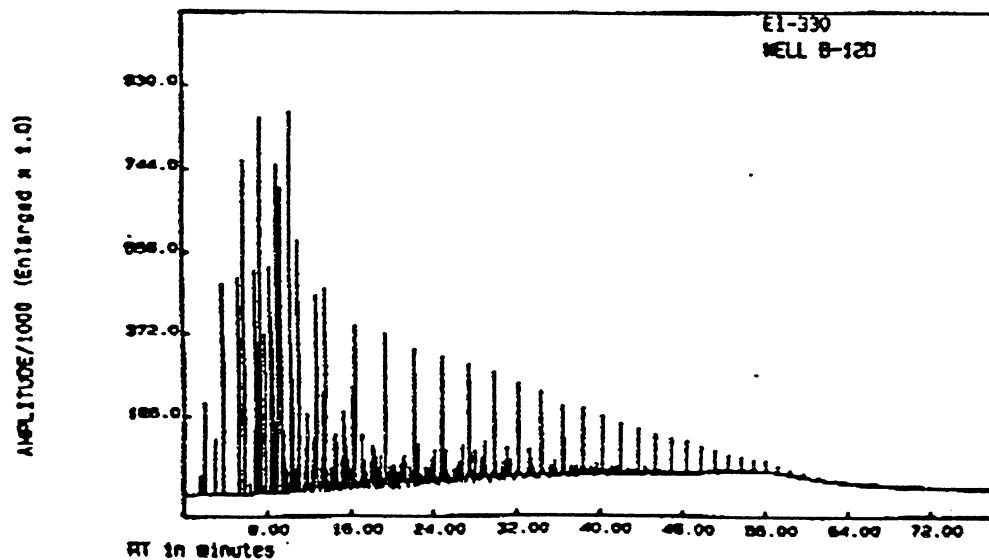
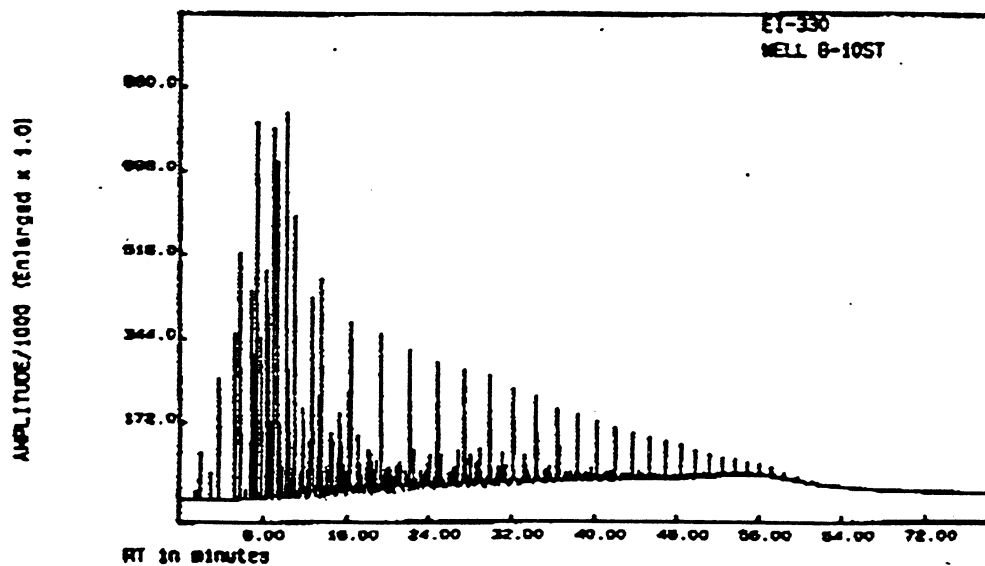
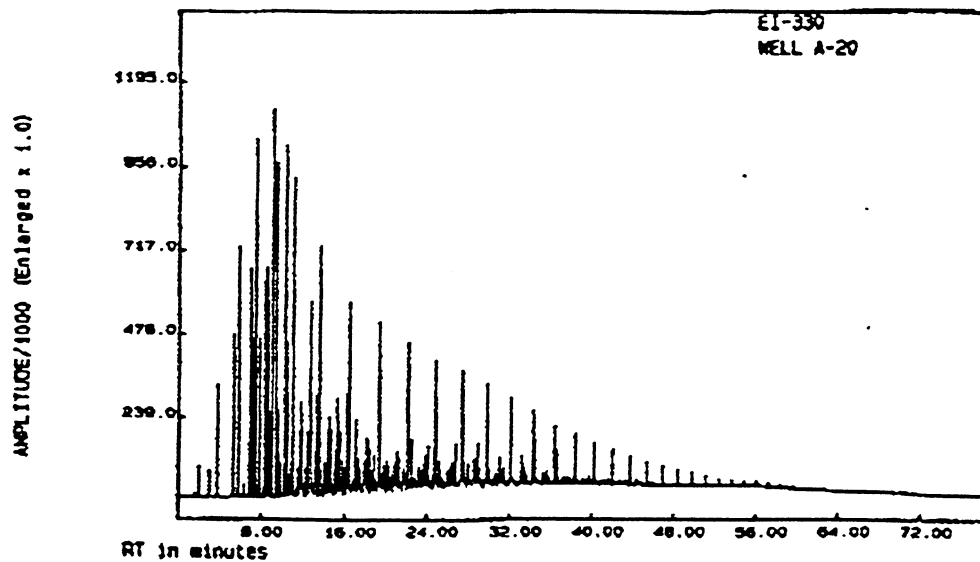
93/88

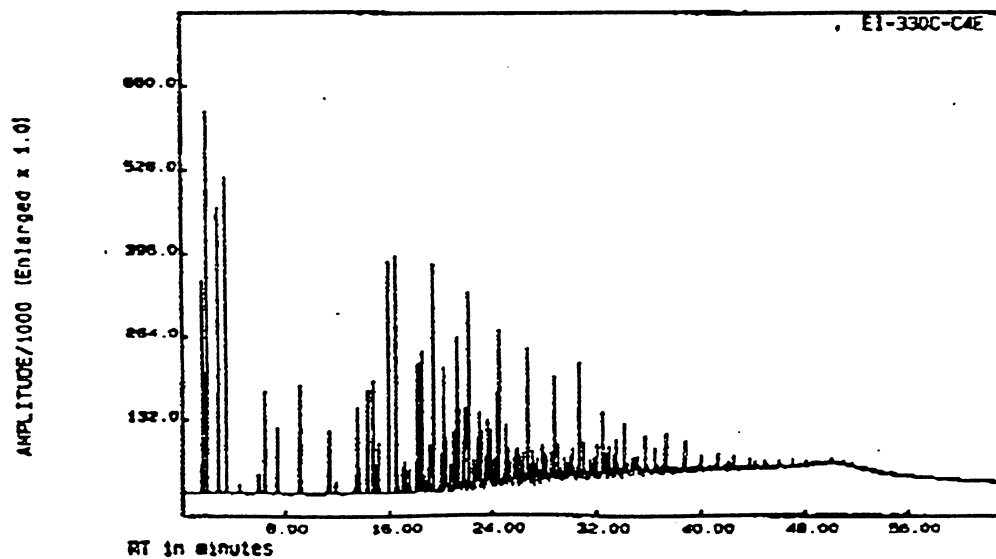
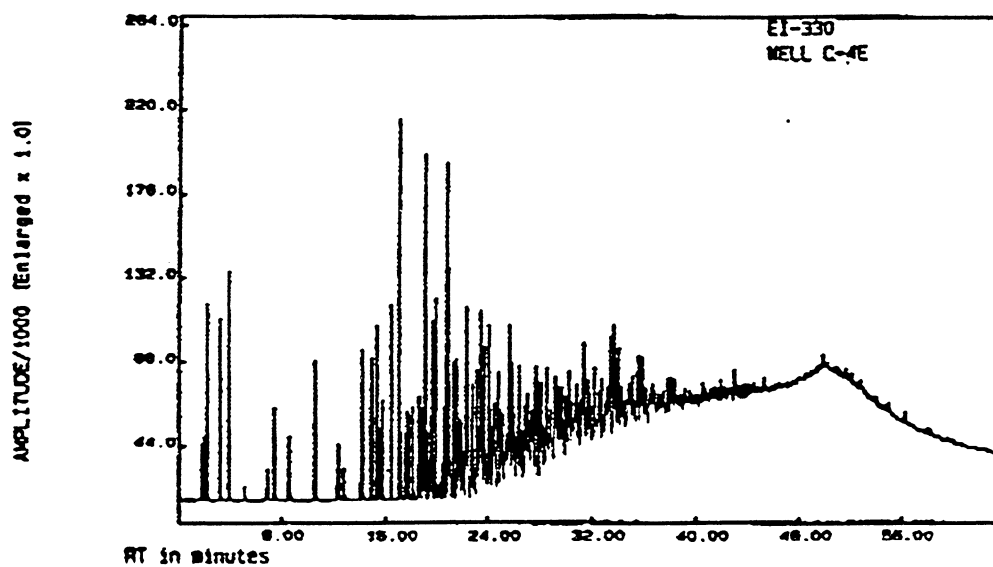
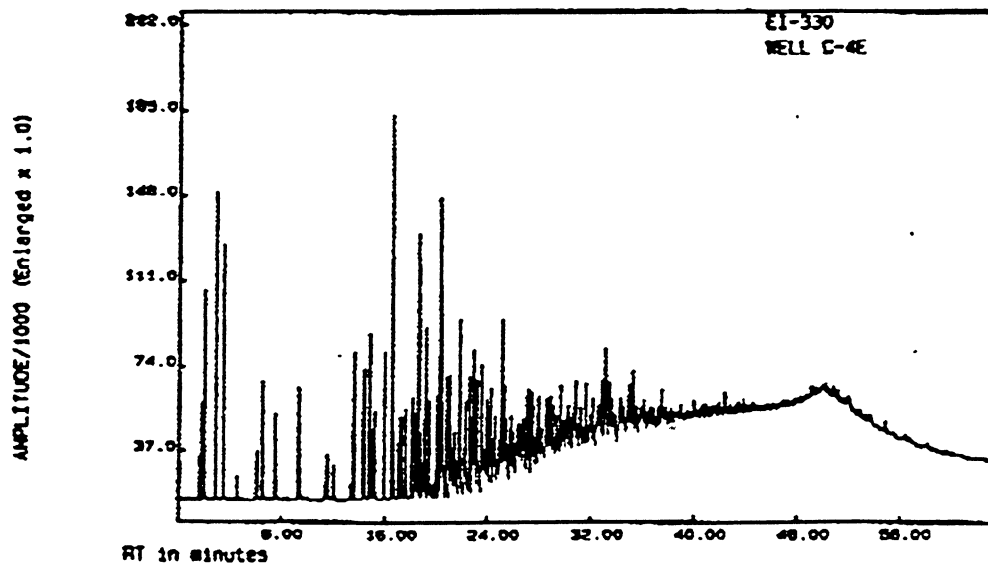


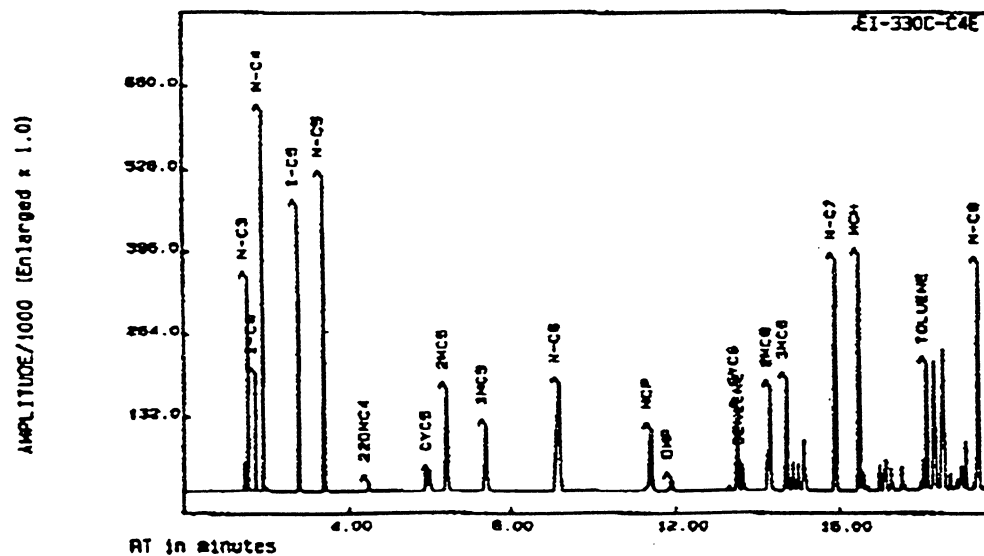
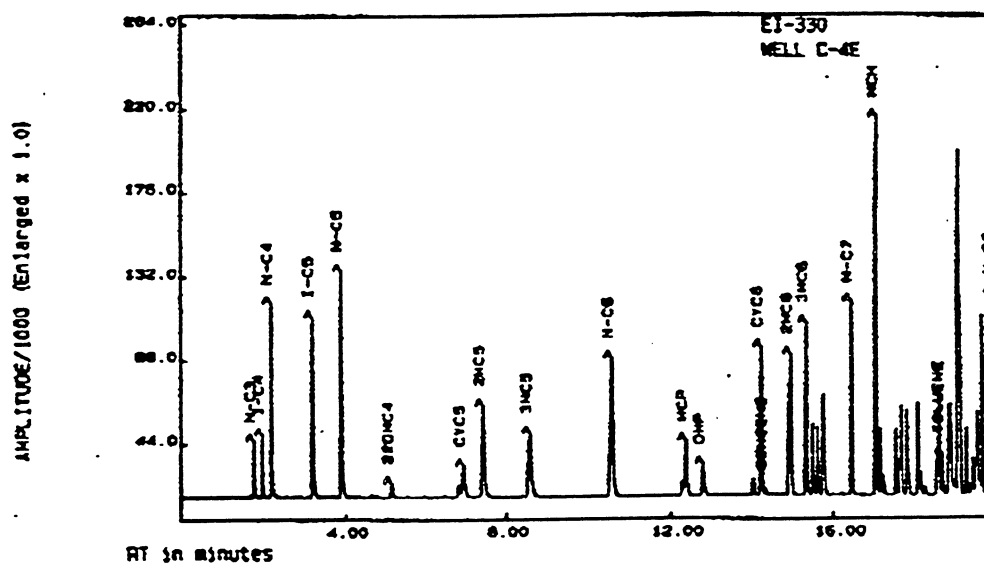
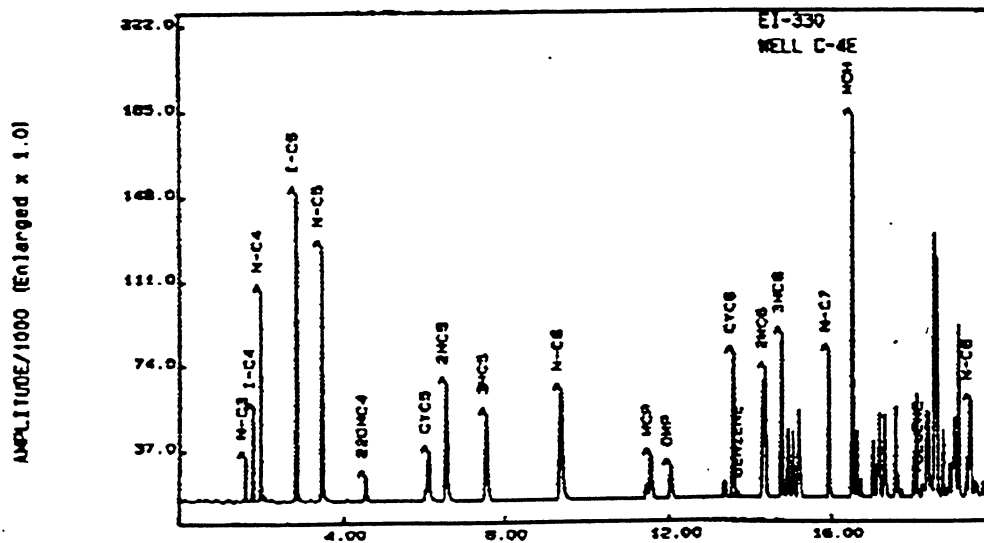


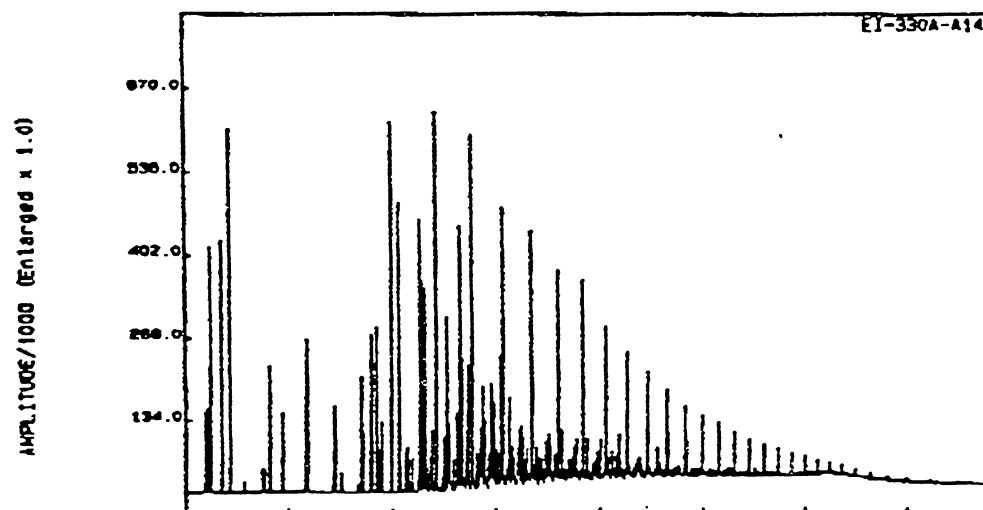
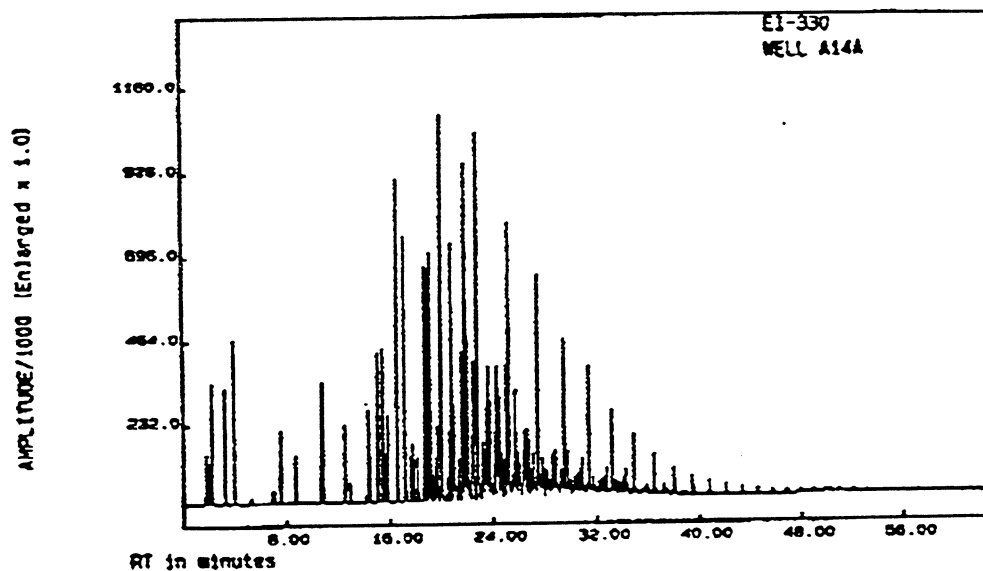
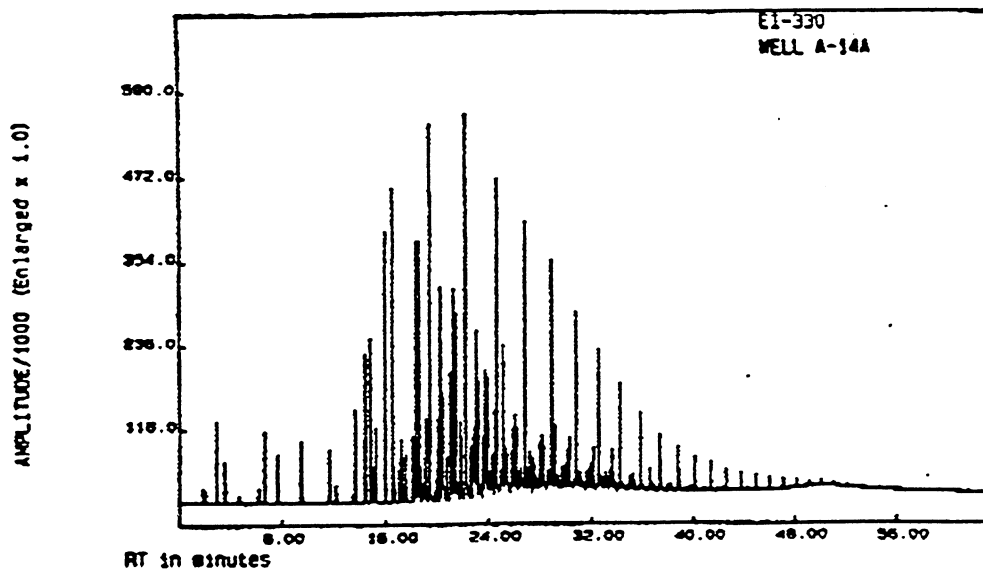


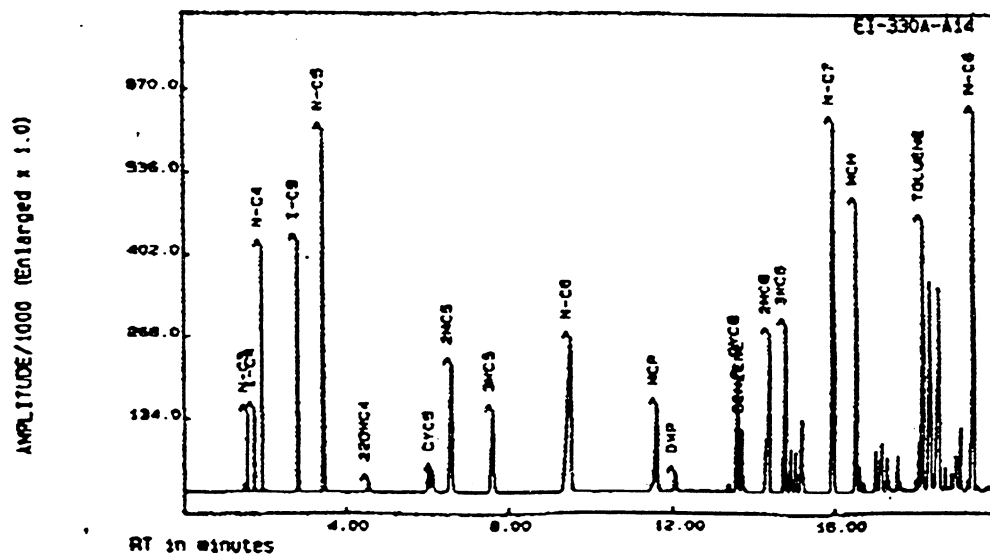
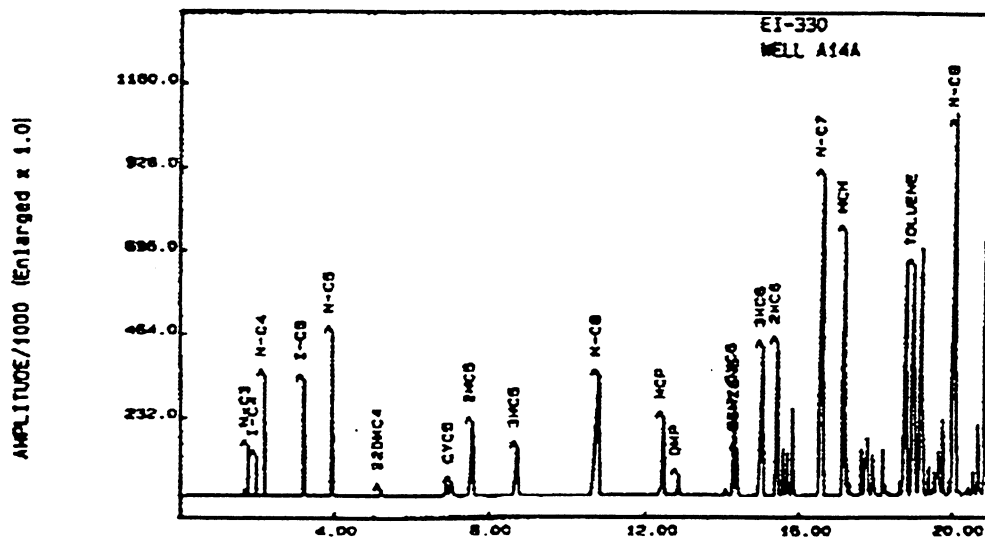
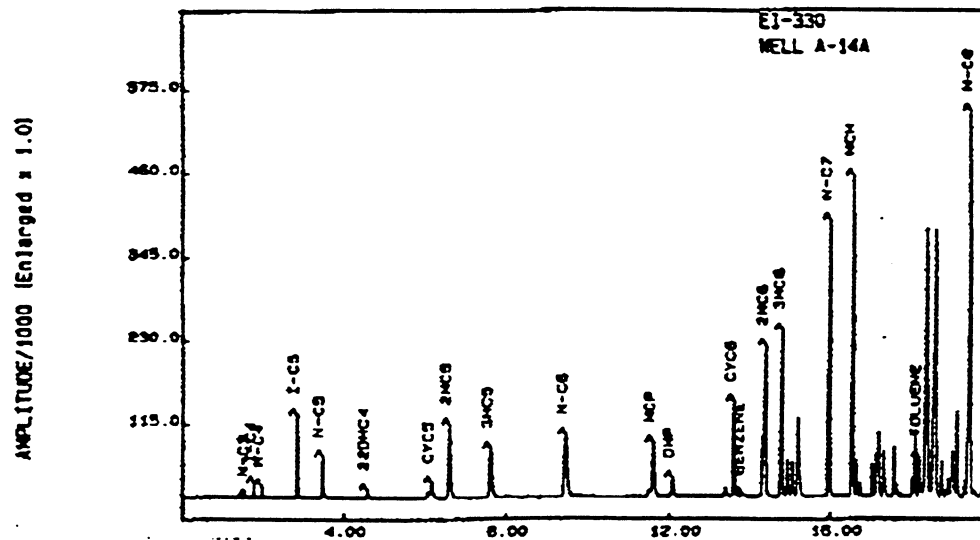












Task Seven - Technology Transfer

Roger N. Anderson - Task Manager

OBJECTIVE:

The purpose of this task was to integrate all results into one comprehensive perspective of the project's objectives and to transfer the results to industry. This will involve the interactions between the various project task outputs and the transfer and dissemination of the major conclusions of the study. There were two main efforts related to technology transfer in the field demonstration project. First, we made special efforts to patent and license technology developed as part of this project so that it would become commercially available to the oil industry. Second, we commissioned a study using the United States Geological Survey's fractal oil and gas reserves techniques to identify whether we were dealing with an additional source of oil and gas in the Eugene Island 330 field's recharge-along-faults.

SUMMARY:

The DOE field Demonstration Project "Dynamic Enhanced Recovery technologies" has been a resounding success by any gauge. It has spawned important new technologies such as 4D Seismic Monitoring, resulted in the placement of successful new wells to drain new and bypassed oil and gas in one of the most prolific oil fields in the U.S. Offshore, grown into industry-only funding consortia for all its major tasks, and promoted Internet collaboration across institutional boundaries at a time before Internet was such a household word. In addition, there is every prospect that the U.S. Treasury will be repaid many times over for the direct investment of funds into the future of the oil industry in America.

7.1 Patents and Licenses.

Two patents and one license were developed during this project. Lamont developed and filed U.S. Letters patents for geopressure mapping and 4D Software technologies. These form the core of one of the outstanding accomplishments of the project--the development of 4D seismic monitoring techniques to track the migration and drainage of oil and gas in reservoirs. Though not solely due to this Class project, 4D seismic technologies have become some of the newest and "hottest" in the industry. There are workshops, industry consortia, AAPG Distinguished lectures, the keynote address at the 1996 Offshore Technologies Conference, 4 separate symposia at the 1996 AAPG convention, all about 4D Seismic technologies. DOE is perceived to be one founder of the technology because of their support of this Class I project.

The 3D Finite Element Model the project developed for fluid flow was licensed to Computational mechanics, and a commercial version, ACCESS.BASIN is currently in the marketplace. ELF, Texaco and Phillips Petroleum are interested in buying it as of this writing.

A key determinant to whether a Class Program was successful might be whether its results were of sufficient interest to the oil industry for them to continue the funding of the Research and Development completely from industry funds. We are pleased to report that all 4 of the major tasks of the project have been continued by industry: Lamont and Penn State have formed a 4D seismic monitoring consortium with 7 oil company supporters; Penn State and Stanford have funded further stress analyses in fault zones through the Gas Research Institute, as have Cornell, Woods hole and LSU for the modeling; and oil

companies are funding a continuation of the organic and inorganic geochemistry analyses in the Eugene Island 330 field through Cornell and Woods Hole.

In addition, the DOE funding of experiments in the pathfinder well resulted in the subsequent placement of the A-8ST by Texaco and partners along the boundary of EI 330 and 338 blocks. That well is still producing at more than 1200 bbl/day, and has had cumulative production of over 800,000 bbl of oil. At the government's royalty rate of 18%, and assuming oil prices of \$20/bbl, \$2.8 million of the DOE project's costs have already been returned to the U.S. Treasury, and the well is targeted to produce at least as much again over the net year or so. In addition, another horizontal well is being planned into 4D seismic targets to the west of the A-8ST in 1996, again paid entirely by industry. The government should be "paid-back" for its direct investment in 2-4 years, and the long-term benefits from the use of 4D seismic technologies in old fields within the United States can hardly be underestimated.

7.2 Estimate of New Hydrocarbon Supplied

As part of the DOE project, we commissioned the University of South Florida, in cooperation with the United States geological Survey to conduct a "fractal" analysis of oil and gas reserves in the offshore Louisiana segment of the northern Gulf of Mexico. That report follows below, but the conclusions are that while substantial gas reserves might lie undiscovered in the currently-drilled portion of both the north and south additions of offshore Louisiana, no significant new oil reserves remain to be discovered. However, the report goes on to say that they do not detect possible new supplied remaining to be discovered at deeper depths--specifically, the sub-salt play.

At Lamont, we have analyzed the fractal distribution of the Eugene Island fields under study, and find that they depart from the fractal slopes detected for the overall offshore by the South Florida report. The oil and gas migrating up the Red Fault in EI 330 appear to come from deeper, "sub-salt" sources. we believe there are substantial new reserves to be found in the sub-salt play of the South Additions. Our project began before the sub-salt play was initiated by the Mahogany discovery of Phillips, et al., in 1994. The industry as a whole now agrees that there are substantial new discoveries to be made deeper in the South Additions of the Gulf, as can be seen from the increase in bidding prices and activity at recent MMS lease sales for the area.

Assessment of the Undiscovered Oil and Gas Potential, Offshore Louisiana in the South Marsh, Eugene Island, and Ship Shoal Areas

Sarah F. Tebbens

*University of South Florida, Department of Marine Science,
St. Petersburg, FL 33701*

Christopher C. Barton

U.S. Geological Survey, 600 4th Street, South, St. Petersburg, FL 33701

Gary L. Lore

*Minerals Management Service, MS 5100, 1201 Elmwood Park Boulevard,
New Orleans, LA 70123-2394*

ABSTRACT

For the South Marsh, Eugene Island and Ship Shoal areas of the U.S. Gulf of Mexico Outer Continental Shelf we calculate the size (volume) and number of undiscovered oil and gas fields. We use a new method (Barton and Scholz, 1995) to assess the size, number, and total volume of undiscovered, conventionally recoverable hydrocarbon fields based on fitting a truncated fractal (power-law) distribution to a log-log plot of the cumulative size-frequency distribution of discovered fields in these three geographically defined areas. The results indicate that there are very few undiscovered oil fields above 1.0 million barrels volume in any of these areas. However, the analysis indicates significant volumes of undiscovered gas. In particular, estimates of remaining undiscovered gas in South Marsh North Addition, Eugene Island Area, and Eugene Island South Addition are 553, 674 and 487 MMBOE, respectively.

Introduction

The Gulf of Mexico basin (figure 1) holds approximately 9% of the world's known recoverable petroleum liquids and approximately 11% of the world's known recoverable natural gas [Nehring, 1991]. Only the Arabian-Iranian province (with nearly half the world's total) holds more petroleum liquids [Nehring, 1991]. Only the Arabian-Iranian and West Siberian provinces hold more natural gas [Nehring, 1991]. No other province contains even 5% of the world's known conventionally recoverable resources of petroleum liquids or natural gas [Nehring, 1991]. The Gulf of Mexico Outer Continental Shelf is a significant source of domestic hydrocarbon resources. Cumulative production in United

States Federal waters (3-200 miles offshore) through 1993 was 9.0 billion barrels of oil (BBO) and 108 trillion cubic feet (TCF) of gas. Ultimate known recoverable reserves in Federal waters in the Gulf of Mexico are 11.2 BBO and 137 TCF of gas [Melcanon *et al.*, 1994]. For the entire Gulf of Mexico Basin, including reserves from Mexico, as of 1987, the ultimate known recoverable reserves (oil and gas combined) are 222.5 billion barrels of oil equivalent (BBOE). This includes 136.6 BB of petroleum liquids and 523.8 TFC of gas [Nehring, 1991]. During 1989, 22% of domestic gas and 10% of domestic oil were produced from the Gulf of Mexico Outer Continental Shelf (United States Federal Waters) [Lore, 1991].

The reserve values cited above are minimum estimates based on known (discovered) reserves. These values demonstrate the significance of the Gulf of Mexico as a petroleum resource. This report assesses the remaining undiscovered oil and gas in South Marsh, Eugene Island, and Ship Shoal areas of the Central Gulf of Mexico, offshore Louisiana (figure 2). These areas lie within the "Gulf Coast Offshore" sub province of the Gulf of Mexico basin, as defined by Salvador [1991] and Nehring [1991] (figure 1B). The assessment method of Barton and Scholz (1995) fits the population of known field sizes (past production plus reserve estimates, not "grown" to their ultimate sizes) with a power law distribution which is, in this report, then extrapolated down to an field size of 1 MMBOE. The total area under the power law distribution is a measure of the ultimate resource and the difference between is a quantitative estimate of the undiscovered conventionally recoverable resource.

Gulf of Mexico Basin Historical Production

A remarkable feature of the exploration history of the Gulf of Mexico basin is the number of economically viable fields discovered annually. Unlike most other petroleum provinces, in which discoveries have been highly concentrated within a period of one to three decades, substantial numbers of new discoveries have been made in the Gulf of Mexico for the past seven decades [Nehring, 1991]. An explanation for this unusual development is that new exploration and development technologies have been developed to take exploration from onshore, to near shore, to progressively deeper waters [Lore, 1991]. This record of success is likely to continue through the 1990's [Nehring, 1991].

The first significant discovery of oil and gas in the Gulf of Mexico basin was made in 1895 at Corsicana, Mexico [Nehring, 1991]. The rate of discovery in the basin accelerated in the 1920's with new geophysical exploration methods.

Prior to 1959, exploration in the offshore Gulf of Mexico was focused on shallow, near shore waters, reflecting extension offshore of active on-shore drilling. South Marsh, Eugene Island and Ship Shoals Block development was active at this time, located near the center of the area, in waters offshore Louisiana, from West Cameron to Main Pass (figure 3A). The average size of fields discovered was 139 MMBOE [Lore, 1991].

Between 1960 and 1969, exploration began to step further offshore, but still on the shelf (<200 m water depth) [Lore, 1991] (figure 3B). A 5-fold increase in the total number of both exploratory and discovery wells resulted in a near doubling of recoverable proved reserves and a 170% increase in the number of fields. In that decade, the average size of fields discovered decreased to 77 MMBOE [Lore, 1991].

In the next decade (1970 to 1979), drilling off Louisiana continued to extend further offshore (figure 3C). Activity on the upper continental slope was at water depths greater than 200 m. Additionally, exploration and development in the western Gulf of Mexico, resulted primarily in the discovery of gas. During the 1970's, the average size of fields discovered on the outer continental shelf decreased to 42 MMBOE, with most of the larger fields discovered further offshore on the upper slope (average field size on the upper slope was 63 MMBOE).

In 1971, the Eugene Island Block 330 field was discovered. The field now includes Eugene Island blocks 313, southern half of blocks 314, 330, 331, 332, 337 and 338 [Holland *et al.*, 1991]). From 1975 to 1980, the field was the largest producing field in United States Federal Outer Continental Shelf waters [Holland *et al.*, 1991] . As of 1991, the field ranked second in annual hydrocarbon production (Minerals Management Service Data as reported in [Holland *et al.*, 1991]) and fourth in cumulative hydrocarbon production (Dwight's Energy Data as reported in [Holland *et al.*, 1991]). Estimated at 671 MMBOE of recoverable oil and gas [Melcanon *et al.*, 1994] the Eugene Island field ranks 437th among the giant oil and gas fields of the world [Carmalt and John, 1986] .

In the 1980's, there was scattered development across the Central and Western Gulf of Mexico Shelf (figure 3D). Exploratory drilling had reached water depths in excess of 7,000 feet. The Auger field, discovered in 1987 in 2,862 feet of water, is estimated to hold 220 MMBOE of recoverable oil and gas [Taylor, 1994; Shirley, 1995]. Even with a few large discoveries, by 1989 the average field size had decreased to only 14 MMBOE.

The 1990's have witnessed discovery of the Mars field in 2,933 feet of water which is estimated to hold 770 MMBOE [Taylor, 1994; Shirley, 1995], making it the largest discovery in the Gulf to date. For a list of deep water reserves (holdings in water 1,000 deep or greater) see Taylor [1994]. Near to shore and in shallow water, Ship Shoal, Eugene Island and South Marsh have been extensively explored through conventional methods and are in the mature stages of exploration and development.

Assessment Methodology

The methodology used to estimate the undiscovered oil and gas fields in the Eugene Island, South Marsh and Ship Shoal Areas was developed by Barton and his colleagues [Barton *et al.*, 1991; Barton and Scholz, 1995; Barton and Troussov, in press] . Barton and Scholz [1995] determined that hydrocarbon fields ranging in size from a single play (i.e. Frio Strand Plain Play, Gulf Coast of Texas, and Cardium Scour Play of western Canada) to individual basins (Permian Basin, 0-5000' depths) to giant fields of the world follow a fractal (power law) distribution. In the following section we provide a brief introduction to fractals in nature and then we describe the methodology as applied to oil and gas resource assessment. In a later section, we discuss the results of this application to regions offshore Louisiana.

Background: Fractals in Nature

Objects in nature are commonly very irregular, such that, within the constraints of Euclidean geometry, one is forced to grossly approximate their shape. A rock fragment, for example, generally is treated as being spherical, and a coastline as straight or smoothly curved. Upon examination, however, these objects are found to be jagged over a wide range of length scales, and these irregularities do not diminish when viewed at ever finer scales. Mandelbrot (1982) developed fractal geometry which is applicable to many irregular natural objects. Fractal objects have a number of definitive characteristics that are identifiable and described by the methods of fractal geometry. The analytical techniques for treating fractal geometry, and their interrelationships, have undergone rapid evolution and broad application (for example, Feder, 1988). Fractal geometry has been applied to a wide variety of geologic and geophysical objects and phenomena (for example, Scholz and Mandelbrot, 1989; Turcotte, 1992; Korvin, 1993; Turcotte and Huang, 1995; and Barton and LaPointe, 1995a,b).

Distribution Function of Hydrocarbon Fields

For the past forty years, the size-frequency distribution of mineral deposits, including oil fields, has been thought to be lognormal (for example, Krige, 1951; Arps and

Roberts, 1958; Kaufman, 1962, 1983; McCrossan, 1968; Barouch and Kaufman, 1976; Lee and Wang, 1983a, b; Forman and Hinde, 1985; Davis and Chang, 1989; Power, 1992). The lognormal distribution resembles a power-law, or fractal, distribution in the middle of its range but is truncated at the lower end. Unlike the scale-independent power-law distribution, it has a characteristic size (mode) at which the distribution peaks and rolls off and has values below the mode. At the upper end, the lognormal distribution tends quickly to zero and therefore has a thin tail. In contrast, the upper end of the power-law or fractal distribution tends to zero slowly and therefore has a fat tail. Figure 4 shows the cumulative size-frequency distribution for six scaling functions, including the lognormal and the power-law. Note that only the fractal (power-law) distribution plots as a straight line. For size versus cumulative frequency distributions, the term fractal is used only for power-law distributions with slope (α) less than 2. Over small ranges in size, portions of the other distributions can be approximated by straight lines, with either steep slopes for large sizes or zero slopes for small sizes. It therefore is important to have data over a sufficient range so that the true distribution is observed. The general rule of thumb for a power law fit is that the data should range over as many orders of magnitude as the absolute value of the scaling exponent (slope of the line in log-log space) (Mandelbrot, pers. com., 1995).

A power-law data set containing a perceptibility limit (the smallest size for which we have a complete census of the population) commonly is well fit by a lognormal distribution. Because all observed distributions will have perceptibility limits; this misidentification is not uncommon. For example, a perceptibility limit occurs in earthquake detection. Because seismometers have lower-magnitude thresholds for event detection this results in a low-side truncation in observed earthquake sizes. Observed earthquake distribution is a power law distribution above the perceptibility limit. Installation of instruments with higher magnification results in detection of a multitude of smaller earthquakes that continue to belong to a power-law size distribution (which is called the Gutenberg-Richter law in seismology).

As progressively smaller hydrocarbon fields are discovered through time, the associated perceptibility limit moves to smaller field sizes, thus extending the power-law size distribution to progressively smaller field sizes. Such temporal change should not occur if the underlying distribution had a characteristic size, such as log normal distribution. A power law distribution, which has no characteristic size, appears to be the correct distribution to describe the size distribution of hydrocarbon fields.

Recognition that the size-frequency distribution of hydrocarbon fields may be a power-law was made by L.J. Drew and his colleagues (*Drew and others*, 1982; *Schuenemeyer and Drew*, 1983; *Attanasi and Drew*, 1985; *Drew and others*, 1988; and *Drew*, 1990; and also by *Baker and others*, 1984; *Houghton*, 1988; *Scholz and Barton*, 1991; *Brett and Feldcamp*, 1993; *Barton and Scholz*, 1995; and *Crovelli and Barton*, 1995). An example from *Drew* (1990) shows the size distribution of discovered fields in the Frio Strand Plain play (onshore Texas) as a function of time (figure 5A); and as replotted by *Barton and Trousoff* [in press] as a cumulative frequency versus field-size distribution in log-log space (figure 5B). At any given time, the distribution in this play looks like a lognormal distribution, but, as exploration proceeds, more small fields are discovered, with associated progressive decreases in the mode. We observe a similar pattern through time for the 200 top discovered oil and gas fields in U.S. Gulf of Mexico waters (based on original reserve estimates) (figure 6).

Drew and his colleagues maintained that the parent distribution in the Frio Strand Plain play is a power-law (or Pareto) distribution that is gradually being revealed by exploration. The roll-over at any given time is determined by economics since uneconomic smaller fields are either undiscovered or not developed. This roll-over is shifted to smaller sizes as price increases and more small fields are discovered and developed. The largest

fields are commonly found early in the exploration cycle, and through time the population fills in with progressively smaller sizes. From this understanding of the discovery process we can infer that in any region at a mature stage of exploration, the right tail in the distribution provides a good estimate of the parent distribution down to the perceptibility limit, which is commonly at or near the economic truncation. Thus, as in figure 5B, the population in the largest size classes (Table 1) remains stable in time. Therefore, in order to obtain an estimate of the true or parent population of hydrocarbon deposits, we fit the right side of the size distribution in regions in the mature stages of exploration.

The Pareto distribution has been used by the U.S. Geological Survey (USGS) in past assessments of the undiscovered conventionally recoverable hydrocarbon resources of the United States. *Houghton and others* (1993) described application of the truncated shifted Pareto distribution in the 1989 USGS national petroleum assessment to fit geologists' estimates of the size and number of undiscovered hydrocarbon fields. In contrast, in the method proposed by Barton and his colleagues, and used in this work, the size and number of undiscovered fields are forecast by fitting a power-law to the distribution of discovered fields larger than the perceptibility limit and then extrapolating to field sizes smaller than the perceptibility limit.

Fractal Size-Frequency Distributions and their Application to Hydrocarbon Fields

A collection of fractal objects may belong to a set that has a power-law size distribution. A fractal distribution is defined where a number of objects $N(r)$ having a characteristic linear dimension equal to or greater than r satisfies the cumulative size-frequency distribution function

$$N(r) = Cr^{-D} \quad (1)$$

where D is the fractal dimension and C is a constant of proportionality. For this work, it is more convenient to consider the cumulative size-frequency distribution of volumes, $V=r^3$, so we look for the distribution

$$N(V) = C(V)^{\frac{-D}{3}} \quad (2)$$

The density function is

$$n(V) = \frac{dN(V)}{dV} \quad (3)$$

and the distribution function is

$$N(V) = \int_{V_{\min}}^{V_{\max}} n(V) dV \quad (4)$$

A variety of geologic objects having the type of distribution described in equation (1) are described by *Turcotte* (1992); *Turcotte and Huang* (1995); and *Barton and LaPointe* (1995a, 1995b). These collections of objects must be defined within some region, which we will call the distribution space. For hydrocarbon accumulations, this space may be a geographical region, such as the world, a basin, a country, or a State, or it may have a geologic definition, such as an oil province or a play. Members of the distribution must also be defined; these may be the field, for example, or the pool. These various members and spaces may constitute different hierarchies nested within one another. For example, there may be a distribution of pools within a reservoir and, at higher hierarchical levels, a distribution of reservoirs within a field within a play, and plays within a basin or province. In this report, we consider the hydrocarbon field sizes, as defined by Minerals Management Service [*Melcanon et al.*, 1994, for example].

As mathematical expressions, equ. (1), (2), and (3) are defined over infinite ranges, but in any finite application the range must be limited by lower and upper fractal limits as indicated in equ. (4) and (5) by V_{\min} and V_{\max} (figure 7). The upper fractal limit (UFL) is always defined by the distribution space and is usually observable. For example,

the largest possible field in a basin is constrained by the size of the basin and its geology. One can always find or estimate this largest field; in regions of mature or semi-mature stages of exploration the largest deposit has probably been discovered, based on the discovery process (see *Drew*, 1990). On the other hand, the lower fractal limit (LFL) is arbitrarily defined. It may be the smallest structural trap within the basin or the smallest oil-filled pore space within the reservoir rock. In either case, we do not know its size. The lower fractal limit is not generally of practical importance because it is always well below a perceptibility limit (PL), the smallest size for which we have a complete census of the population. Thus, in figure 7 the dashed line is the theoretical fractal population, the dotted line is the true population, and the solid line is the observed population.

The size distribution of oil fields within the Eugene Island South Addition is shown in figure 8. The data in this log-log plot, larger than the perceptibility limit (excluding the five largest fields as discussed below), have been fit with a straight line. The significance of deviations from this fit is discussed later in this paper. We first point out an important constraint on fractal distributions. In a region containing n fields of volume V_k where $k=1, 2, \dots, n$ the total volume of hydrocarbons $V_{calc.}$ is given by

$$\sum V_{calc.} = \lim_{n \rightarrow \infty} \sum_{k=1}^n V_k = \int_{V_{min}}^{V_{max}} \frac{dN(V)}{dV} V dV = \frac{CD}{3-D} V^{1-\frac{D}{3}} \Big|_{V_{min}}^{V_{max}} \quad (5)$$

where n is the number of fields of volume V_k where $k=1, 2, \dots, n$ is evaluated between the largest field V_{max} , which is always defined for the region, and the smallest field V_{min} , which may be arbitrarily small or is not defined.

To define a total volume that does not become arbitrarily large as V_{min} goes to zero, the integral in equation (5) must be convergent, which means that the exponent

$$\left(1 - \frac{D}{3}\right) > 0 \quad (6)$$

and therefore $D < 3$, where D is the fractal dimension.

The distribution function (equ. 2) can be written

$$N(V) = C(V)^{-\alpha} \quad (7)$$

where $\alpha = \frac{D}{3}$

The volume distribution, as defined by equation 7, when presented on a graph of log of cumulative frequency versus log of size is fit with a line with slope $-\alpha$. If there is convergence (i.e. most of the total volume is contained in the large fields), the absolute value of α must be less than 1.

For the Eugene Island South Addition oil fields, the fit yields $\alpha = -0.53$, and thus we predict that when all the oil is discovered, most of the total volume will be in the large fields. Because this convergence constraint is a general property of fractal distributions, it follows that, as exploration proceeds from development of large to small fields, the volume discovery rate decreases even though many more small than large fields are present.

If the fit to the data is a good representation of the parent population, the ultimate volume of hydrocarbons ($V_{ultimate}$) in the distribution space can be obtained by summing the discovered volumes (V_{obs}) greater than the perceptibility limit and adding to them the calculated undiscovered volume (V_{calc}) by evaluating equation 5 (where V_{max} is the volume at the perceptibility limit (PL) and V_{min} is some chosen lower fractal limit (LFL) minus the volume of discovered hydrocarbons between the PL and the LFL (see figure 10)). Using this method, the total residual volume of hydrocarbons can be calculated down to any lower threshold. The cumulative size-frequency distribution (equ. 7) is used to

calculate C , α , and D because this distribution smoothes out the noise that results from inaccuracies in determining the volume of each field in the data sets.

Barton and Scholz (1995) fit a power law cumulative size frequency distribution to hydrocarbon populations at different hierarchical levels, each of which exhibits approximate fractal distributions, which means that these populations consist of many nested fractal distributions. Such nesting may persist continuously over a wide range of sizes, all the way down to the porosity of the reservoir rock, which has also been shown to have a fractal size distribution (Krohn, 1988).

For several regions within the study area, the cumulative size-frequency versus field-size distribution will be shown to be strongly curved, concave downward, over the higher size ranges, such that the slope increases with size. If the data are truncated to a size about one order of magnitude smaller than the maximum field size, a power law is fit down to the perceptibility limit. The power law should not be extrapolated to the far right end of the distribution because it predicts an unrealistic maximum field size many times larger than that observed.

Curvature near the upper fractal limit (UFL) (figure 7) is a local feature, affecting only the last one or two data points, and is expected because of the natural truncation associated with the upper fractal limit. Cases where the curvature, or enhanced slope, extends well below the last one or two largest field sizes cannot be explained in this way. We propose, instead, that the observed curvature in the large field sizes results from constructing data sets defined by the artificial boundaries of geographic areas that contain portions of geologically defined plays, thereby including a diverse set of sub populations. Consider the hypothetical case of five sub populations, shown in figure 11 as solid lines. Each of these has cumulative-frequency size distributions with the same a value but different upper fractal limits. When combined, these produce the population shown by the ten data points. The line has curvature in the upper size ranges similar to that observed in figure 8 whereas below the upper fractal limit, the a value for the total population is the same as for each of its parts.

This observation underscores the conventional wisdom in discovery process modeling (for example, *Kaufman*, 1983; *Drew*, 1990) that one must carefully select data sets for homogeneity of geology and source. Data sets for larger regions (*Barton and Scholz*, 1995) are, however, still approximately fractal, and useful analysis can be made of them. The total resource in such a region can be estimated by summing the volume in the larger fields and integrating the remainder in the smaller fields in the way described above, starting from the point at which a becomes representative of the population as a whole (indicated by that part fit by the upper line in figure 11) and by defining the perceptibility limit (PL).

Results

The assessment methodology presented above was applied to determine the size and number, and total volume of undiscovered conventionally recoverable oil and gas fields for Ship Shoal, Eugene Island and South Marsh areas (figure 2). Based on the above discussion, we assume that the underlying distribution of oil and gas fields in these areas is fractal (power law). Field sizes (the sum of cumulative production through 1993 and remaining ungrown recoverable reserves) were provided by Minerals Management Service. They are defined and discussed in *Melcanon et al.* [1994]. The lower fractal limit for this assessment is 1 mmBOE.

Cumulative frequency versus field size plots for oil and gas in each of the three areas are presented in figure 12. The following points made in the methodology section are particularly important for interpretation: 1) To infer a fractal distribution (i.e. to fit a line to a log-log plot (a power law)), the data should span as many orders of magnitude as the absolute value of the slope of the line fit (for this work, the slope is usually less than one so that we need data with a range of values spanning a minimum of roughly one order of

magnitude); 2) Rollover at smaller field sizes suggests undiscovered fields at the smaller field sizes; 3) Rollover at larger field sizes suggests that data from several populations, each with fractal distributions, have been combined (see figure 11). The rollover at larger field sizes is expected for this work since the available data combine all fields at each area; the data are not separated by, for instance, stratigraphic source levels. We observe rollover at smaller field sizes (a perceptibility limit) for all three areas (figure 12). Rollover at larger field sizes is observed for South Marsh South Addition Gas, Eugene Island Oil and Gas, and all Ship Shoal Oil and Gas distributions (figure 12). We note that for four of the fourteen assessments (South Marsh Gas, South Marsh South Addition Gas, Ship Shoal Oil, and Ship Shoal South Addition Gas), the data are sparse and the results should be considered tentative (linear fits denoted with "?" in figure 12 and indicated by "+" after location name in Tables 2 and 3).

Table 2 is a summary of the oil assessment, including the volume of remaining undiscovered oil in each region down to a field size of 1.0 million barrels oil equivalent (mmBOE). Also presented is the calculated fractal scaling exponent, the volume of discovered hydrocarbons, and the predicted ultimate volume of hydrocarbons. Results are also shown in map view (figure 13). The remaining undiscovered volumes are further subdivided into the number of fields remaining to be discovered in each field class in each region. Table 3 is a similar summary of the gas assessment.

In the seven regions studied, the region with the largest total volume of discovered oil is Ship Shoal block (1029 mmBOE) with the next largest discovered volumes in Eugene Island and Eugene Island South Addition areas (697 and 695 mmBOE, respectively) (Table 2). The predicted volume of oil remaining undiscovered in each region is small (less than 90 mmBOE) or none. The largest predicted volume of oil remaining undiscovered is also in Ship Shoal block. We note that the Ship Shoal block oil assessment is one of the four assessments for which the data are scarce, so the results are tentative. If correct, the results predict 87. mmBOE oil remaining undiscovered in Ship Shoal block. These reserves are predicted to be comprised of two class 8 fields (mean field size 5.7 mmBOE), 10 class 7 fields (mean size 2.8 mmBOE) and 23 class 6 fields (mean size 1.4 mmBOE). The next largest predicted volumes of undiscovered oil are in South Marsh Island South Addition Area and Eugene Island South Addition Area, with 20 mmBOE and 11 mmBOE, respectively, remaining undiscovered. There are no remaining undiscovered fields larger than one mmBOE predicted in the South Marsh Island North Addition and South Marsh Island regions.

In the seven regions studied, the region with the largest total volume of discovered gas is Eugene Island South Addition (1449 mmBOE) with the next largest discovered volumes in Ship Shoal block and Eugene Island Block (1315 and 1283 mmBOE, respectively) (Table 3). The analysis estimates significant volumes of undiscovered gas (Table 3, figure 13D), with all regions containing undiscovered fields. The regions with the largest volumes of gas predicted to be remaining undiscovered are Eugene Island Area, South Marsh North Addition, and Eugene Island South Addition, with 674, 553 and 487 mmBOE, respectively. In the region with the largest volume of undiscovered fields, Eugene Island Area, the reserves are predicted to be comprised of 172 class six fields, 73 class seven fields, 30 class eight fields, and 10 class nine fields. The largest fields predicted are two class 10 fields (mean field size 23 mmBOE) in the Eugene Island South Addition Area (Table 2).

We note that this analysis cannot evaluate the undiscovered resources located in plays at depths greater than those currently included in our data sets (subsalt); additional oil and gas plays at deeper horizons cannot be ruled out.

The scaling exponent can be used to infer the relative abundance of small fields to large fields. The smaller the (absolute value of the) scaling exponent, the greater the ratio of the large fields to the small fields. For gas fields, as one moves offshore, the scaling exponent decreases (fig. 13) indicating the ratio of larger fields to smaller fields increases

as one moves offshore. For oil fields, the opposite trend is weakly suggested, with the scaling exponent increasing slightly offshore in the South Marsh and Eugene Island Areas and observed to be roughly constant across the Ship Shoal Area (fig. 13).

Summary

Populations of hydrocarbon fields can be described by the power-law size distribution characteristic of fractal sets. This is true for all hierarchies of populations examined by *Barton and Scholz* (1995), ranging from pools in a play to giant fields in the world. *Barton and Scholz* (1995) suggest that any population of hydrocarbon fields consists of the combination of many fractal sub populations at different hierarchical levels nested within one another. We find that for the U.S. Gulf of Mexico Outer Continental Shelf, the underlying distribution of oil and gas fields appears to be fractal. For the South Marsh, Eugene Island and Ship Shoal areas we assume the underlying distribution is fractal (as is observed by *Barton and Scholz* (1995) to be the case for regions worldwide) and calculate the size, volume and number of undiscovered fields.

Our results indicate that there are minimal (or no) remaining undiscovered oil reserves down to the 1.0 million barrel field size in the regions. However, the analysis indicates significant volumes of undiscovered gas (Tables 2 and 3, figure 13D). In particular, the gas remaining undiscovered is 674, 553 and 487 mmBOE, in Eugene Island Blocks, South Marsh North Addition, and Eugene Island South Addition, respectively. These reserves are predicted to be contained within smaller size fields. The largest fields predicted are three class 10 gas fields (mean field size 23 mmBOE) in the Eugene Island South Addition area.

Acknowledgments: We are grateful to D. Gautier and D. Higley for critical reviews. We thank Roger Anderson and the Global Basins Research Network for encouragement and advice. This work was funded by the Department of Energy Cooperative Agreement DE-FC22-93BC14961 subcontract 1245-187-L3.

References

- Arps, J.J., and Roberts, T.G., 1958, Economics of drilling for Cretaceous oil on the east flank of the Denver-Julesburg Basin: American Association of Petroleum Geologists Bulletin, v. 42, p. 2549-2566.
- Attanasi, E.D., Drew, L.J., 1985, Lognormal field size distributions a consequence of economic truncation: Mathematical Geology, v. 17, p. 335-351.
- Baker, R.A., Gehman, H.M., James, W.R., and White, D.A., 1984, Geologic field number and size assessments of oil and gas plays: American Association of Petroleum Geologists Bulletin, v. 68, p. 426-437.
- Barouch, E. and Kaufman, G.M., 1976, Oil and gas discovery modeled as sampling without replacement and proportional to random size: Sloan School Working Paper No. 888-76.
- Barton, C.C., and La Pointe, P.R., eds., 1995a, Fractals in the earth sciences: New York, Plenum Press, 265 p.
- , 1995b, Fractals in petroleum geology and earth processes: New York, Plenum Press, 317 p.
- Barton, C.C., and Scholz, C.H., 1995, The fractal size and spatial distribution of hydrocarbon accumulations--Implications for resource assessment and exploration strategy, *in* Barton, C.C., and La Pointe, P.R., eds., Fractals in petroleum geology and earth processes: New York, Plenum Press, p. 13-34.
- Barton, C.C., Scholz, C.H., Schutter, T.A., Herring, P.R., and Thomas, W.J., 1991, Fractal nature of hydrocarbon deposits--2, Spatial distribution: American Association of Petroleum Geologists Bulletin, v. 75, no. 3, p. 539.
- Barton, C. C. and Troussov, G.L., Fractal methodology for petroleum resource assessment and FRA – A computer program that calculates the volume and number of undiscovered hydrocarbon accumulations: U.S. Geological Survey Circular 1128, 23 p..
- Brett, J.F., and Feldcamp, L.D., 1993, The evidence for and implications of a fractal distribution of petroleum reserves: Society of Petroleum Engineers, SPE 25826, p. 73-84.
- Carmalt, S.W., and John, B. S., 1986, Giant Oil and Gas Fields of the World, *in* Halbouty, M.T., ed., Future petroleum Provinces of the World: American Association of Petroleum Geologists Memoir 40, p. 11-54.
- Crovelli, R.A., and Barton, C.C., 1995, Fractals and the Pareto distribution applied to petroleum field-size distributions, *in* Barton, C.C., and LaPointe, P.R., eds., Fractals in petroleum geology and earth processes: New York, Plenum Press, p. 59-72.
- Davis, J.C., and Chang, T., 1989, Estimating potential for small fields in mature petroleum province: American Association of Petroleum Geologists Bulletin, v. 73, p. 967-976.
- Drew, L.J., 1990, Oil and gas forecasting: Oxford, England, Oxford University Press, 252 p.
- Drew, L.J., Attanasi, E.D., and Schuenemeyer, J.H., 1988, Observed oil and gas field size distributions--A consequence of the discovery process and prices of oil and gas: Mathematical Geology, v. 20, p. 939-953.
- Drew, L.J., Schuenemeyer, J.H., and Bawiek, W.J., 1982, Estimation of the future rates of oil and gas discoveries in the western Gulf of Mexico: U.S. Geological Survey Professional Paper 1252, 26 p.
- Feder, Jens, 1988, Fractals: New York, Plenum Press, 283 p.
- Forman, D.J., and Hinde, A.L., 1985, Improved statistical method for assessment of undiscovered petroleum resources: American Association of Petroleum Geologists Bulletin, v. 69, p. 106-118.

- Holland, D. S., Leedy, J. B., and Lammlein, D. R., 1991, Eugene Island Block 330 Field – USA Offshore Louisiana: American Association of Petroleum Geologists, Treatise of Petroleum Geology, p.103-143.
- Houghton, J.C., 1988, Use of the truncated shifted Pareto distribution in assessing size distribution of oil and gas fields: *Mathematical Geology*, v. 20, no. 8, p. 907-937.
- Houghton, J.C., Dolton, G.L., Mast, R.F., Masters, C.D., and Root, D.H., 1993, U.S. Geological Survey estimation procedure for accumulation size distributions by play: *American Association of Petroleum Geologists Bulletin*, v. 77, no. 3, p. 454-466.
- Kaufman, G.M., 1962, Statistical decision and related techniques in oil and gas exploration: Englewood Cliffs, N. J., Prentice-Hall, 307 p.
- , 1983, Discovery process models; *in* Adelman, M.A., Houghton, J.C., Kaufman, G.M., and Zimmerman, M.B., eds.: *Energy resources in an uncertain future*: Cambridge, Mass., Balingier Press, p. 213-268.
- Korvin, Gabor, 1993, *Fractal models in the earth sciences*: Amsterdam, Elsevier, 396 p.
- Krige, D.G., 1951, A statistical approach to some basic mine valuation problems on the Witwatersrand: *South Africa* 52, no. 6, p. 119-139.
- Krohn, C.E., 1988, Sandstone fractal and Euclidean pore volume distributions: *Journal of Geophysical Research* 93, p. 3286-3296.
- Lee, P.J., and Wang, P.C.C., 1983a, Probabilistic formulation of a method for the evaluation of petroleum resources: *Mathematical Geology*, v. 15, no. 1, p. 163-181.
- , 1983b, Conditional analysis for petroleum resource evaluation: *Mathematical Geology*, v. 15, no. 2, p. 349-361.
- Lore, G. L., 1991, Exploration and discoveries, 1947-1989, Gulf of Mexico OCS: An historical perspective: Minerals Management Report 91-0078, 87 pp.
- Mandelbrot, B.B., 1982, *The fractal geometry of nature*: San Francisco, W.H. Freeman, 460 p.
- McCrossan, R.G., 1968, An analysis of size frequency distribution of oil and gas reserves of Western Canada: *Canadian Journal of Earth Sciences*, v. 6, p. 201-211.
- Melcanon, J. M., Bacigalupi, S. M., Kinler, C. J., Marin, D. A., and Prendergast, M. T., 1994, Outer continental shelf estimated proved oil and gas reserves, Gulf of Mexico, December 31, 1993: Minerals Management Service Report 94-0045, 49 pp.
- Middlebrooks, E. J., 1976, *Statistical calculations--How to solve statistical problems*: Ann Arbor, Mich., Ann Arbor Science, 120 p.
- Nehring, R., 1991, Oil and Gas resources; *in* Salvador, A., ed., *The Gulf of Mexico Basin*: Boulder, Colorado, Geological Society of America, *The Geology of North America*, v. J, p. 445-494.
- Power, M., 1992, Lognormality in the observed size distribution of oil and gas pools as a consequence of sampling bias; *Mathematical Geology*, v. 24, no. 8, p. 929-945.
- Salvador, A., 1991, Introduction; *in* Salvador, A., ed., *The Gulf of Mexico Basin*: Boulder, Colorado, Geological Society of America, *The Geology of North America*, v. J, p. 1-12.
- Scholz, C.H., and Barton, C.C., 1991, The fractal nature of hydrocarbon deposits--1. Size distributions: *American Association of Petroleum Geologists Bulletin*, v. 75, no. 3, p. 668.
- Scholz, C.H., and Mandelbrot, B.B., eds., 1989, *Fractals in geophysics*: Basel, Birkhauser, 313 p.
- Schuenemeyer, J.H., and Drew, L.J., 1983, A procedure to estimate the parent population of the size of oil and gas fields as revealed by a study of economic truncation: *Mathematical Geology*, v. 15, no. 1, p. 145-161.

- Schuenemeyer, J.H., and Drew, L.J., 1991, A forecast of undiscovered oil and gas in the Frio Strand Plain trend--The unfolding of a very large exploration play: American Association of Petroleum Geologists Bulletin, v. 75, no. 6, p. 1107-1115.
- Schuenemeyer, J.H., Drew, L.J., Root, D.H., and Attanasi, E.D., 1990, Estimating potential for small fields in mature petroleum provinces--Discussion: American Association of Petroleum Geologists Bulletin, v. 74, no. 11, p. 1761-1763.
- Schuster, H.G., 1988, Deterministic Chaos: VCH, Weinheim, 270 p.
- Shirley, Kathy, 1995, Modeling proved a profitable cost: AAPG Explorer, American Association of Petroleum Geologists, May 1995, p. 11-12.
- Taylor, G., 1994, Deep Risks Paying Off: Successes Buoy Gulf Hopes: AAPG Explorer, American Association of Petroleum Geologists, September 1994, p. 1 and 4.
- Turcotte, D. L., 1992, Fractals and chaos in geology and geophysics: Cambridge, Cambridge University Press, 221 p.
- Turcotte, D.L., and Huang, J., 1995, Fractal distributions in geology, scale invariance, and deterministic chaos; *in* Barton, C.C., and LaPointe, P.R., eds., Fractals in the earth sciences: New York, Plenum Press, p. 1-40.

Figure Captions

- Figure 1. A. Map showing location of structural limit of Gulf of Mexico basin. B. Map showing petroleum resources subprovinces of the Gulf of Mexico basin, including "Gulf Coast Offshore" which contains the areas assessed in this report.
- Figure 2. Map showing locations of South Marsh, Eugene Island and Ship Shoal Areas offshore Louisiana.
- Figure 3. Map showing locations of proved fields discovered: A. 1947-1959; B. 1960-1969; C. 1970-1979; D. 1980-1989.
- Figure 4. Log-log plot of six cumulative frequency-size distributions.
- Figure 5. Observed field-size distribution for oil and gas in the Frio Strand Plain exploration play, onshore Texas during three time periods; through 1960, through 1970, and through 1985. A., Histogram of the distribution's three discovery segments over time, when added, show the number of fields of a given size discovered through the specified year. (From Drew, 1990, figure E.4). B., Log-log plot by time segments of the cumulative frequency of oil and gas fields, $N(V)$, versus field size.
- Figure 6. Log-log plot of the cumulative frequency versus field size of oil and gas fields in the Gulf of Mexico Outer Continental Shelf (for all areas shown in figure 2) during three time periods; 1947 through 1959, through 1969, and through 1987.
- Figure 7. Schematic diagram, a log-log plot of cumulative frequency versus size, illustrating the differences between a theoretical fractal distribution (dashed line), a true fractal population between upper and lower fractal limits (UFL and LFL) (dotted line), and an observable population (solid line), which bends away from the theoretical fractal distribution at the perceptibility limit (PL).
- Figure 8. Log-log plot of cumulative frequency of oil field versus field size discovered in Eugene Island Area. Powerlaw line is fit to field sizes shown as solid circles. Field sizes shown as small dots fall below the perceptibility limit or above the upper fractal limit.
- Figure 9. Log-log plots. A, cumulative frequency of oil and gas fields, $N(V)$, versus field size discovered between 0 and 5,000 foot depths in the Permian Basin by December 31, 1974. Data from Schuenemeyer and others (1990, figure 2). B, Net volume of hydrocarbons per field size versus field size for the data shown in A.
- Figure 10. Log-log plot of frequency versus field size of oil and gas fields discovered in the Frio Strand Plain exploration play, onshore Texas, through 1985. Data from Schuenemeyer and Drew (1991, Figure 6). Regions of discovered and undiscovered hydrocarbons are shaded below line fit to data above the perceptibility limit (solid circles).
- Figure 11. Log-log cumulative frequency plot of synthetic data for a population composed of five sub populations, each with a power-law distribution characterized by the same slope a but different upper fractal limits. The combined size distribution shows strong concave-down curvature over the upper size ranges, similar to that of some hydrocarbon populations studied.
- Figure 12. Log-log plots of cumulative frequency vs. field size of oil and gas fields in subsections of the South Marsh, Eugene Island and Ship Shoal areas. Powerlaw line is fit to field sizes shown as solid circles. Field sizes shown as small dots fall below the perceptibility limit or above the upper fractal limit.
- Figure 13. Map view of subsections in the South Marsh, Eugene Island and Ship Shoal areas showing: A. Scaling exponents of the size vs. frequency distribution; B. Volumes of discovered oil and gas fields (MMBOE); C. Ultimate volume (discovered plus undiscovered) of hydrocarbon fields (MMBOE); D. Volume of undiscovered hydrocarbon fields (MMBOE); E. Percent of total hydrocarbon volume remaining undiscovered.

Table 1. Field-class size list

Field Class	Min. Field Size (MMBOE)	Max. Field Size (MMBOE)	Mean (log) (MMBOE)
1	0.0	0.0625	0.044
2	0.0625	0.125	0.088
3	0.125	0.25	0.18
4	0.25	0.5	0.35
5	0.5	1.0	0.71
6	1	2	1.41
7	2	4	2.83
8	4	8	5.66
9	8	16	11.31
10	16	32	22.63
11	32	64	45.25
12	64	128	90.5
13	128	256	181
14	256	512	362
15	512	1,024	724
16	1,024	2,048	1,448
17	2,048	4,096	2,896
18	4,096	8,192	5,792
19	8,192	16,384	11,584
20	16,384	32,768	23,168

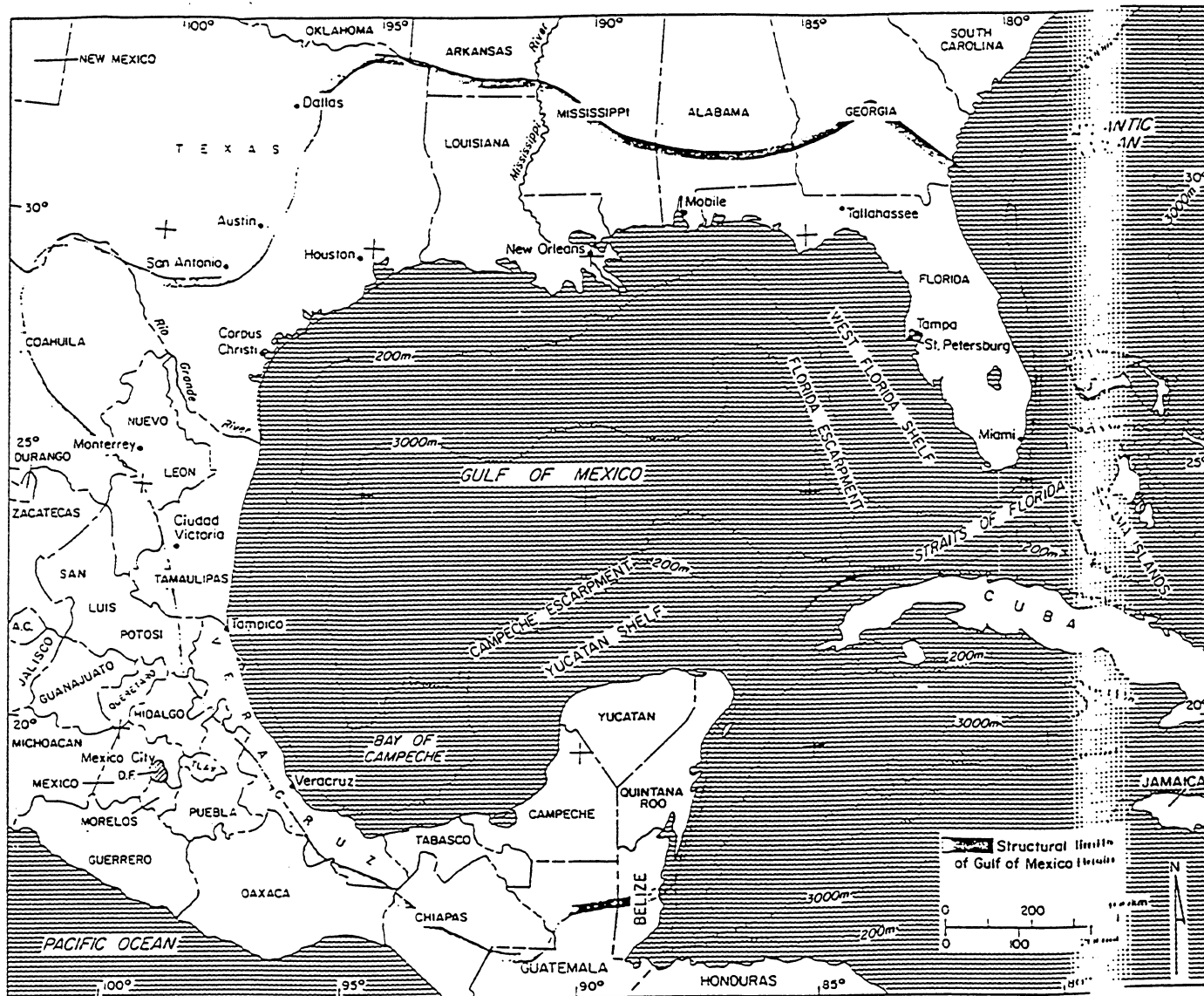


Figure 1A

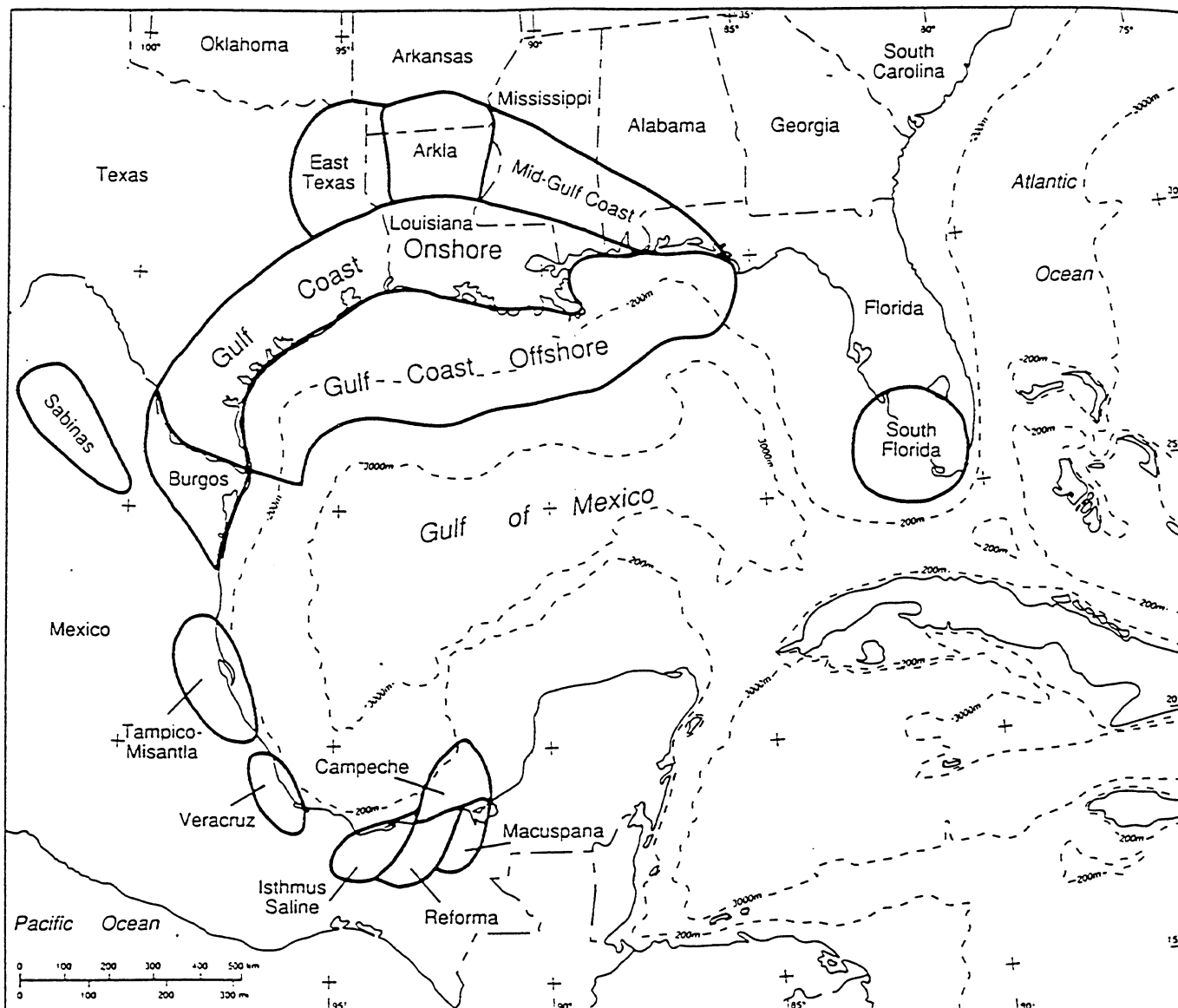
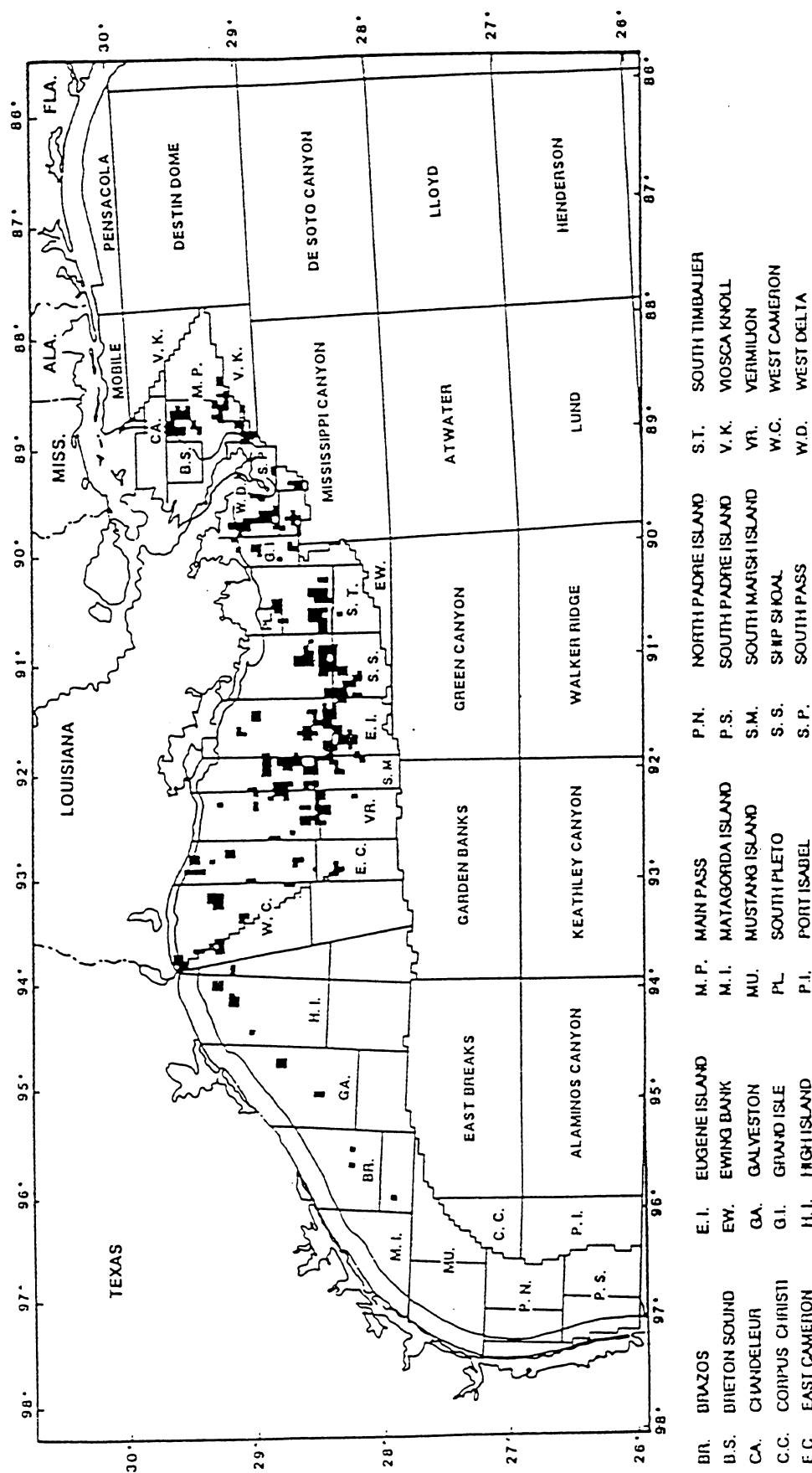


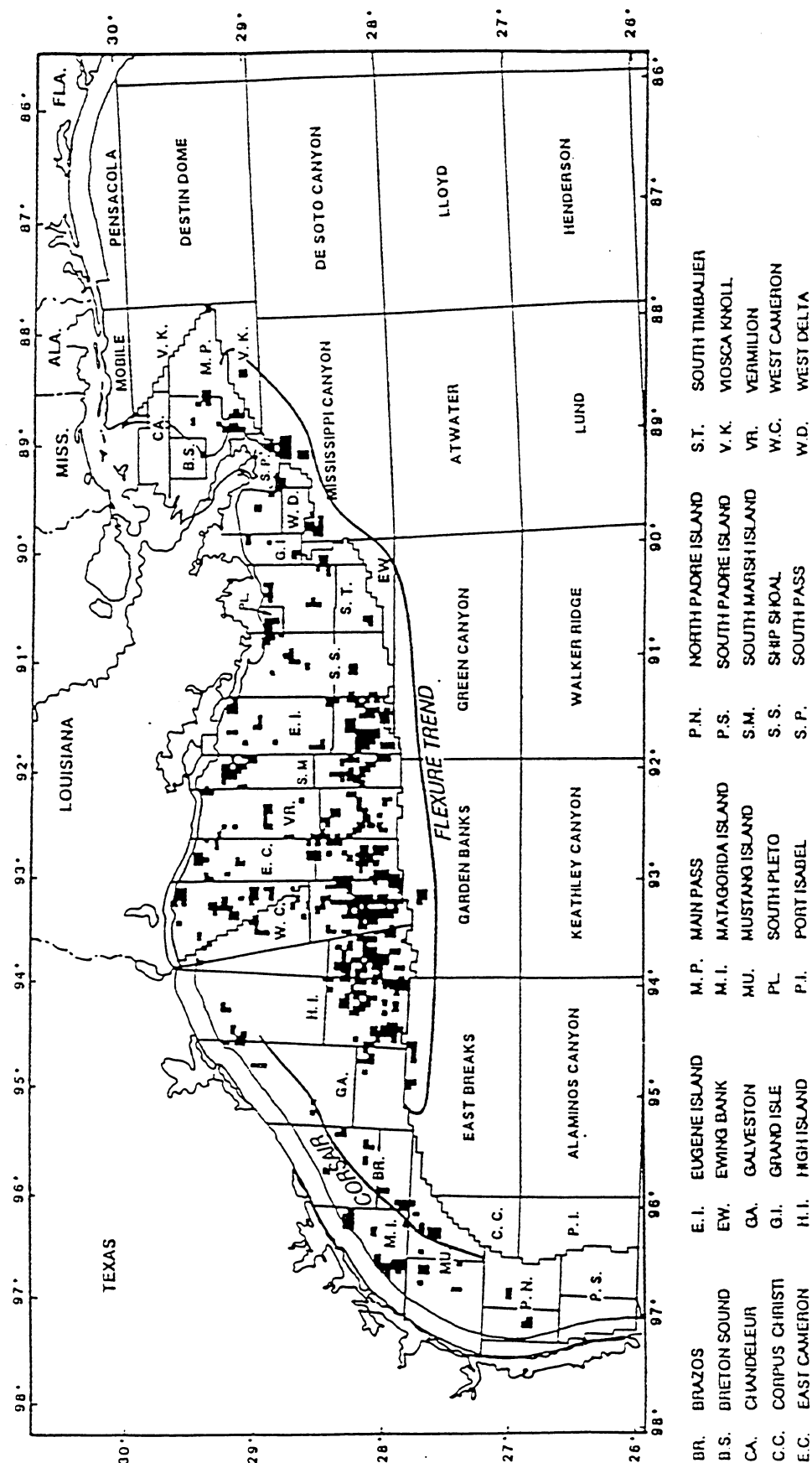
Figure 1B





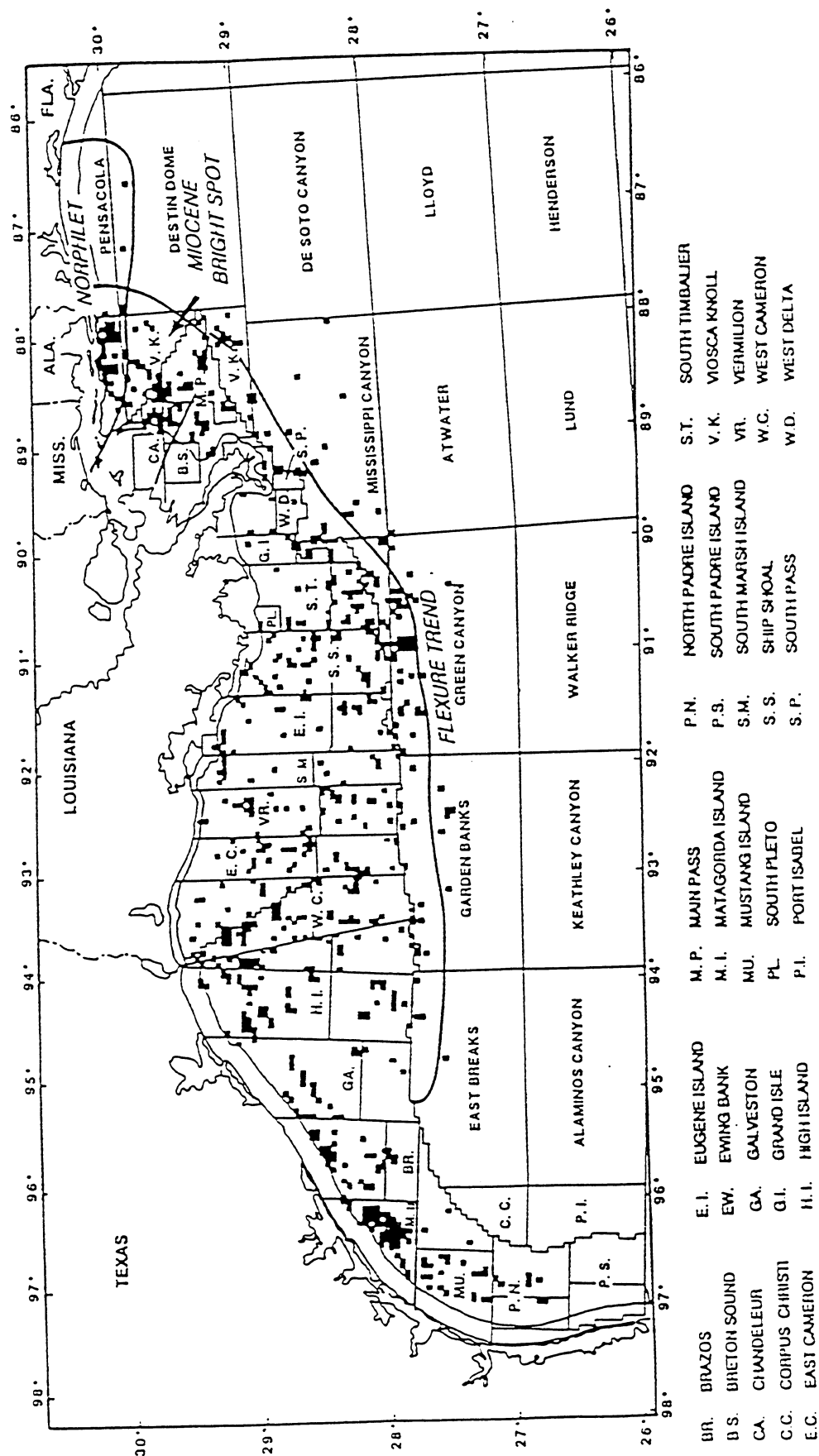
Location of proved fields discovered, 1960 - 1969.

Figure 3B



Location of proved fields discovered, 1970 - 1979.

Figure 3C



Location of proved fields discovered, 1980 - 1989.

Figure 3D

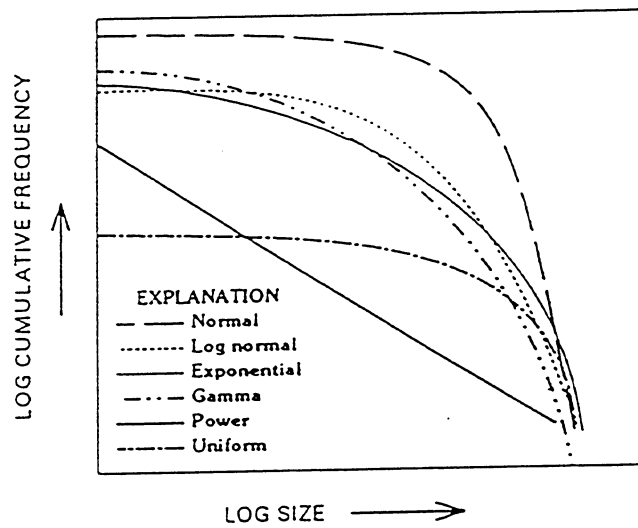


Figure 4

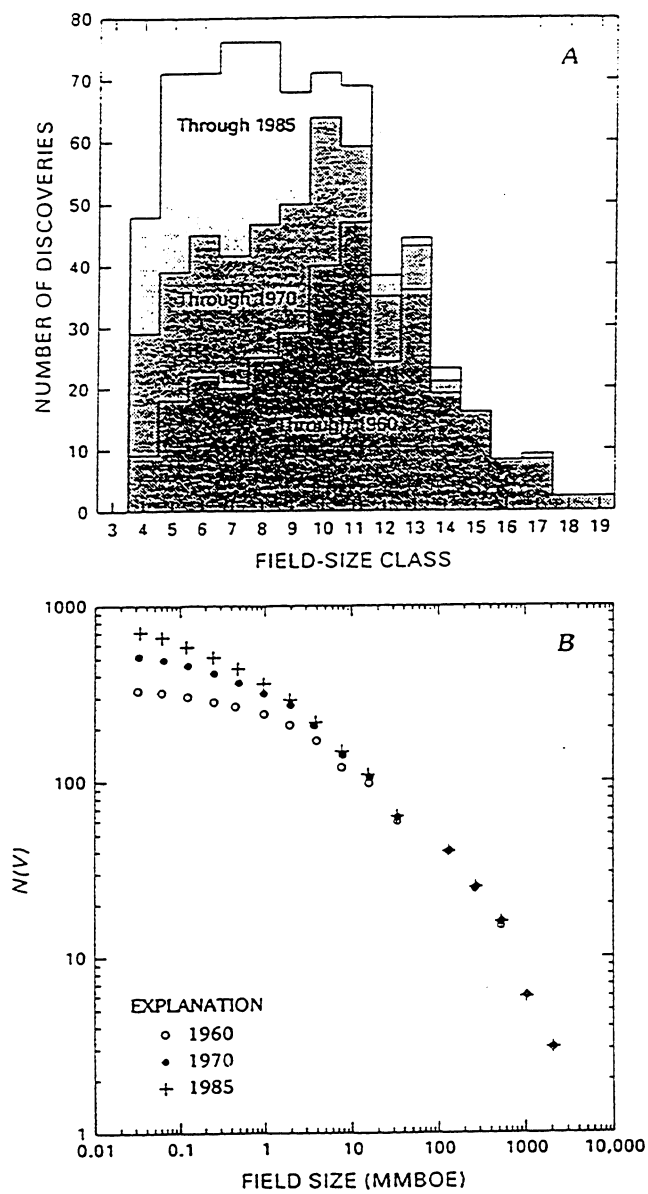


Figure 5

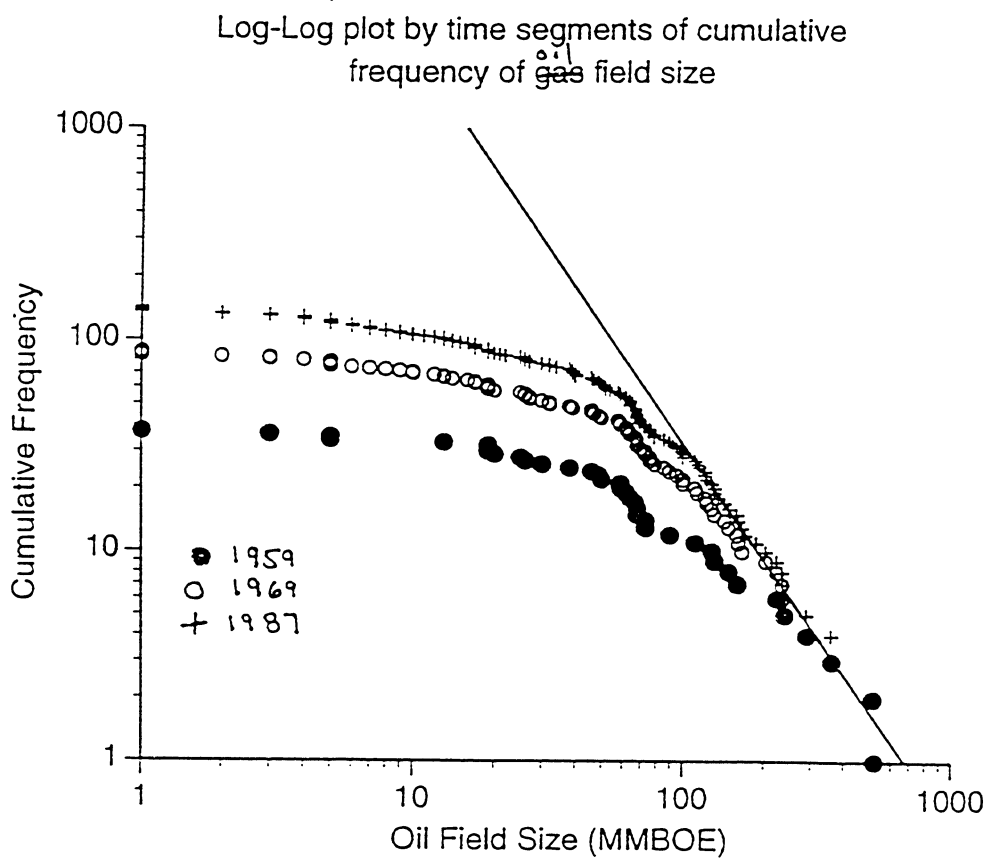
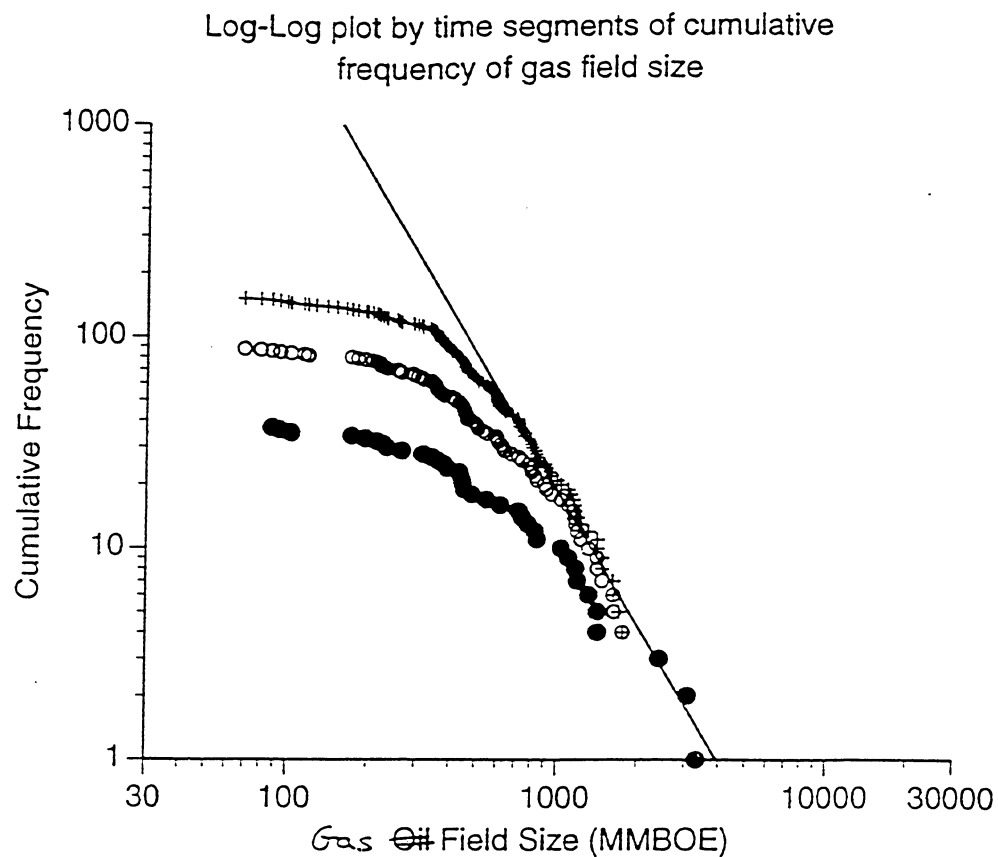


Figure 6

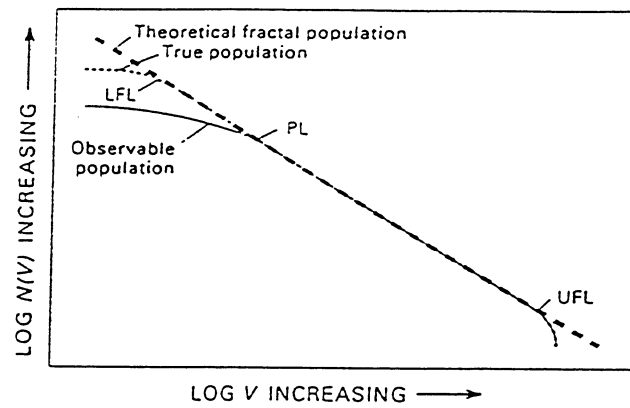


Figure 7

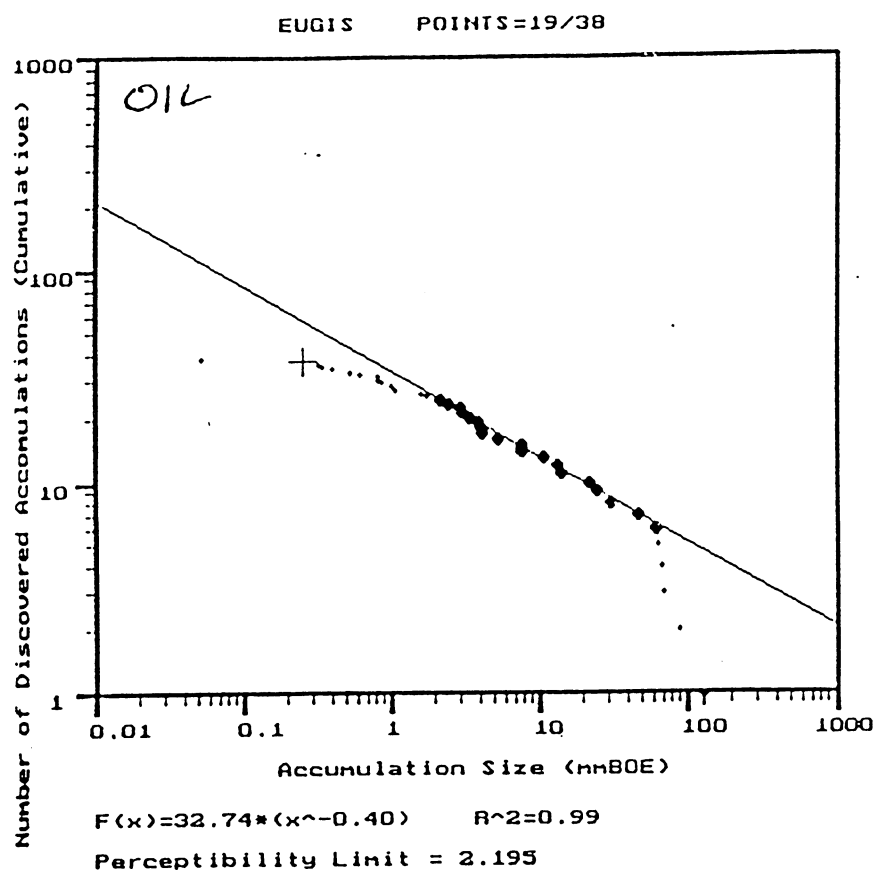


Figure 8

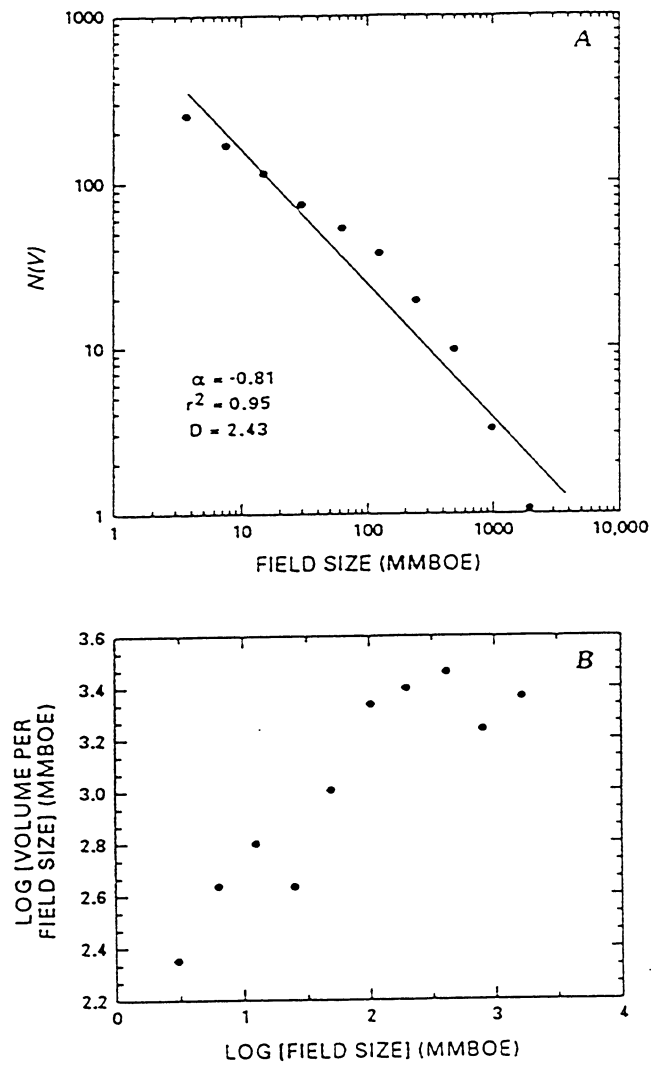


Figure 9

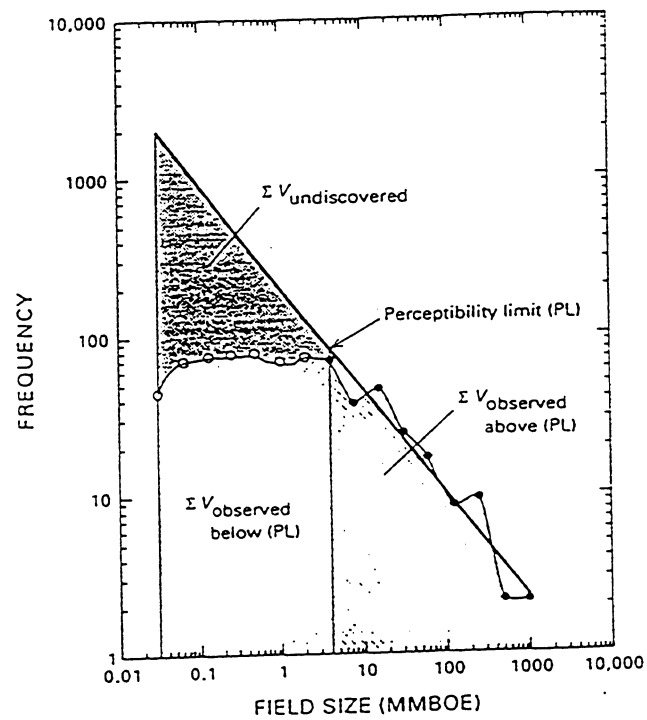


Figure 10

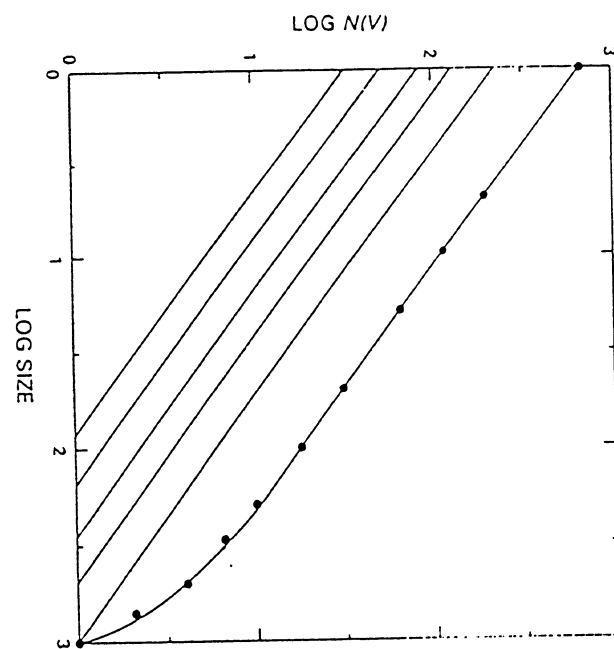
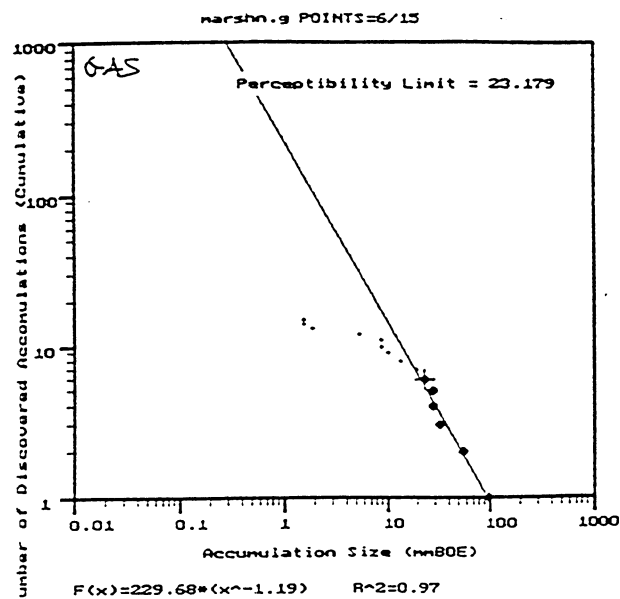
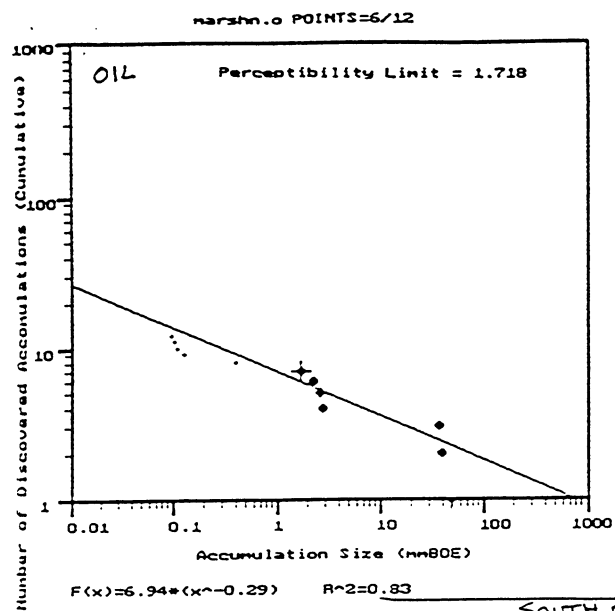
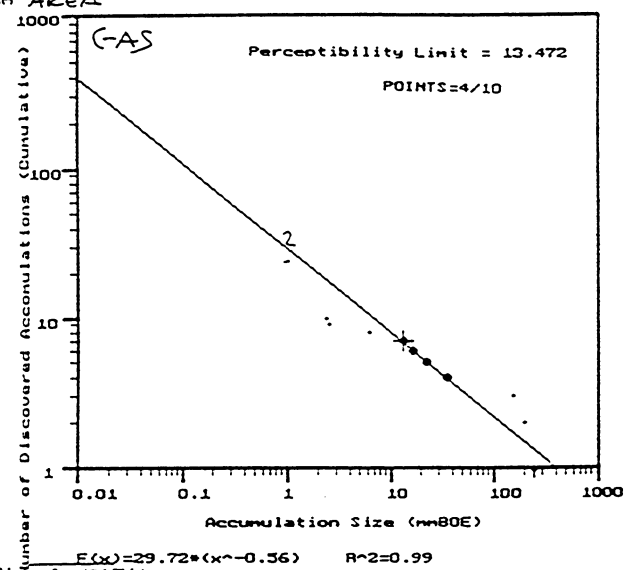
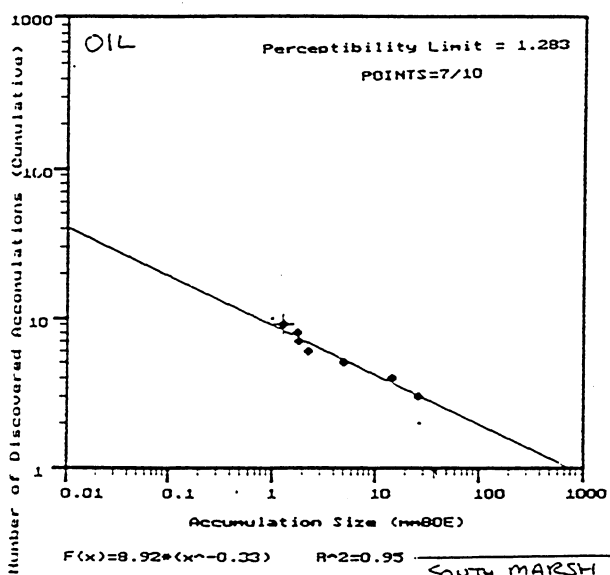


Figure 11



SOUTH MARSH AREA



SOUTH MARSH, SOUTH ADDITION

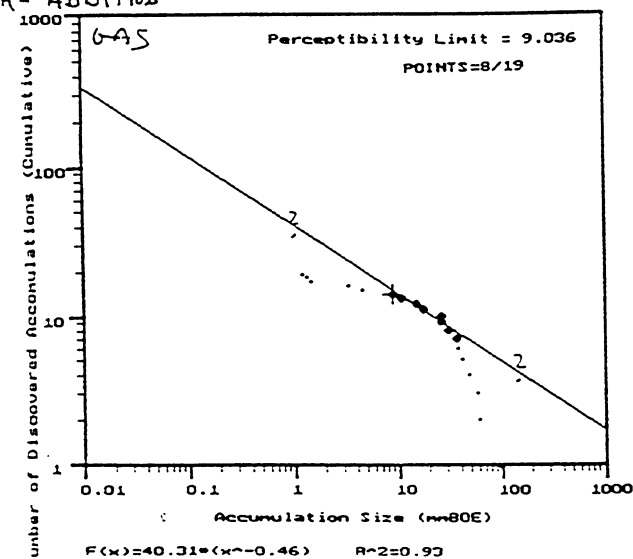
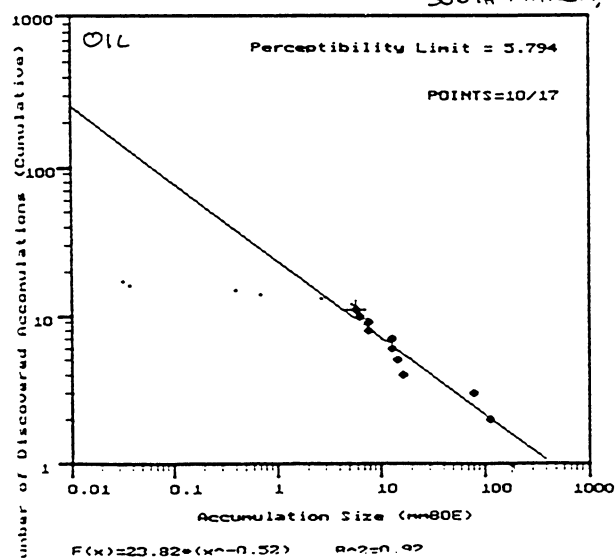
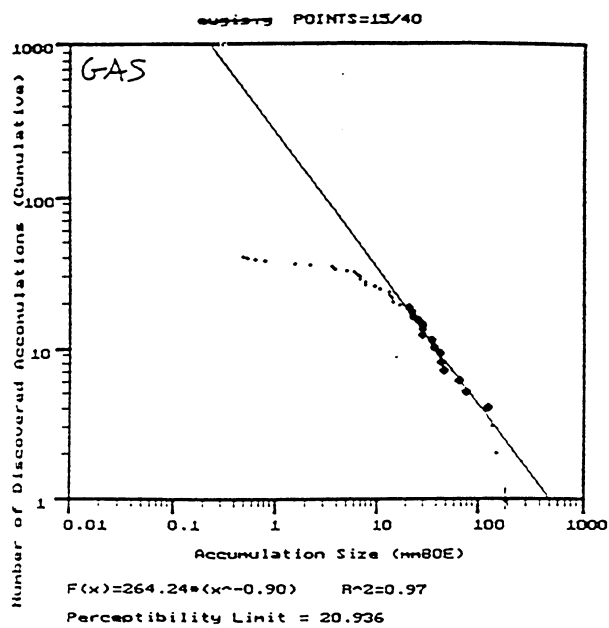
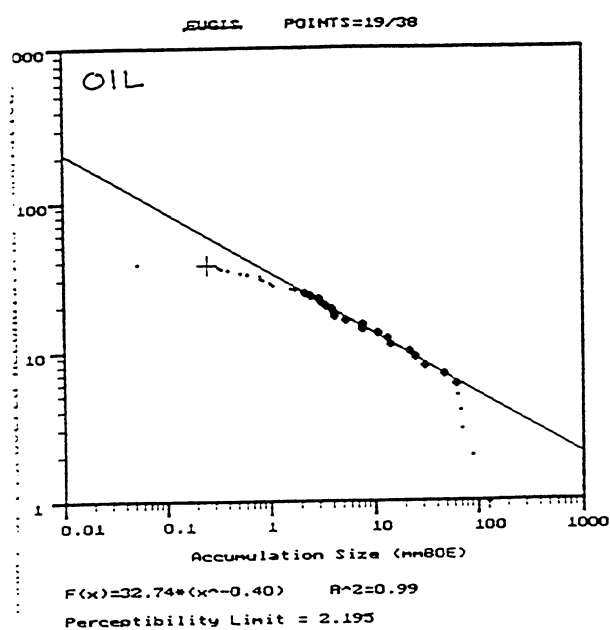


Figure 12 (1 of 3)

EUGENE ISLAND AREA



EUGENE ISLAND, SOUTH ADDITION

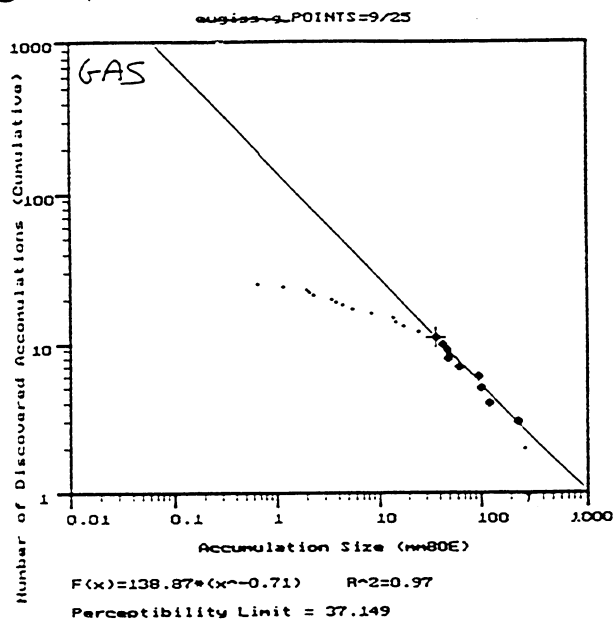
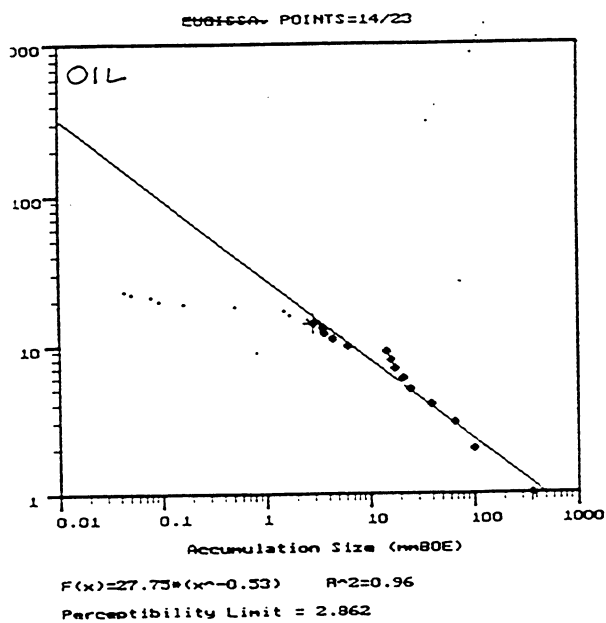
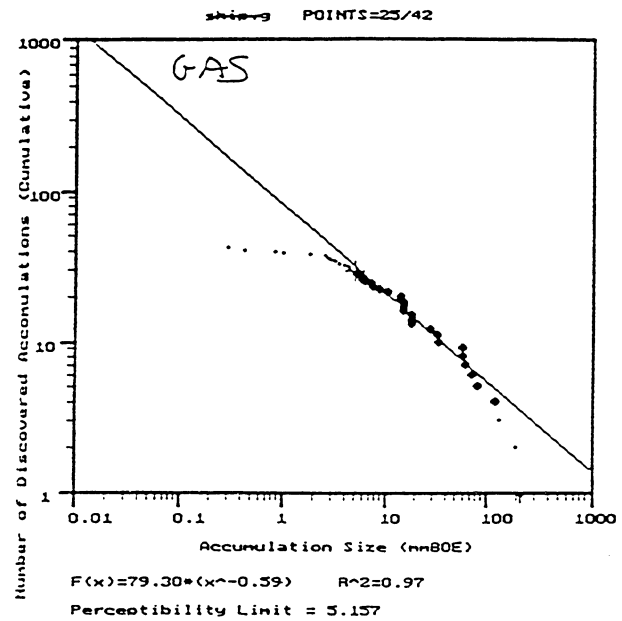
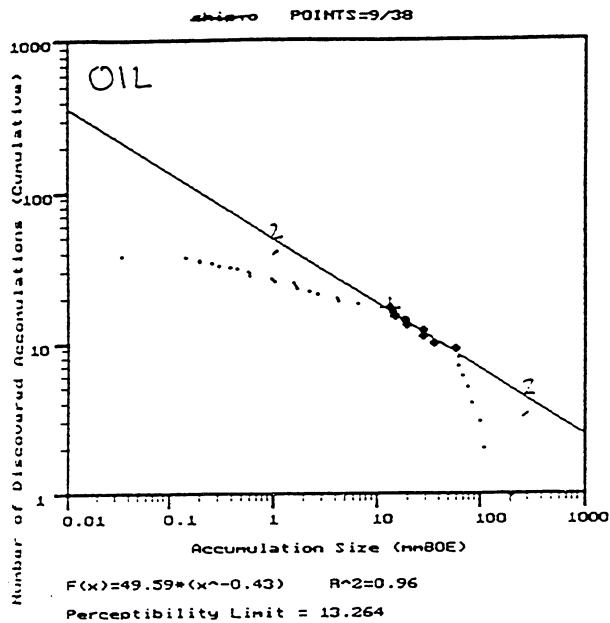


Figure 12 (2 of 3)

SHIP SHOAL AREA



SHIP SHOAL SOUTH ADDITION

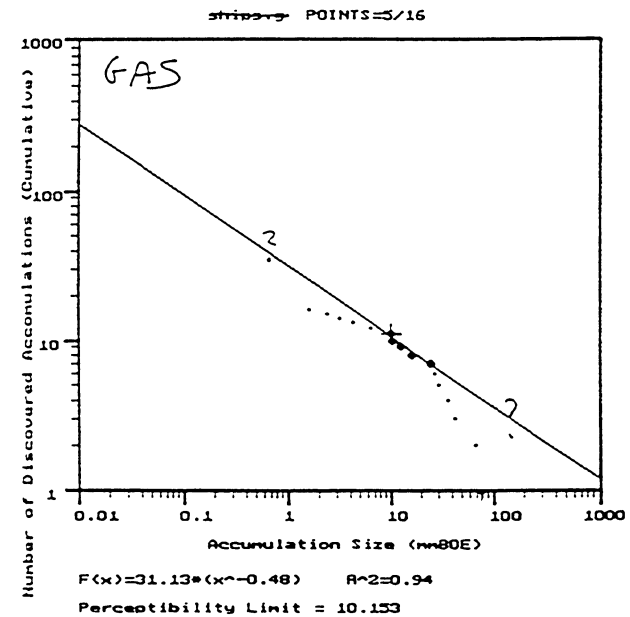
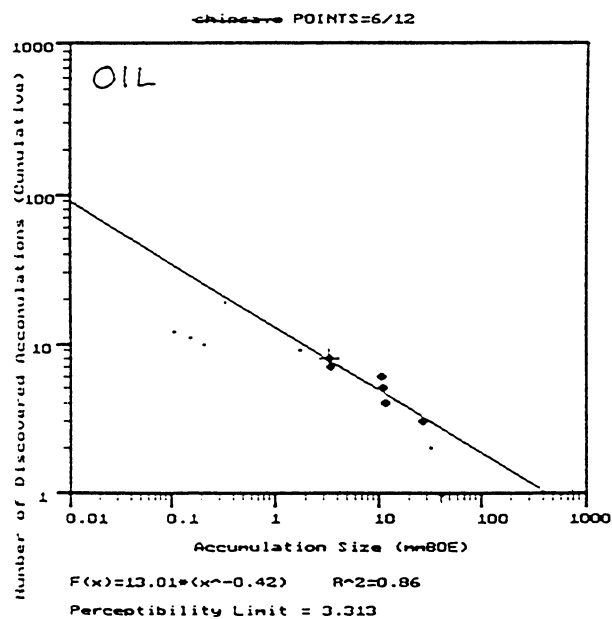
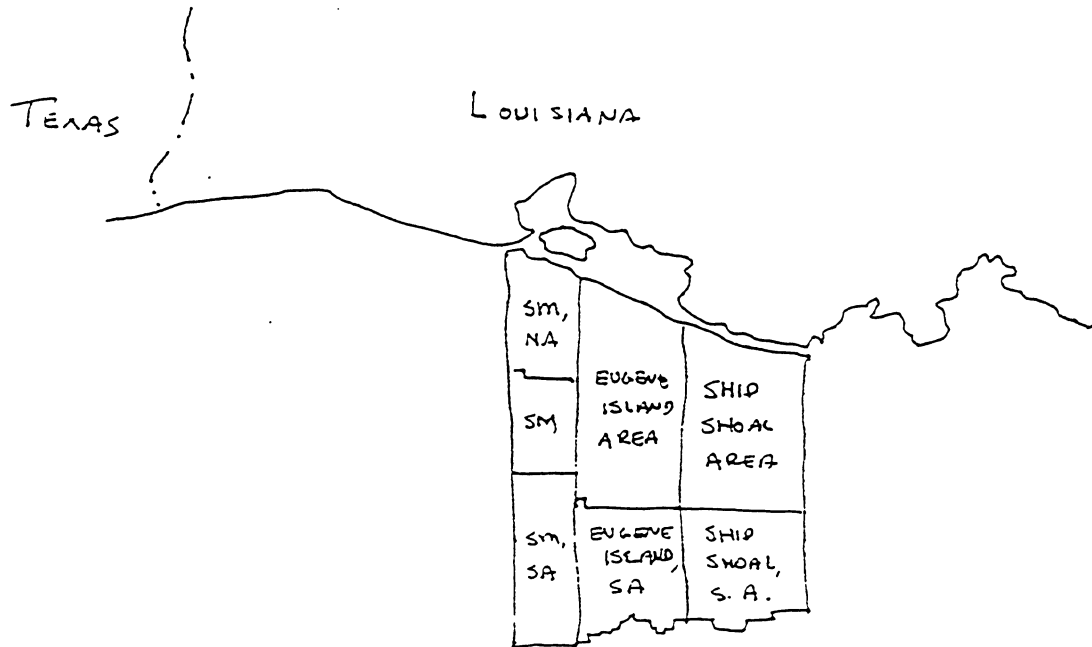


Figure 12 (3 of 3)



SCALING EXPONENTS, MAP VIEW

A

OIL

GAS

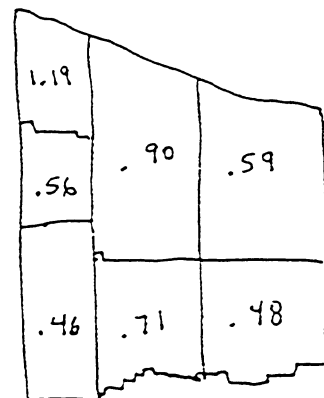
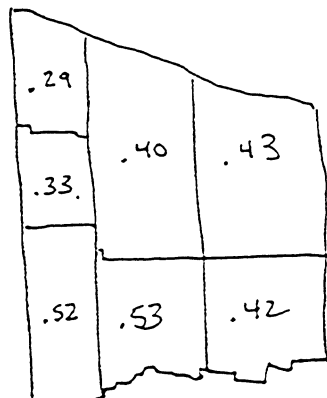


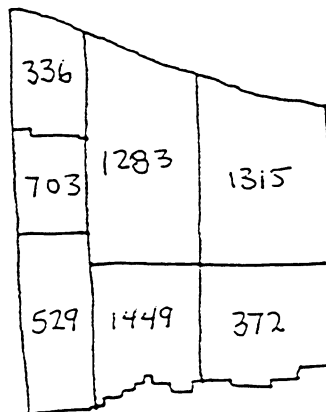
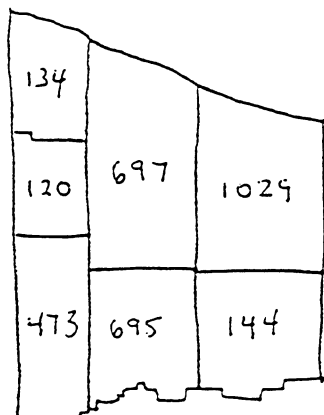
Figure 13 (1 of 3)

B

VOLUME OF DISCOVERED HYDROCARBONS (MMBOE)

OIL

GAS



C

TOTAL VOLUME (DISCOVERED + UNDISCOVERED)
(MMBOE)

OIL

GAS

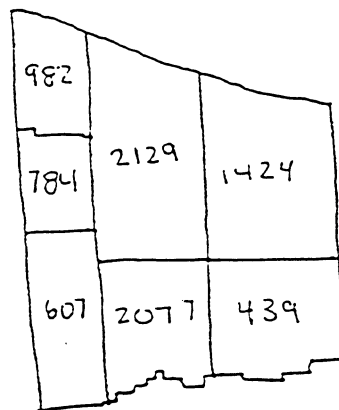
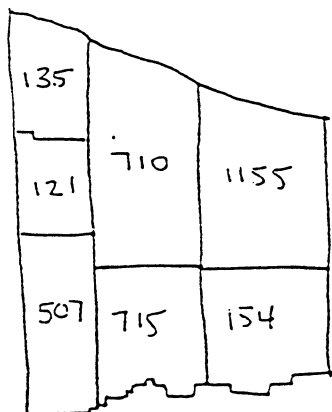
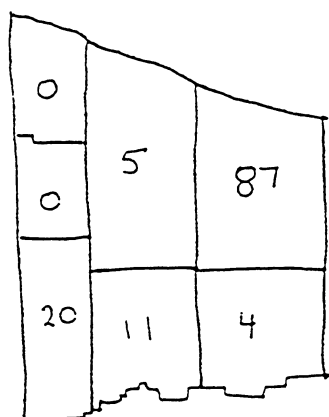


Figure 13 (2 of 3)

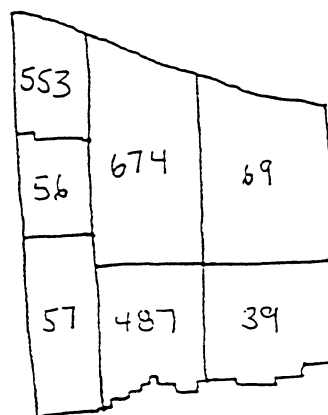
D

VOLUME REMAINING UNDISCOVERED (MMBOE)

OIL



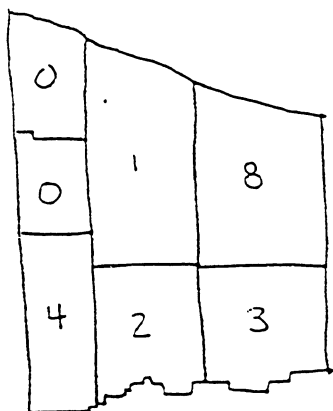
GAS



% REMAINING UNDISCOVERED

E

OIL



GAS

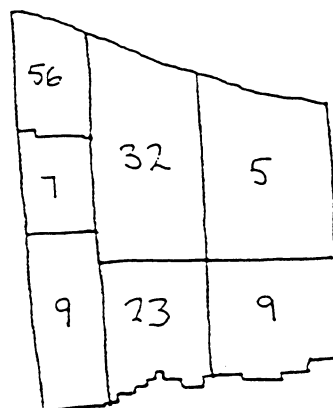


Figure 13 (3 of 3)

